

DISS. ETH NO. 24186

In Search of Charged Lepton Flavor Violating Decays at PSI

**R&D of a Fiber Hodoscope for the Mu3e Experiment and Study
of Novel Calibration Methods for the MEG / MEG II Experiment**

A thesis submitted to attain the degree of
DOCTOR OF SCIENCES of ETH ZURICH
(Dr. sc. ETH Zurich)

presented by

GIADA RUTAR

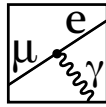
MSc ETH Physics
born on 15.12.1990
citizen of Solothurn SO

accepted on the recommendation of

Prof. Dr. Klaus Kirch, examiner
Prof. Dr. Christoph Grab, co-examiner

2017

ETH
Eidgenössische Technische Hochschule Zürich
Swiss Federal Institute of Technology Zurich



PAUL SCHERRER INSTITUT
PSI



Abstract

Our current best understanding of matter's constituents and the interactions among them is embodied in the Standard Model (SM) of particle physics. Although the SM is a tremendously successful theory, developed over decades by the spectacular interplay of theoretical and experimental efforts, it misses descriptions of phenomena like dark matter, dark energy or gravity, and it does not answer fundamental questions such as to why there is such a sizable matter-antimatter-asymmetry in the Universe. It is evident that there has to exist physics beyond the SM. The contemporary particle physicist's ultimate goal is to unravel it.

This dissertation revolves around two experiments at the intensity frontier looking for the charged lepton flavor violating (cLFV) muon decays $\mu^+ \rightarrow e^+\gamma$ and $\mu^+ \rightarrow e^+e^+e^-$, which constitute two complementary searches. Unlike other SM symmetries, which are fundamental in the sense that they are theoretically very well motivated, lepton flavor is an accidental, "empirical" symmetry. In fact, lepton flavor violation has been observed in the neutral sector through the discovery of the neutrino oscillations. In the charged sector however, no sign of lepton flavor violation has been found yet. Extending the SM by neutrino masses and mixing angles, cLFV decays would in principle be allowed, but the predicted branching ratios of $\mathcal{O}(\ll 10^{-50})$ are immeasurably small. cLFV is a clear sign of new physics and contained in essentially any Beyond the Standard Model theory, which forecast accessible, but nonetheless experimentally challenging branching ratios for $\mu^+ \rightarrow e^+\gamma$ and $\mu^+ \rightarrow e^+e^+e^-$.

The Paul Scherrer Institute (PSI) in Villigen, Switzerland, supplies the most intense continuous surface muon beams in the world with rates of $\mathcal{O}(10^8) \mu^+ / \text{s}$ and therefore hosts the cLFV experiments MEG / MEG II ($\mu^+ \rightarrow e^+\gamma$) as well as the future Mu3e experiment ($\mu^+ \rightarrow e^+e^-e^+$). The MEG experiment ran until 2013 and has recently beaten its own record in setting a new upper limit of $\mathcal{B} < 4.2 \times 10^{-13}$ (90 % confidence level) on the $\mu^+ \rightarrow e^+\gamma$ branching ratio [1]. With the goal to achieve a ten times better sensitivity, the compelling physics case has led the collaboration to pursue the upgraded version of the experiment MEG II [2] for which all sub-detectors and the electronics will either be modified or completely rebuilt. In addition to that, a few novel auxiliary detectors and calibration methods have been proposed to further improve the sensitivity and get a handle on the new components of the experimental apparatus. The Mu3e experiment [3], which follows a staged approach and is currently under development, aims at a sensitivity of 10^{-15} in a first phase and 10^{-16} in a second phase, implicating an improvement of three to four orders of magnitude compared to the predecessor experiment SINDRUM [4].

The first part of this thesis is dedicated to the development of the Mu3e timing detector based on scintillating fibers coupled to Silicon Photomultipliers (SiPMs), which is essential to suppress the accidental background to the $\mu^+ \rightarrow e^+e^-e^+$ search. While expertise on scintillating fibers has been around for a while, the SiPM technology is fairly new and nobody has ever built a detector that measures up with the demands of Mu3e, such that a dedicated R&D for its fiber hodoscope has been initiated. In order to study the attainable efficiencies and timing resolutions, several prototypes based on 250 μm thin fibers were developed and extensively tested in the laboratory and at PSI beam lines, showing that the proposed detector performances are achievable.

The second part of the thesis is dedicated to the MEG / MEG II experiment and focuses on three aspects. First, the development of a scintillating fiber based beam monitor tool which can be used for the fast, quasi-non-invasive and online monitoring of high intensity muon and positron beams, with the specific application to MEG II, is described. Second, a new calibration method for the positron spectrometer based on a Mott scattered positron beam tuned to the signal positron momentum of $\approx 52 \text{ MeV}/c$ is presented. This calibration tool was proposed in view of MEG II, which will feature a completely new positron spectrometer of strongly increased complexity. The potentialities of the Mott scattering calibration were studied with data acquired by the MEG experimental apparatus. It has proven to be a powerful and independent method to determine the resolutions of the positron spectrometer and to address questions related to the alignment of the drift chamber system. Third, the final MEG result, i.e. the above-mentioned upper limit of $\mathcal{B}(\mu^+ \rightarrow e^+\gamma) < 4.2 \times 10^{-13}$, is presented in more detail.

Sommario

La nostra migliore concezione delle componenti che costituiscono la materia e le interazioni tra di esse è sintetizzato nel modello standard (MS) della fisica delle particelle. Nonostante il MS come teoria, sviluppata nel corso di decenni grazie a un gioco d'alternanza spettacolare fra sforzi sperimentali e teorici, abbia un successo straordinario, manca di spiegare fenomeni come la materia oscura, l'energia oscura o la gravità, e non riesce a rispondere a delle domande fondamentali come per esempio sul perché ci sia una notevole asimmetria tra materia ed antimateria nell'universo. È evidente che debba esistere fisica oltre il MS. L'obiettivo più importante del fisico delle particelle odierno è di scoprirla e decifrarla.

Questa tesi di dottorato si incentra su due esperimenti alla frontiera d'alta intensità che cercano due decadimenti specifici del muone, $\mu^+ \rightarrow e^+\gamma$ e $\mu^+ \rightarrow e^+e^-e^+$, che violano la conservazione del sapore leptonico e che rappresentano due ricerche complementari. Al contrario di altre simmetrie nel MS, che sono fondamentali nel senso che sono molto ben motivate dal punto di vista teorico, il sapore leptonico è una simmetria accidentale, "empirica". Di fatto, la violazione del sapore leptonico è stata osservata nel settore neutrale grazie alla scoperta delle oscillazioni dei neutrini. Tuttavia, nel settore carico la violazione del sapore leptonico non è sinora stata individuata. Estendendo il MS a neutrini massicci e ai loro angoli di mescolamento, i decadimenti di particelle cariche che violano il sapore leptonico sarebbero consentiti, però il rapporto di decadimento previsto è dell'ordine di $\ll 10^{-50}$, ed è quindi talmente piccolo che non è misurabile. La violazione del sapore leptonico di particelle cariche è un chiaro segnale di nuova fisica ed è contenuta essenzialmente in tutte le teorie oltre il MS, le quali prevedono rapporti di decadimento per $\mu^+ \rightarrow e^+\gamma$ e $\mu^+ \rightarrow e^+e^-e^+$ che sono accessibili, anche se sperimentalmente sfidanti.

Con $\mathcal{O}(10^8)$ μ^+ /s, l'istituto Paul Scherrer (PSI) a Villigen in Svizzera fornisce i fasci continui di muoni più intensi al mondo e di conseguenza ospita due esperimenti alla caccia della violazione del sapore leptonico, l'esperimento MEG / MEG II ($\mu^+ \rightarrow e^+\gamma$) e il futuro esperimento Mu3e ($\mu^+ \rightarrow e^+e^-e^+$). L'esperimento MEG fu operativo fino al 2013 e ha poco tempo fa migliorato il suo proprio primato ponendo un nuovo limite superiore di $\mathcal{B} < 4.2 \times 10^{-13}$ (90% livello di confidenza) sul rapporto di decadimento di $\mu^+ \rightarrow e^+\gamma$ [1]. Con lo scopo di ottenere una sensibilità dieci volte migliore rispetto a MEG, la collaborazione ha deciso di perseguire la versione aggiornata del esperimento, MEG II [2], per la quale tutti i sottorivelatori e l'elettronica saranno modificati o ricostruiti da capo. Inoltre sono stati proposti dei nuovi rivelatori ausiliari e dei metodi di calibrazione, sia per migliorare ulteriormente la sensibilità che per afferrare le nuovi componenti dell'apparato sperimentale. L'esperimento Mu3e [3], che seguirà un approccio scaglionato e si trova in fase di sviluppo, mira ad una sensibilità al livello di 10^{-15} nella prima fase e 10^{-16} nella seconda fase, implicando un miglioramento di tre a quattro ordini di grandezza in confronto al precedente esperimento SINDRUM [4].

La prima parte di questa tesi è dedicata allo sviluppo del rivelatore temporale di Mu3e, basato sulle fibre scintillanti accoppiate a dei fotosensori capaci di contare singoli fotoni (in inglese

SiPM). Questo rivelatore è essenziale per sopprimere il fondo accidentale alla ricerca di $\mu^+ \rightarrow e^+ e^- e^+$. Sebbene le conoscenze tecniche riguardanti le fibre scintillanti è presente da un po' di tempo, la tecnologia dei SiPM è abbastanza nuova, e nessuno ha mai costruito un rivelatore che rendesse giustizia alle richieste di Mu3e, perciò è stato iniziato un programma di ricerca e sviluppo apposito. Per studiare le efficienze e le risoluzioni temporali ottenibili, sono stati costruiti e testati parecchi prototipi basati su fibre scintillanti sottili (250 μm) sia in laboratorio che lungo le linee di fascio al PSI, dimostrando che le prestazioni proposte sono raggiungibili.

La seconda parte della tesi è dedicato all'esperimento MEG / MEG II e tratta tre aspetti. Per primo viene descritto lo sviluppo di uno strumento, sempre basato su fibre scintillanti, per monitorare fasci di muoni e positroni intensi in un modo rapido, quasi-non-invasivo e online, con la specifica applicazione a MEG II. Poi viene presentato un nuovo metodo di calibrazione per lo spettrometro che misura il positrone. Il metodo si basa su un fascio di positroni diffuso Mott il cui impulso viene impostato al impulso del positrone di segnale ($\approx 52 \text{ MeV}/c$). Questo strumento di calibrazione è stato proposto in vista di MEG II, che sarà corredato di un nuovo spettrometro con una complessità elevata. Le potenzialità della calibrazione Mott sono state studiate con dati acquisiti con l'apparato sperimentale di MEG. Si è dimostrato essere un metodo potente e indipendente per determinare le risoluzioni dello spettrometro e per rispondere a delle questioni a riguardo dell'allineamento delle camere a deriva. Infine viene presentato in un modo più dettagliato il risultato finale di MEG, i.e. il succitato limite superiore di $\mathcal{B}(\mu^+ \rightarrow e^+ \gamma) < 4.2 \times 10^{-13}$.

Acknowledgements

I would like to thank my academic supervisor Prof. Dr. Klaus Kirch and the head of the PSI muon group Dr. Stefan Ritt for giving me the opportunity to work on the MEG and Mu3e experiments, and for the support and advice they gave me throughout my PhD. These were really interesting and enriching years! The one person that I am very much indebted to is my supervisor Dr. Angela Papa – it has truly been a great experience to work with her! Not only has she taught me a great deal about the art of doing science, but she also gave me a lot of food for thought outside the field of physics. I am grateful to the other members of the PSI muon group, especially to Peter-Raymond Kettle, Dr. Andreas Knecht, Dr. Alexander Mtchedlishvili, Felix Berg and Zachary Hodge, for the illuminating discussions. Special thanks go to Zachary for answering my numerous questions concerning the English language, and to both Felix and Zachary for the entertaining conversations.

I am thankful to Anita van Loon for helping me in all the administrative matters. Thanks go to Urs Gut and to René Laube from the Zentral- and Rohmateriallager for their readiness to help. I am grateful to the Versuchsmechanik workshop for providing us with the requested mechanical pieces especially in very urgent cases. Thanks go to Thomas Schneider and Claude David from CERN for introducing me to the technique of physical vapor deposition, and to Michael Horisberger from the PSI LDM sputtering laboratory for supporting our activities. I would also like to thank the people from the electronics pool, specifically Urs Greuter and Ueli Hartmann, for their help concerning the preamplifiers and the SiPM PCBs. Special thanks go to the PSI detector group, in particular to Dr. Malte Hildebrandt and Florian Barchetti for their support in the construction of the fiber prototypes. Thank you to Malte for always having an open ear for me!

Many thanks go to my MEG colleagues Prof. Dr. Fabrizio Cei, Dr. Gordon Lim, Dr. Francesco Renga and Dr. Ryu Sawada for the fruitful discussions for what concerns the analysis of positron data and the MEG software. I am grateful to the MEG TC and the LXe group for letting us use their thermal chambers. Great thanks go to Dr. Yury Yudin for his effort in adapting the PSI preamplifiers to our purposes. I am very much indebted to Dr. Luca Galli and Dr. Stefan Ritt for supporting us for what concerns the electronics during the beam monitor test. I would like to thank the RDC group, especially Ryoto Iwai, who contributed to the characterization of the SiPMs. Big thanks go to Dr. Emanuele Ripiccini: Not only did he give me useful advice, but he also brought a lot of good mood to the small group of ATAR! Thank you to all the students in MEG, in particular to Miki, it has been a pleasure to spend time with them and I truly enjoyed the cultural exchanges! I am grateful to the Mu3e scintillating fiber group, in particular to Prof. Dr. Alessandro Bravar, Prof. Dr. Christoph Grab, Simon Corrodi, Antoaneta Damyanova and Dr. Roman Gredig, for the useful discussions. I would also like to thank Dr. Frederick Gray for his help and advice during the few months that he was working with us.

I am very grateful to Dr. Andreas Eggenberger for proof-reading part of my thesis, and of

course for the wonderful friendship. He and his wife Martina, together with their little son, gave me a lot of moral support! It goes without mentioning that I am deeply indebted to my parents Cinzia and Sacha as well as my sister Viola: If I stand here in the place I am now, it is thanks to all their encouragement, affection and patience! Thanks go to Viola for proof-reading part of my thesis. Last but not least I consider myself extremely lucky to have had the chance to enter MEG, as I was able to meet a very special person – thank you Shota for all your love and support, and for all your positivity!

Contents

I	Introduction to Charged Lepton Flavor Violation Searches and Experiments	1
1	Charged Lepton Flavor Violation Searches	2
1.1	A Rationale for cLFV Searches	2
1.2	Effective Field Theory Approach	4
1.3	Experimental Status and Future cLFV Searches	5
1.4	Event Signatures and Backgrounds	5
1.4.1	The $\mu^+ \rightarrow e^+ \gamma$ Search	8
1.4.2	The $\mu^+ \rightarrow e^+ e^- e^+$ Search	9
2	Muon Beams at PSI	12
2.1	Muon Production	12
2.2	High Intensity Proton Accelerator Facility	13
2.3	Beam Lines	13
2.3.1	The π E5 Channel	14
2.3.2	The π M1 Channel	16
2.3.3	The π E1 Channel	16
3	The Mu3e Experiment	17
3.1	Experimental Concept	17
3.1.1	Coordinate System	18
3.2	Compact Muon Beam Line and Muon Stopping Target	18
3.3	Tracking System	20
3.3.1	Magnet	20
3.3.2	Pixel Detector	22
3.4	Timing System	23
3.4.1	Fiber Detector	23
3.4.2	Tile Detector	25
3.5	Data Acquisition and Online Event Selection	26
4	The MEG and MEG II Experiment	28
4.1	Experimental Concept	28
4.1.1	Coordinate System	28
4.2	MEG Beam Line and Muon Stopping Target	29
4.3	Positron Spectrometer	32
4.3.1	COBRA Magnet	32

Contents

4.3.2	Drift Chamber System	33
4.3.3	Timing Counter	35
4.4	Liquid Xenon Calorimeter	38
4.5	Calibrations and Monitoring	40
4.5.1	Calibrations of the Positron Spectrometer	40
4.5.2	Calibrations of the Liquid Xenon Calorimeter	41
4.5.3	Detector Intercalibrations	43
4.6	Trigger and Data Acquisition	43
4.6.1	Trigger	44
4.6.2	Data Acquisition	44
4.7	Offline Analysis Software and Simulation	45
4.8	Upgrade: The MEG II Experiment	45
4.8.1	Beam Line and Target	47
4.8.2	Positron Spectrometer	49
4.8.3	Liquid Xenon Calorimeter	50
4.8.4	Trigger and Data Acquisition	51
4.8.5	Novel Auxiliary Detectors	53
II	The Mu3e Experiment	54
5	The Mu3e Fiber Hodoscope	56
5.1	Purpose and Requirements	56
5.2	Impact on the Experiment	57
5.3	Baseline Design	57
5.3.1	Mechanics	58
5.3.2	Photosensors	58
5.3.3	Electronics	58
6	R&D of a Scintillating Fiber Detector for Mu3e	60
6.1	Scintillating Fibers	60
6.1.1	Working Principle and Basic Properties	60
6.1.2	Characterization and Quality Control	68
6.1.3	Optical Isolation	70
6.2	Silicon Photomultipliers	76
6.2.1	Working Principle	76
6.2.2	Basic Properties	79
6.2.3	Characterization	83
6.3	Mechanical Considerations	89
6.3.1	Fiber Array Production and Mounting	91
6.3.2	Fiber-SiPM-Alignment	91
6.4	Front-End Electronics	94
6.5	Data Acquisition System	97

Contents

6.6	Hodoscope Prototypes and Experimental Setup	99
6.6.1	Prototypes	99
6.6.2	Standard Setup	100
6.6.3	Waveform Analysis	103
6.7	Results	104
6.7.1	Light Yield	104
6.7.2	Detection Efficiencies	107
6.7.3	Timing Resolution	112
6.7.4	Temperature Dependence	116
6.7.5	Fiber Alignment	116
6.8	Extrapolation of the Performances to the Final Detector	118
6.8.1	Light Yield	118
6.8.2	Detection Efficiency	120
6.8.3	Timing Resolution	122
III	The MEG Experiment	124
7	R&D of Auxiliary Detectors Based on Scintillating Fibers	126
7.1	Beam Monitoring	126
7.1.1	Experimental Setup	126
7.1.2	Results	130
7.2	Particle Identification	138
7.2.1	Charge Discrimination	138
7.2.2	Time-Of-Flight	138
7.3	Radiation Hardness	141
8	The Mott Scattering Calibration Method	144
8.1	Introduction	144
8.1.1	Mott Scattering Mechanism	144
8.1.2	Realization	146
8.2	Distribution of Mott Scattering Vertices on the Target	148
8.3	Mott Monochromatic Energy Line	148
8.4	Theta Angular Distribution	149
8.5	Spectrometer Resolutions from Double Turn Tracks	149
8.5.1	Methodology	150
8.5.2	Results	151
8.6	Drift Chamber Alignment	157
8.6.1	Checks of the Drift Chamber Alignment	157
8.6.2	Performing the Drift Chamber Alignment with Mott Data	159
9	The Final MEG Result	162
9.1	Dataset and Blinding Procedure	162

Contents

9.2	Background Studies	163
9.2.1	Radiative Muon Decay	164
9.2.2	Accidentals	164
9.3	Estimation of the Number of Signal Events	166
9.4	Toy Monte Carlo Simulations	168
9.5	Construction of the Confidence Interval	169
9.6	Evaluation of the Sensitivity	170
9.7	Normalization	170
9.8	Improvements in the Analysis	171
9.8.1	Missing First Turn Algorithm	171
9.8.2	Annihilation-in-Flight Analysis	172
9.9	Target Deformation Issue	172
9.10	Results	176
9.11	Additional Checks	179
IV	Synopsis	181
10	Summary Mu3e	182
11	Summary MEG	184
	Backmatter	186
	Bibliography	186
	Acronyms	192

List of Figures

Title image: Aerial photograph of PSI [5]	3
1.1 SM diagram contributing to the $\mu^+ \rightarrow e^+\gamma$ decay	3
1.2 Complementarity of $\mu^+ \rightarrow e^+\gamma$ and $\mu^+ \rightarrow e^+e^-e^+$	6
1.3 History of muon cLFV searches	7
1.4 Signal and backgrounds of the $\mu^+ \rightarrow e^+\gamma$ search	8
1.5 Signal and backgrounds of the $\mu^+ \rightarrow e^+e^-e^+$ search	10
1.6 Leading order $\mathcal{B}(\mu^+ \rightarrow e^+e^-e^+\nu_e\bar{\nu}_\mu)$ vs. invisible energy	11
2.1 PSI HIPA Cockcroft-Walton accelerator and ring cyclotron	14
2.2 Map of the PSI HIPA facility	15
2.3 The π E5 beam line at PSI	16
3.1 Phases of the Mu3e experiment	19
3.2 Compact Muon Beam Line	21
3.3 Muon stopping target	22
3.4 MuPix 7 chip	23
3.5 Scintillating fiber timing detector	24
3.6 Scintillating tile timing detector	25
3.7 Mu3e readout	27
4.1 Layout of the MEG experiment	30
4.2 MEG beam line	31
4.3 Muon stopping target	32
4.4 COBRA gradient magnetic field	34
4.5 Drift chamber system	36
4.6 Sketch of a drift chamber module	37
4.7 Timing counter	38
4.8 Liquid xenon calorimeter	40
4.9 MEG Cockcroft-Walton accelerator	42
4.10 MEG crate	46
4.11 Layout of the MEG II experiment	48
4.12 MEG II cylindrical drift chamber	49
4.13 MEG II pixelized timing counter	51
4.14 MEG II liquid xenon calorimeter	52
5.1 Mu3e scintillating fiber hodoscope	56
5.2 Timing suppression of accidental background	57

List of Figures

5.3	SiPM array readout	59
6.1	Benzene structure	61
6.2	Energy level diagram of an organic molecule's π -electrons	62
6.3	Meridional and skew rays for squared fibers	65
6.4	Simulated attenuation length	66
6.5	Emission spectrum of the BCF-12 scintillator	68
6.6	Fiber geometry	70
6.7	Setup to measure the attenuation length	71
6.8	Comparison between a bare and an aluminum coated fiber	72
6.9	Setup to measure light losses due to high refractive index surroundings	73
6.10	Crosstalk among fibers with and without aluminum coating	74
6.11	Aluminum deposit through sputtering and PVD	75
6.12	Sketch of an APD	77
6.13	Schematic I-V-curve	78
6.14	SiPM architecture	79
6.15	Equivalent electrical circuit and a sketch of a SiPM's waveform	80
6.16	PDE as a function of wavelength	82
6.17	Hamamatsu 13360-1350CS	85
6.18	SiPM I-V-curves at different temperatures	85
6.19	Dark count spectra and rates for the new vs. old SiPM series	86
6.20	Illustration of the method used to extract the CTP	87
6.21	CTP for the old vs. new SiPM series	88
6.22	Average NPhe and relative efficiency of a single fiber vs. bias voltage	90
6.23	Device to construct the fiber arrays	92
6.24	Simulated photon distribution on the SiPM	94
6.25	Fiber-SiPM-alignment	95
6.26	PSI preamplifier	96
6.27	Waveforms with and without pole-zero cancellation	97
6.28	Novosibirsk preamplifier	98
6.29	DRS evaluation board	99
6.30	Prototype history	100
6.31	The Large Prototype	101
6.32	Sketch of the laboratory setup	102
6.33	Pictures of the laboratory and beam test setup	103
6.34	Sketch of the two offline trigger configurations AND and OR	105
6.35	Typical charge spectra for the two SiPM logic configurations	106
6.36	Average number of photoelectrons upon the passage of a MIP	106
6.37	Sketch of the inclined illumination	107
6.38	Light yield increase for a non-zero θ -angle	107
6.39	Particle tracks for different ϕ -angles	108
6.40	Measured SiPM charge spectrum with overlaid probability distribution	110
6.41	Configurations to evaluate the fiber detection efficiencies and crosstalk	111
6.42	Single fiber timing distribution	114

List of Figures

6.43	Multifiber timing distributions	115
6.44	Thermal chamber setup	116
6.45	Temperature dependence of the light yield and the timing	117
6.46	Collimator scans to measure the relative fiber alignment	118
6.47	Fibers combined offline to emulate the SiPM array readout	119
6.48	Typical offline array charge spectra for the two SiPM logic configurations	119
6.49	Sketch of the axial fiber scan	121
6.50	Light yield vs. impact position on the fiber	121
6.51	Timing for the emulated array readout	123
7.1	Scintillating fiber beam monitor prototype	127
7.2	WaveDREAM crate	128
7.3	Setup of the scintillating fiber beam monitor prototype in $\pi E5$	129
7.4	Muon beam profiles measured with the beam monitor prototype	131
7.5	3D muon beam profile	132
7.6	Muon beam profiles for different beam focusing	133
7.7	Muon beam profiles for different separator settings	134
7.8	Muon range curve in Mylar measured with the beam monitor prototype	136
7.9	Beam profile as a function of the degrader thickness	137
7.10	Particle identification by charge discrimination	139
7.11	Particle identification by time-of-flight	140
7.12	Radiation damage	143
8.1	Theoretical angular distribution of Mott scattered positrons	146
8.2	Time-of-flight spectrum of the Mott calibration's positron beam	147
8.3	Distribution of reconstructed Mott scattering vertices on the target	148
8.4	Mott monochromatic energy spectrum	149
8.5	Measured angular distribution of Mott scattered positrons	150
8.6	Sketch of the acceptance in θ vs. the scattering vertex' z -coordinate	151
8.7	Double turn track method	151
8.8	Double turn resolutions measured with Mott 2012 data	154
8.9	Number of hits per track Mott vs. Michel positrons	155
8.10	Number of hits per track for different pile-up conditions	156
8.11	Drift chamber alignment check with Mott data	158
8.12	Distributions of the hit-track residuals in r and z	159
8.13	Wire hit map for the Mott 2013 data	160
8.14	Results of the DCH alignment based on the Mott 2013 data	161
9.1	Accumulated number of muons stopped on target as a function of time	163
9.2	Blinding box, analysis window and sidebands	164
9.3	Sideband data	165
9.4	Differential distributions of RMD events	166
9.5	Effective background branching ratios in the MEG analysis window	167
9.6	Normalization factor for the different years	171

List of Figures

9.7	Missing first turn recovery algorithm	173
9.8	AIF identification	174
9.9	Target deformation	175
9.10	Sensitivity of the MEG experiment	176
9.11	Event distribution in the analysis window	177
9.12	Negative log-likelihood ratio as a function of the branching ratio	177
9.13	Best fitted likelihood projections	178
9.14	Upper limits obtained with event-by-event vs. constant PDFs	180

List of Tables

1.1	Experimental limits and planned sensitivities of cLFV muon decay experiments	7
4.1	Average signal detector resolutions and efficiencies of the MEG experiment . . .	29
4.2	Properties of liquid xenon	39
4.3	Average signal detector resolutions and efficiencies of the MEG II experiment .	47
5.1	Properties of the Hamamatsu S10943 SiPM array series	58
6.1	Properties of the BCF-12 multicladd scintillating fibers	69
6.2	Measured light loss caused by materials with high refractive index	74
6.3	Properties of the Hamamatsu S12825-050C and S13360-1350CS SiPM series .	84
6.4	Comparison of the light yield measured by the old vs. new SiPM series	89
6.5	Amplitude of the first photoelectron for the old vs. new SiPM series	97
6.6	Summary table of the Large Prototype efficiencies (single fiber readout)	112
6.7	Summary table of the Large Prototype timing resolutions	113
6.8	Summary table of the Large Prototype efficiencies (emulated array readout) . .	120
6.9	Summary table of the Mu3e fiber detector prototyping	122
8.1	Comparison of the double turn resolutions for the Mott vs. Michel data	152
8.2	Comparison of the monochromatic energy spectrum for the Mott vs. Michel alignment	160
9.1	MEG best fitted branching ratios, upper limits and sensitivities	179
10.1	Summary table of the Mu3e fiber detector prototyping	182

Part I

Introduction to Charged Lepton Flavor Violation Searches and Experiments

1 Charged Lepton Flavor Violation Searches

The Standard Model (SM) of particle physics is one of the most beautiful and successful theories mankind has ever come up with. Put shortly, the SM is a quantum field theory that describes matter's basic constituents and the interactions among them. Matter's building blocks, as described by the SM, consist of fermions (leptons and quarks). The quarks and leptons are both organized in three flavor generations, where transitions from one generation to another have been observed both in the quark sector as well as in the neutral lepton sector, but not for charged leptons. Even though no obvious contradictions to the SM have been found so far, it is known to be incomplete: It lacks an explanation for the flavor structure, it does not explain dark matter or dark energy and it does not provide a mechanism which could explain the observed baryon asymmetry in the Universe, just to name a few of the questions which it is not capable of addressing. Nowadays, the SM is regarded as a low-energy approximation of a more general theory. It is also clear that there must be physics Beyond the Standard Model (BSM), waiting to be discovered.

The experiments looking for new physics can be categorized into three groups: The first class tries to produce the new physics' particles directly in high energy collisions, thus exploring energy scales $\mathcal{O}(10)$ TeV ("energy frontier"). The second class of experiments attempts to observe effects of the new physics on interactions of SM particles by performing precision experiments testing energy scales $\mathcal{O}(\gg 10)$ TeV ("intensity frontier"). The third class tries to understand the nature of dark matter and dark energy by means of astrophysical observations and underground experiments ("cosmic frontier"), also accessing large energy scales. Indirect searches at the intensity frontier are a powerful tool when it comes to discovering new physics. On the one hand, they explore energy scale way above the ones investigated by direct searches, since the new physics' particles are not required to be present in the final state, but remain virtual. On the other hand, they are (as is also the case for direct searches) sensitive to the structure of the new physics. One important class of experiments at the intensity frontier are searches for charged Lepton Flavor Violation (cLFV) in muon decays. It is worthy to mention that other precision experiments involving muons, such as the $g - 2$ experiment at BNL [6] and the proton radius measurement with muonic atoms at PSI [7, 8], showed intriguing discrepancies from the theoretical expectations. Whether these anomalies are truly related to new physics or not remains to be seen.

1.1 A Rationale for cLFV Searches

The requirement of the physical laws to be invariant under a certain gauge transformation implicates, by Noether's theorem, the conservation of a corresponding quantity. However, there are some quantities which seem to be accidentally conserved in nature, one of which is the flavor of leptons. As a matter of fact, lepton flavor is *not* a gauge theoretically motivated symmetry of

1 Charged Lepton Flavor Violation Searches

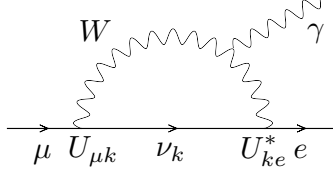


Figure 1.1: One of the SM diagrams contributing to the $\mu^+ \rightarrow e^+\gamma$ decay.

the SM, on the contrary: It was the non-observation of decays such as $\mu \rightarrow e\gamma$ which led physicists back in the fifties to introduce the notion of distinct lepton flavors and their conservation. In particular, it was also assumed that the neutrinos were massless, in which case lepton flavor mixing in both the neutral and the charged lepton sector would be absent. However, meanwhile neutrinos were discovered to flavor oscillate, meaning that they are indeed able to change flavor and that they have tiny masses (which are yet to be measured). Extending the SM to include also small neutrino masses and flavor mixing, cLFV decays would in principle be allowed. An example of a Feynman diagram contributing to the $\mu^+ \rightarrow e^+\gamma$ decay is shown in Fig. 1.1. Even so, these decays are so absurdly suppressed that they are essentially impossible to observe. The branching fraction $\mathcal{B}(\mu^+ \rightarrow e^+\gamma)$ for instance is [9, 10, 11]

$$\mathcal{B}(\mu^+ \rightarrow e^+\gamma) \simeq \frac{\alpha}{2\pi} \left| \sum_{i=2,3} U_{\mu i}^* U_{ei} \frac{\Delta m_{\nu_{i1}}^2}{m_W^2} \right|^2 < 10^{-54}, \quad (1.1)$$

with the fine-structure constant α , the W -boson mass m_W , the neutrino mass-squared differences $\Delta m_{\nu_{ij}}^2$ and the Pontecorvo-Maki-Nakagawa-Sakata (PMNS) matrix ($U_{\alpha j}$) describing the relation between the neutrinos' flavor and mass eigenstates ν_α and ν_i . Thanks to the fact that the neutrino mass differences are so small compared to m_W^2 , cLFV searches can be considered free from background, given the SM with the extension of massive neutrinos only. Conversely, any cLFV signal would be an unequivocal evidence for the existence of new physics. If cLFV is not observed, then at least one is able to constrain the parameter spaces of BSM models, which in general predict branching ratios which are (or are about to be) experimentally accessible.

Currently, the most sensitive cLFV searches rely on muons. In principle, the tau lepton would be the best object to be studied thanks to the stronger couplings to the new physics and to the additional cLFV channels (such as $\tau \rightarrow e\gamma$, $\tau \rightarrow \mu\gamma$, $\tau \rightarrow eee$, $\tau \rightarrow e\mu\mu$ etc.) that would open up. However, the fact that muons are available in huge quantities at accelerators renders the muon cLFV searches much more powerful. For the muon, one is interested in the following three ‘‘golden’’ cLFV channels:

- $\mu \rightarrow e\gamma$;
- $\mu \rightarrow eee$;
- $\mu N \rightarrow eN$ (‘‘muon conversion’’, with N denoting an atomic nucleus).

The sensitivity of the three different channels to new physics depends strongly on the nature of the BSM physics. By consequence, once cLFV has been discovered in one channel, it is

important to measure also the decay rates of the other channels in order to learn something about how the new physics is structured.

1.2 Effective Field Theory Approach

As mentioned before, the predictions for the various cLFV decay rates depend on how the new physics looks like and are therefore heavily model-dependent. Nonetheless, the different cLFV decay channels and results obtained from different experiments can be compared and combined in a model-independent, systematic fashion by following the bottom-top approach of effective field theory. An effective field theory is a quantum field theory which is valid up to a scale Λ corresponding to the yet unknown energy scale where the new physics appears. This is in analogy to the Fermi theory of weak interaction being valid at energies below the W -boson mass M_W . At low energies ($\ll \Lambda$), the interactions with the new physics particles are described as point-interactions, whereas at high energies they need to be included explicitly. The effective Lagrangian at low energies, i.e. at energies at which the SM is an adequate description of reality, is systematically expanded in $1/\Lambda$:

$$\mathcal{L} = \mathcal{L}_{\text{SM}} + \frac{1}{\Lambda} \sum_k C_k^{(5)} Q_k^{(5)} + \frac{1}{\Lambda^2} \sum_k C_k^{(6)} Q_k^{(6)} + \mathcal{O}\left(\frac{1}{\Lambda^3}\right). \quad (1.2)$$

This Lagrangian contains the operators $Q_k^{(5)}$ and $Q_k^{(6)}$ of dimension 5 and 6, respectively, which are composed of SM fields. The summation index k runs over all possible such operators that one can write down while complying with the requirement that they respect the SM gauge symmetries. The coefficients $C_k^{(5)}$ and $C_k^{(6)}$, also known as ‘‘Wilson coefficients’’, describe the corresponding couplings. Experiments looking for BSM may either find traces of new particles and thus help to determine the couplings, or in case no BSM signal is observed, they are able to set constraints on them, thus providing a guard rail along the road to a new theory. The Wilson coefficients are a function of the energy scale under consideration, where the running of the couplings is given by Renormalization Group Equations (RGEs), and in particular the operators may mix under the evolution. Once the new physics is known or a specific model is chosen, one can go a step further by evolving the Wilson coefficients to the high scale Λ and match them with the parameters of the full, explicit BSM theory.

It turns out that only one dimension 5 operator satisfies the condition of gauge invariance, and that it provides the neutrino masses and flavor mixing. From neutrino oscillation experiments, the neutrino masses and hence the coefficient $C^{(5)}$ is known to be very small. For what concerns the dimension 6 operators, there are 19 operators which respect the gauge symmetry and are capable of causing cLFV. The one-loop calculation of $\mu^+ \rightarrow e^+ \gamma$ and the tree-level computation of $\mu^+ \rightarrow e^+ e^- e^+$ were performed and combined with the experimental limits in [12, 13]. There, the limits on the Wilson coefficients obtained at low-energy scales ($\Lambda \sim m_\mu$) were compared with the ones obtained at higher scales ($\Lambda \sim m_Z$, e.g. $Z \rightarrow e^\pm \mu^\mp$), assuming that only one operator at a time is non-vanishing and that the coefficients are real. It turns out that the low-energy physics experiments such as MEG and Mu3e are much more powerful in constraining the Wilson coefficients than similar searches at high energy colliders [ibid].

1 Charged Lepton Flavor Violation Searches

The complementarity of $\mu^+ \rightarrow e^+\gamma$ and $\mu^+ \rightarrow e^+e^-e^+$ can be illustrated by considering $\Lambda \sim m_Z$ as the high energy scale [14]. Extracting from the effective Lagrangian in Eq. (1.2) the partial decay widths at the muon mass scale $\Lambda \sim m_\mu$, one discovers that the $\mu^+ \rightarrow e^+\gamma$ branching ratio is related only to the dipole operators, while the $\mu^+ \rightarrow e^+e^-e^+$ partial width depends also on the scalar and vectorial operators. In addition, there are only two kind of operators which are correlated through the RGEs at leading order, namely the dipole operators (Wilson coefficients C_L^D and C_R^D , with L, R denoting the chirality) and scalar operators (Wilson coefficients C_{ee}^{SLL} and C_{ee}^{SRR}). Therefore, assuming that these are the only two relevant operators and applying the experimental limits at the muon mass scale $\Lambda \sim m_\mu$, one obtains the constraints on the Wilson coefficients plotted in Fig. 1.2 once they are evolved to $\Lambda \sim m_Z$. It becomes clear from Fig. 1.2 that there is a direction of the parameter space to which the $\mu^+ \rightarrow e^+\gamma$ decay is not sensitive to, whereas the $\mu^+ \rightarrow e^+e^-e^+$ decay does not suffer from blind spots. The situation can get much more complicated once all the operators are taken into account. However, the complementarity of the two decay modes is a persistent feature, and thus it is important to look for new physics in either channel. Muon conversion has not been discussed here, but this channel is of course also of great interest and equally complementary. In fact, once the proposed sensitivities are reached, $\mu N \rightarrow e N$ will constitute a highly competitive cLFV search.

1.3 Experimental Status and Future cLFV Searches

The hunt for cLFV decays has started nearly 70 years ago, soon after the discovery of the muon. So far, no cLFV decay was observed. The steady improvements of the upper limits on branching ratios of cLFV muon decays are depicted in Fig. 1.3, and the current limits together with the planned sensitivities of future experiments are summarized in Table 1.1. The MEG experiment at PSI has just recently set a new upper limit $\mathcal{B} < 4.2 \times 10^{-13}$ (90% confidence level) on the branching ratio of the $\mu^+ \rightarrow e^+\gamma$ decay [1]. An upgraded version of the experiment (MEG II) [2], featuring a sensitivity improved by about a factor of ten, will start soon. The current best upper limit on the $\mu^+ \rightarrow e^+e^-e^+$ branching ratio of $\mathcal{B} < 1.0 \times 10^{-12}$ (90% confidence level) was provided by the SINDRUM experiment at PSI [4, 15]. The upcoming Mu3e experiment [3], also hosted at PSI, seeks to look for this decay with a sensitivity improved by a factor of 10^4 with respect to the current limit. This ambitious goal will be pursued stepwise: In a first phase, Mu3e is planned to achieve a 1000 times better sensitivity than SINDRUM, in the second phase the sensitivity is expected to increase by another factor of ten. For what concerns the muon conversion, there are three experiments which are currently under preparation, Mu2e at Fermilab [16] as well as DeeMe [17] and COMET at J-PARC [18]. All experiments are supposed to start by the end of this decade, with Mu2e and COMET aiming at a final sensitivity of 6×10^{-17} , which is again four orders of magnitudes better than the current experimental limit $\mathcal{B} < 7 \times 10^{-13}$ (90% confidence level) from the SINDRUM II experiment performed at PSI [19].

1.4 Event Signatures and Backgrounds

This section is dedicated to the description of the signal event signatures and backgrounds of the $\mu^+ \rightarrow e^+e^-e^+$ and $\mu^+ \rightarrow e^+\gamma$ decays in the MEG and Mu3e experiment, respectively. Both ex-

1 Charged Lepton Flavor Violation Searches

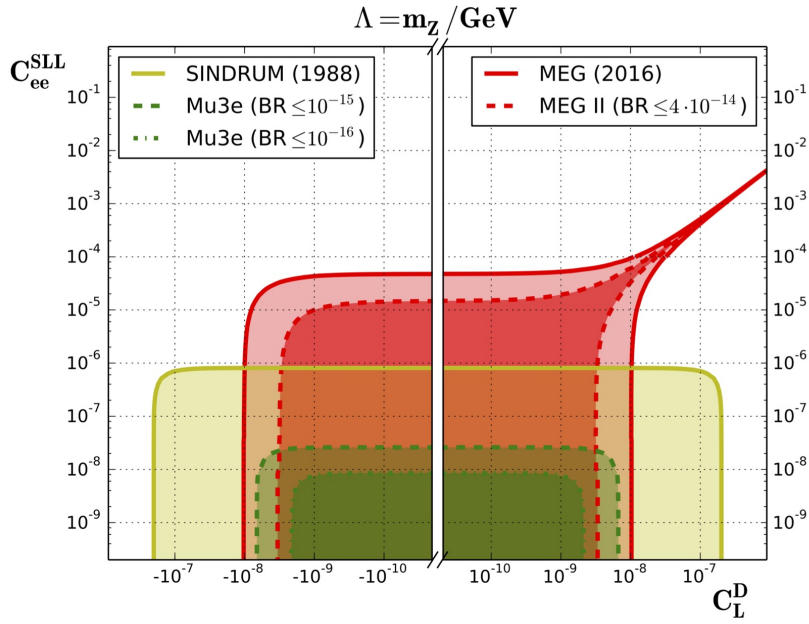
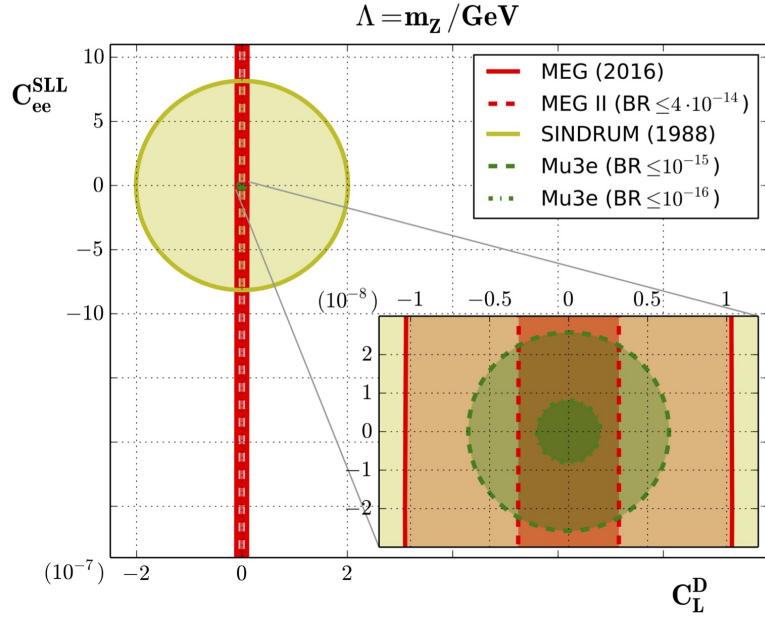


Figure 1.2: Present and future bounds provided by experiments looking for $\mu^+ \rightarrow e^+ \gamma$ (MEG, MEG II) and $\mu^+ \rightarrow e^+ e^- e^+$ (SINDRUM, Mu3e) on the two Wilson coefficients described in the text, evaluated at the energy scale $\Lambda \sim m_Z$ [14]. The shaded areas correspond to the experimentally allowed regions.

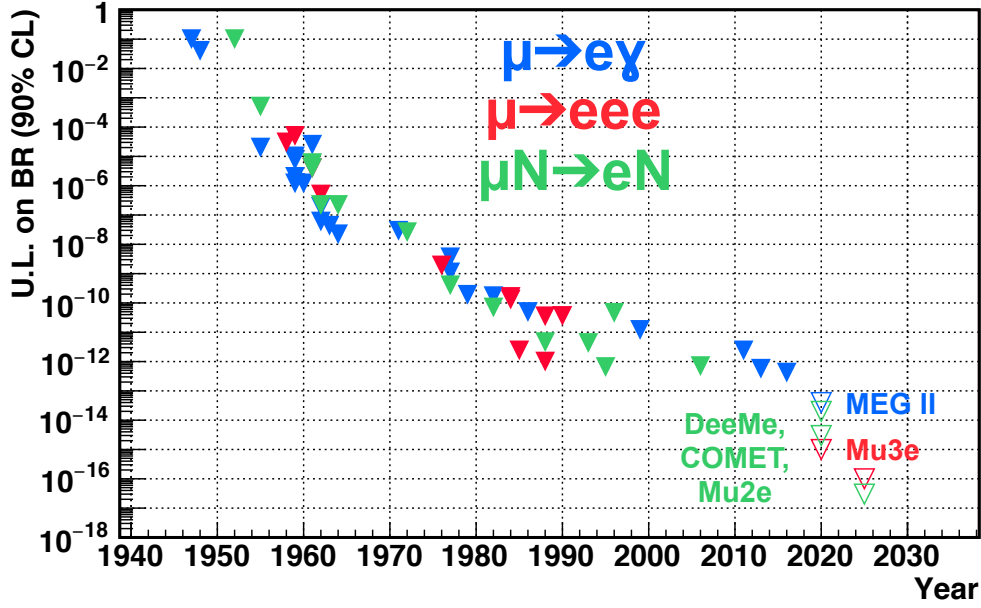


Figure 1.3: History of the upper limits set on the branching ratios of the three golden cLFV muon decay channels. The open triangles correspond to future experiments.

Table 1.1: Current experimental limits (90 % confidence level) and planned sensitivities of future experiments exploring the golden cLFV muon decay channels.

Process	Current	Provided By	Future Exp.	Planned Sens.
$\mu^+ \rightarrow e^+ \gamma$	4.2×10^{-13}	MEG	MEG II	5×10^{-14}
$\mu^+ \rightarrow e^+ e^- e^+$	1.0×10^{-12}	SINDRUM	Mu3e phase I Mu3e phase II	10^{-15} 10^{-16}
$\mu N \rightarrow e N$	7×10^{-13}	SINDRUM II	DeeMe COMET phase I COMET phase II, Mu2e	2×10^{-14} 3×10^{-15} 6×10^{-17}

periments consider positive muons which are stopped on a target prior to their decay, i.e. muons decaying at rest. This means that both experiments look for time-coincident positrons and electrons whose invariant mass is equal to the muon mass and whose vectorial momenta add up to zero. The sources of background can be categorized into two groups: (1) irreducible (or correlated) background, due to standard decays of single muons faking a signal by giving off little energy to the (undetectable) neutrinos, and (2) accidental (or uncorrelated) background, which involves the accidental overlap of several muon decay products mimicking a cLFV signal. The suppression of the first type of background requires good momentum resolution in both direction and magnitude, whereas the rejection of the second type of background asks for excellent timing resolution, vertexing and a continuous muon beam. For coincidence experiments, continuous beams, as opposed to pulsed beams, have the advantage that the accidental background is

1 Charged Lepton Flavor Violation Searches

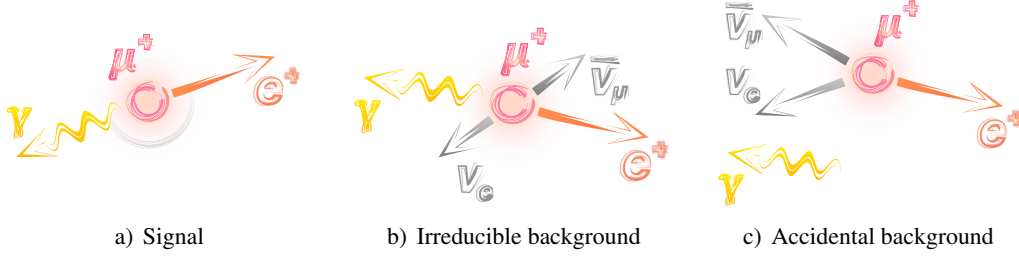


Figure 1.4: Signal and backgrounds of the $\mu^+ \rightarrow e^+ \gamma$ search.

reduced, since the rate for accidental overlaps scales with the instantaneous muon stopping rate.

1.4.1 The $\mu^+ \rightarrow e^+ \gamma$ Search

The $\mu^+ \rightarrow e^+ \gamma$ signal event is characterized by the elegantly simple kinematics of a two-body decay at rest, i.e. a back-to-back, time-coincident emission of a positron and gamma-ray, each carrying an energy equal to half of the muon's mass energy ($E_{e^+} = E_\gamma = E_\mu/2 = 52.8$ MeV). The number of expected signal events, assuming a $\mu^+ \rightarrow e^+ \gamma$ branching ratio \mathcal{B} , is given by

$$N_{sig} = \mathcal{B} \cdot \Omega \cdot \varepsilon_e \cdot \varepsilon_\gamma \cdot \varepsilon_s \cdot R_\mu^{\text{total}} \cdot T, \quad (1.3)$$

where Ω corresponds to the experimental apparatus' geometrical acceptance, ε_e and ε_γ are the positron and photon detection efficiencies, ε_s designates the selection efficiency, T denotes the measurement time and R_μ^{total} is the stopped muon rate, which in the case of a continuous muon beam coincides with the instantaneous stopping rate R_μ .

The two background sources to the measurement of the $\mu^+ \rightarrow e^+ \gamma$ decay are (see Fig. 1.4):

1. **Irreducible background:** Radiative Muon Decays (RMDs) $\mu^+ \rightarrow e^+ \gamma \bar{\nu}_\mu \nu_e$ in which the neutrinos carry away little energy.
2. **Accidental background:** Accidental overlaps of positrons and photons, both carrying an energy close to half the muon mass energy, being time-coincident and moving in opposite directions within the detector resolutions. The positrons originate in Michel decays $\mu^+ \rightarrow e^+ \bar{\nu}_\mu \nu_e$, whereas the photons may stem from either RMDs, Annihilation-In-Flight (AIF) $e^+ e^- \rightarrow \gamma \gamma$ or Bremsstrahlung.

The rate of RMD irreducible background events can be estimated by considering the differential $\mu^+ \rightarrow e^+ \nu_e \bar{\nu}_\mu \gamma$ decay width and integrating it over the signal region, whose size is dictated by the resolutions on the kinematic variables of the positrons and gammas. The number of irreducible background events measured in the experiment is

$$N_{irr} = \mathcal{B}_{irr} \cdot R_\mu^{\text{tot}} \cdot T, \quad (1.4)$$

where \mathcal{B}_{irr} corresponds to the effective RMD branching ratio in the signal region under consideration. The rate of accidental background within the signal region normalized to the total decay

1 Charged Lepton Flavor Violation Searches

rate is given by

$$\mathcal{B}_{acc} = R_\mu \cdot f_e^0 \cdot f_\gamma^0 \cdot \Delta t_{e\gamma} \cdot \frac{\Delta\Theta_{e\gamma}}{4\pi}, \quad (1.5)$$

where $\Delta t_{e\gamma}$ and $\Delta\Theta_{e\gamma}$ denote the full widths of the signal window in terms of the relative time and angle between the positron and the gamma, and the factors f_e^0 and f_γ^0 correspond to the fractions of positrons and gammas which fall into the signal region. The latter are obtained by integrating the energy spectrum of the positron and gammas stemming from normal muon decay over the signal window. Evaluation of these fractions leads to

$$\mathcal{B}_{acc} \propto R_\mu \cdot \delta E_\gamma^2 \cdot \delta E_e \cdot \delta\Theta_{e\gamma}^2 \cdot \delta t_{e\gamma} \quad (1.6)$$

with the δ 's designating the resolutions on the corresponding variables. Consequently the number of accidental background events within the signal window is

$$N_{acc} \propto \mathcal{B}_{acc} \cdot R_\mu \cdot T \quad (1.7)$$

$$\propto \delta E_\gamma^2 \cdot \delta E_e \cdot \delta\Theta_{e\gamma}^2 \cdot \delta t_{e\gamma} \cdot R_\mu^2 \cdot T. \quad (1.8)$$

Due to its quadratic scaling with the beam intensity, the accidental background poses a far more serious challenge to the experiment than the irreducible background.

1.4.2 The $\mu^+ \rightarrow e^+e^-e^+$ Search

The $\mu^+ \rightarrow e^+e^-e^+$ signal event signature consists of two positrons and one electron emitted from a common vertex in space and time and whose momenta \vec{p}_i and energies E_i ($i = 1, 2, 3$) by conservation laws obey

$$\vec{p}_{tot} = \sum_{i=1}^3 \vec{p}_i = \vec{0} \quad (1.9)$$

and

$$E_{tot} = \sum_{i=1}^3 E_i = m_\mu, \quad (1.10)$$

where m_μ denotes the muon mass. Momentum conservation implicates that the momentum vectors of the three particles have to lie in a plane. The maximum energy that can be carried away by a positron / electron is equal to half the muon mass energy $E_\mu/2$. The phase space distribution of the decay particles depends on the new physics inducing cLFV and is therefore not known a priori.

The backgrounds to the $\mu^+ \rightarrow e^+e^-e^+$ decay search are (see Fig. 1.5):

1. **Irreducible background:** Internal Conversions (ICs) $\mu^+ \rightarrow e^+e^-e^+\nu_e\bar{\nu}_\mu$ in which the neutrinos carry away little energy. The branching ratio for this process is 3.4×10^{-5} [15].
2. **Accidental background:** Accidental overlap of two positron tracks with an electron track mimicking a $\mu^+ \rightarrow e^+e^-e^+$ signal. The positrons emanate from the usual Michel decays or RMDs. The electrons stem mainly from Bhabha scattering $e^+e^- \rightarrow e^+e^-$ of muon decay positrons and the electrons in the material. Other sources of fake signal electrons

1 Charged Lepton Flavor Violation Searches

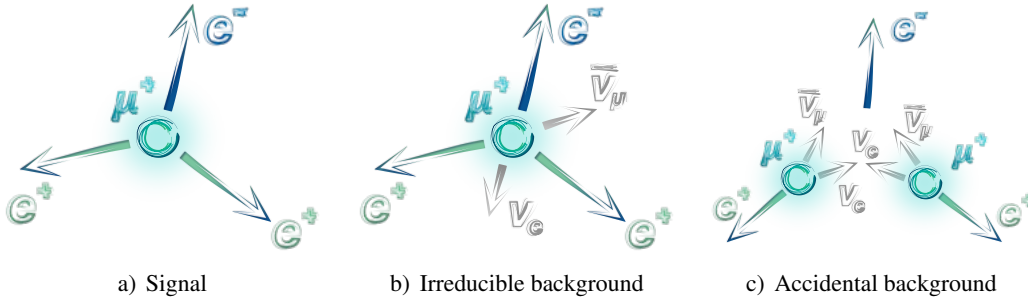


Figure 1.5: Signal and backgrounds of the $\mu^+ \rightarrow e^+e^-e^+$ search.

are gammas from RMD converting in the detector or target material, Compton scattering or simply mis-reconstructed tracks. The largest fraction of accidentals is caused by an e^+e^- -pair from Bhabha scattering with a Michel positron emitted in spatial and temporal proximity.

The accidental background due to the e^+e^- -pair plus the Michel positron increases linearly, the background due to two Michel positrons plus an electron quadratically with the beam rate. The branching ratio for IC exhibits a steep fall-off with increasing total energy of the charged leptons, as can be understood from Fig. 1.6. The plot shows the corresponding leading order computation as a function of the invisible energy $m_\mu - E_{\text{tot}}$, with m_μ equal the muon mass and E_{tot} corresponding to the total energy of the charged leptons. Very recent next-to-leading order predictions found that the experimental situation is even more favorable, as the predicted branching fraction for IC decreases by 10 to 20 %, and the more so the stronger the cut on the neutrino energies is [20, 21]. The steep fall-off implies that good momentum resolution is a very powerful handle on the suppression of the irreducible background.

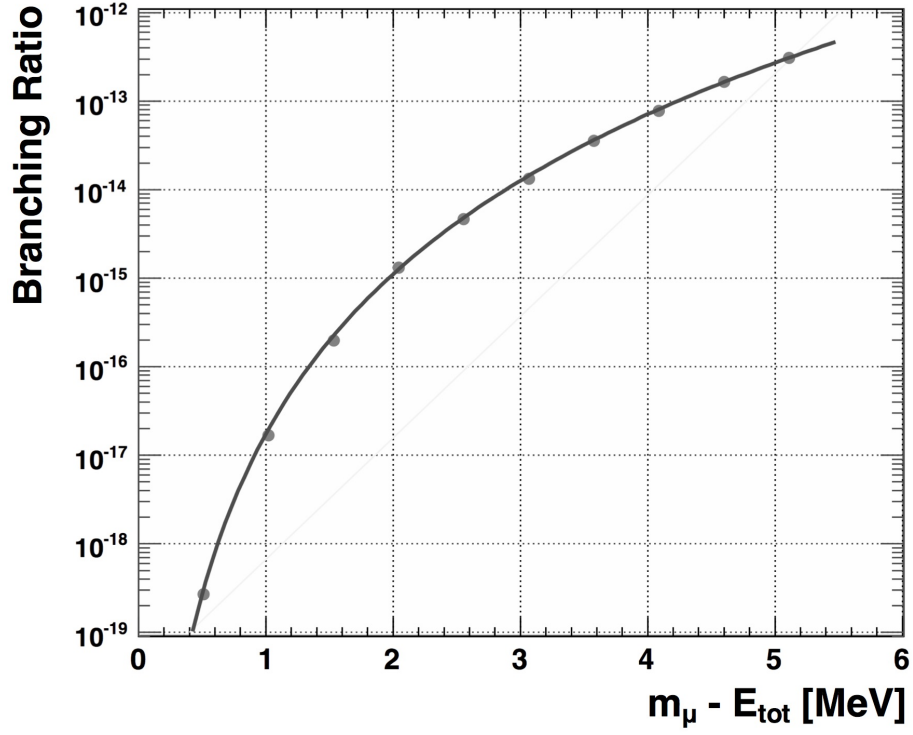


Figure 1.6: Leading order computation of the IC $\mu^+ \rightarrow e^+ e^- e^+ \nu_e \bar{\nu}_\mu$ branching ratio \mathcal{B} as a function of the cut on the invisible energy $m_\mu - E_{\text{tot}}$ [22]. The branching ratio features a steep fall-off for increasingly stringent cuts on the total energy. In the regime shown in this plot, they are approximately related by $\mathcal{B} \sim (m_\mu - E_{\text{tot}})^6$ (solid line).

2 Muon Beams at PSI

The Paul Scherrer Institute (PSI) in Villigen, Switzerland is a unique place for cLFV experiments because it provides the most intense continuous (“DC”) muon beams in the world. The π E5 beam line for instance is able to deliver $\mathcal{O}(10^8) \mu^+ / \text{s}$. This beam line does not only serve the MEG and Mu3e experiments, but has also been home to the muonic hydrogen lamb shift experiment [7], which raised the issue of the proton radius puzzle.

The first section in this chapter will describe the production mechanism of muon beams, the second section will introduce the High Intensity Proton Accelerator facility at PSI and the last section describes the π E5 beam line as well as the other muon beam lines at PSI at which several beam tests of the detector prototypes presented in Chapter 6 and 7 were performed.

2.1 Muon Production

The starting point of a muon production facility is an infrastructure that provides a proton beam. This proton beam hits a meson production target (e.g. graphite), where pions are produced through a variety of proton-nucleus interactions. From the pion decays $\pi^+ \rightarrow \mu^+ + \nu_\mu$ and $\pi^- \rightarrow \mu^- + \bar{\nu}_\mu$ arise the muons. Depending on the location within the target at which the pion decays, one distinguishes among three kinds of muons [23]:

- **Decay-in-flight muons:** Muons which stem from decays of pions with moderate momenta $\mathcal{O}(100) \text{ MeV}/c$.
- **Cloud muons:** Muons which stem from pions that decay in flight in the vicinity of the production target, forming a “cloud” around it.
- **Surface muons:** A considerable amount of low-energy positive pions actually stop in the target and decay at rest. The muons stemming from these pions have a momentum of $29.8 \text{ MeV}/c$, equivalent to a kinetic energy of 4.12 MeV , and are 100 % polarized. Due to their small momentum, only muons which are produced close to the target surface manage to escape from it. Depolarization effects caused by multiple scattering are at a negligible level. Negative pions are not able to generate surface muons because they are promptly captured by nuclei before they can decay.

Surface muons are the most interesting kind of muons to the MEG and Mu3e experiment because of the small momentum byte¹ of $\mathcal{O}(10 \%)$ and the fact that they can be stopped in very little material due to their low momentum. This allows to minimize the amount of target material with which the muon decay particles are faced on their way from the muon decay vertex to

¹The momentum byte is defined as the fraction $\Delta p/p$ of the momentum range Δp transmitted by the beam line and the central momentum p .

the detectors, therefore safeguarding the resolutions on their kinematical variables. Moreover, positive muons have the benefit that they are not captured by atomic nuclei to form muonic atoms (as would be the case with negative muons). Note that the surface muon beam usually contains a substantial contamination of electrons and positrons which have their origin in $\pi^0 \rightarrow \gamma\gamma$ and the subsequent pair production or in muon decays. This contamination can be removed by a Wien filter (see Sect. 2.3.1).

2.2 High Intensity Proton Accelerator Facility

The High Intensity Proton Accelerator (HIPA) facility at PSI features the most powerful proton cyclotron in the world. It delivers a proton current of up to 2.4 mA and accelerates the protons to an energy of 590 MeV, operating at a power of about 1.4 MW. The protons are provided by an Electron Cyclotron Resonance (ECR) source. The protons are injected into three staged accelerators, namely a Cockcroft-Walton to pre-accelerate the protons to 870 keV (shown in Fig. 2.1a)), an injector cyclotron accelerating them to 72 MeV and finally a big cyclotron (displayed in Fig. 2.1b)) with four Radio Frequency (RF) plus one flat top accelerating cavities, from which the protons leave after 186 turns with their final energy of 590 MeV. Strictly speaking, the proton beam is not perfectly continuous but is structured into bunches with a period of 20 ns, given by the RF cavities running at 50 MHz. In the experiments, the sinusoidal signal from the RF cavities can be used to reject the beam correlated background, see e.g. Sect. 7.2.2. The proton beam hits two production targets, Target M and Target E². Both these targets consist of rotating graphite wheels of 5 mm (Target M) and 40 mm (Target E) thickness along the proton beam direction. The proton beam is finally dumped on a spallation target, which serves the neutron scattering community (SINQ facility).

In order to keep PSI at the forefront of high intensity continuous muon sources, several upgrade activities are ongoing. In the mid-term future, the proton current will be increased to 3 mA after replacing the RF accelerating cavities. Additional 30 to 60 % gains in the surface muon beam rate could be achieved by optimizing the geometry of the production targets, and an extra 10 % by replacing the graphite by another material with a higher pion production cross section and sufficiently low atomic number, such as boron carbide [24]. Moreover, a new surface muon beam line which should deliver $O(10^{10}) \mu^+ / s$ is currently under study [25].

2.3 Beam Lines

In addition to $\pi E5$, PSI possesses several other beam lines such as $\pi E1$ or $\pi M1$, which on the one hand host(ed) a variety of experiments such as the Muon Lifetime Analysis (MuLan) experiment [26] or the Muon Scattering Experiment (MUSE), and on the other hand act as beam test facilities supplying tunable electron / positron, muon and pion beams. In the context of this thesis they have been utilized to test several detector prototypes. A map of the HIPA facility with the layout of the different beam lines is displayed in Fig. 2.2.

²The denominations for the two production targets have their origin in the French words *épais* (= thick) and *mince* (= thin).

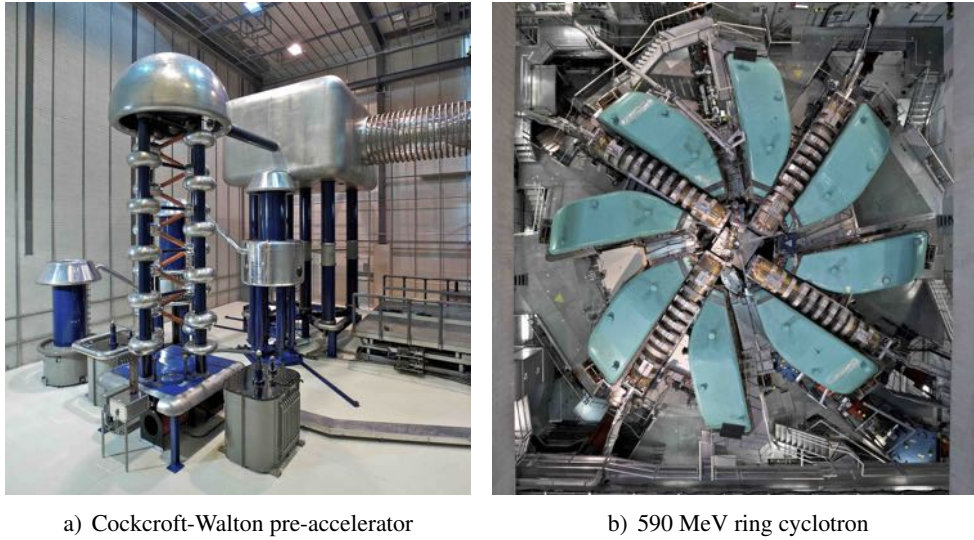


Figure 2.1: Two of the three staged accelerators of PSI's HIPA facility: The Cockcroft-Walton 870 keV pre-accelerator and the 590 MeV ring cyclotron, delivering a proton beam of 1.4 MW power [5].

2.3.1 The π E5 Channel

The π E5 beam line [27] is one of the most intense muon beam line in the world and is able to deliver up to 10^8 surface μ^+ /s. The particles that can be accepted by the beam channel are positive or negative pions, muons or electrons of a momentum up to 120 MeV/c. The following paragraphs describe the π E5 channel's layout up to the point where the beam lines for the two cLFV experiments Mu3e and MEG coincide. Further details concerning the respective beam lines for the experiments can be found in Sect. 3.2 and 4.2.

In the special case of the MEG and Mu3e experiments, surface muons with a momentum around $p = 28$ MeV/c are used. This working point is able to satisfy the need for a high intensity surface muon source with a small beam emittance and a momentum byte of $\mathcal{O}(10\%)$. At this momentum, the pion contamination is extremely low, and the eight-times higher positron contamination is removed by means of a dedicated Wien filter described further below.

With respect to the proton beam impinging on Target E, the π E5 channel is oriented backwards at 165° , as shown in Fig. 2.3, with a solid angle acceptance of 150 msr. The particles are transported to the π E5 area through a quadrupole triplet to the Wien filter, which allows to separate the muons from the positrons using crossed electric and magnetic fields ($E \times B$) along a length of ≈ 80 cm in the direction of the beam. Its electric field is produced by two electrodes separated by a gap of ≈ 20 cm, across which a potential of 190 kV is applied. Finally, the beam is transported through a second quadrupole triplet and a collimator system. The collimator acts as a positron dump.

2 Muon Beams at PSI

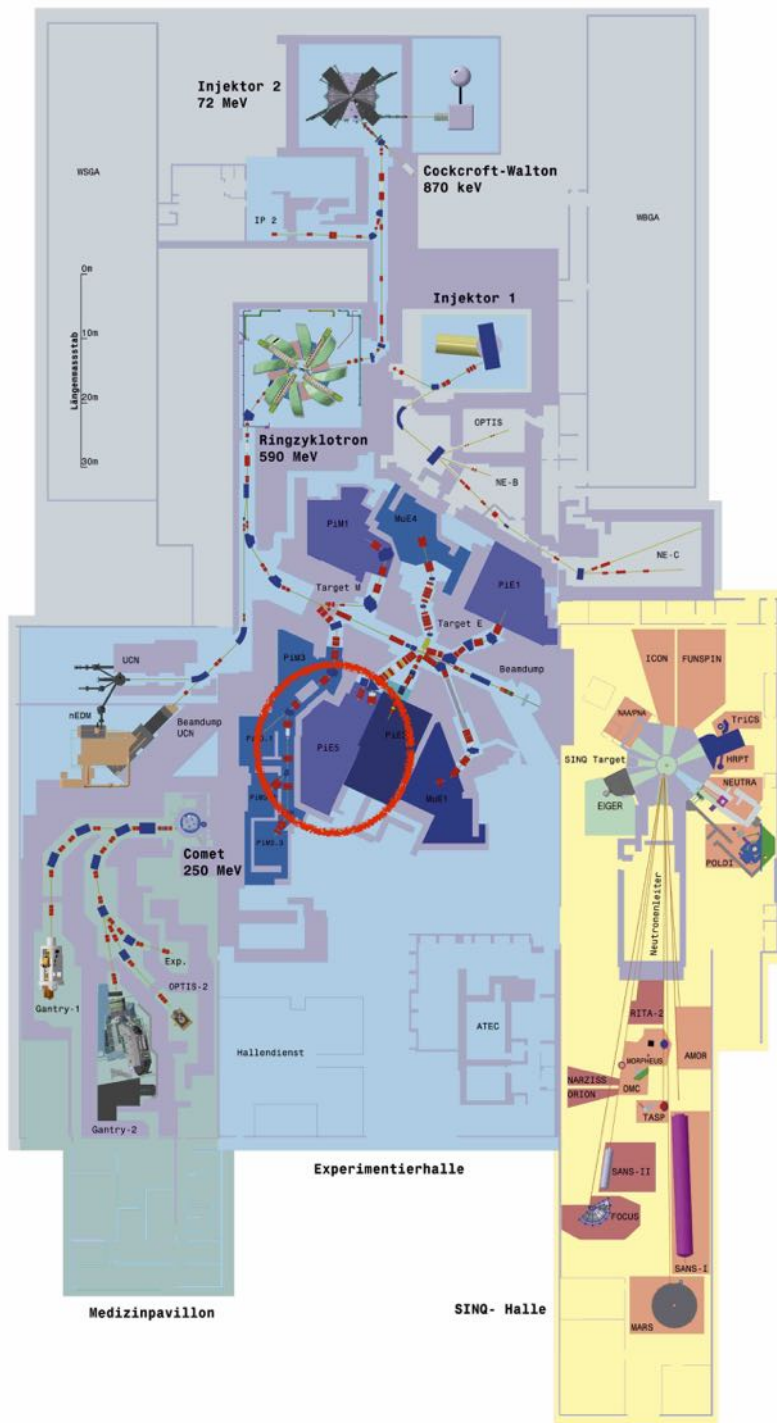


Figure 2.2: Map of the PSI HIPA facility [5]. The $\pi E5$ area, which is home to the MEG / MEG II and Mu3e experiments, is encircled in red.

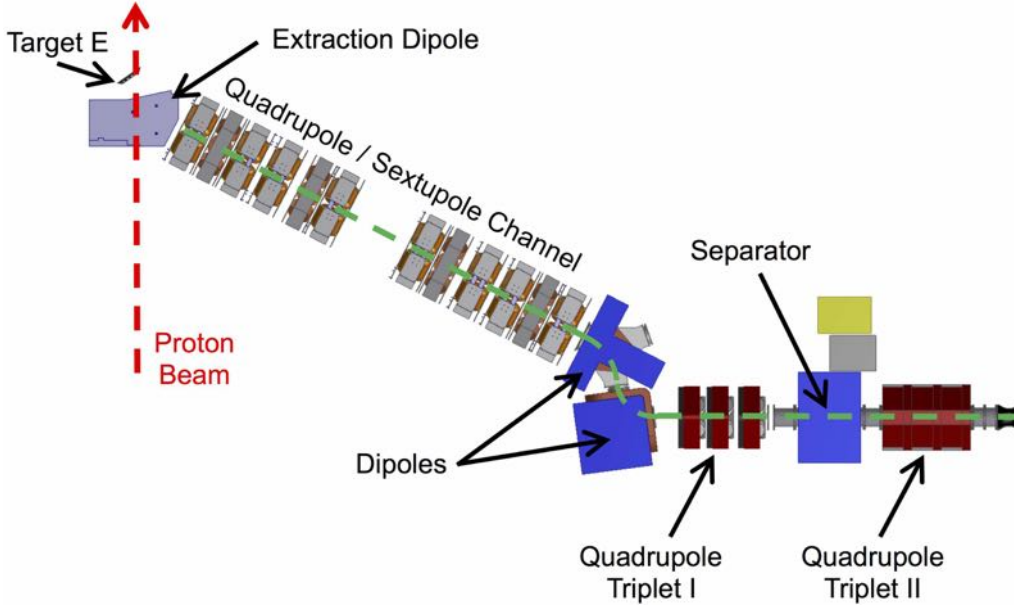


Figure 2.3: Sketch of the $\pi E5$ channel at PSI up to the collimator system. Up to this point, the beam lines for the MEG / MEG II and the Mu3e experiment coincide.

2.3.2 The $\pi M1$ Channel

The $\pi M1$ channel [28] provides pions, muons, electrons of both polarities with a momentum between 100 and 500 MeV/c produced by the proton beam hitting Target M. Apart from hosting the future MUSE experiment [29], it is mainly used for beam test campaigns. The $\pi M1$ channel is located at an extraction angle of 22° with respect to Target M. The beam spot size is typically $\sigma \approx 1$ cm at the final focus in both transverse directions. It does not feature any separator system, meaning that the beam contains several kinds of particles (pions, muons, electrons). The different particle types can be distinguished by considering their Time-Of-Flight (TOF) with respect to the cyclotron RF signal, see also Sect. 7.2.2. One of the momenta p at which the particles are best separated in terms of the TOF is $p \approx 115$ MeV/c. The fractions of the particle types present in the beam depend on the momentum setting. For a low momentum ($\lesssim 150$ MeV/c) the vast majority of the particles are electrons / positrons. The reader may refer to [29] for more details.

2.3.3 The $\pi E1$ Channel

The $\pi E1$ channel [30] serves both the particle physics and Muon Spin Resonance (μSR) community by delivering pion and muon beams with momenta between 10 and 500 MeV/c. The secondary particles are extracted at a 10° forward angle with respect to Target E. For surface muons, the beam rate is typically $\mathcal{O}(5 \times 10^6) \mu^+ / s$.

3 The Mu3e Experiment

The Mu3e experiment, which has been proposed in 2013, aims to look for the $\mu^+ \rightarrow e^+e^-e^+$ decay with an ultimate sensitivity of 10^{-16} , i.e. four orders of magnitude lower than what the predecessor experiment SINDRUM [4, 15] has achieved in the past. It follows a staged approach with three phases (phase Ia, phase Ib, phase II), where at every stage the muon beam rate is increased by one order of magnitude and the experimental apparatus is upgraded to keep up with the high rate environment. A first engineering run is foreseen in 2019, with possible data taking from 2020 onwards. At present, the Mu3e collaboration consists of about 30 scientists from Germany and Switzerland. The following sections give an overview on the Mu3e experimental apparatus. A more detailed description can be found in [3, 31].

3.1 Experimental Concept

The Mu3e experiment looks for three time-coincident positron and electron tracks stemming from a muon decaying at rest on a target. Precise vertex, timing and momentum measurement allows to keep the accidental background rate low, whereas for the suppression of Internal Conversions (ICs), excellent momentum measurement is required. The Mu3e experiment's material budget needs to be minimal in order to reduce the induced background and to minimize the multiple scattering of the decay particles.

The improvement on the sensitivity to the $\mu^+ \rightarrow e^+e^-e^+$ decay will occur stepwise: In phase Ia, the experiment is supposed to run at a muon beam intensity of $\mathcal{O}(10^7) \mu^+/s$ with a minimal detector setup consisting of the central tracking apparatus (see below) and possibly the timing detectors if they are available. The background which limits the sensitivity of the Mu3e experiment during this phase is the IC $\mu^+ \rightarrow e^+e^-e^+\nu_e\bar{\nu}_\mu$ because the particle tracking system will not have reached its final performance yet. For phase Ib, muon rates of $\mathcal{O}(10^8) \mu^+/s$ are foreseen, while at the same time the tracking system will be extended and the complete timing system will be put into operation. During this phase of the experiment, it is going to be the accidental background which will constitute the limiting factor on the sensitivity due to the increased beam rate and the enhanced tracking capability. On a longer timescale, phase II is planned to run at an intensity of $\mathcal{O}(10^9) \mu^+/s$, which to this day is not available yet and would require the construction of a new high intensity continuous muon beam currently under investigation at PSI [24, 25]. Sketches of the setups for the different phases of the experiment are shown in Fig. 3.1.

The momentum and vertex measurements are based on a tracking system made of four layers of novel ultra-thin silicon pixels, which are presently being developed, immersed in a solenoidal magnetic field. The goal is to reach a resolution on the total energy of the charged leptons $\sigma_{E_{\text{tot}}} \leq 0.5 \text{ MeV}$ and a vertex resolution of $\sigma_{\text{vtx}} \approx 250 \mu\text{m}$. In order to reduce the amount of accidental background, a precise timing measurement is required. The timing system consists

3 The Mu3e Experiment

of two detectors, namely a scintillating fiber hodoscope and a tile timing detector. The time resolution provided by the scintillating fibers should stay below 1 ns, whereas the tiles are required to feature a time resolution of about 100 ps.

The Mu3e experiment will find itself in a situation where the multiple scattering, as opposed to the sensors' spatial resolution, dominates the momentum resolution. On the one hand this implies that the material budget should be kept at a minimum. On the other hand it means that it does not help to add additional pixel layers to obtain extra measurement points along the particle tracks. In order to further improve the momentum resolution, one can make use of the trick that, at first order, multiple scattering effects on the momentum measurement cancel after exactly half a turn. Thus, the experimental layout features a long, narrow tube of pixels such that the electron and positrons are able to curl back towards the central axis of the magnet onto so-called "recurl stations", using the "exterior" (exterior to the pixel layers) half of the track's circle as a measure of the momentum. This also allows to place additional timing detectors within the pixel layer barrels without affecting too much the momentum resolution. In addition, the experiment should have a large acceptance because the phase space of the decay particles, which depends on the nature of the new physics, is currently unknown. The geometrical acceptance of the Mu3e baseline design is about 70 %.

The Mu3e experimental apparatus is segmented into several detector stations, each detector station being 36 cm long. The central detector station encompasses the target, the first two pixel layers, the fiber tracker and the outer two pixel layers. For phase Ia, only this central detector station will be installed, see again Fig. 3.1a). For phase Ib, the apparatus will be extended by two additional detector stations constituting the recurl stations, see Fig. 3.1b). The recurl stations consist of the beam pipe onto which the tile timing detector and the outer two pixel layers are mounted. For phase II, another two recurl detector stations will be added, summing up to five detector stations, see Fig. 3.1c).

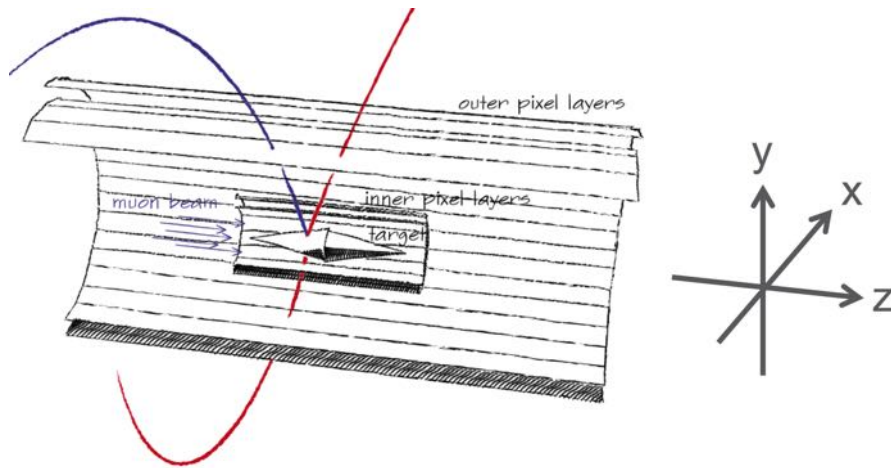
3.1.1 Coordinate System

Throughout this thesis we will use a right-handed cylindrical coordinate system (r, ϕ, z) with its origin at the center of the Mu3e magnet (which ideally coincides with the center of the muon stopping target), and the z -axis oriented along the direction of the beam. The polar angle θ refers to the angle enclosed by the z -axis and the vector under consideration. The region with (or the direction towards) $z < 0$ is referred to as Upstream (US), the region for which $z > 0$ as Downstream (DS).

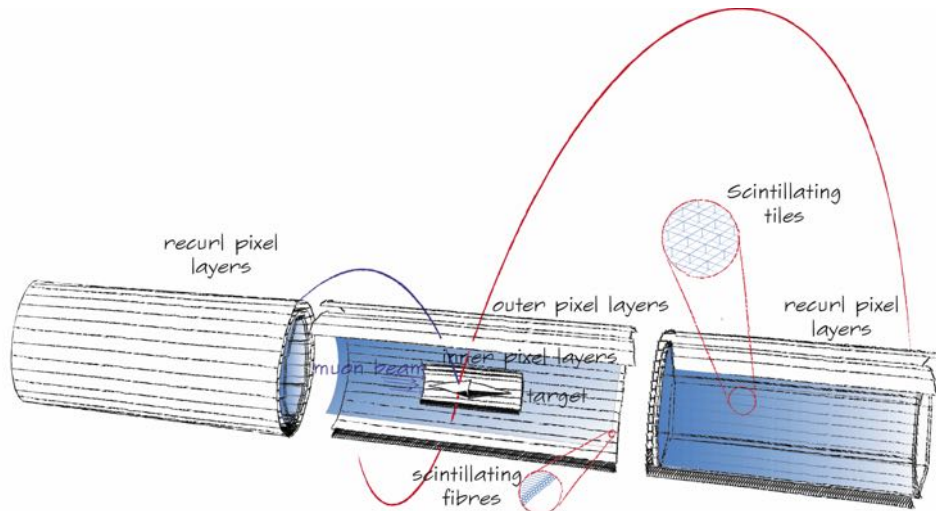
3.2 Compact Muon Beam Line and Muon Stopping Target

During phase I, for which muon beam rates of 10^7 to $10^8 \mu^+ / s$ are envisaged, the Mu3e experiment will make use of the $\pi E5$ channel, thus sharing it with the upcoming MEG II experiment. The Mu3e experiment will be located in the front, the MEG II experiment in the rear part of the $\pi E5$ area, as shown in Fig. 3.2a). In order to allow the coexistence of the MEG II and Mu3e apparatuses with a minimal transition time from one to the other experiment, a new beam line, the so-called Compact Muon Beam Line (CMBL), has been developed. The results of a first

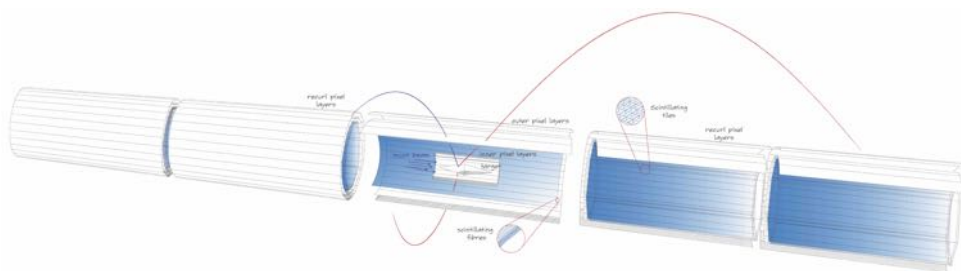
3 The Mu3e Experiment



a) Phase Ia



b) Phase Ib



c) Phase II

Figure 3.1: The experimental setups for the different phases of the Mu3e experiment. The labels in c) are identical to the ones in b).

3 The Mu3e Experiment

commissioning of the CMBL are very promising [31].

The CMBL, depicted in Fig. 3.2b), starts right after the collimator system, which is the element up to which the beam lines for MEG and Mu3e coincide (see Sect. 2.3.1). In order to switch from the MEG to the Mu3e experiment, one of MEG's beam line elements (the BTS, see Sect. 4.2) has to be removed and replaced by a 90° bending dipole. The CMBL is completed by an additional 65° bending dipole and a "split" triplet of quadrupoles (two quadrupoles before and one after the 65° bend), injecting the beam into the Mu3e solenoid. Inside the solenoid, the beam is transported up to the muon stopping target within a beam vacuum pipe of 60 mm diameter, which contains a degrader consisting of a $600\ \mu\text{m}$ thin Mylar foil to optimize the muon stopping rate on the target. The beam pipe is eventually sealed with a $35\ \mu\text{m}$ thin Mylar vacuum window, separating the beam vacuum from the helium gas environment inside the solenoid.

The muon stopping target is on the one hand supposed to stop as many muons as possible, but on the other hand it should feature a minimum amount of material with low atomic number to reduce the induced background (i.e. Bhabha scattering, gamma conversion, Compton scattering) and multiple scattering, which impairs the momentum and vertex resolutions. Ideally, the muon decay vertices are evenly spread across the whole target, therefore diminishing the accidental background. The target's baseline design, which follows the approach of the SINDRUM experiment [15], foresees a hollow double cone of 100 mm length and 19 mm radius with its center line aligned along the z -axis. The target is made of a few Mylar foils glued by epoxy to a sandwich of $75\ \mu\text{m}$ (US part) and $85\ \mu\text{m}$ (DS part) thickness, respectively. A sketch of the target is shown in Fig. 3.3. The total projected thickness of the target is $450\ \mu\text{m}$, equivalent to 0.16% radiation lengths X_0 . The target will be held by six thin nylon strings (three lines US, three DS) which will be attached to the support structure of the pixel detector.

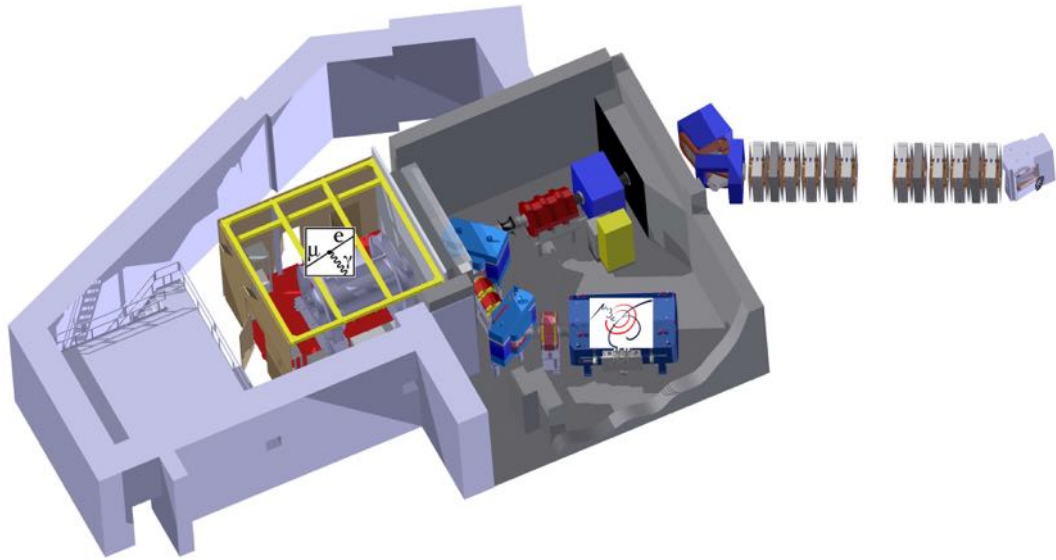
3.3 Tracking System

The particles' trajectories will be measured by a silicon pixel tracker system immersed in a magnetic field. Both these components are described in what follows.

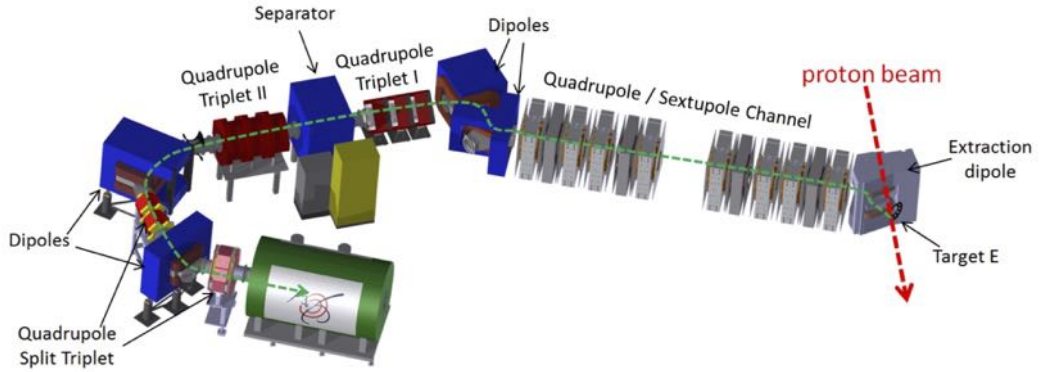
3.3.1 Magnet

The superconducting magnet of the Mu3e experiment needs to provide a homogeneous field of $B = 1.0\ \text{T}$. This field strength constitutes an optimal solution to the tradeoff between the acceptance for low momentum particles (for which the magnetic field should be ideally weak) and good momentum resolution (for which the magnetic field should be ideally strong). The magnet will be made by five identical superconducting coils. Its bore will have a diameter of 1.0 m and a length of 2.7 m. Correction coils on both of the magnet's ends ensure that the magnetic field does not drop towards the ends (as usually happens with real, non-ideal solenoidal magnets). In order to account for field-variations in the track reconstruction, especially at large $|z|$ where the recur stations are located, it is planned to use a field map look-up table with a precision at the level of $\Delta B/B \leq 0.1\ \%$.

3 The Mu3e Experiment



a) $\pi E5$ area layout



b) The CMBL

Figure 3.2: CAD drawings of the $\pi E5$ area and the Compact Muon Beam Line (CMBL).

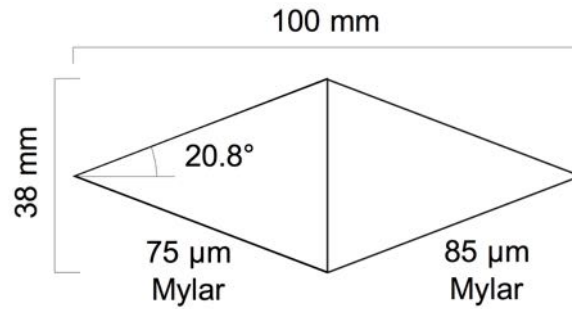


Figure 3.3: The Mu3e muon stopping target.

3.3.2 Pixel Detector

The Mu3e tracking system consists of four concentric barrels (“layers”) of pixel detectors made of a chip which is currently under development, the so-called Mu3e Pixel Sensor (MuPix). These chips are based upon the fairly new High Voltage Monolithic Active Pixel Sensor (HV-MAPS) technology [32, 33], which combines both the sensor and the digital readout into one device. This enables the chips to be thinned down to 50 μm, equivalent to 0.1 % X_0 per tracking layer.

The MuPix chip will feature a size of $2 \times 2 \text{ cm}^2$ and a pixel size of $80 \times 80 \text{ μm}^2$. It provides the addresses of the pixels which measured a hit together with the corresponding time stamp: The sensor diodes of a pixel receive the hit signals which are then amplified and forwarded to the periphery of the chip. There, the signals are digitized by means of comparators, which provide the time-over-threshold. The output data are serialized and transmitted via fast Low Voltage Differential Signaling (LVDS) links with a speed of 1.250 Gbit / s.

The latest chip that has been tested both in the laboratory and in beam tests, the MuPix 7 [34] shown in Fig. 3.4, includes nearly all properties required for Mu3e, namely a thickness of 50 μm, the analog and digital electronics as well as the fast serial readout. It features an area of $0.3 \times 0.3 \text{ cm}^2$ and pixels of $100 \times 80 \text{ μm}^2$ size. With this chip, spatial resolutions better than 30 μm at an efficiency $\geq 99 \%$ have been achieved [31]. The items that will be addressed in the next version, MuPix 8, are amongst others an increased chip size ($1.3 \times 2.3 \text{ cm}^2$), slow control functionalities (temperature sensors, switches to turn off dead pixels etc.), a better signal-to-noise ratio and it will offer the possibility to electrically and mechanically integrate several chips into submodules. An additional version is foreseen to fix the bugs in the MuPix 8, and in case it is successful, MuPix 10 could be the full-sized $2 \times 2 \text{ cm}^2$ chip used to build the Mu3e phase I pixel detector. The MuPix chips will be glued and bonded on flex prints which provide the operating and high voltage as well as the ground and signal readout lines. In addition, the flex prints will offer slow control and monitoring functionalities. They will be mounted onto a frame made of a 25 μm thin Kapton foil folded to prisms and glued to plastic end pieces. The two innermost layers, located at an average radius of 2.1 and 2.5 cm respectively, have a length of 12 cm along the z -axis. The two outermost layers have a length of 36 cm along z and are located at radii of 7.6 cm and 8.9 cm. A full detector layer, i.e. the MuPix chips, the flex print with all the required lines, the Kapton frame and glues, equalling 200 μm in total, has a thickness

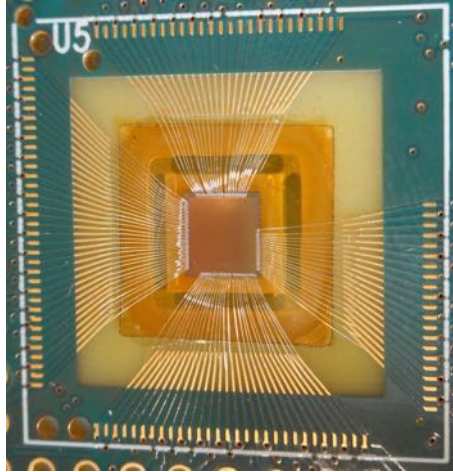


Figure 3.4: The MuPix 7 chip, which nearly fulfills all the requirements of the Mu3e pixel tracker. It features a size of $0.3 \times 0.3 \text{ cm}^2$ and is $50 \text{ }\mu\text{m}$ thin.

of $0.14 X_0$.

3.4 Timing System

The task of the timing system is to discern accidental overlaps of particles faking a $\mu^+ \rightarrow e^+e^-e^+$ signal. The timing system comprises of a fiber hodoscope within the central detector station and a tile detector located in the outer detector stations. Both detectors employ Silicon Photomultipliers (SiPMs), which offer the advantage of being insensitive to magnetic fields and featuring a comparably high Photon Detection Efficiency (PDE) as well as a fast time response. In addition, they are of compact size, which is important given the tight space constraints, and they can be directly coupled to the scintillating fibers or tiles, without the need for a light guide. For the explanation of the technical terms related to the SiPMs appearing in the following paragraphs, the reader may refer to Sect. 6.2.

3.4.1 Fiber Detector

The scintillating fiber detector's purpose is to measure the (minimum ionizing) particles' timing with a resolution of 1 ns or better at a reasonably high efficiency, while minimizing the amount of material with which the decay particles are faced. The latter point is important in order to not impair the resolution on the measurement of the particle's momentum and to allow the reconstruction algorithm to be fully efficient, since additional material introduces further scattering which makes it more difficult to correctly match track segments. Moreover, the fiber hodoscope should feature a sufficiently high granularity to cope with the high rate environment and it has to deal with very tight space constraints. These paragraphs intend to give a rough description of the fiber detector, more details can be found in the dedicated Chapter 5.

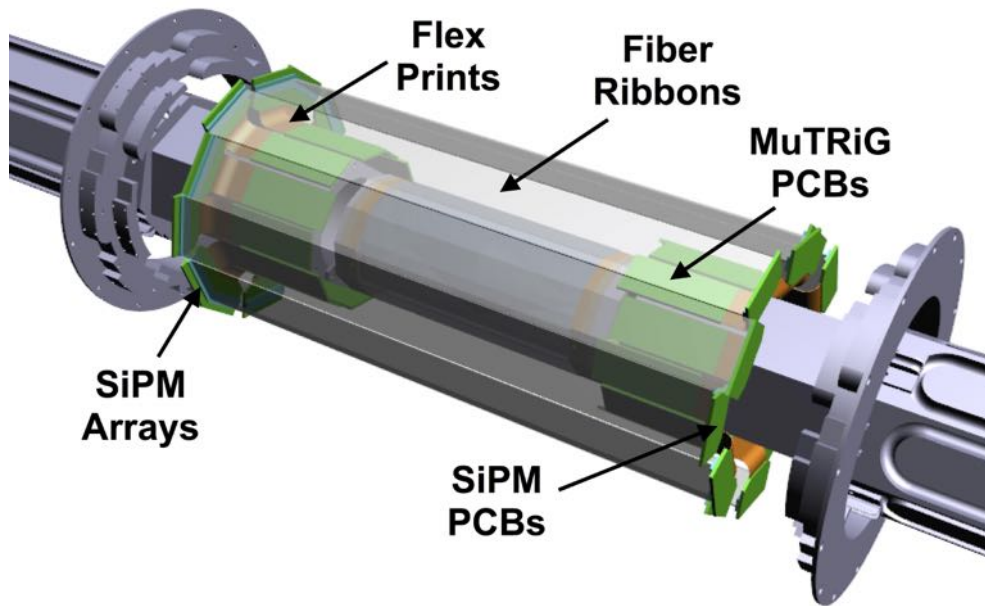


Figure 3.5: CAD drawing of the scintillating fiber timing detector. The sketch shows the fiber ribbons together with the corresponding readout PCBs, the support structure and the beam pipe.

A sketch of the scintillating fiber detector is given in Fig. 3.5. The fiber detector will consist of modules made of three or four layers of $250\ \mu\text{m}$ thin scintillating fibers glued to ribbons, which are arranged cylindrically in the central detector station at a radius of 6 cm (just before the outer two pixel layers). The ribbons have a length of about 30 cm, and the detector will be formed by 4608 fibers in total. The ribbon's thickness, given by the fiber thickness and the glue, should not exceed $900\ \mu\text{m}$. The fiber ribbons are coupled on both sides to SiPM arrays, collecting light of several fibers onto one cell of the array (see also Sect. 5.3 for more details).

The SiPM signals are read out by the Muon Timing Resolver Gigabit-link (MuTRiG) electronics presently under development [35]. These electronics should be capable of coping with high signal rates in the MHz range and should be able to trigger at low thresholds, as the signal from the scintillating fibers is at a level of few photoelectrons. The current baseline design foresees to solder the SiPMs onto support PCBs which are connected via flex prints to the PCBs housing the MuTRiG (“readout boards”). The readout boards are placed onto a cooled support plate. Apart from hosting the MuTRiGs, the readout board should provide the high voltage supply to the SiPM arrays, the clock distribution and carry slow control sensors. These are used to measure the temperature of both SiPM arrays and the MuTRiGs, the common SiPM array voltage and current as well as the MuTRiG power consumption.

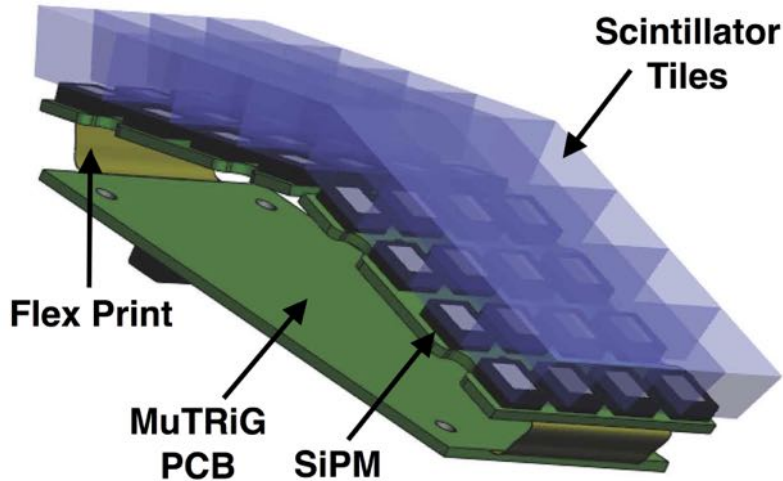


Figure 3.6: CAD drawing of a scintillating tile detector submodule (32 channels), showing the scintillating crystal cubes attached to their respective SiPMs. The SiPM PCBs are connected via flex prints to the PCBs hosting the readout chips (STiC).

3.4.2 Tile Detector

The tile detector’s goal is to measure the particles’ timing with a resolution of less than 100 ps with a detection efficiency close to 100 % and a sufficiently high granularity. Every recurv station will feature a tile detector module inside the pixel layer barrels. In contrast to the scintillating fiber detector, the tile detector does not have to comply with the requirement of minimal material because the particles are allowed to stop there.

Each of the outer detector station features 60 (z -direction) \times 56 (ϕ -direction) = 3360 tiles, located at a radius of 6.3 cm. They are organized in small, independent units (“submodules”) of 32 tiles, shown in Fig. 3.6. A tile consists of a BC418 plastic scintillator cube of $6.5 \times 6.0 \times 5.0$ mm³ size, which is glued to a SiPM of 3×3 mm² active area. For the current design, $\mathcal{O}(1000)$ photoelectrons are expected. Every tile is coated with a reflective TiO₂ paint in order to optically isolate the tiles and to maximize the light yield. The SiPM is soldered to a PCB which is connected via a flex print to the readout chip. The tiles are mounted together with their readout PCBs onto a metal support, which at the same time provides SiPM and readout chip cooling. The SiPM signals are read out by the SiPM Timing Chip (STiC), which was originally developed for Positron Emission Tomography (PET) applications and which serves also as basis for the design of the MuTRiG mentioned previously. It is further described in Sect. 5.3.3.

The tile detector has been studied extensively by simulations and measurements, proving that the time resolution of $\mathcal{O}(100)$ ps at 100 % efficiency is achievable, and thus its R&D is considered to be concluded.

3.5 Data Acquisition and Online Event Selection

The Mu3e experiment Data Acquisition (DAQ) runs without any hardware trigger, meaning that the detectors continuously send their (zero-suppressed) outputs, which are collected into temporal slices or “reconstruction frames”. A sketch of the readout scheme in Mu3e is given in Fig. 3.7. All detectors deliver timestamps of their hits. The timestamps are collected and time-ordered by front-end FPGAs into reconstruction frames of 50 ns length. The data is forwarded to switching boards, which merge the information from the different FPGAs, and sent from there to a PC filter farm for event building, buffering and running simple online reconstruction algorithms. Only the information from the central detector station’s pixel layers is used, because apart from not being necessary for the preselection of the events, the information from the remaining detectors is too hard to reconstruct and correctly match online. In a first step, a few topological cuts on the hits belonging to an individual frame are applied by the FPGAs in order to reduce the combinatorics of possible hit combinations from the first three layers (“triplets”). In a second step, the data are transferred to the memory of a GPU which performs track fitting of the triplets and vertex selection. Frames with two positron tracks and one electron track are selected and sent together with monitoring data to the central data acquisition computer, which runs the Maximally Integrated Data Acquisition System (MIDAS) software [36]. The central DAQ computer collects data from all farm PCs, combines them with slow control data, compresses and finally stores them. The expected data rate is about 50 MB /s.

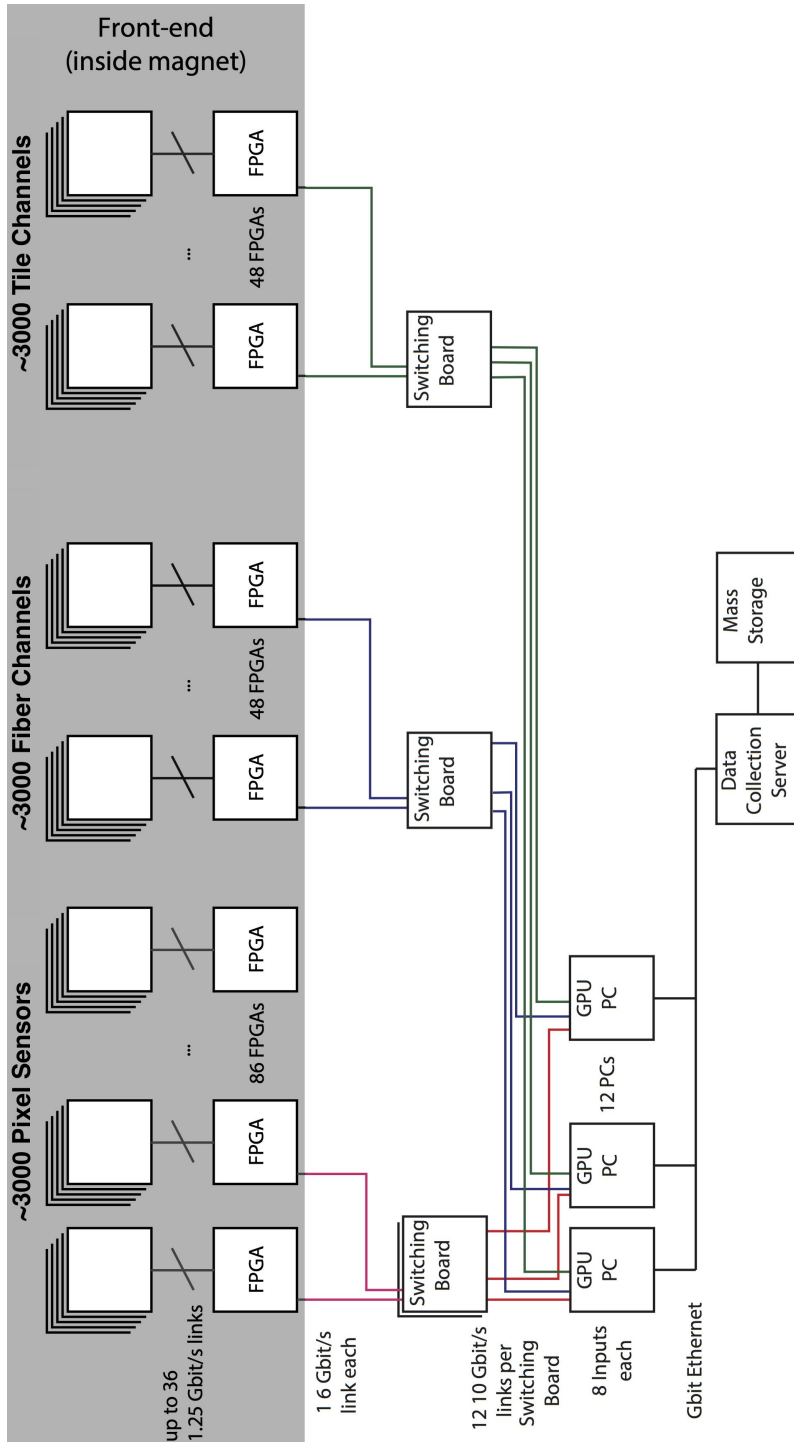


Figure 3.7: Scheme of the Mu3e readout.

4 The MEG and MEG II Experiment

In 1999 the MEG collaboration, which is currently formed by about 70 scientists from Italy, Japan, Russia, Switzerland and the US, set out to build a new experiment in search of the $\mu^+ \rightarrow e^+\gamma$ decay. First data were taken in 2008, and the experiment ran at its maximum performance from 2009 to 2013. Based upon the dataset collected during that time, the world's most stringent upper limit on the $\mu^+ \rightarrow e^+\gamma$ branching ratio of $< 4.2 \times 10^{-13}$ at 90% confidence level has been set [1]. This limit is 30 times better than what MEG's precursor experiment MEGA [37] had established previously. A detailed discussion of the above-mentioned result can be found in Chapter 9. The following sections describe MEG's experimental apparatus and the future upgraded version of the experiment, MEG II. A more detailed account is given in [2, 27].

4.1 Experimental Concept

The MEG / MEG II experiment looks for a muon decaying at rest into a positron and a gamma, each carrying half of the muon's mass energy and emitted time-coincidentally in a back-to-back configuration. In order to suppress the backgrounds and to achieve competitive momentum, timing and angular resolutions, the experiment makes use of the world's largest Liquid Xenon (LXe) calorimeter, a spectrometer with a gradient magnetic field and a custom-made trigger and data acquisition system which allows to record the waveforms of all channels. A sketch of the MEG experimental apparatus is shown in Fig. 4.1. The muons are stopped on a thin plastic target at the center of a solenoid magnet called COBRA. The kinematical observables of the decay positrons are measured by several low-mass drift chamber modules and an array of scintillating bars, while the gamma is measured by the LXe calorimeter. The detector's geometrical acceptance for the $\mu^+ \rightarrow e^+\gamma$ signal is $\approx 11\%$. The average signal detector resolutions and efficiencies are reported in Table 4.1 and will be discussed in the respective sections.

4.1.1 Coordinate System

Throughout this thesis we will use a right-handed cylindrical coordinate system (r, ϕ, z) with its origin at the center of the COBRA magnet (which ideally coincides with the center of the muon stopping target), and the z -axis oriented along the direction of the beam, see Fig. 4.1. The y -axis of the corresponding Cartesian coordinate system (x, y, z) is pointing vertically upwards to the ceiling, and the x -axis is directed away from the LXe calorimeter. The polar angle θ refers to the angle enclosed by the z -axis and the vector under consideration, see again Fig. 4.1. The region with (or the direction towards) $z < 0$ is referred to as Upstream (US), the region for which $z > 0$ as Downstream (DS). The positrons are forced by the magnetic field to propagate along helicoidal tracks, moving in the negative ϕ -sense. For the LXe calorimeter, there is an additional coordinate system (u, v, w) . The coordinates u and v denote the coordinates along

Table 4.1: Average signal detector resolutions (Gaussian standard deviations) and efficiencies of the MEG experiment.

Parameter of Interest	Resolution / Efficiency
Positron polar angle θ_e	9.4 mrad
Positron azimuthal angle ϕ_e	8.7 mrad
Positron vertex (y, z)	(2.4 mm, 1.2 mm)
Gamma conversion point (u, v, w)	(5 mm, 5 mm, 6 mm)
Relative positron-photon polar angle $\theta_{e\gamma}$	(15.0 – 16.2) mrad
Relative positron-photon azimuthal angle $\phi_{e\gamma}$	(8.9 – 9.0) mrad
Relative positron-photon timing $t_{e\gamma}$	122 ± 4 ps
Positron energy resolution E_e	≈ 330 keV (core)
Photon energy resolution E_γ	$\approx 2\%$
Positron detection efficiency ε_e	$\approx 48\%$
Photon detection efficiency ε_γ	$\approx 63\%$
Signal trigger efficiency ε_{trg}	$\approx 97\%$

the LXe surface (with u along the z -direction and v along the negative ϕ -direction) and the w -coordinate describes the depth measured from the inner face of the calorimeter, see Fig. 4.1.

4.2 MEG Beam Line and Muon Stopping Target

The $\pi E5$ channel at PSI is the number one choice of the MEG experiment because it provides one of the world's most intense and continuous surface muon beams. In addition, the $\pi E5$ channel is able to furnish beams for calibrations purposes, such as a positron beam with a momentum of 52 MeV/c and a negative pion beam of 70.5 MeV/c momentum. The aspects of the $\pi E5$ channel relevant to both the Mu3e and MEG experiments have been discussed previously in Sect. 2.3.1. The remaining part of the beam line specific to MEG is shown in Fig. 4.2. The distance from Target E up to the center of COBRA, where the muon stopping target is located, is approximately 22 m. For the MEG experiment, surface muons bearing a momentum $p = 28$ MeV/c are used. We recall the presence of a Wien filter, which separates the muons from the positrons, with the positron flux being about eight times as large as the muon's. The positrons are dumped in the collimator system. The muon beam is transported in vacuum through the Beam Transport Solenoid (BTS), a superconducting solenoid of 2.8 m length which contains a 300 μm thick Mylar degrader foil at the beam's intermediate focus. The degrader reduces the muon momentum such that the stopping density on the target is maximal. Finally, the beam enters the COBRA magnet, whose helium-filled bore contains the muon stopping target and the positron spectrometer.

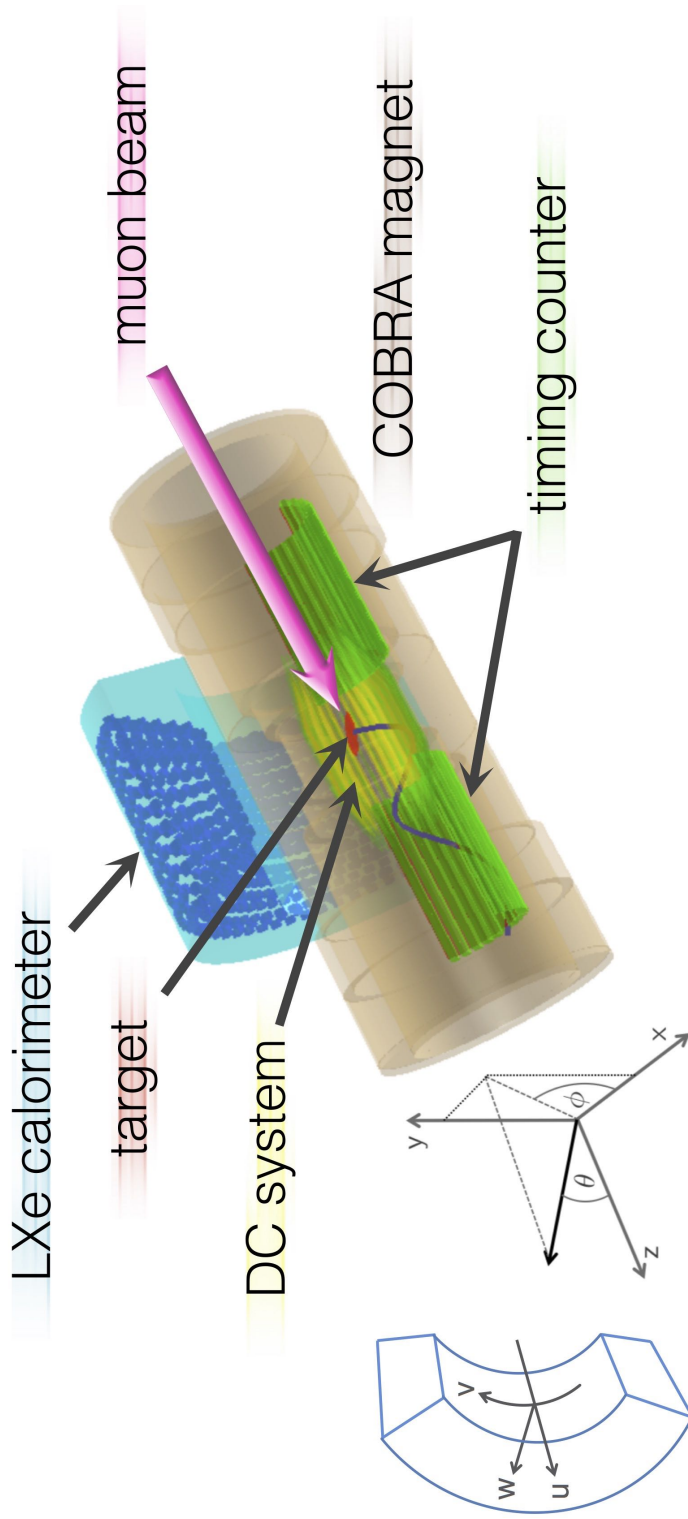


Figure 4.1: Layout of the MEG experiment. The muons are stopped on a thin plastic target, where they decay. The gamma is detected by a liquid xenon calorimeter, the positron by a magnetic spectrometer consisting of drift chamber modules, a timing counter and a gradient magnetic field provided by the COBRA magnet. MEG's Cartesian coordinate system (with the origin at COBRA's center) as well as the LXe local coordinate system are shown on the left.

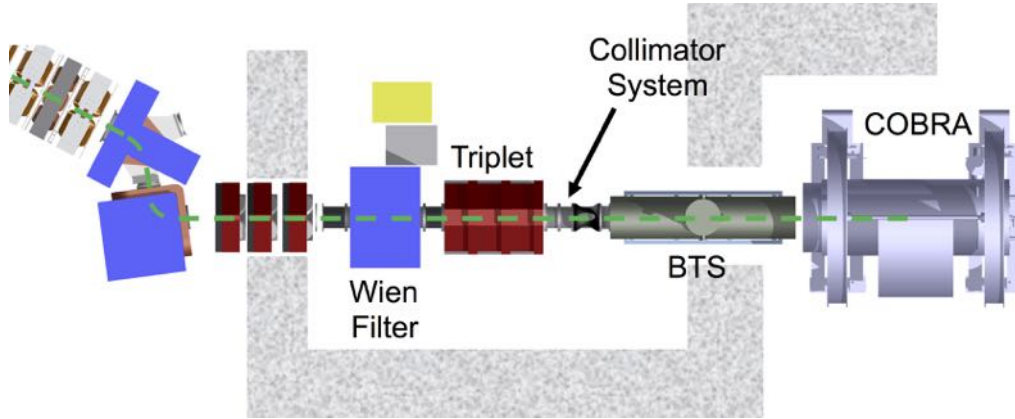


Figure 4.2: The MEG beam line. The Wien filter removes the beam positrons, which are dumped in the collimator system. The BTS ensures an efficient transport to the COBRA magnet.

The helium atmosphere inside COBRA is separated from the vacuum and the environment by means of endcaps consisting of 4 mm thick aluminum plates with a diameter of 1.2 m. On the US side, the endcap contains a Mylar beam vacuum window of 190 μm thickness. The DS side features a bellows insertion system with a 20 μm Mylar window and which can extend up to 1.7 m into the COBRA volume. It is used for calibration purposes, e.g. to insert the lithium tetraborate target which is used in conjunction with a dedicated Cockcroft-Walton proton accelerator, see Sect. 4.5.2.

On the target, about $3 \times 10^7 \mu^+ / \text{s}$ are stopped¹. The beam spot at the target is round and has a size of $\sigma_{x,y} \approx 10 \text{ mm}$. Both the predicted and the measured degree of polarization of the muons at the stopping target is $\approx 85 \%$ [38].

The target is required to stop the vast majority of the incident muons, while at the same time it should represent as little material as possible to the decay particles in order to minimize the induced gamma-background as well as multiple scattering. In addition, the target has to be thin and stable, and its position with respect to the spectrometer needs to be known to a precision of 100 μm in order to accurately reconstruct the angles at which the positron is emitted, since the muon decay vertex and the positron direction at that point are not directly measured, but rather derived by projecting the reconstructed positron track back to the target. To mitigate the effects of gamma-ray conversion and multiple scattering, the target is rotated by $\theta \approx 20^\circ$ (where the target face onto which the muon beam is incident is oriented towards the LXe calorimeter, see Fig. 4.1).

The target, shown in Fig. 4.3, has an elliptical shape with a semi-major axis of 10 cm and a semi-minor axis of 4 cm. It consists of a 205 μm thin sheet made of polyethylene and polyester (chemical composition: CH_2), which are stacked in a sandwich-like structure. The sheet is framed by two Rohacell[®] foam rings and is attached to an actuator device by means of a Ro-

¹In principle, the MEG beam line would be capable of delivering even higher rates, but the lower rate optimizes the sensitivity to the $\mu^+ \rightarrow e^+ \gamma$ decay, taking into account the detector performances.



Figure 4.3: The MEG muon stopping target, made of polyethylene and polyester. The crosses and holes are used for alignment purposes.

hacell hanger and a fishing line. The actuator is fixed to the drift chamber support frame and allows to retract the target to a parking position located US during e.g. calibrations requiring the Cockcroft-Walton accelerator (see Sect. 4.5.2).

The target features holes of 1 cm diameter and crosses drawn on its surface, which are both used for alignment purposes. Before the start of a run period, the target position is optically surveyed with the help of the crosses. The holes on the other hand are used for a software-based cross-check. From the reconstructed position of the holes, one can infer the target planarity and orientation.

4.3 Positron Spectrometer

The positron spectrometer's purpose is to ensure an excellent measurement of the positron's kinematical observables while operating at high muon rates. It consists of three parts: (1) A gradient magnetic field together with (2) a low-mass drift chamber system to track the positron's trajectory and (3) a timing counter which measures the positron's time of flight. All three components have been designed in such a way that only positrons with an energy close to the $\mu^+ \rightarrow e^+\gamma$ signal energy are accepted, while the copious amount of low energy Michel positrons is swept away without getting into the spectrometer's detectors. The three components listed above are going to be presented in more detail in the next few sections.

4.3.1 COBRA Magnet

The magnetic field of the positron spectrometer is provided by a superconducting, thin-walled magnet named COBRA (COntant Bending RAdius) of 3 m length. The magnetic field is not homogeneous, but features a gradient along the z -direction. The gradient magnetic field provides two advantages compared to a uniform solenoidal magnetic field:

1. Low energy positrons do not reach the detectors, because the gradient magnetic field is designed in such a way that particles with equal total momentum (rather than just transverse

momentum) follow helicoidal tracks with equal projected bending radii, see Fig. 4.4a). This means that positrons with momenta close to the $\mu^+ \rightarrow e^+\gamma$ signal can be selected over the vast background of low momentum Michel positrons by placing the detectors at a sufficiently large radial distance from the target.

2. Particles with little longitudinal momentum (emitted at $\theta \approx 90^\circ$) leave the spectrometer after following a few turns such that they do not unnecessarily occupy the drift chambers, see Fig. 4.4b). This facilitates the pattern recognition and guarantees a stable operation of the spectrometer even at high beam rates.

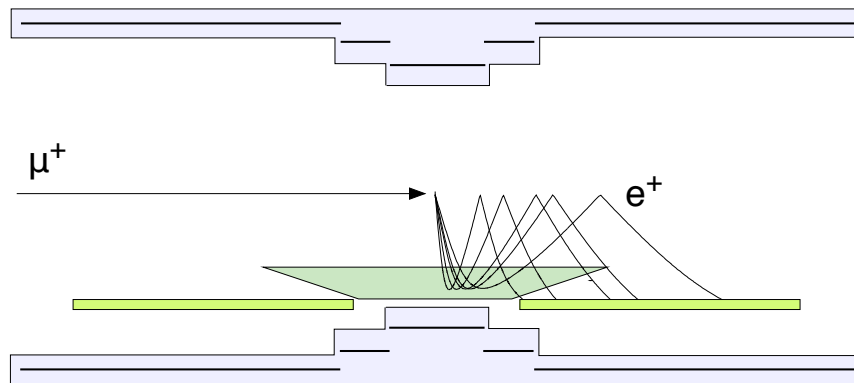
The gradient field is provided by five coils of three different radii ($r_1 = 70$ cm for the central coil, $r_2 = 81$ cm for the two adjacent coils and $r_3 = 92$ cm for the end coils) and different winding densities. The field at the center of COBRA ($z = 0$) amounts to 1.27 T and gradually decreases to 0.49 T towards the endcaps. In order to ensure the smooth functioning of the gamma-ray calorimeter's Photomultiplier tubes (PMTs), two compensations coils have been added to reduce the stray field of the COBRA magnet. The interior of COBRA's bore is filled with helium at 1 atm pressure in order to reduce the multiple scattering of the positrons along their path.

4.3.2 Drift Chamber System

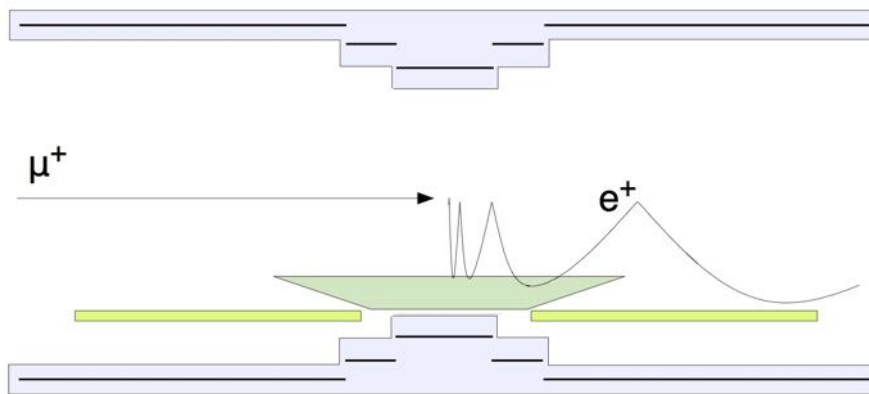
The positron is tracked by a set of Drift Chamber (DCH) modules, which are designed such as to feature as little material as possible, since the resolutions on the momentum and the angle are mainly dominated by multiple scattering of the positron along its path through the chambers. The low mass also reduces the probability of positron AIF, which generates background gammas to the calorimeter. The amount of material with which a signal positron is confronted with corresponds to $2 \times 10^{-3} X_0$ along the whole positron track.

The DCH system is made of 16 identical, independent modules arranged radially in a semi-circle inside COBRA's bore, as shown in Fig. 4.5a). It spans the azimuthal range $191.25^\circ < \phi < 348.75^\circ$ with an interval of 10.5° and the radial region $19.3 \text{ cm} < r < 27.9 \text{ cm}$. Note that since the projected bending radius of the positron track is constant and independent of the angle at which the positron is emitted, the radial range directly determines the acceptance of the spectrometer in terms of momentum, which in this case is equal to $40 \text{ MeV}/c < p_{acc} < 55 \text{ MeV}/c$. The modules have a trapezoidal shape with 40 cm and 104 cm base lengths, with the longer side oriented towards the central axis of COBRA, and are mounted in a carbon fiber support structure. The trapezoidal shape allows an open frame geometry, see Fig. 4.5b), and therefore minimizes the amount of material in the inner part of the spectrometer. Every module is made of two independent detector planes shown in Fig. 4.6a). Each detector plane consists of two grounded, aluminized polyimide foils of $12.5 \mu\text{m}$ thickness separated by a 7 mm gap which act as cathodes. The gap is filled with a 50:50 mixture of He:C₂H₆. A detector plane contains nine anode wires of $25 \mu\text{m}$ diameter oriented along z , which are alternated with potential wires² of $50 \mu\text{m}$ diameter with a pitch of 4.5 mm and which are centered between the two cathode walls. In order to avoid left-right ambiguities, the wires of one of the two planes are staggered

²The anode wires (or sense wires) are the wires collecting the signals, the potential wires (or field wires) shape and optimize the electric field.



a) Constant projected bending radius for positrons with equal momentum



b) Quick sweep-out of particles with $\cos \theta_{e^+} \approx 0$

Figure 4.4: The COBRA gradient magnetic field. Low energy positrons do not reach the detectors, because the gradient magnetic field is designed in such a way that particles with equal total momentum (rather than just transverse momentum) follow helicoidal tracks with equal projected bending radii. In addition, particles with little longitudinal momentum are swept out quickly, thus facilitating the pattern recognition and guaranteeing a stable operation of the drift chamber system.

by half a cell in the radial direction. The shortest wire has a length of 38 cm, the longest one 83 cm, and the voltage supplied to the anode wires is 1800 V.

The radial coordinate of a DCH "hit" (= information provided by a cell) is determined with an accuracy of $\approx 200 \mu\text{m}$ by considering the time difference of the drift times of two adjacent cells. The z -coordinate of the hit is determined by measuring the charges at each end of the anode wire and taking the ratio thereof ("charge division"), with a resolution of $\approx 2\%$ of the wire length. Due to the periodic double-wedge structure ("Vernier pattern") etched on the cathode planes, the z -position resolution is improved to $\approx 800 \mu\text{m}$: After a rough determination of the z -position using the anode wire, a more precise position information can be extracted by measuring the charge induced on each of the four cathode strips (which depends periodically on z , but the period is fixed by the anode), as shown schematically in Fig. 4.6b).

The average amount of material along a positron track is $\approx 2 \times 10^{-3} X_0$. The average angular resolutions on the positron tracks extracted from double turn tracks (including Monte Carlo simulation corrections) are estimated to be $\sigma_\theta = 9.4 \text{ mrad}$ and $\sigma_\phi = 8.4 \text{ mrad}$, the corresponding vertex resolutions $\sigma_y = 1.1 \text{ mm}$ and $\sigma_z = 2.5 \text{ mm}$. The momentum resolution, extracted from a fit to the energy spectrum of Michel positrons, is $\sigma_E \approx 330 \text{ keV}$. The positron detection efficiency of the DCH system alone is estimated to be $\varepsilon_e^{\text{DCH}} \approx 83\%$, with the largest inefficiency being caused by tracks emitted at polar angles close to 90° . For the total positron detection efficiency, the reader is referred to the next section about the timing counter.

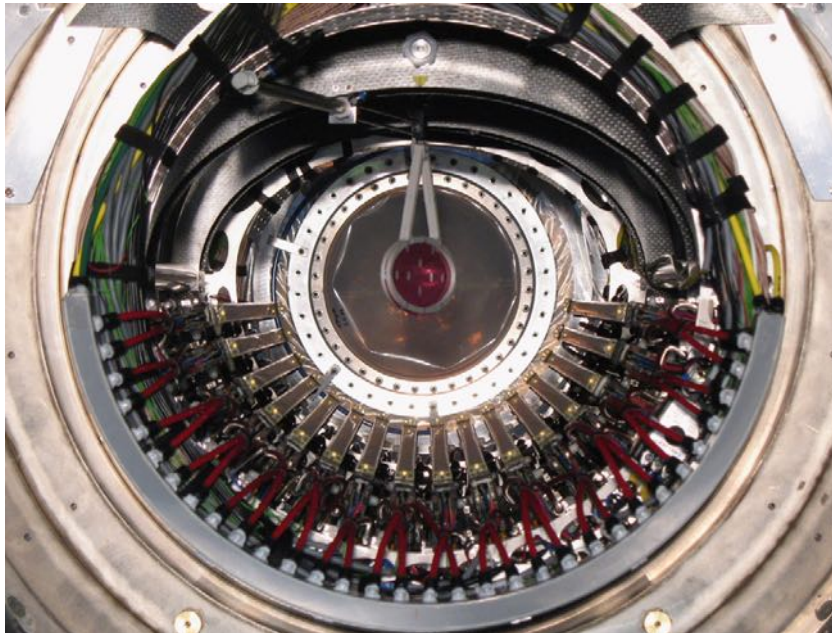
4.3.3 Timing Counter

The two tasks of the Timing Counter (TC) are to provide (1) a precise measurement of the positron time-of-flight and (2) a rough estimate of the positron's direction and time for trigger purposes, since the DCH system is relatively slow compared to the other detectors and is thus not included in the $\mu^+ \rightarrow e^+\gamma$ signal trigger.

The TC consists of two modules (one US, one DS) made of fifteen plastic scintillator bars coupled to PMTs arranged in a semi-circle ("longitudinal detector") and a mat of scintillating fibers attached to Avalanche Photodiodes (APDs) placed on top of the bars ("transverse detector"), as displayed in Fig. 4.7. It is designed in such a way that it is capable of accepting all signal positrons whose corresponding gamma-ray points to the calorimeter. Similarly to the DCH, the module's inner radius $r = 29.5 \text{ cm}$ is chosen such that only positrons with a momentum close to the signal positron are accepted. In addition, the TC is rotated by about 20° around the z -axis with respect to the DCH, optimizing the path length of the positrons in the scintillating bars, therefore maximizing the light yield and improving the time resolution. Apart from providing the time measurement of the positron, the longitudinal detector also gives a rough estimate of both the impact z and impact ϕ coordinates through the time difference of the two attached PMTs and the detector's segmentation, respectively. In principle, the fiber mat would provide a more precise measurement of the impact z -coordinate, helping to match the DCH track with the TC impact point. However, due to noise problems, the transverse detector was not used in the analysis.

Each scintillating bar of the longitudinal detector has a size of $4 \times 4 \times 80 \text{ cm}^3$ and is made of Bicron BC404 scintillating material. The bars are positioned in a semi-circle in steps of 10.5° , thus matching the arrangement of the DCH modules. Every bar is read out on both ends by

4 The MEG and MEG II Experiment



a) DS view of the installed DCH system



b) Frame with wires (front), one plane of a DCH module (middle) and a full DCH module (back)

Figure 4.5: The MEG drift chamber system consists of 16 independent, identical modules with two planes each, arranged in a semi-circle around COBRA's center.

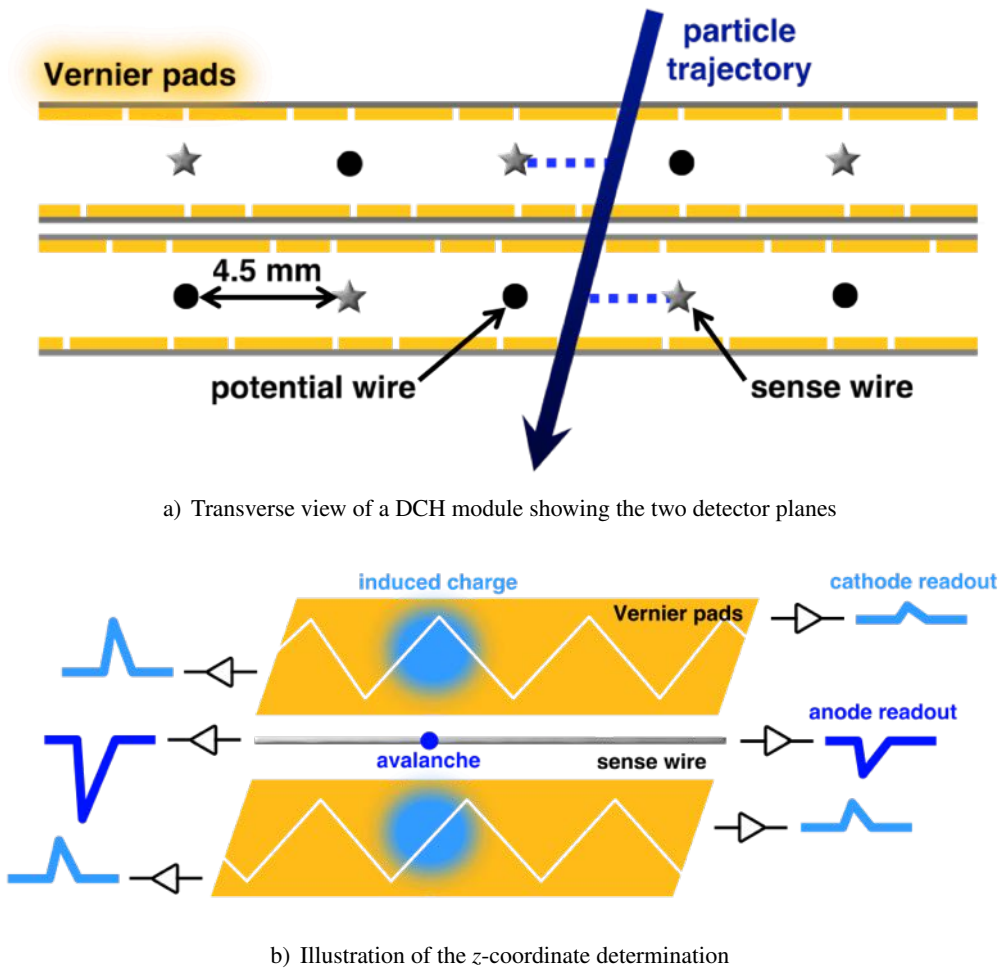


Figure 4.6: Sketch of a drift chamber module. The z -coordinate of the DCH hit is determined by charge division and with the help of the Vernier pattern etched on the cathode planes.

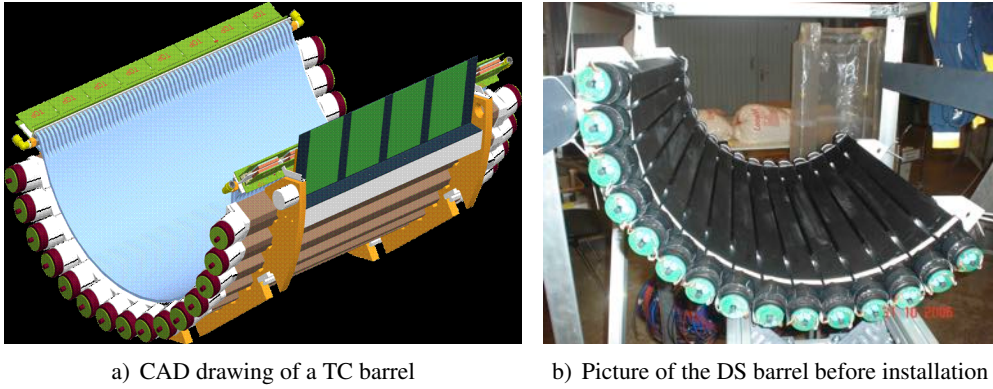


Figure 4.7: The MEG timing counter is made of two barrel-shaped detectors (one US, one DS) composed of scintillating bars coupled to PMTs.

PMTs of 2" size which are able to operate in magnetic fields of up to 1.5 T and which are glued to the bar ends. The PMTs windows are subject to helium leakage, leading to internal discharge inside the PMTs. Therefore, in order to separate the PMTs from the helium atmosphere inside COBRA, each module is wrapped in an EVAL[®] foil bag flushed with nitrogen.

The resolution on the impact point position on the bar is ≈ 1 cm in the offline event analysis. The time at which the positron has been emitted from a muon decay is obtained by extrapolating the impact time back to the target using the information from the DCHs. The positron timing resolution, including the contribution due to track length fluctuations, is $\sigma_{t_{e^+}} = 107$ ps (FWHM). The detection efficiency for signal positrons of the TC alone is given by $\varepsilon_e^{TC} \approx 100\%$. The total signal positron detection efficiency (i.e. the efficiency to have a track in the DCH, a hit in the TC and that the track matches the TC hit) is estimated to be $\varepsilon_e \approx 48\%$ based on Monte Carlo simulations. This rather low efficiency is caused by the DCH support frame intercepting a significant amount of tracks which exit the DCH tracking volume, where the particles may suffer from either energy loss or large deflections.

4.4 Liquid Xenon Calorimeter

The scope of the LXe calorimeter, shown in Fig. 4.8, is to measure the gamma-ray's energy, position and time with excellent resolutions and high detection efficiency. It constitutes the most innovative part of the experiment, and with ca. 850 ℓ of LXe viewed by 846 PMTs it is currently the world's largest calorimeter based on scintillation light only.

LXe has the beneficial properties that it has a high atomic number, that it is very dense and that it has a short radiation length, making it an efficient detection medium for gamma-rays. At the same time it provides a high light yield, which is important to achieve excellent timing and energy resolution, as well as fast scintillation, which helps to reduce events with pile-up. Being in a liquid phase, it also offers good homogeneity. Table 4.2 summarizes the most important LXe properties. The scintillation light emitted by LXe has a wavelength of $\lambda = 178$ nm, lying in the Vacuum Ultra Violet (VUV) region. Impurities such as H₂O, O₂ or N₂ may absorb the

4 The MEG and MEG II Experiment

scintillation light and therefore drastically reduce the LXe's transparency, which is why the LXe is purified by a dedicated system and is frequently monitored (see Sect. 4.5.2). The operational temperature of the LXe is 165 K maintained by a pulse-tube cryocooler, and it is kept at a pressure of 1.2 bar.

Table 4.2: Properties of liquid xenon.

Properties	
Atomic number	54
Density (at 161.35 K)	2.98 g / cm ³
Radiation length X_0	2.77 cm
Time constant τ_1 (fast)	4 ns
Time constant τ_2 (slow)	22 ns
Time constant τ_3 (recombination)	45 ns
Number of scintillation photons	40000 photons / MeV
Emission peak wavelength λ_{scint}	178 nm (VUV)

The LXe calorimeter consists of an inner and outer C-shaped vessel coaxially encompassing the COBRA magnet: The inner vessels holds the LXe and the PMT support structure, whereas the outer vessel is under vacuum and acts as thermal insulator. The PMTs, which have been developed together with Hamamatsu in order to work at cryogenic temperatures, to sustain high rates and to detect VUV light, are directly submerged into the LXe and are placed over all faces of the calorimeter. The detector has a depth of 38.5 cm, equivalent to 14 X_0 , and is thus able to fully contain showers induced by signal gammas. The material traversed by a gamma entering the LXe comprises of the drift chamber frame, its support, the COBRA magnet, the entrance windows of the two vessels, the PMTs and their support structure. The largest contribution comes from the COBRA magnet. The amount of material of the coil plus cryostat with which the gammas are faced before reaching the calorimeter corresponds to 0.2 X_0 .

Because the LXe calorimeter is a large, unique detector volume, there is a fair chance for low energy gammas to create pile-up. Therefore, the waveforms of all PMTs are registered in order to single out events with gamma-ray pile-up. The energy E_γ of a gamma-ray is extracted by summing the number of scintillation photons detected by the PMTs. The direction of the gamma-ray is not directly measured, instead one determines the gamma-ray conversion point and the reconstructed positron vertex. The line given by these two points defines the gamma direction. In order to reconstruct the gammas conversion point, one uses the light distribution of the PMTs. The reconstructed time of the gamma-ray is obtained by considering the time of the gamma-ray conversion and correcting it for the time-of-flight to the positron vertex.

The energy resolution (RMS) ranges from 1.6 to 2.7 %, depending on where the gamma converts. The energy resolution is worse for "shallow" events in which the gamma converts near the entrance surface (i.e. at low w). The measured resolution on the gamma-ray conversion point is 5 mm in the u - and v -direction, and 6 mm in the w -direction. The measured detection efficiency of the LXe calorimeter is $\varepsilon_\gamma \approx 63\%$. A large part of the efficiency loss is due to the material along the gammas path into the active volume of the calorimeter.

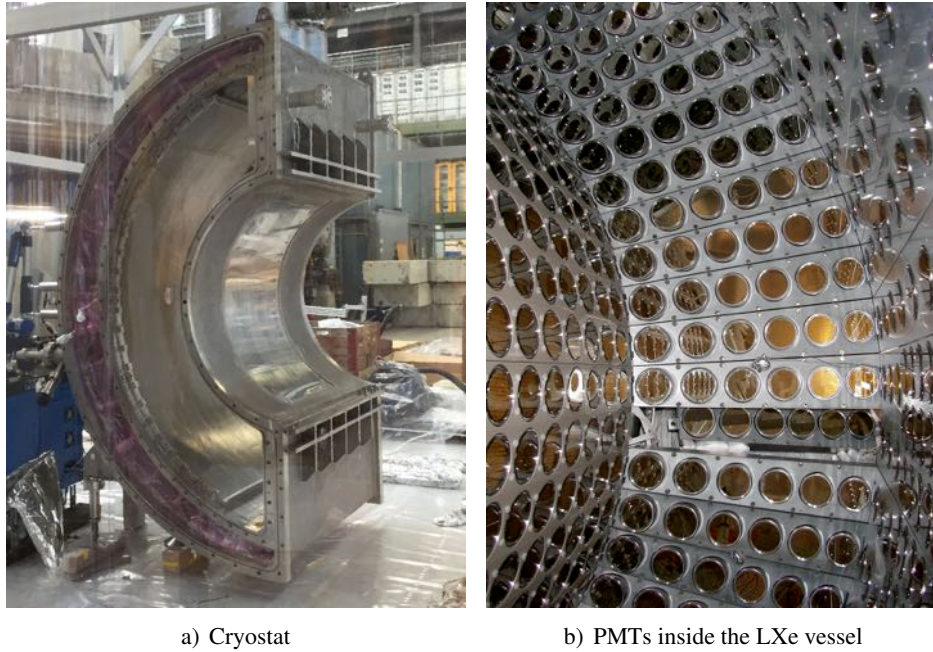


Figure 4.8: The MEG calorimeter comprises of 900 liters of liquid xenon viewed by 846 PMTs.

4.5 Calibrations and Monitoring

For the MEG experiment, detector calibrations are of paramount importance, since the absolute energy scales and the zero positions as well as the resolutions of the kinematical variables need to be known for the analysis. Moreover, it is indispensable to constantly monitor the detectors in order to not only notice any anomalous detector behavior at an early stage, but also to keep under control the systematics and the conditions (e.g. thresholds) under which the data are taken. Certain calibrations are performed on a weekly or even on a daily basis. Other calibration methods are incompatible with the usual MEG setup, limiting their data acquisition to a certain period of time. In addition, control samples (e.g. Michel positrons) are constantly being collected during normal operation using dedicated triggers.

4.5.1 Calibrations of the Positron Spectrometer

Michel Positrons (*continuously*) Positrons from Michel decay $\mu^+ \rightarrow e^+ \nu_e \bar{\nu}_\mu$, which are continuously collected during the physics run, are used for target and DCH alignment purposes as well as to determine the time offsets between different TC bars. Moreover, Michel positron data are utilized to measure the resolutions on the positron kinematical variables.

Mott Scattered Positron Beam (*1 – 2 times a year*) The vast amount of beam positrons, which is usually rejected during normal MEG operation, can be used to the experiment's advantage. The quasi-monochromatic positron beam, tuned to a momentum of ≈ 52 MeV/c and

scattered off the MEG target, provides tracks which resemble a lot those left by a signal positron. This calibration tool is discussed in depth in Chapter 8 of this thesis.

Cosmic Rays (1 – 2 times a year) The cosmic rays' applications concerning the positron spectrometer alone are threefold: (1) They are used to align the DCH system, (2) they are utilized to equalize the PMTs gains of the TC, since the inner and outer PMTs operate under different conditions due to the COBRA magnetic field and (3) they allow to correct for intra-bar time offsets due to the electronics.

4.5.2 Calibrations of the Liquid Xenon Calorimeter

The one kinematical variable that is extracted solely using the LXe calorimeter is the gamma-ray energy. For that purpose, it is necessary to know the proportionality factor between the number of detected scintillation photons and the gamma-ray energy. This factor may vary considerably over time (e.g. due to changes in the PMT gains or LXe purity). Therefore, several calibration methods have been developed, with which the energy scale is known to a level of a few-per-mil:

LED (daily) About 40 LEDs are permanently installed in the LXe calorimeter and used to estimate the PMT gains by flashing them at different intensities during dedicated calibration runs performed every other day. In addition, during the physics run, LED events are collected with a rate of 1 Hz. Typically, the PMT gains decrease by 0.1 % per normal data taking day.

α Sources (daily) Inside the LXe calorimeter, five thin wires, each carrying five point-like ^{241}Am sources emitting 5.5 MeV alphas with a total activity of 25 kBq, are suspended. These alpha sources are used to surveil the transparency and the light yield of the LXe, as well as to measure the relative quantum efficiency of every PMT. Due to the different pulse shapes, events associated to the alpha sources can easily be distinguished from those of low energy gammas. This allows for permanent collection of alpha events also during physics data taking. Furthermore, dedicated runs of alpha source data are recorded on a daily basis.

Neutron Generator (daily) This calibration method is particularly useful because it provides low energy gamma-rays (rather than just alphas) that can be collected during normal physics data taking. Neutrons supplied by a pulsed neutron generator, surrounded by a polyethylene moderator interleaved with layers of nickel and placed in front of the LXe calorimeter, are captured by the nickel, which emits a 9 MeV gamma-ray that is used to monitor the LXe. The pulsed mode together with a dedicated trigger allows to reduce overlaps with gammas from the beam.

Am/Be Source (daily, optionally) In order to have a feedback on the LXe light yield and the scintillation time constants, a 50 kBq Am/Be source which yields 4.4 MeV gamma-rays is placed once a day in front of the LXe detector by means of a compressed-air circuit. These data need to be taken in the absence of the muon beam. The Am/Be source is used as a backup solution whenever the CW accelerator described below cannot be used (e.g. due to maintenance).

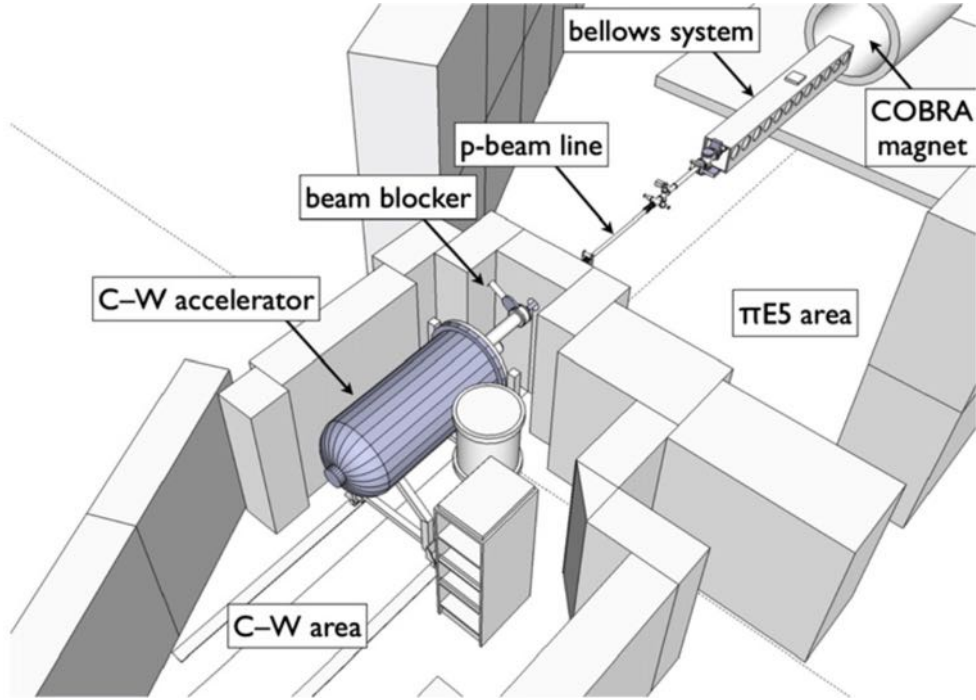


Figure 4.9: The Cockcroft-Walton proton accelerator is used in conjunction with a lithium tetraborate target to calibrate the LXe calorimeter. During the calibration procedure, the MEG stopping target is retracted while the proton target and the vacuum beam pipe in which it is contained are inserted from DS into COBRA via a bellows system.

Cockcroft-Walton (CW) Accelerator (2 – 3 times a week) One of the highlights in terms of calibrations is the usage of a dedicated Cockcroft-Walton (CW) proton accelerator in combination with a lithium tetraborate ($\text{Li}_2\text{B}_4\text{O}_7$) target, shown in Fig. 4.9. During normal data taking, the proton target stays outside COBRA. For the calibration procedure, the usual MEG muon stopping target is brought into its parking position located US, while the proton target and the vacuum beam pipe in which it is contained are moved from DS to COBRA's center via a bellows system. The CW accelerator sends protons with an energy of 400 to 900 keV directed along the negative z -axis onto the target, inducing the nuclear reaction ${}^7\text{Li}(p,\gamma){}^8\text{Be}$ and producing a sharp gamma-line at 17.6 MeV and a broader, less intense line at 14.8 MeV. In addition, the CW accelerator is used to intercalibrate the LXe with the TC and the TC itself by exploiting the nuclear reaction ${}^{11}\text{B}(p,\gamma\gamma){}^{12}\text{C}$ (see Sect. 4.5.3).

Charge Exchange (CEX) Reaction (1 – 2 times a year) The charge exchange reaction $\pi^- p \rightarrow \pi^0 n$ of negative pions on protons at rest allows to calibrate the LXe calorimeter at energies close to the ones of the $\mu^+ \rightarrow e^+ \gamma$ signal by considering the gamma-rays from the $\pi^0 \rightarrow \gamma\gamma$ decay. To that end, the polarity of the beam is switched to negative pions of 70.5 MeV/c momentum and it is sent onto a target made of a cylindrical cell of 50 mm diameter and 75 mm

length containing liquid hydrogen inserted at the center of COBRA. In the laboratory frame, in which the π^0 has a momentum of 28 MeV/c, the energies of the gammas are strongly correlated with their relative opening angle. By selecting an opening angle of $\approx 180^\circ$, one obtains gammas with an energy of 55.1 MeV, i.e. close to the signal energy. Opposite to the LXe, an auxiliary detector made of NaI (2008 to 2009) or BGO (2010 to 2013) scintillating crystals mounted onto a movable stage is used to select the back-to-back gamma-pairs, scanning the whole entrance face of the LXe detector.

4.5.3 Detector Intercalibrations

Calibrations among different subdetectors are necessary to keep under control the relative timing and the relative angle between the gamma and the positron.

Cosmic Rays The position of the DCHs frame with respect to the LXe calorimeter is measured by considering cosmic rays which traverse both subdetectors and comparing the position of incidence on the LXe detector reconstructed by the PMTs with the one extrapolated from the DCHs. The accuracy with which the two detectors can be aligned is ≈ 1 mm in each direction (x, y, z).

RMD Data Radiative muon decays $\mu^+ \rightarrow e^+ \nu_e \bar{\nu}_\mu \gamma$ enable us to determine the zero position of the relative timing between the LXe calorimeter and the TC as well as the global timing resolution for particles emitted time-coincidentally. In order to accurately assess the resolution $\sigma_{t_{e\gamma}}$ on the relative timing of the signal positron and gamma, the global timing resolution extracted from RMDs (corrected for both the gamma-ray and the positron energy dependence by Monte Carlo simulations) is $\sigma_{t_{e\gamma}} \approx 120$ ps.

CW Accelerator: Boron Reaction As we have already seen in Sect. 4.5.2, the CW accelerator shoots protons on a $\text{Li}_2\text{B}_4\text{O}_7$ target placed at COBRA center during dedicated calibration runs. The nuclear reaction of protons on boron, $^{11}\text{B}(p, \gamma\gamma)^{12}\text{C}$, produces two time-coincident gamma-rays with an energy of 4.4 MeV and 11.6 MeV, respectively. One gamma is detected by the LXe calorimeter, the other gamma may convert either before or in the TC material such that it is detected by the TC, allowing to measure the relative timing between the two detectors.

4.6 Trigger and Data Acquisition

In the MEG experiment, all detector signals are digitized. The detector signals are sent to active splitters, which provide a fraction of the signal to the trigger system and the remaining part of the signal to the DRS waveform digitizers. An ancillary system distributes the clock signal and a control signal (start / stop) to all the digitizers. The DAQ is controlled by the MIDAS software [36].

4.6.1 Trigger

The trigger system is required to supply an efficient and fast event selection while rejecting a significant amount of background. At the same time the trigger rate should remain below 10 Hz to keep the DAQ dead time at a minimum. As a figure of merit, one can consider the overall DAQ efficiency, which is the product of the trigger efficiency and the DAQ live time. In the years 2009 to 2010, the DAQ efficiency was $\approx 75\%$, from 2011 on (after improving the readout scheme) it reached $\approx 97\%$. Apart from the $\mu^+ \rightarrow e^+\gamma$ signal trigger, there are about twenty additional triggers adapted to particular calibration and monitoring processes. For some of these (usually pre-scaled) triggers, events are acquired during the normal physics data taking, such that the experimental apparatus can be constantly monitored.

For the purpose of an efficient and rapid event selection, the analog detector signals are processed and sent to FPGAs housed on VME boards arranged in a tree-like structure. This tree-like structure is organized in three levels: The first level consists of VME boards which on the one hand receive and digitize the detector signals by means of 100 MHz flash ADCs, and on the other hand processes the waveforms through the FPGAs. On the next level, the information from the waveforms (such as timing or amplitude) is used to calculate a rough estimate of the kinematical observables of interest. The last level, the master board, combines the information obtained by the different subdetectors at the second level to one event and issues the trigger (stop signal) to the Domino Ring Sampler (DRS) digitizers if the trigger condition is met.

The observables which are reconstructed at trigger level are the gamma-ray energy, the relative positron-gamma timing and the relative positron-gamma direction. The trigger latency needs to be less than 450 ns, otherwise the information stored in the DRS is overwritten (see next section). The positron momentum is not included, because the DCH signals are relatively slow due to the drift time of the electrons towards the anode wires, such that they would not match the requirement on the trigger latency time. The most important factor in terms of background suppression is the gamma-ray energy, because the gamma-ray of RMDs spectrum features a rapid decrease towards its endpoint. The MEG physics trigger runs at a rate of about 10 Hz.

4.6.2 Data Acquisition

The MEG experiment records all the waveforms of all detectors. Storing the waveform allows to perform a detailed offline waveform analysis, including pedestal subtraction, noise filtering, constant fraction discrimination etc. Moreover, keeping the raw waveforms has the advantage that the data can be reprocessed whenever needed, for example after the improvement of the analysis algorithms or for the sake of consistency when combining datasets from different years. The signals (in total about 3000 channels) are digitized with the Domino Ring Sampler (DRS)4 chip, which has been developed at PSI. This chip records the waveforms with a sampling speed of 1.6 GSPS (TC, LXe detector) and 0.8 GSPS (DCH), enabling the MEG experiment to push the detector time resolutions to a state-of-the-art level and to efficiently recognize pile-up.

The DRS4 chip is based on the principle of Switched Capacitor Arrays (SCAs): A channel of the DRS 4 chip consists of 1024 storage capacitors (or "cells") and an inverter chain. The capacitors are "filled" upon a trigger provided by the inverter chain, through which a signal propagates like a domino wave. The frequency of the domino signal is stabilized by a Phase-

Locked Loop (PLL), which locks the frequency to an adjustable external reference clock. The wave continues to propagate until it is stopped by the trigger of the experiment. After the stop signal, the cells are read out with a speed of 16 MHz to a shift register, which feeds the signals to a 12 bit flash ADC. The analog inputs and outputs of the chip are all differential. One DRS4 chip contains eight data channels and an extra channel which samples the external reference clock, hence allowing to correct offline for the timing jitter induced by the domino wave circuit. Two DRS4 chips are mounted onto one mezzanine board, and two of these mezzanine boards are attached to a custom VME board, such that one VME board can accommodate 32 readout channels. A MEG crate housing these VME boards is shown in Fig. 4.10.

4.7 Offline Analysis Software and Simulation

For the offline analysis, the MEG experiment uses a FORTRAN77 and C++ based software framework which is divided into three parts: `megmc`, `megbartender` and `meganalyzer`. The `megmc` provides event generation and simulation of the particles' interaction with the detectors based on GEANT3. Apart from the $\mu^+ \rightarrow e^+\gamma$ and the usual Michel decay $\mu^+ \rightarrow e^+\nu_e\bar{\nu}_\mu$, also the calibration processes (such as Mott scattered positrons, ^{241}Am alphas in the LXe etc.) are implemented in the Monte Carlo simulation. The `megbartender` simulates the detector electronics, triggering and digitization. In addition, it offers the possibility to mix events in order to simulate the accidental background. The `meganalyzer` reconstructs, selects and displays events. This part of the software is the same for both real and simulated data.

4.8 Upgrade: The MEG II Experiment

The MEG experiment has concluded its first phase of data taking in 2013, reaching a sensitivity of 5.3×10^{-13} and setting a new upper limit on the $\mu^+ \rightarrow e^+\gamma$ decay. Beyond this point, only little improvement is expected from running the experiment for another couple of years because the sensitivity is predominantly limited by the amount of (accidental) background events in the signal region, not by the statistics. Motivated by the strong physics case, the upgraded version of the experiment MEG II seeks to improve the sensitivity to the $\mu^+ \rightarrow e^+\gamma$ decay by another order of magnitude. This is achieved by running at a muon beam rate of $10^8 \mu^+/\text{s}$, while improving all the detector resolutions by roughly a factor of two as well as the detection efficiencies, especially for what concerns the positron. The upgrade entails the modification or rebuilding of all subdetectors and the electronics. Additionally, a few novel auxiliary detectors and calibration methods have been proposed to further improve the sensitivity and get a handle on the new components of the experimental apparatus. The layout of the MEG II experiment is displayed in Fig. 4.11. The first engineering run is scheduled for the beginning of 2018, followed by the physics data taking, which lasts three years.

Table 4.3 summarizes the foreseen performances of the MEG II detectors. The key elements of the upgrade are:

- Stopping at least $7 \times 10^7 \mu^+/\text{s}$ on target (before: $3 \times 10^7 \mu^+/\text{s}$);

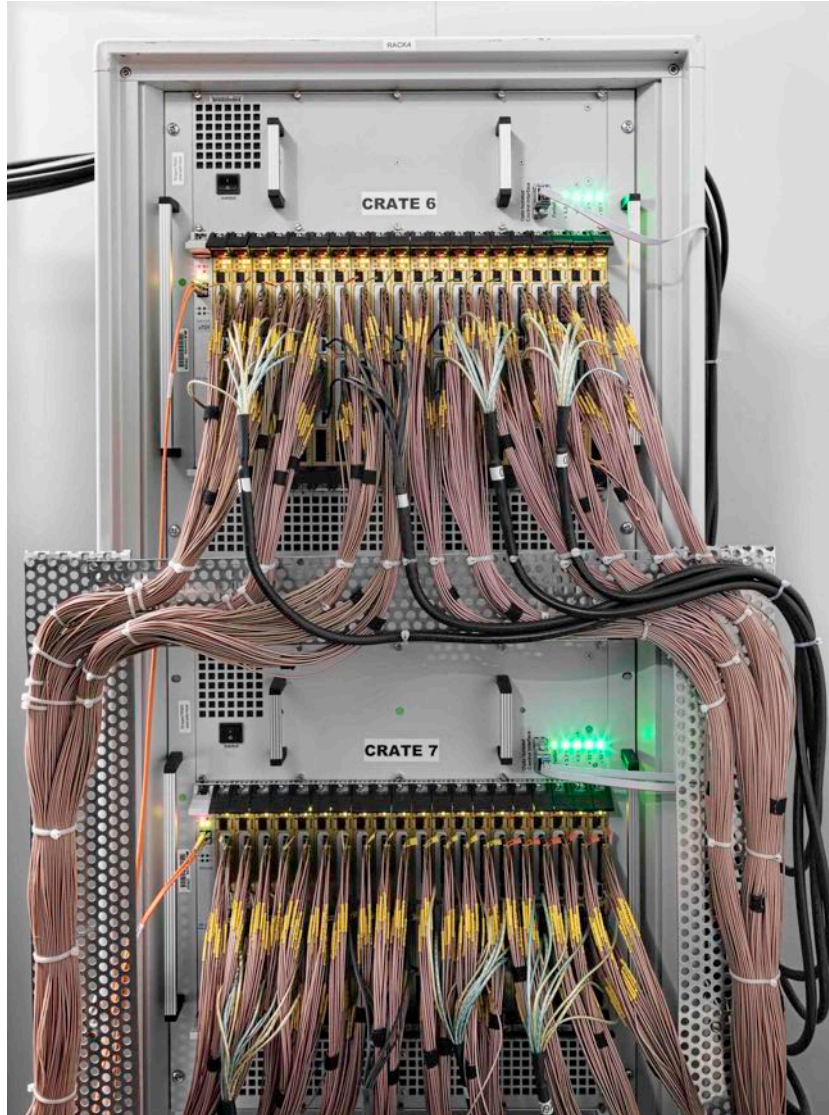


Figure 4.10: Two MEG crates housing the custom VME boards. Each VME board is equipped with four DRS4 chips which digitize the signals at a sampling speed of 1.6 GSPS (TC, LXe detector) and 0.8 GSPS (DCH).

4 The MEG and MEG II Experiment

- Minimize the target thickness, thus reducing the amount of material traversed by the positrons and gammas on their way to the detectors;
- Improve the positron tracking by replacing the drift chamber modules by a single volume drift chamber with reduced radiation length, higher granularity and better resolutions;
- Improve the positron timing and enable tracking by replacing the TC bar by an array of scintillating tiles;
- Improve the matching of the drift chamber system with the TC by measuring the positron trajectory up to the TC, thus improving the positron detection efficiency;
- Improve the gamma-ray energy, position and timing resolutions (especially for shallow events);
- Integrating the splitter, trigger and DAQ into one system which provides the necessary bandwidth.

Table 4.3: Average signal detector resolutions (Gaussian standard deviations) and efficiencies of the MEG II experiment. For the sake of comparison, the values for MEG are reported, too.

Parameter of Interest	Res. / Eff. MEG II	Res. / Eff. MEG
Positron polar angle θ_e	5.3 mrad	9.4 mrad
Positron azimuthal angle ϕ_e	3.7 mrad	8.7 mrad
Positron vertex (y, z)	(1.6 mm, 0.7 mm)	(2.4 mm, 1.2 mm)
Gamma conversion point (u, v, w)	(2.6 mm, 2.2 mm, 5 mm)	(5 mm, 5 mm, 6 mm)
Relative positron-photon timing $t_{e\gamma}$	84 ps	122 ps
Positron energy E_e	130 keV (core)	330 keV (core)
Photon energy E_γ	$\approx 1\%$	$\approx 2\%$
Positron detection efficiency ε_e	$\approx 88\%$	$\approx 48\%$
Photon detection efficiency ε_γ	$\approx 69\%$	$\approx 63\%$
Signal trigger efficiency ε_{trg}	$\approx 97\%$	$\approx 99\%$

4.8.1 Beam Line and Target

As we have already seen in Sect. 4.2, the MEG experiment was able to sustain $3 \times 10^7 \mu^+ / s$. The planned $7 \times 10^7 \mu^+ / s$ stopped on the target can be obtained without upgrading the beam line. In fact, beam tests in $\pi E5$ have shown that a beam rate of $9 \times 10^7 \mu^+ / s$ at a proton current of 2.2 mA and a beam size on target of $\sigma \approx 10$ mm in both x and y are achievable. For what concerns the target, it should on the one hand maximize the muon stopping rate and on the other hand minimize multiple scattering and the induced background to the LXe. The present baseline design for the target consists of a 140 μm thin polyethylene foil (CH_2) placed at $\theta = 15^\circ$. Based on the experience with MEG's target, which suffered from deformation during

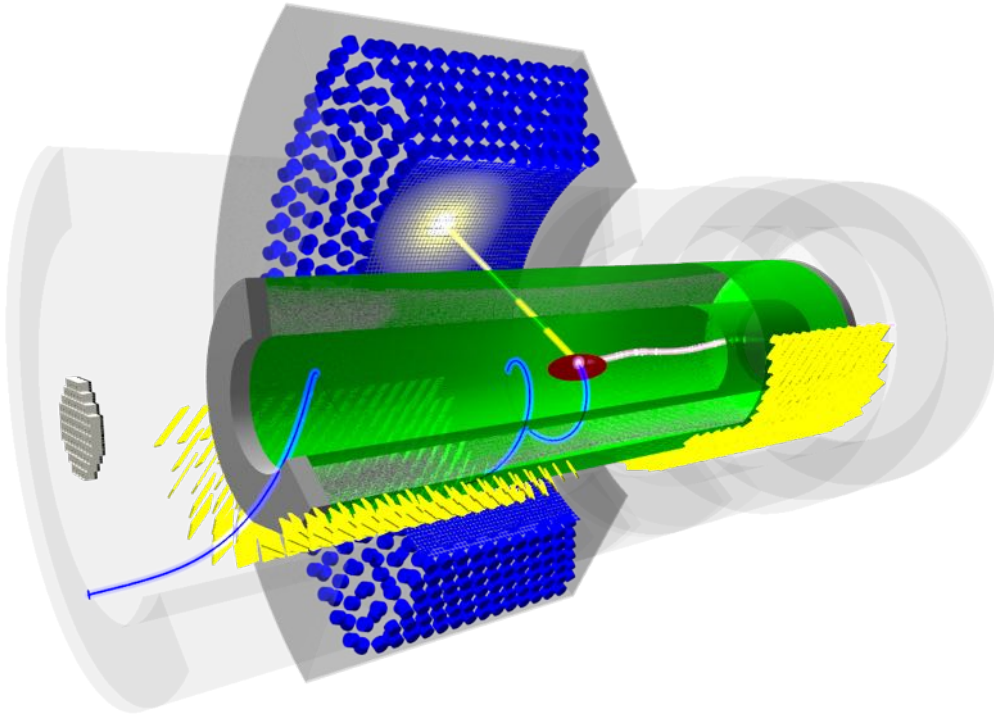


Figure 4.11: Layout of the MEG II experiment. The experimental resolutions on the kinematical variables of interest are roughly all improved by a factor two with respect to MEG, and the matching efficiency of the drift chamber system with the timing counter is drastically improved. The key elements of the upgrade comprise of an increased muon stopping rate, a thinner muon stopping target, a single volume, cylindrical stereo wire drift chamber, a pixelized timing counter, a modified entrance face of the LXe calorimeter (with SiPMs replacing the PMTs) and new trigger and data acquisition electronics. Additional auxiliary devices, such as a beam monitor tool or the radiative decay counter, are introduced to further improve the sensitivity to the $\mu^+ \rightarrow e^+ \gamma$ decay.



Figure 4.12: The MEG II cylindrical drift chamber under construction.

the run (see Sect. 9.9 for details), other target materials are under consideration, among them Beryllium and a target made of a 150 μm thin scintillating plate, which could be viewed by a CCD camera via a movable mirror system for beam monitoring purposes. In addition, an Active Target (ATAR) solution providing one of the two decay vertex coordinates has been studied, too, see also Sect. 4.8.5.

4.8.2 Positron Spectrometer

In order to improve the resolutions on the positron variables, the modular drift chamber system of MEG will be replaced by a single volume drift chamber, and the timing counter bars will be substituted by an array of scintillating tiles. As in MEG, the two subdetectors will be placed inside the COBRA magnet.

Single Volume Drift Chamber

The new drift chamber system should provide several benefits. Most importantly, the resolutions on the positron momentum and angular resolutions should substantially be improved, and the matching efficiency between the DCH and the TC should be recovered. In addition, the new DCH should be more immune against the high rate environment. In order to fulfill the above requirements, a unique-volume, low mass stereo drift wire detector has been devised. A picture of the drift chamber currently under construction is shown in Fig. 4.12. The chamber features a length of ≈ 180 cm in the z -direction, which is sufficiently long to follow the positron's trajectories up to the point where it enters the TC and at the same time increases the positron detection efficiency, thanks to the absence of the DCH support structure and front-end electronics along the positron's path towards the TC.

The wires are arranged in concentric layers and mounted in a criss-crossed fashion with a stereo angle of $\alpha_s \approx 8^\circ$, allowing to measure the z -coordinate with a resolution of a few mm. In

4 The MEG and MEG II Experiment

total, there will be about 1200 sense wires (diameter: 25 μm) and 6400 field wires (diameter: 80 μm). The chamber will be filled with a (90:10) He:IC₄H₁₀ gas mixture.

The wires are soldered to their corresponding front-end PCBs, which are mounted onto two aluminum end plates. The front-end PCBs provide on the one hand the high voltage to the wires and on the other hand host a signal preamplifier. In addition, the front-end electronics is designed to feature a sufficiently high bandwidth in order to enable the application of the cluster timing technique. This technique allows to further push the spatial resolutions by exploiting not only the information (i.e. arrival time) of the first ionization cluster, but also considering the time information of the clusters which succeed the first one [39].

Monte Carlo simulations suggest an average number of wire hits around 60, compared to the $\mathcal{O}(20)$ hits for MEG. The increased number of hits facilitates the pattern recognition and leads to a substantial improvement in the momentum and angular resolutions. Again from simulation, the momentum and angular resolutions are estimated to be $\Delta\phi_e \approx 4$ mrad, $\Delta\theta_e \approx 5$ mrad and $\Delta p_e \approx 130$ keV/c (assuming the baseline design target of 140 μm thickness oriented at an angle of 15°). With the new drift chamber design, the positron reconstruction efficiency is expected to increase from the present spectrometer's $\varepsilon_{e^+} = 48\%$ to $\varepsilon_{e^+} \approx 85\%$.

Pixelized Timing Counter

In order to keep up with the increased event rate, to circumvent the PMTs (whose usage in magnetic field environments is somewhat constrained) and to reduce the time spread caused by the tracks being spread out over a large fraction of a single scintillator bar, a new, highly segmented TC detector has been conceived. The TC consists of 512 scintillating plastic tiles (“pixels” or “counters”) of about $120 \times 50 \times 5$ mm³ size, equipped with twelve SiPMs each. The pixels will again be arranged in two semi-cylindrical sections. The pixels’ orientation and location is optimized in such a way that signal positrons will leave hits in several counters, with the advantage of further improving the timing resolution and of providing additional track information. The time resolution of a single pixel was measured to be 70 to 80 ps. Beam test measurements with one quarter of the TC assembled showed that a timing resolution better than 40 ps for tracks with multiple hits can be achieved. The assembled DS barrel is shown in Fig. 4.13.

4.8.3 Liquid Xenon Calorimeter

The LXe detector will be improved through the replacement of the front-face PMTs by 4092 SiPMs and the optimization of the arrangement of the PMTs on the remaining faces, leading to an increased granularity and a better uniformity of the detected scintillation light as well as to the reduction of energy leakage. A picture of the LXe calorimeter under construction is shown in Fig. 4.14. The energy and position resolutions are expected to be 0.7 to 1.5 % and 2.5 mm, respectively. The timing resolution is also expected to improve to about 50 ps. The SiPMs have the additional advantage that they are much thinner compared to the PMTs, thus increasing the gamma detection efficiency to 69 %. The custom-developed VUV-sensitive SiPMs feature a size of 12×12 mm². They are mounted on PCB strips that are installed along the calorimeter’s entrance face. In order to compensate the additional heat flow due to the increased number of

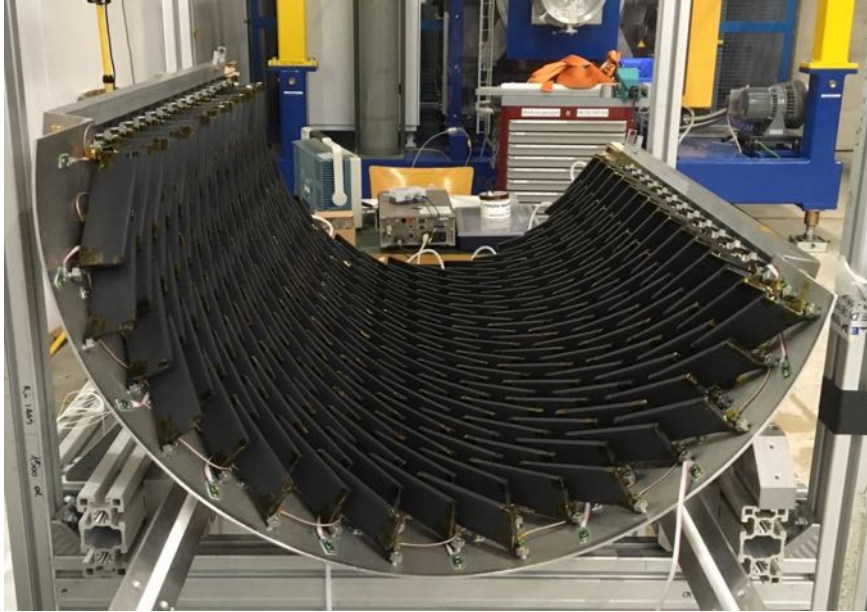


Figure 4.13: The DS half of the MEG II timing counter.

signal cables, a new refrigerator system will be installed as well.

4.8.4 Trigger and Data Acquisition

The higher beam intensity in MEG II implicates a higher trigger rate, which could not be sustained by the MEG trigger and DAQ system. Moreover, the MEG II detectors sum up to 9000 channels that need to be digitized and call for an increased bandwidth with respect to MEG in order to improve the timing resolution and the rejection of pile-up. Therefore, a new custom-made system consisting of Waveform DRS4 based Readout Module (WaveDREAM) boards, Data Concentrator Boards (DCBs) and Trigger Concentrator Boards (TCBs) has been devised. The WaveDREAM board will incorporate both the trigger and the DAQ into one board. The front-end of the WaveDREAM board enables signal amplification and shaping, inspired by the PSI preamplifier presented in Sect. 6.4. It is also capable of supplying the bias voltage to the SiPMs and providing current as well as temperature measurements in order to monitor the SiPM working points. The waveforms can be digitized at a speed of 1 to 5 GSPS. A WaveDREAM crate is equipped with 16 WaveDREAM boards (equivalent to 256 channels) and a DCB that collects, combines and sends the data from the boards to a PC via Gigabit Ethernet. In addition, every crate possesses a TCB which receives and processes a copy of the detector signals (digitized by flash ADCs) using FPGAs. The triggers from the individual crates are sent to the TCBs at an intermediate level, which combine the event information and forward it to a master TCB issuing the global start and stop signals to the system. Improvements in the online event reconstruction resolutions compensate the higher muon beam intensity, such that the expected trigger rate is, similarly to MEG, about 10 Hz.

4.8.5 Novel Auxiliary Detectors

A few new auxiliary detectors have been proposed in order to further increase the sensitivity to the $\mu^+ \rightarrow e^+ \gamma$ decay by introducing either new detectors which support the background rejection, or by providing new monitoring systems. Three of these auxiliary detectors are based on 250 μm thin scintillating fibers coupled to SiPMs, namely (1) a beam monitor system, (2) an active target and (3) the US part of a radiative decay counter. All three of them require the separation ("particle ID") of surface muons ($p \approx 28 \text{ MeV}/c$) and positrons.

Beam Monitor Tool

It would be highly desirable to have a tool which allows to perpetually and rapidly measure the beam's position, size and rate. On the one hand, this would of course be beneficial to the physics run, because in case of anomalous behavior one may figure out the cause much faster. On the other hand, this beam monitor tool could support calibration runs such as the Mott scattering calibration described in Chapter 8, which makes use of a positron beam. The scintillating fiber beam monitor tool, developed and tested in the framework of this thesis (see Chapter 7), is strongly supported by the MEG collaboration. Two additional beam monitor systems are currently under study [40, 41]: These are on the one hand a scintillating plate replacing the muon stopping target and on the other hand novel scintillating foils of a few micrometer thickness viewed by CCD cameras.

Active Target

The Active Target (ATAR) is a detector consisting of a single layer of fibers (240 pieces) replacing the passive muon stopping target such that one can detect the stopped muon and the corresponding decay positron, thus measuring the y -coordinate of the muon decay vertex. This solution is considered to be a backup in case that the new drift chamber would significantly underperform. The reader may find a detailed discussion in [42].

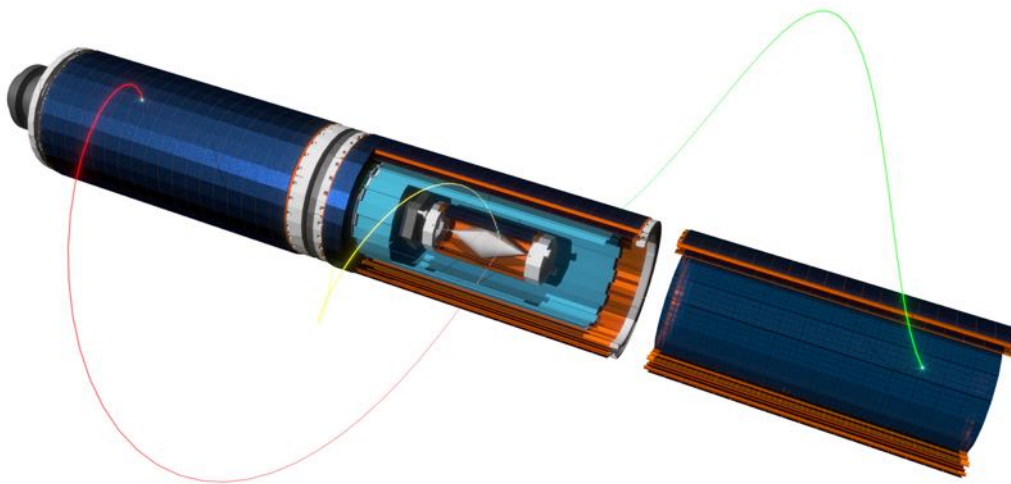
Radiative Decay Counter

The Radiative Decay Counter (RDC) detector helps to reject high energy gammas stemming from radiative muon decay by identifying the corresponding positron, which has typically little energy and whose track therefore features a small bending radius. The RDC, composed of two parts explained below, is placed on the central axis of the COBRA magnet such as to detect these positrons which would normally lie outside of the spectrometer acceptance. The RDC consists of a DS part made of a LYSO crystal array in combination with plastic scintillators, and an US part, which is traversed by the muon beam, made of a single layer of 250 μm scintillating fibers read out in bundles by SiPMs. The DS RDC counter has been approved by the collaboration, the US part is still under study.

Part II

The Mu3e Experiment

Detectors based on scintillating fibers coupled to silicon photomultipliers provide a powerful solution for a variety of applications in particle physics such as beam monitoring, vertex tagging, particle tracking and timing. Both components, the fibers and the photosensors, are compatible with magnetic fields and vacuum. The challenge of such a detector consists in the ability to detect minimum ionizing particles with a reasonably high efficiency while keeping the material budget low. This is of special importance to the Mu3e fiber hodoscope, since the experiment's sensitivity will be limited by the multiple scattering of the electrons and positrons in the fibers and the pixel detector. In this part, the reader is first introduced to the purpose and design of the Mu3e fiber detector. Second, the results of the dedicated R&D activities carried out within the framework of this thesis are presented in detail. A summary and the conclusions drawn from the work presented here are given in Chapter 10.



5 The Mu3e Fiber Hodoscope

This chapter presents in more depth the fiber hodoscope, which is one of the two timing systems used in the Mu3e experiment. The first section describes the purpose and demands on the fiber detector, the second section delineates the detector's impact on the performance of the experiment and the third section is dedicated to the hodoscope's baseline design.

5.1 Purpose and Requirements

The task of the fiber hodoscope, shown schematically in Fig. 5.1, is to provide the timing information of the electrons and positrons with a time resolution < 1 ns and with a detection efficiency close to 100%. Moreover, it is required to cope with rates of up to 250 kHz per fiber at a muon stopping rate of $10^8 \mu^+ / s$. The timing information is essential to suppress the accidental background. For instance during phase I, about ten tracks per reconstruction frame (see Sect. 3.5) are expected. For about one third of the tracks one needs to rely on the timing measured by the fiber detector alone, because the corresponding particles do not end up in the tile detector, which would provide a more precise timing information. In addition, the fiber detector helps to match pixel hits in the central detector station with those in the recur stations. The fiber hodoscope's thickness, given by the fiber thickness and the glue, should not exceed $900 \mu\text{m}$ (equivalent to $0.4\% X_0$) in order to not impair the momentum resolution and to allow the reconstruction algorithm to be fully efficient, since additional material introduces further scattering which makes it more difficult to correctly match track segments. Lastly, the detector should comply with very tight space constraints for the photosensors, readout, cables and cooling.

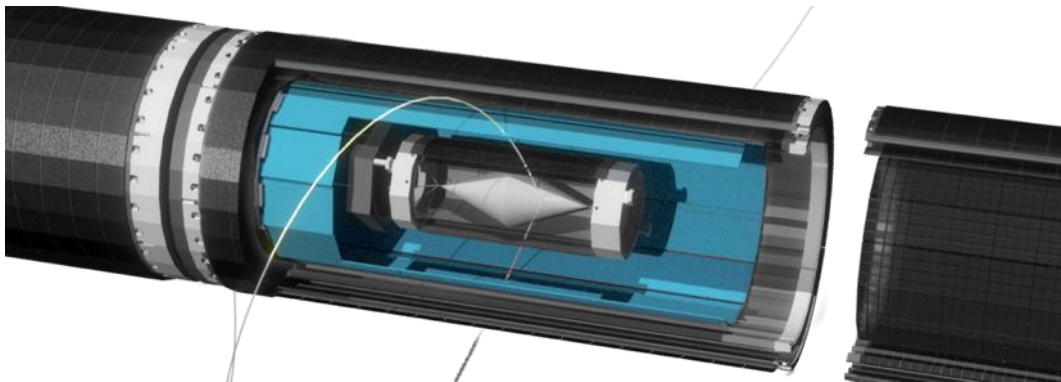


Figure 5.1: Rendering of the scintillating fiber hodoscope (blue) in the Mu3e experiment.

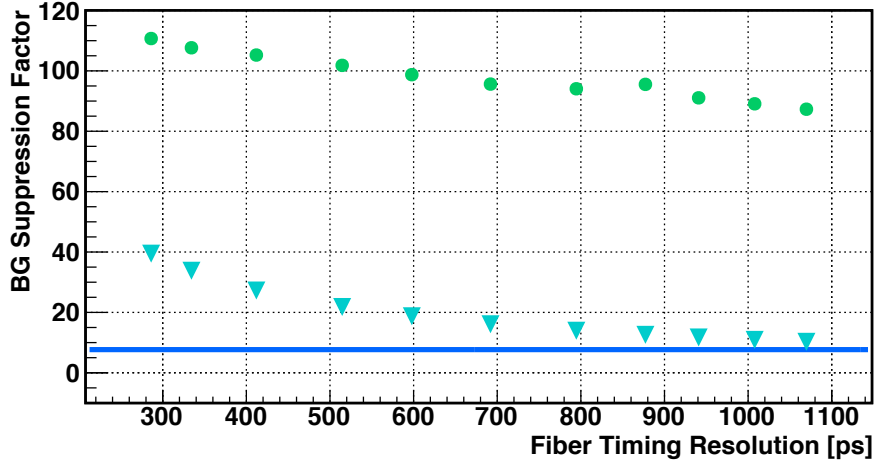


Figure 5.2: Simulated suppression factors of accidental background caused by Bhabha electron-positron pairs in coincidence with positrons from Michel decays, assuming a 95 % efficient fiber detector and a fully efficient tile detector with a timing resolution of 60 ps [31]. The plot shows the suppression factor for the fiber detector alone (triangles), for the tile detector alone (solid line) and for the combination of both (dots).

5.2 Impact on the Experiment

The types of accidental backgrounds that the fiber hodoscope helps to reject can be categorized in two classes: (1) Accidental background where two of the three tracks are time-correlated (i.e. an electron-positron pair from either Bhabha scattering or internal conversion plus a Michel positron) and (2) accidental background where the three particles are uncorrelated in time. The second type of background is about ten times more suppressed compared to the first one. The simulated suppression factors of accidental background caused by Bhabha electron-positron pairs in coincidence with positrons from Michel decays is shown in Fig. 5.2 as a function of the fiber detector timing resolution. There, a reconstruction frame length of 50 ns, a 95 % efficient fiber detector and a fully efficient tile detector with a timing resolution of 60 ps was assumed. The tile detector alone gives a suppression factor of $\mathcal{O}(10)$, while the fiber detector alone provides a suppression of $\mathcal{O}(20)$, assuming a fiber timing resolution of 500 ps. Both timing detectors combined result a suppression factor of $\mathcal{O}(100)$.

5.3 Baseline Design

The baseline design, which is presently still subject to optimizations, foresees twelve fiber ribbons made of three to four staggered layers of 250 μm thin multicladd round or squared scintillating plastic fibers. The fiber ribbons are arranged cylindrically in the central detector station and are read out on both ends by SiPM arrays described further below. The readout on both sides of the fiber ribbon is beneficial to the rejection of SiPM dark counts, the detection efficiency and the timing resolution.

Table 5.1: Properties of the proposed S10943 SiPM array series from Hamamatsu.

Properties	
Breakdown voltage	55 V
Gain	1.25×10^6
PDE (max.)	32 %
Fill factor	61 %
Dark count rate	170 – 350 kHz
Crosstalk probability	4 %
Temperature coefficient	53.7 mV / °C

5.3.1 Mechanics

Each fiber ribbon is made of 384 scintillating fibers (assuming three layers of fibers) with a length of 28 cm, summing up to 4608 fibers for the whole detector. The ribbons themselves are grouped into modules fixed to support rings. The fiber ribbons are placed at a radius of 6 cm, corresponding to the location which is furthest away from the target and thus minimizes the fiber occupancy, but which at the same time is still contained within the second pixel detector barrel, allowing to exploit the recurling principle to achieve a good momentum resolution (see also Sect. 3.1).

5.3.2 Photosensors

Silicon Photomultipliers (SiPMs), which are described in more detail in Sect. 6.2, offer a lot of advantages compared to other photosensors: They are compact in size, require a comparably low high voltage, allow to detect single photons with a relatively high Photon Detection Efficiency (PDE) and are insensitive to magnetic fields. They come along in various sizes and packagings. The Mu3e baseline option is the S10943 SiPM array from Hamamatsu, see Fig. 5.3a), which is made of 128 SiPM chips or “columns” with a width of 250 μm each. By coupling a fiber ribbon to a SiPM array, several fibers are read out by one array column as shown in Fig. 5.3b), such that in total there will be about 1500 readout channels on each side (US and DS) of the detector. The most important properties of the S10943 SiPM array are summarized in Table 5.1. One disadvantage of the SiPMs is their relatively high dark count rate, which is typically 100 kHz. The dark count rate is known to increase after exposing a SiPM to ionizing radiation. The radiation may also induce gain variations. Radiation effects on the SiPMs in the context of the Mu3e fiber detector will be addressed in future tests.

5.3.3 Electronics

The SiPM arrays will be mounted on small PCBs, which will be brought into contact with a water-cooled support ring. A SiPM array is connected through a short flex print to a PCB that hosts the readout chips as well as the high voltage distribution, some slow control sensors (e.g. for the temperature, SiPM array current and voltage) and potentially also some LEDs for calibration purposes. The MuTRiG readout chip [35] described below has 32 input channels, and

5 The Mu3e Fiber Hodoscope

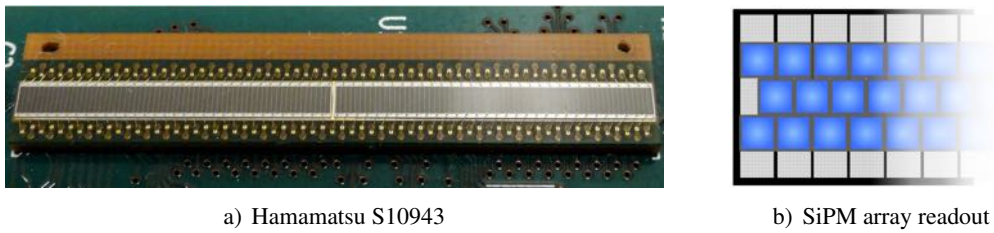


Figure 5.3: A picture of the proposed SiPM array and a sketch of a fiber ribbon coupled to a SiPM array.

every readout board carries two MuTRiG chips, such that 24 readout board are needed on each side of the detector. The readout PCBs will sit on the water-cooled beam pipe. The dedicated development of the readout chip MuTRiG is based on the SiPM Timing Chip (STiC). The STiC is a mixed mode ASIC chip that provides leading-edge timing (with a timing bin size of 50 ps) and time-over-threshold (i.e. energy) information. It was originally designed for applications with signal of thousands of photons. For the fiber detector, the MuTRiG chip should be able to trigger on single photon signals. In addition, the MuTRiG (and STiC) allows to adjust the voltage at each signal input within a range of ca. 700 mV, which is useful to tune the SiPMs to their optimal working point. The latest version of the STiC includes also pole-zero cancellation in order to reduce the signal tails and consequently the channel dead time. The MuTRiG chip is expected to be able to cope with rates of up to 1.2 MHz per channel, compatible with the expected rate of $\lesssim 1$ MHz per SiPM array channel.

6 R&D of a Scintillating Fiber Detector for Mu3e

The first few sections in this chapter are dedicated to the basic fiber detector components, namely the scintillating fibers and the photosensors as well as some mechanical aspects. The subsequent sections are devoted to the fiber prototypes, the experimental setups and the results obtained within these R&D activities. Lastly, the performances of the final Mu3e hodoscope are extrapolated on the basis of the prototype studies.

6.1 Scintillating Fibers

Scintillating fibers are plastic waveguides doped with luminescent fluors, allowing them to produce scintillation light upon the passage of a particle and guide the so-produced light towards a photosensor through total internal reflection. The first section describes the scintillating fibers' working principle and their basic properties. The second section is dedicated to the characterization procedures and quality control. The last section deals with the optical isolation of the fibers.

6.1.1 Working Principle and Basic Properties

The next paragraphs describe the scintillation mechanism, the scintillator response, the light propagation and the light attenuation, concluding with an estimate of the number of photons which we expect to detect when we consider a single 250 μm thin scintillating fiber.

Scintillation Mechanism

Charged particles passing through what we call a “scintillator” cause luminescence: The atoms or molecules of the scintillating medium are ionized or excited by the particles and emit light (“scintillation light”) through the subsequent recombination or de-excitation. In organic scintillators, as are plastic scintillating fibers, the scintillation light emission is based on the transition of electrons belonging to π -orbitals in carbon compounds, e.g. in aromatic compounds. Let us take a closer look at this mechanism [43].

Generally speaking, when the carbon atoms bond to form a molecule, their electronic configuration changes from the original $1s^2 2s^2 2p^2$ to a $1s^2 2s^1 2p^3$ configuration. The corresponding atomic orbitals mix (“hybridization”), giving rise to either: (1) sp^3 orbitals in which all four orbitals $2s^1 2p^3$ participate; (2) sp^2 orbitals in which the three orbitals $2s^1 2p^2$ mix, with one p -orbital remaining; (3) sp orbitals in which only the $2s^1 2p^1$ orbitals mix, with two p -orbitals left over. The electrons belonging to one of the mixed orbitals are called σ -electrons, the ones

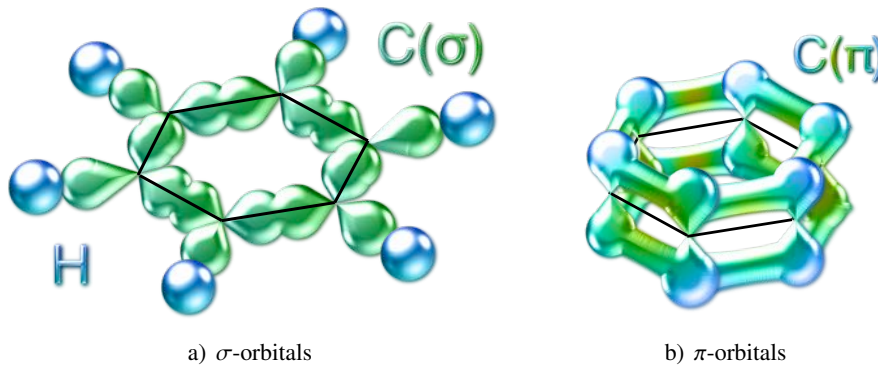


Figure 6.1: Benzene structure: The six carbon atoms feature a sp^2 hybridization, giving rise to the hexagonal structure of benzene. σ -orbitals strongly overlap among themselves and with the hydrogen orbitals. The bar-bell-shaped π -orbitals are orthogonal to the σ -orbitals. The π -electrons are delocalized within the benzene ring. Picture inspired by [44].

belonging to p -orbitals which do not mix are called π -electrons. Let us consider for example the benzene molecule (C_6H_6) shown in Fig. 6.1: There, the six carbon atoms feature a sp^2 hybridization, giving rise to the hexagonal structure of benzene. The σ -orbitals strongly overlap among themselves and with the hydrogen orbitals, meaning that the σ -electrons are strongly bound. Orthogonally to the σ -orbitals lie the bar-bell-shaped π -orbitals, where the electrons are bound more loosely and are in fact delocalized within the ring. It is the transition of these π -electrons that causes luminescence. An example of an organic molecule's π -electron energy level diagram is given in Fig. 6.2. It is characterized by a sequence of singlet states (S_0, S_1, S_2, \dots) and a sequence of excited π -electron triplet states (T_1, T_2, \dots), both of which bear vibrational sub-levels ($S_{00}, S_{01}, T_{00}, \dots$). The vibrational sub-levels are typically 0.1 eV apart, whereas the distance between S_0 and S_1 is equal to 3 to 4 eV, corresponding to wavelengths of 300 to 400 nm. At room temperature, the predominantly populated state is the ground state S_{00} . Absorption occurs from S_{00} to one of the singlet states on a time scale of several hundred picoseconds, transitions from the ground state to a triplet state are spin forbidden. The de-excitation of the molecule can happen through three different processes, which bring about three different kinds of luminescence:

1. **Fluorescence** These are transitions from the S_1 to the vibrational sub-levels of the ground state S_0 with a lifetime of $\tau_f \sim ns$. The fluorescence emission intensity decreases exponentially with time t :

$$I(t) = I_0 e^{-t/\tau_f} \quad (6.1)$$

where I_0 denotes the initial and $I(t)$ the instantaneous intensity. Usually, the molecule reaches the S_{10} state before transiting to S_0 , since the period of molecular vibrations is about 1 ps, i.e. much shorter than τ_f . Molecules which are excited into one of the higher singlet states (S_2, S_3, \dots) de-excite by radiation less internal conversion (~ 10 ps) into the S_1 level with the subsequent fluorescent emission described above.

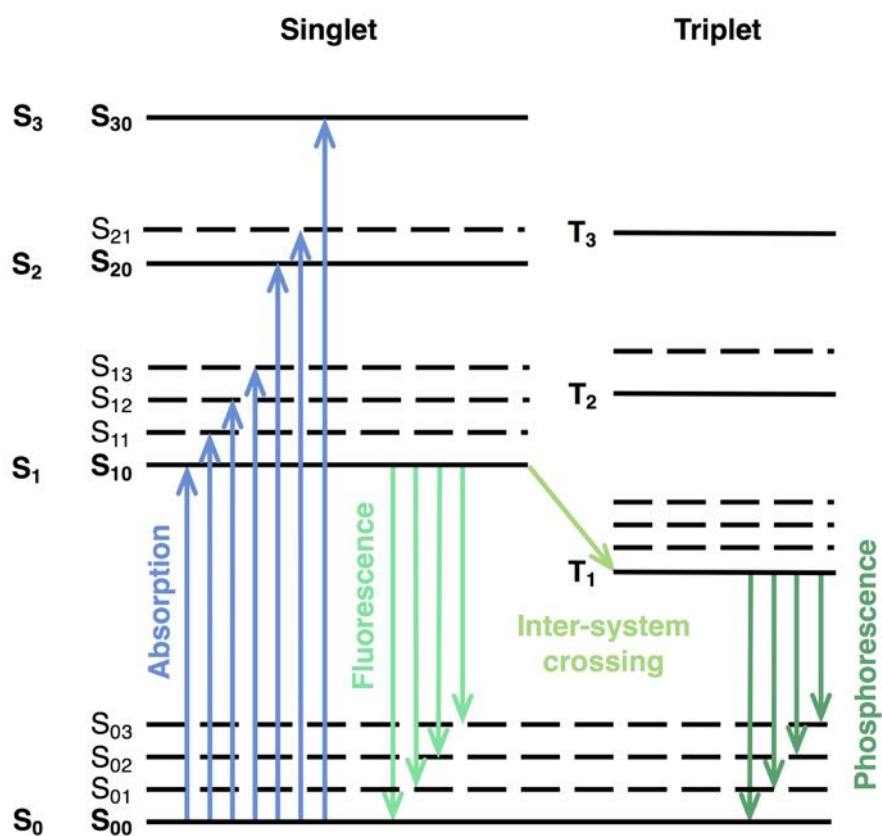


Figure 6.2: Energy level diagram of an organic molecule's π -electrons, characterized by a sequence of singlet states (S_0, S_1, S_2, \dots) and a sequence of triplet states (T_1, T_2, \dots) which feature vibrational sub-levels ($S_{00}, S_{01}, S_{02}, \dots$). Picture inspired by [43].

2. **Phosphorescence** Similarly to fluorescence, this kind of emission decays exponentially. However, the decay time is considerably longer, typically $\tau_p \sim \text{ms}$. The phosphorescence emission is caused by electrons which first transit in a radiation less manner from the singlet S_1 to the metastable triplet state T_1 (a process called “inter-system crossing”, enabled by e.g. spin-orbit coupling effects or vibrational interactions), and from there go back to the ground state S_0 .
3. **Delayed fluorescence** Some of the electrons in the triplet states may go back to one of the singlet states through energy supplied for example thermally, causing fluorescence emission with some time delay of up to ms.

Plastic scintillators are polymerized aromatic solutions containing a small fraction of fluorescent dopants, which are added because even if the aromatic molecules are capable of producing scintillation light, they do so with a rather low energy-to-light conversion efficiency (“scintillation efficiency”). The dopants help to overcome this problem by taking over the excitation energy from the base material and emitting light more efficiently. Additional dopants render the scintillator more transparent to its own light by increasing the scintillation light’s wavelengths, or in other words by increasing the “Stokes shift”. The Stokes shift corresponds to the shift between the maxima of the absorption and the emission spectra of the scintillator. The dopants may also increase the resistance to radiation [45].

Light Output

Most of the energy deposited by a particle in a plastic scintillator is dissipated as heat. Only a few percent of the energy is converted into fluorescence light. The scintillation process can effectively be triggered by illuminating the scintillator with UV light. In that case, a large fraction is converted into fluorescence emission (this is especially interesting if one wants to characterize fiber samples in terms of light yield circumventing the usage of radioactive sources by utilizing UV LEDs instead).

For Minimum Ionizing Particles (MIPs), the differential light output $dL(\lambda)/dx$, which is the number of scintillation photons of a certain wavelength λ per unit path length, upon the passage of a particle is approximately given by

$$\frac{dL}{dx} = S \frac{dE}{dx}, \quad (6.2)$$

where the proportionality constant S corresponds to the scintillation efficiency (or numbers of photons of wavelength λ per unit energy) and dE/dx denotes the particle’s stopping power. For MIPs, the excited and ionized molecules along the particle’s path are typically several molecular distances apart. Instead, when dealing with highly ionizing particles, the plastic scintillators suffer from quenching effects due to the molecules being already excited or ionized. This effect is well-described by a non-linear relationship of dL/dx and dE/dx known as Birks’ Law [43]:

$$\frac{dL}{dx} = S \frac{dE}{dx} \cdot \frac{1}{1 + k_B \frac{dE}{dx}} \stackrel{dE/dx \rightarrow \infty}{\approx} \frac{S}{k_B} \quad (6.3)$$

where the constant k_B (“Birks constant”) has to be determined empirically (e.g. for the NE102 scintillator, which is the predecessor of BC400: $k_B \approx 10^{-2} \text{ g cm}^{-2} \text{ MeV}^{-1}$ [43]). In the Mu3e experiment we will never find ourselves in a situation where this quenching effect sets in, since the fiber hodoscope is dealing with MIPs.

Time Response

Thanks to the fast fluorescence process, organic scintillators are commonly used for timing purposes. A typical scintillation pulse shape $I(t)$ caused by a particle traversing an organic scintillator is characterized by the three time constants τ_r , τ_f and τ_s [44]:

$$I(t) = I_1 \left(e^{-\frac{t}{\tau_f}} - e^{-\frac{t}{\tau_r}} \right) + I_2 e^{-\frac{t}{\tau_s}} \quad (6.4)$$

The time constant $\tau_r \sim 100 \text{ ps}$ is associated to the time needed to populate the excited state S_1 (“rise time”). The time constant $\tau_f \sim \text{ns}$ already appeared before: It is the time constant describing the fluorescence emission (“fast”). Phosphorescence and delayed fluorescence are encapsulated in the “slow” time constant $\tau_s \sim \mu\text{s}$ to ms . The relative fractions I_1 and I_2 depend on the kind of particle (or more specifically on their stopping power) traversing the scintillator and allow to discriminate particles on the basis of their corresponding pulse shapes.

Light Propagation

Scintillating fibers are composed of a core with a constant high refractive index surrounded by a cladding with a lower refractive index, where the size of the cladding typically corresponds to a few percent of the fiber size. The scintillation light propagates along straight lines within the core or through total internal reflection at the core-cladding interface (“core-mode”). Total internal reflection at the cladding-air boundary can occur as well, but these light rays are often lost due to the fact that the cladding may be bordering zones with a similar or higher refractive index. Multiclad fibers mitigate this problem by featuring a second cladding with an even lower refractive index than the first cladding. Typically, the wavelength of the light transported inside a scintillating fiber is much shorter than the fiber size, which means that the light propagation can be reasonably well described by geometrical optics. Generally speaking, a light ray’s deflection angle at a boundary of two media (for example the core and the cladding) with distinct refractive indices is given by Snell’s Law [46]

$$n_{core} \cdot \sin(\alpha_{core}) = n_{clad} \cdot \sin(\alpha_{clad}), \quad (6.5)$$

where the incident angle α_{core} and refraction angle α_{clad} are measured with respect to the axis perpendicular to the interface between the two media. With the premise that $n_{core} > n_{clad}$ and the requirement that α_{clad} should be $\geq 90^\circ$ for total internal reflection to occur, we obtain an expression for the critical angle α_{crit} :

$$\alpha_{crit} = \arcsin\left(\frac{n_{clad}}{n_{core}}\right). \quad (6.6)$$

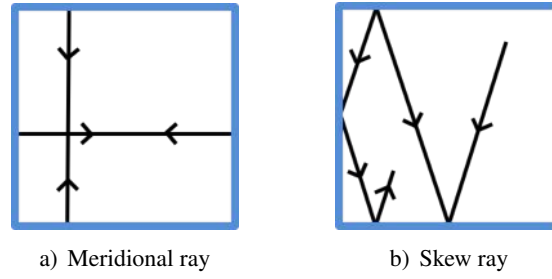


Figure 6.3: Illustration of meridional and skew rays for squared fibers. Meridional rays are rays which propagate within a single plane. The path of skew rays is not confined to a single plane. Picture inspired by [46].

Rays with $\alpha_{core} \geq \alpha_{crit}$ undergo total internal reflection at the core-cladding interface. One distinguishes two kind of light rays confined within the fiber: Meridional and skew rays. The first ones are rays whose path lies in a single plane: for cylindrical waveguides, these are rays which cross the central fiber axis; for squared fibers, these are rays whose propagation plane is parallel to one of the square's sides. Instead, the path of a skew ray is not confined to a single plane. A sketch of the two kinds of rays for squared fibers is shown in Fig. 6.3.

Light Attenuation

Part of the scintillation light will be lost when it propagates through the fiber. In an ideal world, the attenuation of the light is governed by the law

$$I(x, \lambda) = I_0 e^{-x/L_{att}(\lambda)} \quad (6.7)$$

where I describes the intensity after the light has propagated a distance x , I_0 denotes the initial light intensity and $L_{att}(\lambda)$ corresponds to the characteristic attenuation length, which in general depends on the wavelength λ . The attenuation of light is caused by Rayleigh scattering as well as absorption by the scintillating material, by chemical impurities and by radiation induced traps. In a real situation, additional losses arise due to the imperfect core-cladding and cladding-air boundaries. The former is a consequence of e.g. imperfect merger of the core and the cladding during the fiber production process, the latter is caused for example by non-ideal surface finishing (i.e. a “rough” surface) or dust and grease on the surface. Thus, the light yield of real fibers is best described by an exponential decay with two components $L_{att,short}$ and $L_{att,long}$:

$$I(x, \lambda) = I_{0,1} e^{-x/L_{att,short}(\lambda)} + I_{0,2} e^{-x/L_{att,long}(\lambda)} \quad (6.8)$$

where the long component $L_{att,long}$ has its origin in the absorption and Rayleigh scattering, while the short component $L_{att,short}$ comes from the surface effects described above. An example of a Monte Carlo simulation for the case of real and of ideal surface boundaries is shown in Fig. 6.4. Note that again, both $L_{att,long}$ and $L_{att,short}$ are a function of the wavelength, implying that the light's spectral composition changes upon propagation through the fiber, since some (usually the shorter) wavelengths tend to be attenuated more than others.

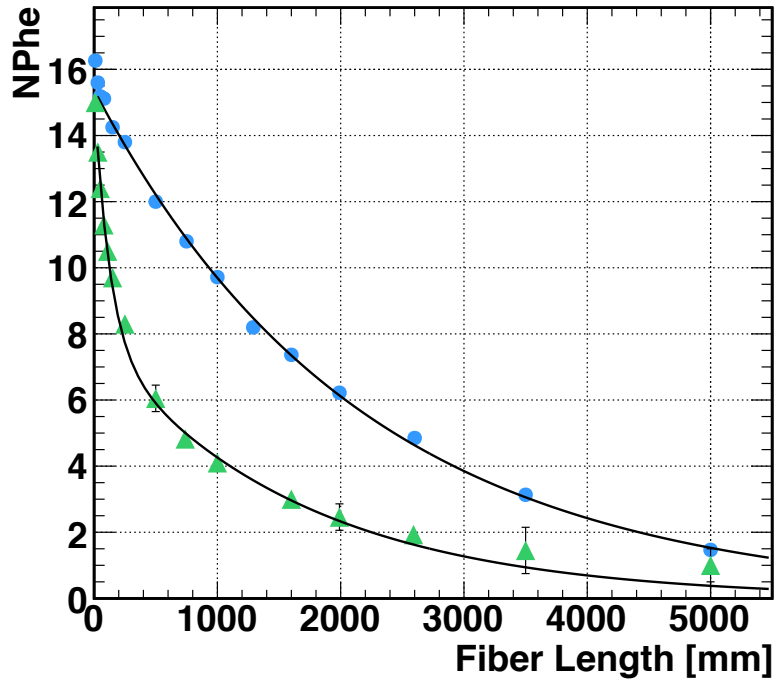


Figure 6.4: Monte Carlo simulation of the number of photons collected on one end of a $250\ \mu\text{m}$ thin fiber as a function of the fiber length in the case of ideal (“polished”, blue dots) and real (“rough”, green triangles) surface boundaries. The ideal case is described by an exponential decay with one decay constant $L_{att} \approx 2\ \text{m}$. The real case requires a double exponential decay description with a short component $L_{att,short} \approx 12\ \text{cm}$ and a long component $L_{att,long} \approx 1.7\ \text{m}$.

Estimation Of Number Of Photoelectrons

Let us give a back-of-the-envelope estimation of the average number photoelectrons N_{Phe} (i.e. the number of detected scintillation photons) that we expect from a 250 μm thin fiber of $L \approx 30$ cm total length upon the passage of a MIP. Ideally we would compute the following integral over the scintillator's emission spectrum $\Delta\lambda$:

$$\langle N_{Phe} \rangle = \int_{\Delta\lambda} S(\lambda) T(\lambda, L) Q(\lambda) d\lambda, \quad (6.9)$$

where $S(\lambda)$ denotes the differential source term and is given such that $\int S(\lambda) d\lambda$ equals the number of produced scintillation photons, $T(\lambda)$ is the light collection and transfer factor, and $Q(\lambda)$ describes the photodetector's quantum efficiency (in this case the SiPM's PDE, see Sect. 6.2). For a rough estimation we can assume

$$\langle N_{Phe} \rangle \approx \langle S \rangle \langle T \rangle \langle Q \rangle \quad (6.10)$$

where $\langle S \rangle$, $\langle T \rangle$ and $\langle Q \rangle$ are average values. The source term $\langle S \rangle$ for instance can be approximated by

$$\langle S \rangle = \frac{\Delta N_\gamma}{\Delta E} \left\langle \frac{dE}{dx} \right\rangle \langle \Delta x \rangle, \quad (6.11)$$

with $\Delta N_\gamma/\Delta E$ equal to the number of scintillation photons produced per deposited energy E , $\langle dE/dx \rangle$ the mean energy loss per unit path length and the average path length $\langle \Delta x \rangle$ of a particle traversing the fiber. With the values provided in Table 6.1 and assuming that the MIP impinge perpendicularly with respect to the central fiber axis we find:

$$\langle S \rangle = \frac{8000 \text{ photons}}{\text{MeV}} \times \frac{2 \text{ MeV cm}^2}{\text{g}} \times 1.05 \frac{\text{g}}{\text{cm}^2} \times 250 \mu\text{m} = 420 \text{ photons}. \quad (6.12)$$

The collection and transfer factor T is approximately given by:

$$T(\lambda, L) = \frac{\delta\Omega}{4\pi} \times e^{-L/L_{att}}, \quad (6.13)$$

where $\frac{\delta\Omega}{4\pi}$ denotes the trapping efficiency of the fiber (i.e. the fraction of solid angle that comprises the light which will be propagated through the fiber by total internal reflection) and the second factor describes attenuation effects. For the sake of simplicity we assume the latter to be dominated by the short component only ($L_{att} \approx 15$ cm), and we consider the case in which the particles hit the fiber at the center. In addition, we assume that all the light that exits the fiber is able to reach the photosensor (i.e. a 100 % transmission efficiency from the end of the fiber to the photosensitive area). Using again the values shown in Table 6.1 we get:

$$T(\lambda, L) \approx 7 \% \times \frac{1}{e} \approx 2.6 \%. \quad (6.14)$$

Together with the SiPM's PDE of $Q \approx 40 \%$ we obtain:

$$\langle N_{Phe} \rangle \approx \langle S \rangle \langle T \rangle \langle Q \rangle \approx 420 \text{ photons} \times 0.026 \times 0.40 \approx 4.3 \text{ photons}. \quad (6.15)$$

From these considerations it becomes clear that detecting minimum ionizing particles with 250 μm thin fibers with high efficiency is a challenging task, as we are talking about detecting just a handful of photons.

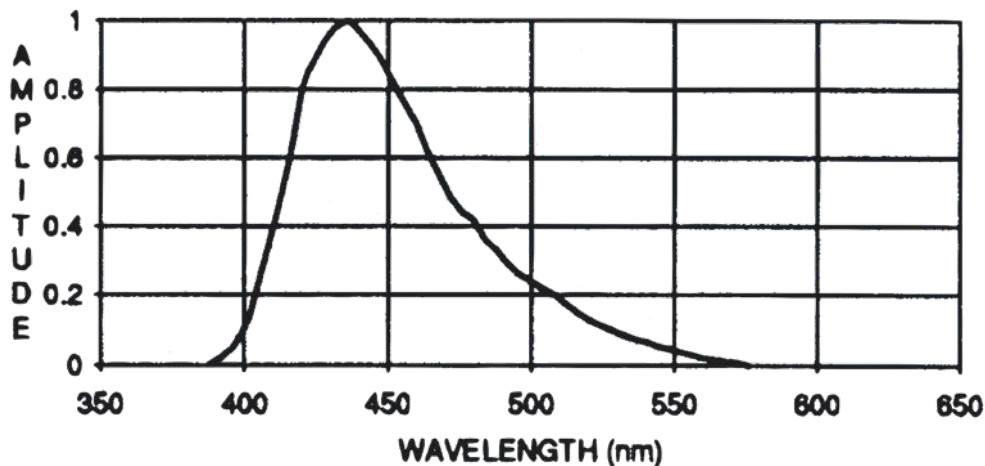


Figure 6.5: Emission spectrum of the BCF-12 scintillator [45].

Radiation Hardness

A detailed discussion about radiation hardness of the scintillating fibers can be found in Sect. 7.3; for the Mu3e hodoscope it is not an issue since we are dealing with MIPs and sufficiently low fiber hit rates.

6.1.2 Characterization and Quality Control

The scintillating fibers of 250 μm thickness and squared cross section used here are manufactured by Saint-Gobain Crystals. Currently, it is the only company providing squared 250 μm multiclad fibers¹. Table 6.1 reports some of their properties. The fibers possess a polystyrene (= polyvinylbenzene) core with a combination of not further specified fluorescent dopants, clad by PMMA (first cladding) and fluor-acrylic (second cladding) [45]. The emission spectrum of the BCF-12 scintillator as reported in the data sheet is shown in Fig. 6.5. The BCF-12 scintillator has its emission maximum in the visible blue light and thus matches approximately the peak in the photon detection efficiency of the SiPMs adopted here (see also Sect. 6.2).

The scintillating fibers are delivered as one single, mile-long filament wound up on a spool from which pieces of arbitrary length can be cut. The fibers used for the construction of the prototypes presented in this thesis have typically a length between 20 and 50 cm, depending on the prototype under consideration. They were taken from two fiber productions referred to as “old” (spool from 2013) and “new” (spool from 2015) sample, where the old sample was found to be qualitatively inferior to the new one for what concerns the fiber geometry (see below). The following paragraphs describe a few tests to which the fibers were subjected to. They were very useful to select fibers for the prototype construction and for general characterization purposes. In the future, one will have to think about refined setups which allow rapid mass tests.

¹Kuraray for example also produces squared 250 μm fibers, but not multiclad ones.

Table 6.1: Properties of the BCF-12 multicladd scintillating fibers as reported by Saint-Gobain Crystals [45].

Properties	
Scintillator	BCF-12
Emission color	blue
Emission peak	435 nm
Decay time	3.2 ns
Scintillation efficiency	2.4 %
No. of photons per MeV from a MIP	≈ 8000
Attenuation length (fiber with 1 mm diameter)	2.7 m
Core material	Polystyrene
Core refractive index	1.60
Mass density	1.05 g/cm ³
First cladding material	PMMA
Second cladding material	Fluor-acrylic
First cladding refractive index	1.49
Second cladding refractive index	1.42
First cladding thickness	4 % of the fiber size
Second cladding thickness	2 % of the fiber size
Light trapping efficiency squared multicladd fibers	7.3 %
Light trapping efficiency squared singlecladd fibers	4.4 %
Light trapping efficiency round multicladd fibers	5.6 % (min.)
Light trapping efficiency round singlecladd fibers	3.4 % (min.)
Numerical aperture	0.74
Radiation length	42 cm
No. of H atoms per cm ³ (core)	4.82×10^{22}
No. of C atoms per cm ³ (core)	4.85×10^{22}
Operating temperature	-20 °C to +50 °C

Geometry

The tolerances on the fiber thickness quoted in the data sheet amount to 3 % of the fiber size [45]. It turned out that the fibers are not perfectly squared, but have a slightly rectangular cross section of $240 \times 260 \mu\text{m}^2$. Moreover, at some points the fiber showed significant defects, mainly little blobs and damages of the cladding. Some parts of the filament stemming from the old fiber spool exhibited large thickness variations, as can be seen for instance in Fig. 6.6a), and some were found to be twisted. In order to easily spot these faulty pieces, the fiber coming from the spool was pulled through a small precision measuring device [47] shown in Fig. 6.6b). The measuring device bears a little spring tip. Whenever there is a significant defect on the piece of fiber beneath the spring tip, the needle on the instrument dial is strongly deflected.

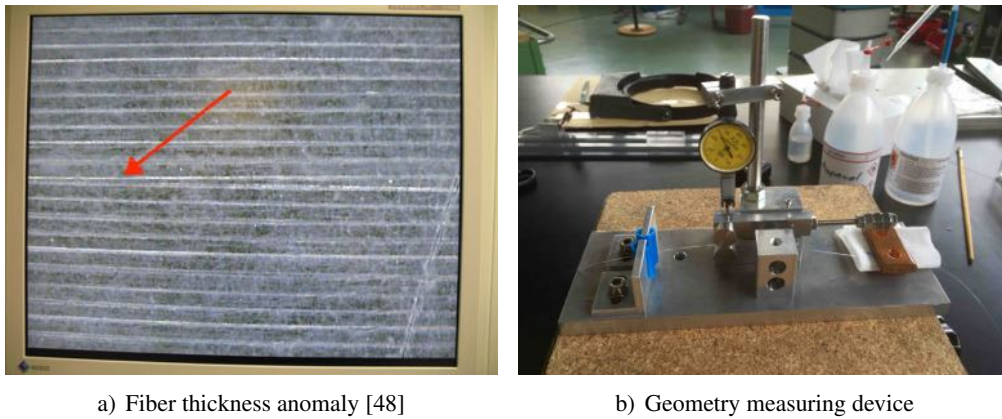


Figure 6.6: The left picture shows a fiber array viewed under the microscope, where one of the fibers features a significantly different thickness (red arrow). The right pictures shows the tool to check the fiber quality when unrolling the fiber strand from the spool.

Attenuation Length

As we have seen in Sect. 6.1.1, the attenuation as a function of the light's traversed distance is best described by an exponential decay with two components, where one is associated to the absorption and Rayleigh scattering, whereas the other is related to the imperfect surface boundaries. The measurement of the attenuation length is important to estimate the short attenuation component, which is not reported in the data sheet, and it is especially interesting to Mu3e since it strongly affects the light yield of fibers with $\mathcal{O}(10)$ cm length. In order to overcome the limitation of low light yield when using a radioactive source such as ^{90}Sr , the attenuation length setup makes use of an UV LED (Thorlabs LED285W) and a blue LED (Thorlabs LED405E). The fiber sample of about 5 m length is clamped by small, custom designed posts at several points along the fiber's first 2.5 m, the remaining part is wound up on a teflon cylinder with a spiraling groove, as shown in Fig. 6.7. One end of the fiber is coupled first to a calibrated photodiode (Newport 818-UV) with its own power meter (Newport 843-R). In a second step, the fiber end is decoupled from the photodiode and coupled to a spectrometer (Ocean Optics USB2000+UV-VIS-ES) sensitive in the region between 200 nm and 1000 nm in order to keep under control the spectrum of the propagated light. Preliminary measurements have shown that the light attenuation is indeed well-described by a two-component exponential decay, and that the short attenuation component is of $\mathcal{O}(10)$ cm. More detailed studies are ongoing.

6.1.3 Optical Isolation

At the beginning of the R&D it turned out that bare fibers suffered from significant light losses whenever they were glued with optical cement. Already a centimeter of glue along the fiber is enough to make the light yield drop substantially, as one can understand qualitatively from Fig. 6.8a) and 6.8b). They show an example of the measured light yield for a bare fiber and a

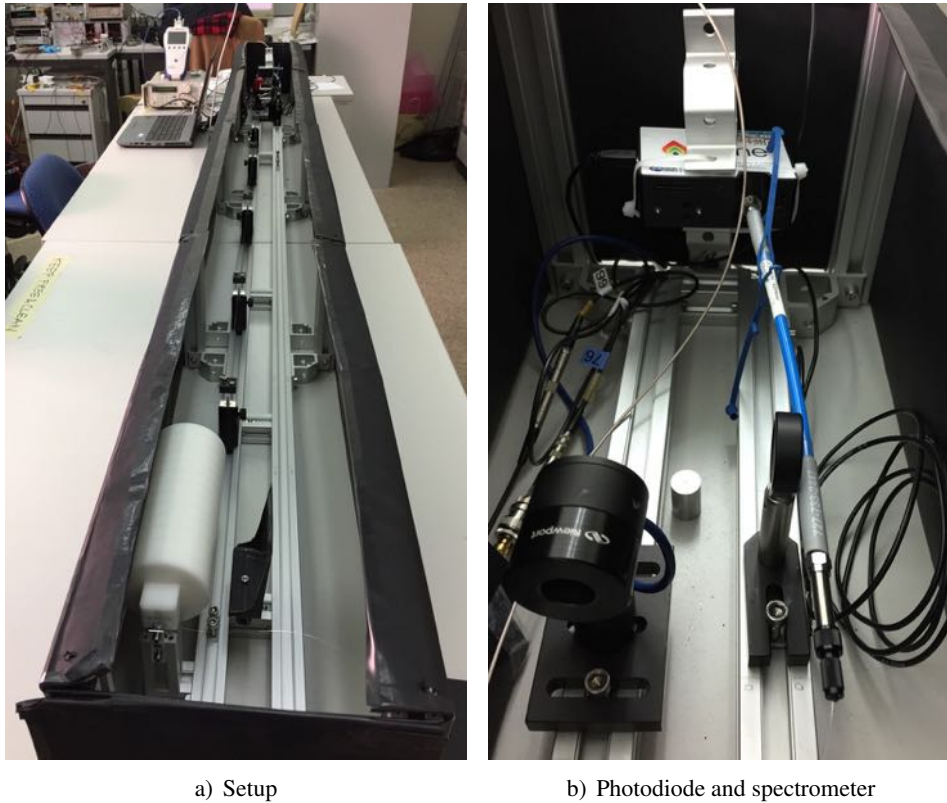


Figure 6.7: Setup to measure the attenuation length with the help of a blue and a UV LED. The fiber sample of about 5 m length is mounted onto custom designed posts, with the final part of the fiber being wound up on a teflon cylinder, as displayed in a). One fiber end is coupled to a photodiode, shown on the bottom left in b). In a second step, the spectrum of the propagated light is measured with a spectrometer, depicted on the top right in b). The whole setup is encased in a black box.

6 R&D of a Scintillating Fiber Detector for Mu3e

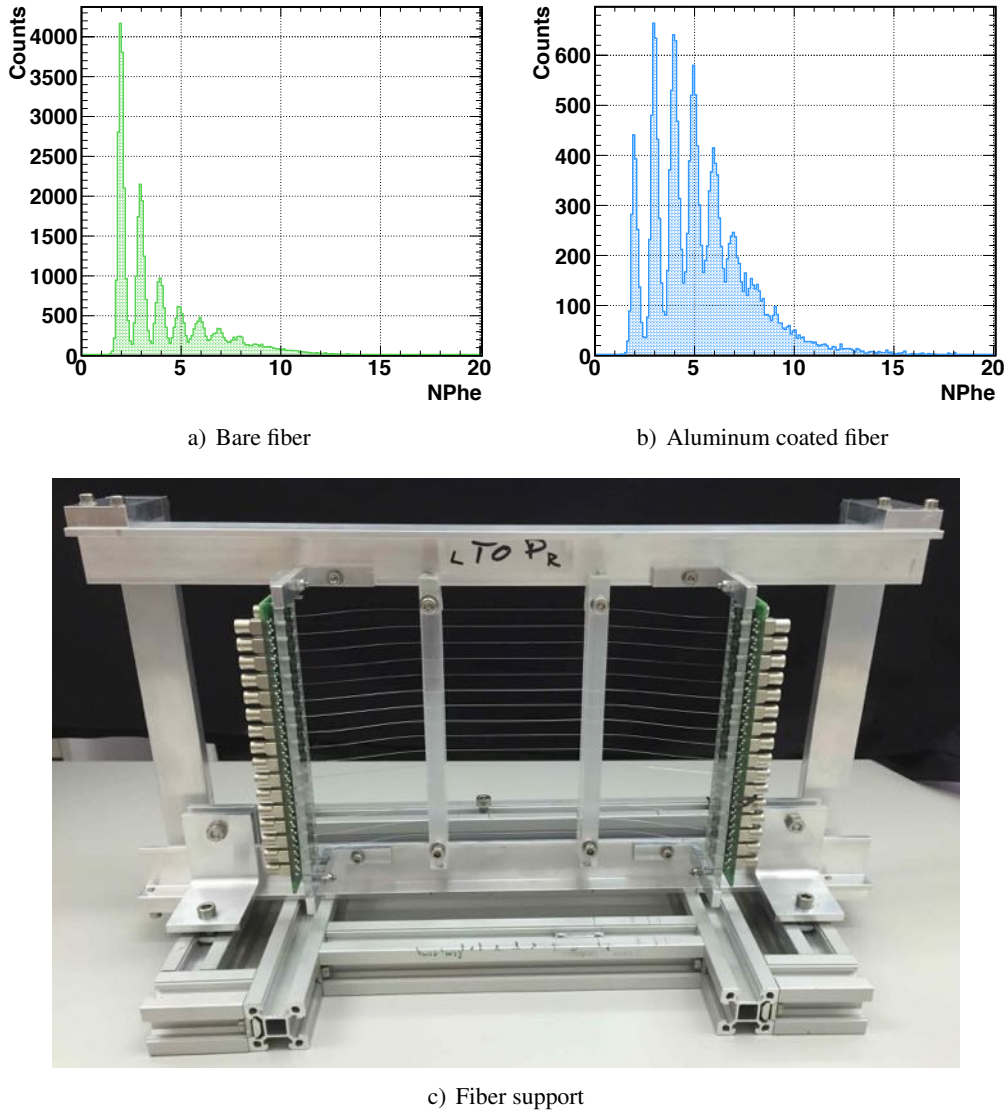


Figure 6.8: Comparison between a bare and an aluminum coated fiber: The top plots show the light yield (for the SiPM AND logic, see Sect. 6.7.1) measured with a ^{90}Sr source. Both fibers were glued with optical cement to the mechanical support structure (which is very similar to the Large Prototype, see Sect. 6.3 and 6.6) shown in the bottom picture. Since the optical cement has a relatively high refractive index, the bare fiber loses a considerable amount of light, whereas the aluminized fiber is optically isolated and is therefore much less prone to light losses.

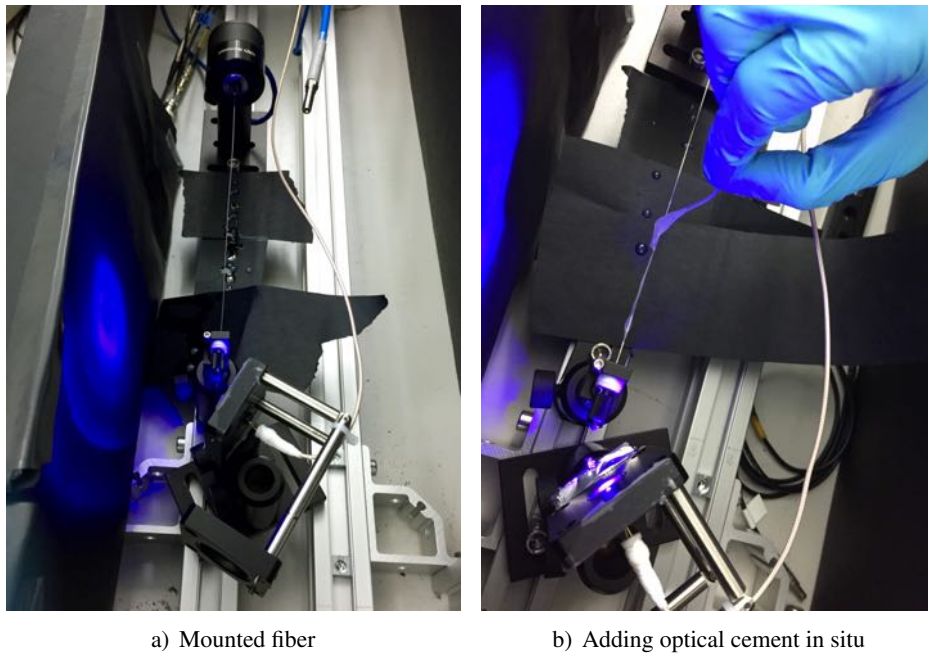


Figure 6.9: Setup to measure the light loss caused by bringing the fiber into contact with a material featuring a high refractive index, in particular optical cement ($n = 1.56$). Bare fibers suffer from $\approx 40\%$ light losses, whereas the aluminum coated fibers are essentially unaffected and thus optically well-isolated.

fiber coated with 100 nm of aluminum, respectively, where both fibers were glued with BC600 [49] optical cement to the support structure depicted in Fig. 6.8c). These losses are actually not surprising considering that the refractive index of the optical cement is $n = 1.56$, i.e. a value which is adapted to the refractive index of the fiber core ($n = 1.60$). With such high a refractive index of the glue, the second cladding ($n = 1.42$) has essentially no leverage anymore since no total reflection can occur at the cladding-cement-boundary. A more quantitative measurement of the effect of having a material with a high refractive index surrounding the fiber was performed using a setup resembling the one from the measurement of the attenuation length described in Sect. 6.1.2: One end of the fiber (with a length ≈ 23 cm) was coupled to the calibrated photodiode, whereas the other end was fixed in a support such that one could illuminate the last few mm of the fiber by a blue LED (Thorlabs LED430L), see Fig. 6.9a). Once the fiber was mounted, the quantity of light transmitted by the fiber was measured first without optical cement, then adding the cement in situ, as shown in Fig. 6.9b). With the optical cement, the amount of light dropped by as much as 40 % in the case of the bare fiber, and by 1 % or less for the aluminized fiber. The exercise was repeated also with Araldite[®] glue ($n \approx 1.5$) and with optical grease ($n = 1.47$), yielding light losses of 30 % and 20 %, respectively. The results of these tests are summarized in Table 6.2.

Thanks to the optically isolating aluminum coating, not only can one recover at least partially the light which would normally be lost when bringing into contact the fiber with the cement, but

Table 6.2: Measured light loss with respect to air when surrounding the fibers by materials with high refractive indices n . Bare fibers are prone to important light losses. An aluminum coating of 100 nm is enough to mitigate this effect.

Material	n	Light loss bare	Light loss alum.
Optical cement (BC600)	1.56	40 %	≤ 1 %
Araldite [®]	≈ 1.5	30 %	≤ 1 %
Optical grease (BC630)	1.47	20 %	≤ 1 %

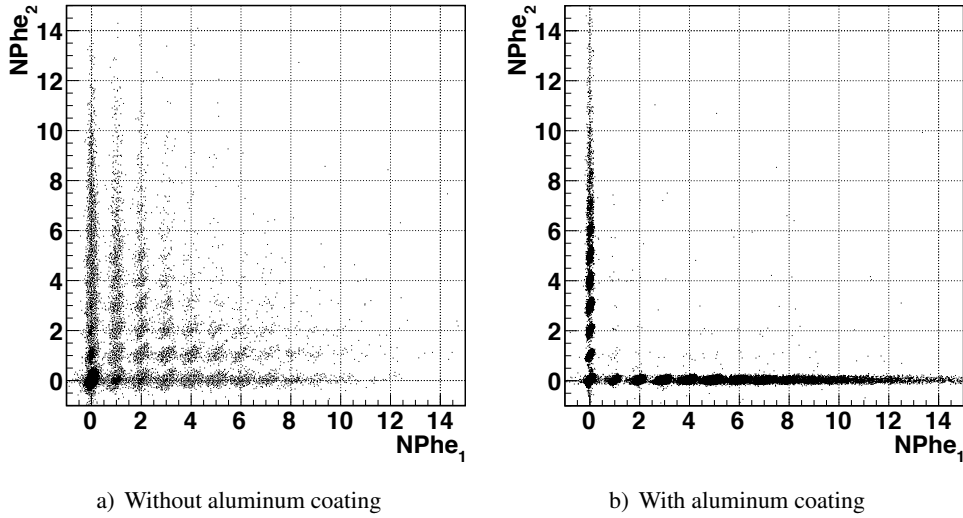


Figure 6.10: Crosstalk among fibers with and without aluminum coating. The scatter plots show the number of photoelectrons measured by the SiPMs of two neighboring fibers upon irradiation by a ^{90}Sr source.

one is also able to suppress crosstalk among fibers whenever they are glued to form a fiber array (see also Sect. 6.3.1). The crosstalk rate among fibers amounts to ≈ 30 % without any optical isolation of the fibers, and is reduced to < 1 % when the fibers are coated, as is clearly visible in Fig. 6.10.

The aluminum can be deposited in different ways. One method is to sputter the aluminum onto the fibers, a service which is provided by PSI's Laboratory for Scientific Developments and Novel Materials (LDM) [50]. Simply speaking, the scintillating fibers (= the substrate) and an aluminum target are placed into a chamber filled with argon gas. By applying a negative voltage to the aluminum target, the argon atoms are ionized through glow discharge and subsequently impinge onto the aluminum, thus kicking out some atoms, which then adhere to the substrate thanks to their elevated kinetic energy. The sputtering machine used to coat the fibers is shown in Fig. 6.11a). The second method that has been tested is based on Physical Vapor Deposition (PVD), with the fibers being coated at the Thin Film Lab at CERN [51]. The fibers are fixed

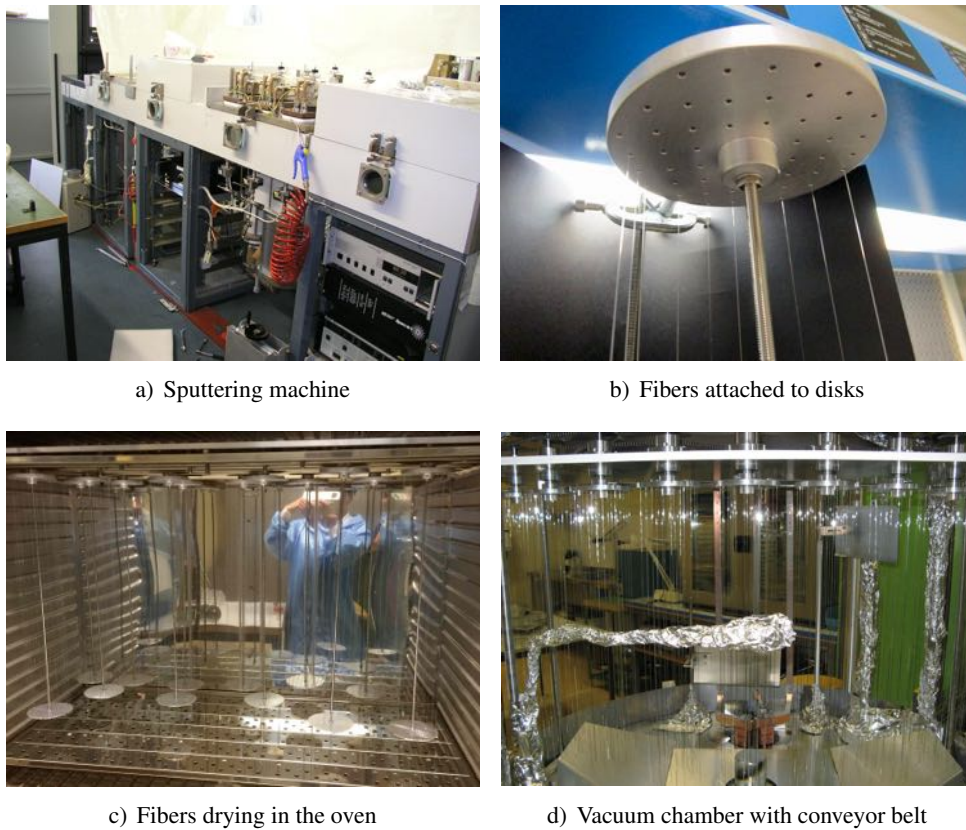


Figure 6.11: Aluminum deposit through sputtering and physical vapor deposition. Picture a) shows the sputtering chamber Leybold Z600 at PSI [50], b)-d) show the setup for the PVD at CERN. For the latter, up to ten fibers are fixed between two disks connected by a rod. These disks are first mounted into an oven in which the fibers dry, then they are fixed to the conveyor belt inside the vacuum chamber in which the fibers are coated.

between two disks which are connected by a rod, see Fig. 6.11b). After letting them dry in an oven at a temperature of 35 °C (Fig. 6.11c)), they are mounted inside a vacuum chamber (Fig. 6.11d)) in which a tungsten coiled filament heats a sample made of aluminum, which is then deposited onto the fibers. The disk suspension mechanism allows to attach the disks to a conveyor belt contained in the vacuum chamber and enables them to revolve around the rods' axes, such that the fibers are evenly exposed to the aluminum vapor. Prior to either process (PVD or sputtering), the fibers are cleaned with methyl alcohol in order to remove dust and grease, therefore guaranteeing a better adhesion of the aluminum.

6.2 Silicon Photomultipliers

Silicon Photomultipliers (SiPMs) are solid-state devices which are able to count single photons. They are also called Geiger Avalanche Photodiodes (G-APDs) or Multi Pixel Photon Counters (MPPCs). Compared to Photomultiplier tubes (PMTs), they offer a lot of advantages:

- Competitive photon detection efficiency;
- Insensitive to magnetic fields;
- Low bias voltage ($\mathcal{O}(100)$ V compared to $\mathcal{O}(1)$ kV);
- Small size, useful for highly granular and compact detectors;
- Longer lifetime and less prone to damage (e.g. if the ambient light accidentally illuminates the photodetector);
- Low cost.

The first two sections deal with their principles of operations and their basic properties, the third section is dedicated to their characterization.

6.2.1 Working Principle

In order to understand how a SiPM works, let us first consider the mechanism of a PIN photodiode and an APD. All three photosensors rely on the principle of converting light into current via the photoelectric effect using semiconducting materials.

PIN Photodiode

A PIN photodiode is the simplest realization of a semiconductor based photodetector. It is structured into three regions: A region which is highly p-doped containing a lot of freely moving holes, an undoped (“intrinsic”) zone containing very few freely moving charge carriers and a highly n-doped region containing a lot of freely moving electrons. By operating the PIN photodiode in a reverse mode (i.e. by applying a negative voltage at the p-zone’s electrode and a positive one at the n-zone’s electrode) the charge-carrier-free, intrinsic region grows. If a photon impinges with an energy larger than the band gap energy² in this charge-depleted region, it may create an electron-hole-pair thanks to the inner photoelectric effect. The electron-hole-pair is immediately separated due to the electric field, with the electron going to the n-zone’s electrode and the hole going to the p-zone’s electrode. This process generates a photocurrent, which is proportional to the incident light intensity. Photodiodes are not suitable to detect low light levels, because the signal caused by a few photons without any additional internal amplification is just too small to be detected.

²The band gap energy is the energy needed to lift an electron from the valence band to the conduction band. For silicon it is typically 1.1 eV [52].

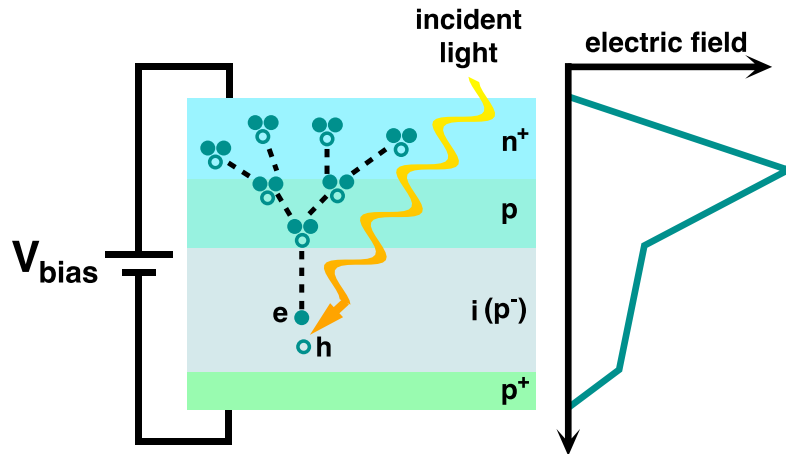


Figure 6.12: Sketch of an APD and the corresponding electric field as a function of depth.

APD

Avalanche Photodiodes (APDs) constitute the next step towards the detection of single photons. The composition of an APD is similar to the one of a PIN photodiode, with the difference that it contains an additional p-n junction, see Fig. 6.12. Together with a large reverse bias voltage of $\mathcal{O}(200)$ V, a region with a large electrical field (“avalanche region”, with fields of ≈ 1 kV/mm [44]) is created. There, the charge carriers generated by the absorption of photons are strongly accelerated, such that they are able to create additional electron-hole pairs through impact ionization. The extent of the impact ionization (and therefore the gain = number of electron-hole pairs generated per absorbed photon) depends on the bias voltage V_{bias} applied. The relationship between the two is usually represented by an “I-V-curve” as shown in Fig. 6.13. One distinguishes three regions in this plot:

1. A region in which the gain is $g = 1$. In this operating mode, the electric field in the avalanche region is too weak for the charge carriers to generate secondary carriers, such that the APD is equivalent to a photodiode.
2. A region in which $\log(g)$ increases linearly with V_{bias} . Here, the electric field is sufficiently strong for the charge carriers to generate an avalanche of additional carriers, which eventually stops once they are all collected by the electrodes. Typical gains lie between 10 and 100 when operating in the linear region, and the produced charge is directly proportional to the number of absorbed photons.
3. A region in which g increases steeply above the so-called “breakdown voltage” V_{br} . An APD operated in this mode is also called Geiger Avalanche Photodiode (G-APD). In this case the electric field is so strong that the avalanche is self-supporting and will only terminate when the bias voltage drops to V_{br} or lower. This is achieved by a quenching mechanism discussed below.

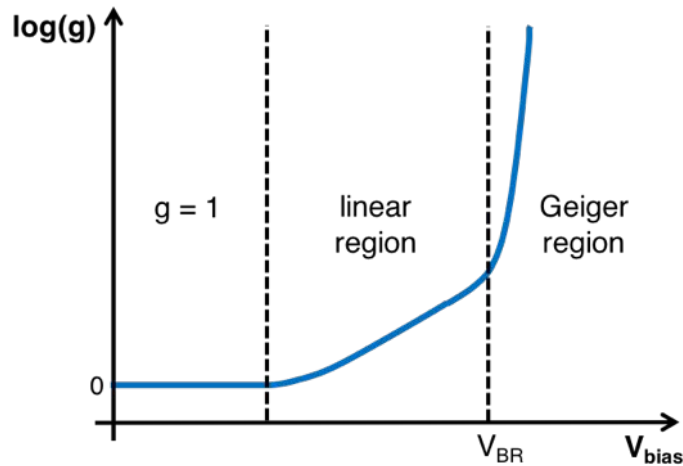


Figure 6.13: Schematic I-V-curve. Picture inspired by [52].

Let us focus on the G-APD. As has already been mentioned, the avalanche is self-sustaining and can only be stopped by quenching it. In the case of *passive quenching*, this is achieved by connecting a resistor R_q in series with the APD. In the condition where no avalanche is present (and thus no current is flowing), the whole bias voltage drops off across the APD. As soon as an avalanche is set off, a current flows, meaning that there is a voltage drop across the quenching resistor with the consequence that also the voltage across the APD drops. At some point, the electric field in the depletion zone becomes too weak to maintain a self-supporting avalanche, i.e. the avalanche is eventually quenched, and the initial voltage condition $V_{APD} = V_{bias}$ is restored. G-APDs with an *active quenching* mechanism feature an electronic circuit which actively lowers the bias voltage once the G-APD fires.

When operated in Geiger mode, the APD is able to detect a single photon. However, the large current flowing upon photon absorption no longer depends on the incident light intensity, but solely on the overvoltage $\Delta V = V_{bias} - V_{br}$. In order to be able to count individual photons, one needs to turn towards SiPMs.

SiPM

A SiPM is a collection of G-APD cells (or “pixels”), where each of the pixels has its own quenching resistor. The pixels are identical and connected in parallel to a common output. By making the pixels appropriately small (with typical sizes between $25 \times 25 \mu\text{m}^2$ and $100 \times 100 \mu\text{m}^2$), the number of photons N_γ impinging on the photosensor can be estimated by counting how many pixels N_{phe} have fired. The number of fired pixels N_{phe} are called “photoelectrons” in analogy to the PMTs. A typical SiPM charge spectrum is shown in Fig. 6.19a): the individual peaks correspond to one photoelectron, two photoelectrons, three photoelectrons etc. Ideally, the number of fired pixels equals exactly the number of incident photons, $N_\gamma = N_{phe}$. However, due to effects explained in the next section (and also the photon detection efficiency being less than 100%), that is usually not the case. An example of a SiPM architecture is displayed in

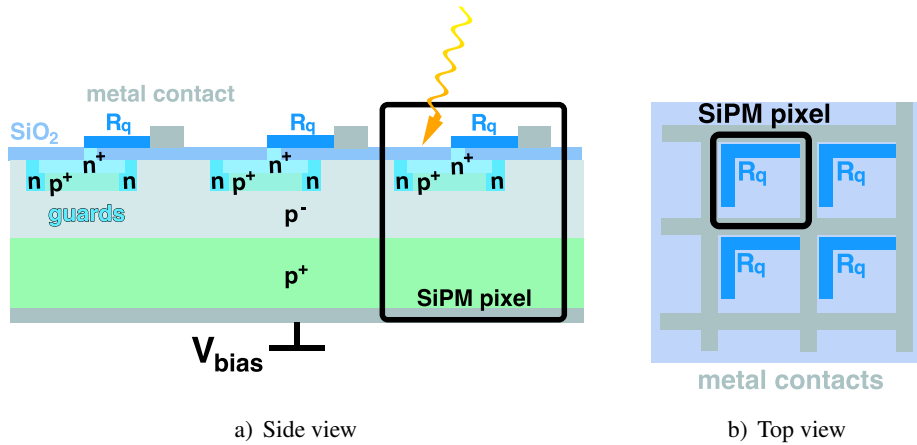


Figure 6.14: Sketch of a SiPM's architecture. The black box represents one SiPM pixel. Pictures inspired by [52].

Fig. 6.14. The avalanche is created in the region of the p⁺-n⁺ junction, which is formed by a heavily doped n⁺-layer and a heavily doped p⁺-layer of few μm thickness [52]. The n⁺-layer is connected to the metal contact through the quenching resistor R_q . On top of this layer, an additional, transparent SiO₂ layer insulates the semiconductor material from the metal contacts above. The electron-hole pair is generated in a lightly doped p⁻-layer of about 300 μm thickness. The electric field that prevails in this region is strong enough to make the electrons and holes drift towards the avalanche region and the substrate, respectively. Guard rings separate the individual pixels and lowers the electrical field at the edges, suppressing premature discharges. In some cases, additional separation between the pixels is provided by so-called “trenches”, which are dielectric structures. Typically, the operation voltage V_{bias} lies between 30 and 70 V and the overvoltage is of the order of a few volts.

6.2.2 Basic Properties

The next few paragraphs describe the time characteristics of a SiPM, its gain and detection efficiency as well as effects which affect the counting of photons.

Rise Time and Recovery Time

To understand the time characteristics of the signal pulse generated by a firing SiPM, let us look at the electrical circuit drawn in Fig. 6.15a) [53]. It represents one pixel, consisting of a quenching resistor R_q connected in series with an APD. When the APD is in the state of awaiting a photon (i.e. no current is flowing), the junction capacitance C_j is fully charged, with the whole bias voltage V_{bias} dropping off across it, meaning that in Fig. 6.15a) the switch is OFF. As soon as the APD fires (be it due to a photon, be it due to a dark count, see next paragraphs), the switch changes to the ON state such that C_j discharges through the resistor R_s , which represents the resistance of the depletion region and the neutral regions of the APD, until the voltage drops to

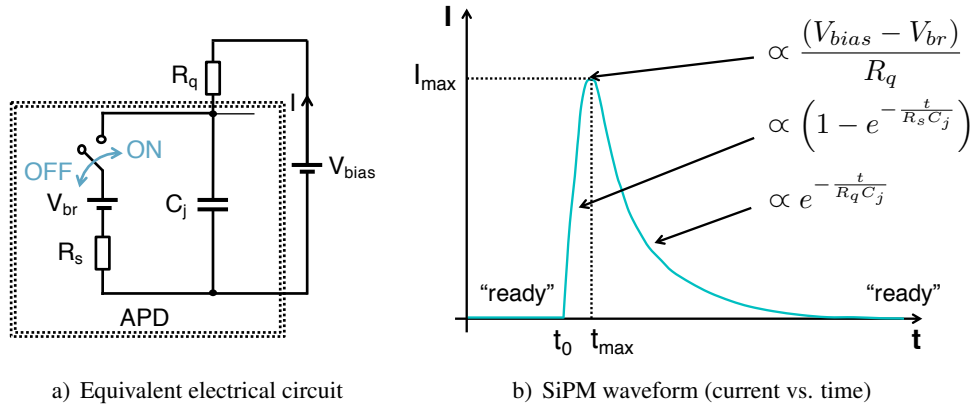


Figure 6.15: Equivalent electrical circuit of a SiPM pixel and a sketch of a SiPM's waveform. Pictures inspired by [53].

approximately the breakdown voltage V_{br} . At that point, R_q causes the avalanche to quench and the switch is opened again. The time constant associated to this discharge, which corresponds to the rise time of a SiPM signal, is given by $\tau_{rise} \sim R_s C_j$. Typical values are $R_s = 1 \text{ k}\Omega$, $C_j = 0.1 \text{ pF}$ and $\tau_{rise} \sim 100 \text{ ps}$. The recovery time is given by the time constant with which C_j is charged again, namely $\tau_{recovery} \sim R_q C_j$, after which the APD is ready to receive the next signal. Typical values are $R_q = 150 \text{ k}\Omega$, $C_j = 0.1 \text{ pF}$ and $\tau_{recovery} \sim 15 \text{ ns}$. A sketch of a waveform generated by a SiPM is shown in Fig. 6.15b).

Single Photon Time Resolution

Ideally, the temporal distance between the instant when the photon impinges on the SiPM and the moment when the electrical output is produced is always the same. However, in reality this time distribution exhibits a certain spread, also called Single Photon Timing Resolution (SPTR), which may ultimately limit the time resolution of a detector. The reason for the SPTR not being zero is the non-deterministic nature of the processes involved: For example the location where the electron-hole pair is generated or the drift times of the charge carriers on their way to the avalanche region, the time at which an avalanche is created and even if an avalanche is created at all are subject to stochastics. The pixel time constants may slightly differ, too, since the corresponding resistance and capacitance as well as the quenching resistor are not completely identical. In addition to that, also the length of the paths between the pixels and the common output signal line depends on where the pixel is located within the SiPM structure. Measurements of SiPMs from the Hamamatsu series 13360-1350CS used here yielded a SPTR of $\sigma \approx 70 \text{ ps}$ (RMS) [54].

Gain

The gain is the proportionality factor between the number of pixels fired and the electric charge collected. Considering again the circuit drawn in Fig. 6.15a) and integrating the waveform

caused by a single pixel firing shown in Fig. 6.15b) with respect to time, one finds that the corresponding charge Q is given by

$$Q = C_j (V_{bias} - V_{br}) = C_j \Delta V. \quad (6.16)$$

Keeping in mind that C_j for a fully depleted junction is constant with respect to the bias voltage, one can immediately see that the gain g , which is defined through $Q = g \cdot e$ with e equal to the elementary electric charge, is linearly proportional to the overvoltage ΔV . In particular, if one wants to equalize the gains of several SiPMs on a hardware-level, one needs to supply them the same overvoltage. This usually implies biasing every SiPM individually, as the breakdown voltage varies from sensor to sensor. Moreover, the breakdown voltage and thus the gain depend on the temperature. For example for the SiPMs used here, the breakdown voltage increases by ≈ 60 mV/°C. Typically, the gain is of order 10^6 at room temperature and when supplying the SiPM with the suggested operation voltage.

Photon Detection Efficiency (PDE)

The PDE is defined as the ratio of the number of incident photons per unit time and the number of detected photons per unit time. It is composed of the fill factor F , the quantum efficiency η and the probability P_a for an avalanche to occur:

$$\text{PDE} = F \cdot \eta \cdot P_a \quad (6.17)$$

Not all of the pixel's area is photosensitive since it includes also the metal contacts, the quenching resistor, the guard rings etc., see also Fig. 6.14b). The ratio between the effective photosensitive area and the total area of the pixel is referred to as "geometrical fill factor" F . The fill factor grows with increasing pixel size, for example for $100 \times 100 \mu\text{m}^2$ pixels, the fill factor is 80 %, for $25 \times 25 \mu\text{m}^2$ pixels it is 50 %. The quantum efficiency $\eta = \eta(\lambda)$ is defined as the ratio of the number of photons impinging on a photosensitive area per unit time and the number of electron-hole pairs that are generated by the photoelectric effect per unit time. It is a function of the wavelength λ . The probability P_a for the electrons and holes initiating a Geiger avalanche increases with monotonically increasing overvoltage.

A plot of the PDE as a function of the wavelength for the Hamamatsu SiPM series S13360-1350CS used here is shown in Fig. 6.16. These SiPMs are most efficient at a wavelength of $\lambda_p = 450$ nm (i.e. in the visible blue), thus matching the emission spectrum of the BCF-12 scintillating fibers from Saint-Gobain (peak emission at $\lambda = 435$ nm). Typically, the PDE at the wavelength $\lambda = \lambda_p$ is 40 %.

Dark count

Sometimes a pixel can fire through a self-triggered process. Since in that case there was no actual photon impinging on the pixel, the occurrence of such an event is called a "dark count" (or "dark current"). It is completely uncorrelated with the signals generated by true photons, and it occurs randomly in time. Dark count signals are caused by charge carriers which are able to reach the avalanche region. The origin of these charge carriers lies in thermal fluctuations, which generate an electron-hole pair inside the depletion region or inside the avalanche

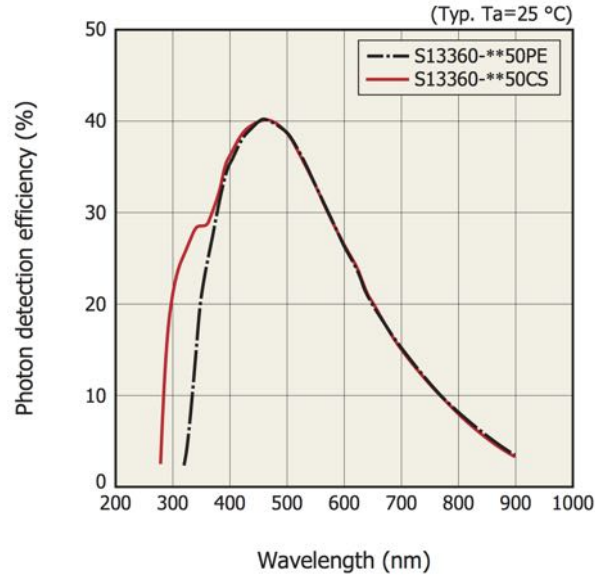


Figure 6.16: PDE as a function of wavelength for the Hamamatsu SiPM 13360-1350CS used here [55]. The PDE is maximal for a wavelength $\lambda_p = 450$ nm [ibid].

region. The rate of the dark counts is a linear function of the bias voltage provided to the SiPM. Moreover, the rate depends also on the temperature: For a fixed overvoltage, the dark count rate increases exponentially with increasing temperature. In addition, it depends on the pixel size, with increasing dark count rates with increasing pixel size, and the quality of the semiconductor. Biasing the SiPMs used here with the operation voltage suggested by Hamamatsu, they exhibit dark count rates of $\mathcal{O}(100)$ kHz at room temperature and when setting the threshold at the level of 0.5 photoelectrons. By requiring the coincidence of two independent SiPMs in a time window of about 20 ns^3 , the dark count rate is suppressed by roughly a factor 100.

Crosstalk

During an avalanche in a pixel, some of the charge carriers may recombine and generate a photon which is able to induce another avalanche in one of the neighboring pixels (“crosstalk”). The time for the photon to reach the neighboring pixel is less than 1 ns. The likelihood for crosstalk to occur increases with increasing overvoltage, because on the one hand more charge carriers (which can potentially recombine) are created, and on the other hand the avalanche probability is higher. The crosstalk probability decreases with increasing pixel size, because the photon is more likely to be absorbed again in the same pixel which has generated it in the first place. Throughout the development of the SiPM technology, substantial improvement in the suppression of the crosstalk has been achieved by introducing trenches (see Sect. 6.2.1).

³The 20 ns time window corresponds to the typical length of a waveform caused by a particle traversing a scintillating fiber as measured in our setup.

Afterpulsing

Sometimes, lattice defects trap some of the charge created by an avalanche and release it at a later ($\mathcal{O}(1-100)$ ns) point in time. This effect is called “afterpulsing”. If the release occurs at a time t_{AP} during the recovery time of the pixel, the charge creates a secondary avalanche with a gain proportional to the overvoltage $\Delta V(t_{AP}) < \Delta V = (V_{bias} - V_{br})$. If it occurs later, the signal corresponds to one photoelectron. The probability of having an afterpulse increases with increasing overvoltage, because the amount of charge carriers (which could potentially be trapped) generated in an avalanche and also the avalanche probability per se is higher.

Saturation Effects

It may happen that two photons hit the same pixel simultaneously⁴. In that case we would identify only one photon, since the amplitude and the pulse length of the signal provided by the pixel is the same as if just one photon had hit the pixel. This effect may lead to saturation phenomena ($N_\gamma \gg N_{phe}$) when the pixel size is too large compared to the spatial spread of the photons across the active area of the SiPM and / or the rate with which the photons impinge on the SiPM is very high. In the specific case of a scintillation detector, saturation effects can occur when the pixel size is too large compared to the light yield of the scintillator. For the squared fiber prototypes discussed here (and also for the potential future hodoscope) this kind of saturation effect is negligible, since the expected light yield upon the passage of a particle is very low, and Monte Carlo simulations show that these few photons spread out over an area of $750 \times 750 \mu\text{m}^2$ (see also Sect. 6.3.2).

6.2.3 Characterization

For the prototypes under consideration here (see Sect. 6.6.1), SiPMs of the Hamamatsu S12825-050C (Prototype V4.1, “old series”) [56] and S13360-1350CS (Large Prototype, “new series”) [55] series were used. A SiPM of the new series is shown in Fig. 6.17. Both types of SiPMs possess pixels with a size of $50 \times 50 \mu\text{m}^2$, which are arranged in a rectangular fashion, forming a photosensitive area of $1.3 \times 1.3 \text{mm}^2$ that contains 676 pixels in total. The SiPM active area is hosted in a ceramic packaging. The active area is protected by a few 100 μm thin silicone resin window with a refractive index of $n = 1.41$. Table 6.3 summarizes all the relevant SiPM characteristics as reported in the data sheet.

Several SiPMs of both the new and the old series were characterized as a function of the bias voltage and the temperature. For that purpose, an Array 3645A DC power supply, a Keithley 6487 picoammeter and a ESPEC SU-241 thermal chamber were used. The temperatures were varied between 8 °C and 32°C.

I-V-curves

We have met the I-V-curve already in Sect. 6.2.1: It is the characteristic curve of a SiPM (or any diode for that purpose) obtained by applying a certain voltage and measuring the corresponding

⁴Simultaneously means that the time between the two photon’s arrivals is significantly shorter than the recovery time of the pixel.

Table 6.3: Properties of the SiPM series from Hamamatsu used in the framework of this thesis [56, 55]. The parameters are given for standard operation conditions (overvoltage and temperature).

Properties	S12825-050C (old)	S13360-1350CS (new)
Breakdown voltage V_{bd}	65 ± 10 V	53 ± 10 V
Operation voltage	$V_{bd} + 2.6$ V	$V_{bd} + 3$ V
Gain	1.25×10^6	1.7×10^6
PDE (max.)	35 %	40 %
Fill factor	62 %	74 %
Typical (max.) dark count rate	170 (350) kHz	90 (270) kHz
Crosstalk probability	40 %	1 %
Temperature coefficient	60 mV / °C	54 mV / °C

current that flows through the SiPM. From this curve one can extract the breakdown voltage, above which the photosensor acts as a single photon detector (see again Sect. 6.2.1). A set of IV-curves for three different temperatures is shown in Fig. 6.18. As expected, the breakdown voltage increases for increasing temperatures.

Dark count

A typical dark count spectrum is shown in Fig. 6.19a) and 6.19b) for the old and the new SiPM series, respectively. As explained in the previous paragraphs, the dark count rate depends linearly on the breakdown voltage and exponentially on the temperature. Both these behaviors are clearly visible in Fig. 6.19c) and 6.19d).

Crosstalk Probability

The Crosstalk Probability (CTP) p_{CTP} is estimated by considering the SiPM's dark count spectrum, as illustrated in Fig. 6.20. For that purpose, one calculates the ratio of the number of events for which at least two SiPM pixels fired (threshold at 1.5 photoelectrons) and the number of events for which at least one pixel fired (threshold at 0.5 photoelectrons):

$$p_{CTP} = \frac{\# \text{ events } (N_{Phe} > 1.5)}{\# \text{ events } (N_{Phe} > 0.5)}. \quad (6.18)$$

Strictly speaking, this method (which, by the way, is also utilized by Hamamatsu to characterize their products) provides an upper limit on the CTP, since we assume that all events with $N_{Phe} > 1.5$ are due to pixel crosstalk. However, the occurrence of two pixels firing coincidentally in time and independently is negligibly rare.

The newer SiPM series features a significantly lower crosstalk probability, as one can already imagine from the dark count spectra shown in Fig. 6.19a) and 6.19b). The upper limit on the CTP extracted from these dark count spectra amounts to about 30 % for the old series and a few percent for the new series when biasing the SiPM with the suggested operation voltage. Moreover, both the new and the old SiPMs show the expected linear behavior of the CTP as

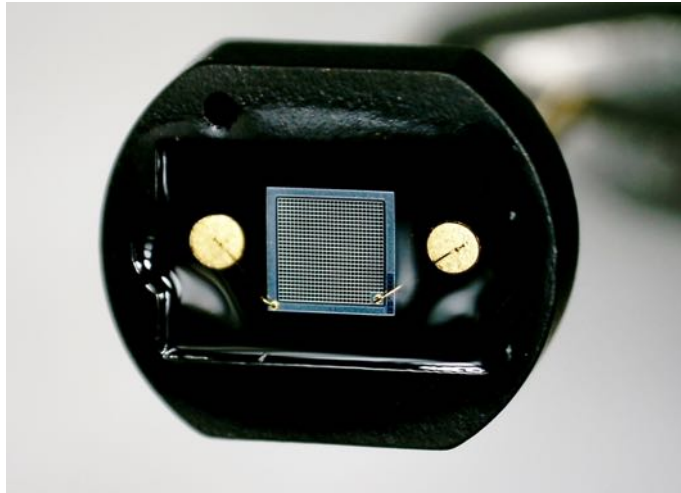


Figure 6.17: SiPMs used for the Large Prototype (Hamamatsu series 13360-1350CS) with an active area of $1.3 \times 1.3 \text{ mm}^2$. The $50 \mu\text{m}$ pixels are well visible. The photosensor is hosted in a ceramic packaging (black).

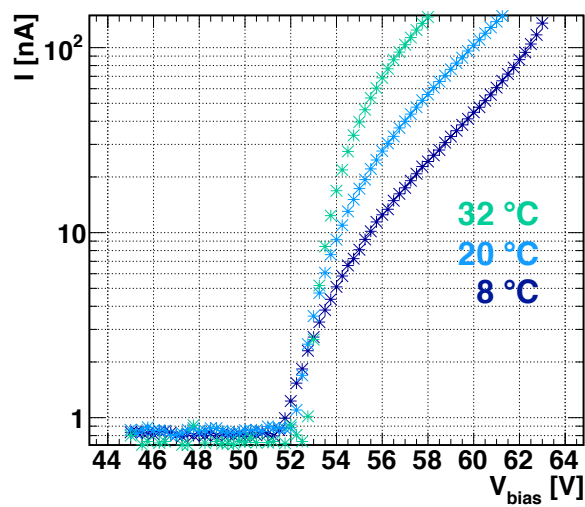


Figure 6.18: I-V-curves for a SiPM from the new series measured at different temperatures. The breakdown voltage increases for increasing temperatures.

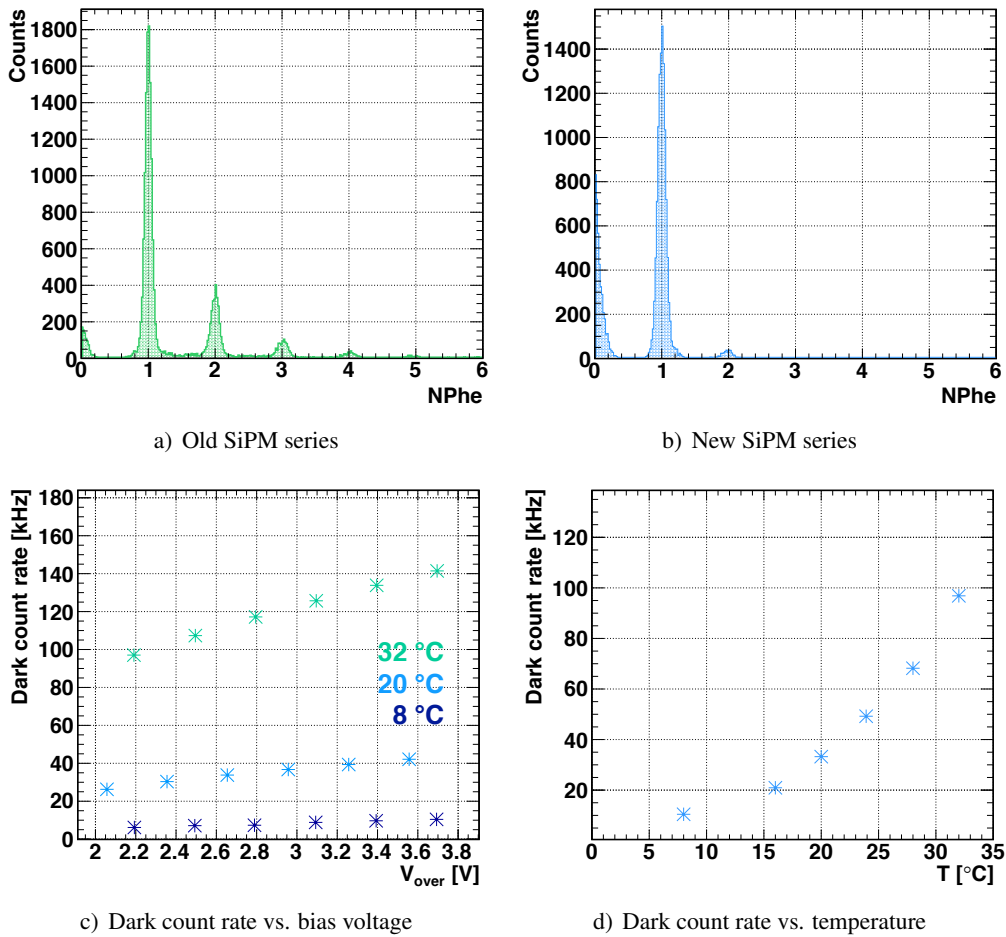


Figure 6.19: The top plots show the dark count spectra for the old and the new SiPM series. The bottom plots show the dark count rates as a function of bias voltage and temperature for the new SiPM series.

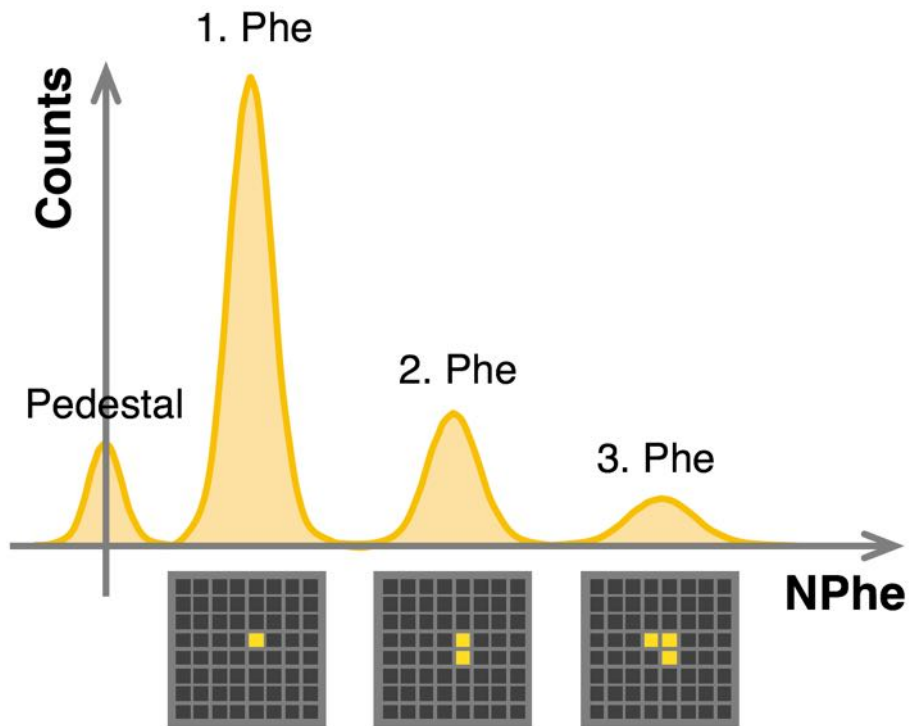


Figure 6.20: Illustration of the method used to extract the Crosstalk Probability (CTP) from the dark count spectrum. The dark count spectrum of the SiPM is shown in dark yellow, the grey boxes indicate the SiPM active area with the corresponding amount of pixels firing (yellow). The (upper limit on the) CTP is given by the number of events for which at least two pixels fire divided by the number of events in which at least one pixel fires.

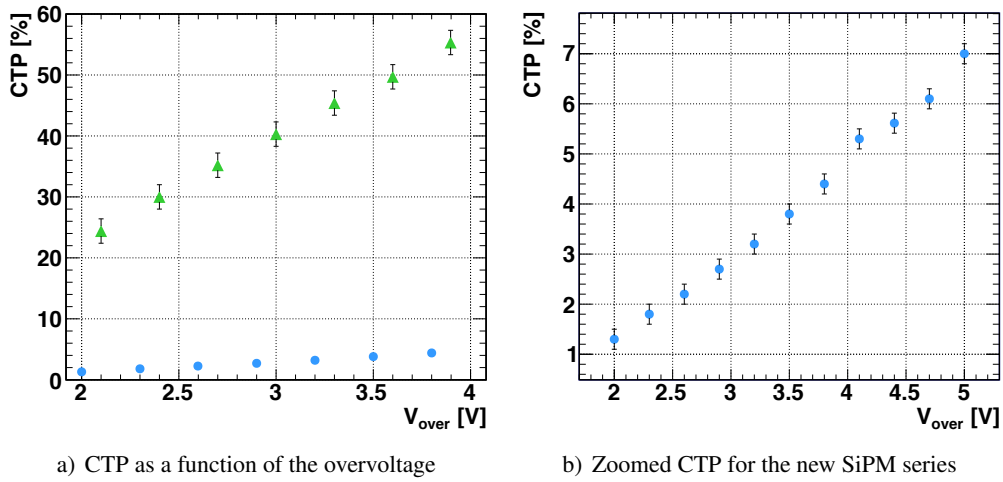


Figure 6.21: The two plots show the CTP of the old vs. new series as a function of the bias voltage. Both the old and the new SiPMs show the expected linear behavior. The new SiPMs feature a significantly lower CTP compared to the old ones.

a function of the SiPM overvoltage. From the plots in Fig. 6.21, the rate with which the CTP increases is $\approx 2\%/V$ for the new SiPMs and $\approx 16\%/V$ for the old ones.

Two additional cross-checks were carried out to get an idea of how the pixel crosstalk influences the measurements with setups in which a true signal is present: One in which the SiPMs were illuminated by a LED and one in which the SiPMs were coupled to scintillating fibers irradiated by a radioactive source. For what concerns the measurements of the LED, the following setup was used: A blue LED was mounted at a distance of about 7 cm from a PCB carrying one SiPM from the old series and one SiPM from the new series. The LED was flashed at different intensities, illuminating the old and the new SiPM simultaneously such as to circumvent the monitoring of the LED's stability. The LED intensities were not calibrated, rendering the measurement more qualitative than quantitative. The light yield measured by the SiPMs is reported in Table 6.4. The old SiPM measured consistently more photoelectrons than the new one, as expected. In addition, the discrepancy between the light yield measured by the old and the new one became smaller the higher the LED intensity. The reason is that the more light is incident on the SiPM, the more pixels are already occupied by actual photons and are in that sense not subject to crosstalk anymore (or it may happen also the other way round: A pixel onto which a photon impinges may have already fired due to the crosstalk induced by its neighbors). In other words, by increasing the illumination of the SiPM, the "error" in the photon counting due to the crosstalk becomes smaller, such that the old and the new SiPM exhibit more and more similar performances. The second measurement was conducted using the SiPMs from the new series in conjunction with the Large Prototype presented in Sect. 6.6.1, which features 250 μm thin scintillating fibers that read out individually by two SiPMs on the left and the right side of each fiber. The fibers were irradiated by a ^{90}Sr source while triggering on an external trig-

Table 6.4: Comparison of the light yield measured by the old and new SiPM series upon illumination by a blue LED. The LED intensities I_1 up to I_7 are listed in increasing order, $\langle N_{Phe} \rangle$ denotes the mean number of photoelectrons measured by the SiPM. The old SiPM measures a consistently higher light yield, and the discrepancy between the old and the new SiPM becomes smaller for increasing LED intensities.

LED Intensity [AU]	$\langle N_{Phe} \rangle$ old	$\langle N_{Phe} \rangle$ new	$\langle N_{Phe} \rangle$ old / $\langle N_{Phe} \rangle$ new
I_1	2.7	1.7	1.59
I_2	3.4	2.2	1.55
I_3	18.3	12.4	1.48
I_4	22.6	15.2	1.49
I_5	24.6	16.7	1.47
I_6	38.3	27.0	1.42
I_7	38.8	27.4	1.42

ger (see Sect. 6.6.2) which helped to reject the SiPMs' dark noise ⁵. The goal was to see how the measured mean number of photoelectrons behaves as a function of the SiPM bias voltage, because a higher bias voltage comes along with a higher CTP. At the same time one has to keep in mind that an increased bias voltage translates also into a higher PDE. As one can see from Fig. 6.22, the number of photoelectrons continuously increases with higher bias voltage, whereas the relative electron detection efficiency (which in this case is entirely related to the photosensor's PDE, since the rest of the setup is identical) reaches a plateau after a certain point that approximately corresponds to the operation voltage indicated on the SiPM data sheet. This means that for voltages above the suggested operation voltage, the number of photoelectrons is biased towards higher values by the crosstalk, for voltages below, the PDE is not at its maximum and consequently the number of photoelectrons is lower.

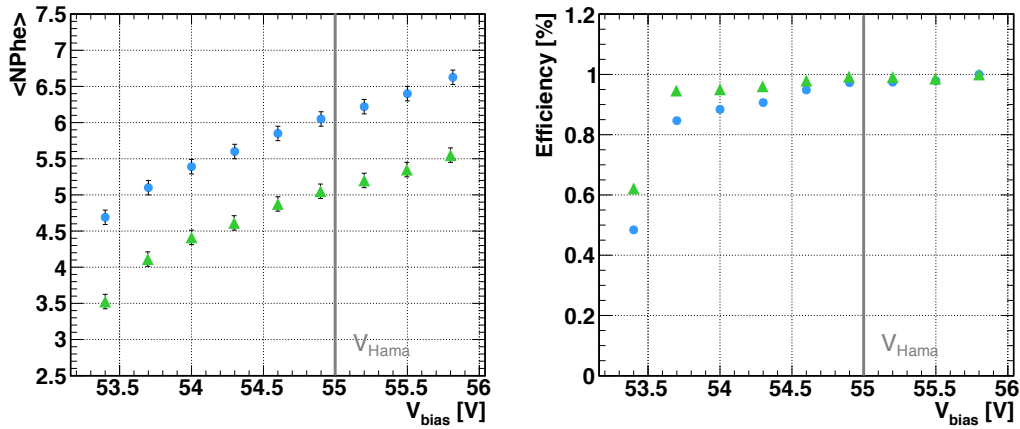
PDE

For the measurement of the relative PDE, one may bring forward an argument similar to the one in the previous paragraph: By considering a system composed of a scintillating fiber read out by a SiPMs on every end and irradiated by a ^{90}Sr source, the relative PDE of the SiPM is given by the course of the system's relative electron detection efficiency as a function of the bias voltage, see again Fig. 6.22b). The determination of the absolute PDE would require a setup which allows to control or measure the amount of photons impinging on the SiPM.

6.3 Mechanical Considerations

The fiber prototypes presented in Sect. 6.6 are modular in the sense that the mechanics and the optical coupling allows to mount and dismount the SiPMs at will, without having a permanent

⁵The careful reader will notice that the number of photoelectrons measured in this setup is higher than what is presented in Sect. 6.7.1. The reason is that in this measurement we did not specifically select MIP.



a) Mean number of photoelectrons as a function of the bias voltage b) Relative efficiency as a function of the bias voltage (the statistical error bars are not visible)

Figure 6.22: Average number of photoelectrons and relative electron detection efficiency measured with a single fiber coupled to a SiPM on every end as a function of the bias voltage. The grey line indicates the operation voltage V_{hama} suggested by Hamamatsu. The blue dots (green triangles) correspond to the measured mean number of photoelectrons in the SiPM AND (OR) logic (see also Sect. 6.7.1). The number of photoelectrons continuously grows with increasing bias voltage. In contrast, beyond the operation voltage V_{hama} , the relative electron detection efficiency is roughly constant (the efficiency is normalized to the point measured at the highest bias voltage $V_{bias} = 55.8$ V). This suggests that the number of photoelectrons above the operating voltage is biased by pixel crosstalk. Note that the right plot can also be seen as a measurement of the relative PDE as a function of the bias voltage.

connection between the fibers and the SiPMs⁶. The optical cement (BC600 [49]) is only used to glue the fibers to layers or to fix them to their mechanical structure. As an optical coupler, optical grease (BC630) is used instead.

6.3.1 Fiber Array Production and Mounting

The key point to obtain a uniform, regular fiber array with a minimal amount of dead material (glue) lies in the quality assurance of the fiber geometry. As has already been mentioned in Sect. 6.1.2, the fibers have not a perfectly square but a rectangular cross section of $240 \times 260 \mu\text{m}^2$. Additionally, some parts of the fiber filament coming from the spool exhibit defects in the form of blobs and cladding damages. In a few cases, the fiber thickness varies considerably or the strand is even twisted. These quality defects imply that when we construct a fiber ribbon, the fiber filament cannot simply be wound from the spool onto a wheel. To complicate matters further, by simple winding one is not able to guarantee a minimal spacing between two neighboring fibers. For these reasons, a special tool, shown in Fig. 6.23, to glue fibers into an array was developed [47]. The fibers, after having checked that they are faultless in terms of geometry and after having made sure that they are oriented such that their shorter side is parallel to the normal incidence direction, are placed piece by piece onto a metal plate with a non-stick coating and are lined up flush with the neighboring fiber. In a second step, the optical cement is applied, pressing the array with a dedicated plate loaded with additional weight. The glued part extends over a length of 11 cm. With this device, single fiber layers with up to 256 fibers were produced. The thickness of such a layer was typically $265 \mu\text{m}$, with a uniformity of $\pm 5 \mu\text{m}$ across its whole length, except for the boundary lines between the glued part and the part where the fibers are loose. The width of a layer made of eight fibers was measured to be between 2.08 and 2.10 mm. This tool was also used to stack several fiber layers on top of each other, as for example for the Large Prototype introduced in Sect. 6.6.

In order for every individual fiber end to be read out by a SiPM, the fiber ribbon needed to be fanned out. For the Large Prototype, each loose fiber end was fed through a hole of $400 \mu\text{m}$ diameter⁷ drilled in a 5 mm thick plexiglass plate (“endplate”) and fixed with optical cement. Afterwards, the excess fiber length were truncated and the plexiglass plate was subjected to a machine with a diamond-cutting blade in order to polish the exit faces of the fibers. The fiber array and the endplates were eventually fixed to an aluminum support structure. For earlier prototypes (e.g. the Prototype V4.1, see Sect. 6.6.1), the fibers were directly fixed onto a plexiglass support which featured grooves with a cross section of $270 \times 270 \mu\text{m}^2$ to house the fibers. Similarly to the endplates, the plexiglass frame was polished with the diamond-cutting blade.

6.3.2 Fiber-SiPM-Alignment

The modular design requires a mechanics which guarantees a sufficiently good and reproducible alignment of the fiber with the active area of the SiPM. Given that we expect only a few photons to be detected by the SiPM at the end of the fiber, even in the ideal case where the fiber and

⁶The reason for adopting this system is mainly of financial nature.

⁷the fiber diameter being $\sqrt{2} \cdot 260 \mu\text{m} \approx 370 \mu\text{m}$

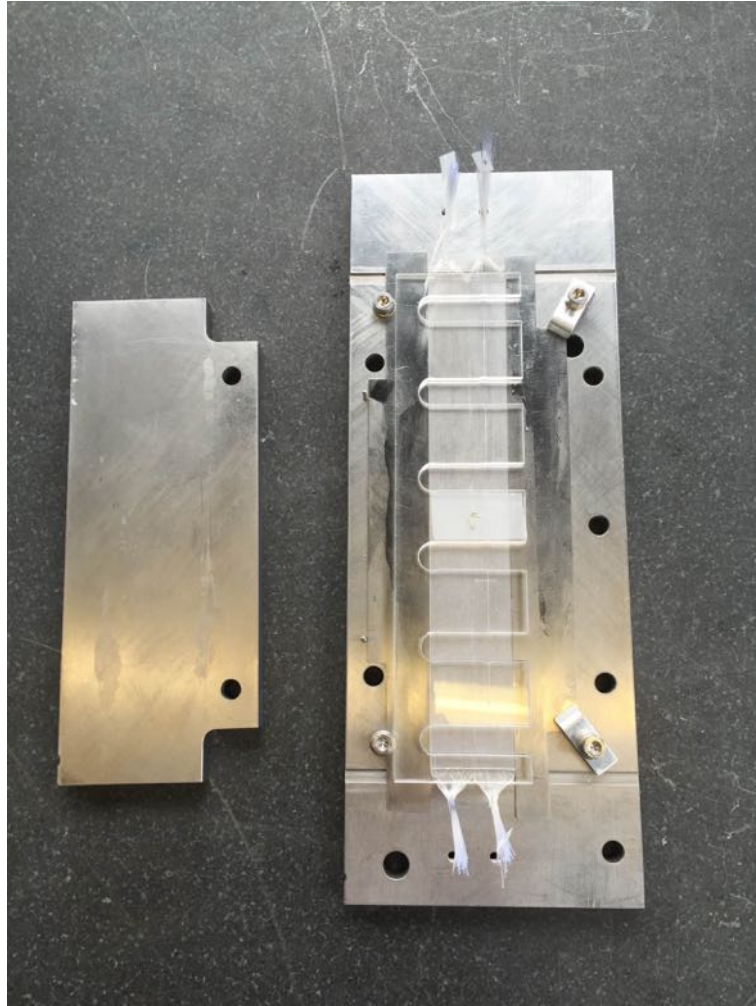


Figure 6.23: Device to construct the fiber arrays. The fibers are placed piece by piece onto a metal plate (right) with a non-stick coating and are lined up flush with the neighboring fiber. The plexiglass comb helps to keep the fibers in position during this operation. In a second step, the glue is applied, pressing the array with a dedicated plate (left) loaded with additional weight. The array in the picture was a mechanical prototype for the US RDC counter described in Sect. 4.8.5.

SiPM are well-centered with respect to each other (see Sect. 6.1.1), a lot of care was taken in the fiber-SiPM-alignment.

Alignment in transverse direction

A simulated spatial distribution of photons impinging on a SiPM after exiting a 250 μm thin squared fiber is shown in Fig. 6.24. Taking into account that the optical grease has a refractive index of $n = 1.465$, a transmission efficiency which is flat in the region between 280 nm and 700 nm and that the SiPM's silicone resin window has a refractive index $n = 1.41$, the Monte Carlo simulations show that the active area illuminated by a squared fiber of 250 μm thickness has a size of $750 \times 750 \mu\text{m}^2$ [42]. In the case of the SiPM active area being $1.3 \times 1.3 \text{ mm}^2$, this means that one can afford transverse displacements of the fiber axis with respect to the active area's center of $\approx 300 \mu\text{m}$ in either direction; larger shifts imply light losses.

The fibers were either glued to a plexiglass frame (Prototype V4.1), or they were glued to a plexiglass endplate (Large Prototype). The frame / endplate possesses four precision peg holes, which are echoed on the PCB onto which the SiPMs were soldered. The plexiglass groove / endplate hole together with the precision pegs provide an alignment accuracy of $\mathcal{O}(100) \mu\text{m}$ of the PCB with respect to the fiber support. The next step consisted in aligning the SiPM on the PCB, because the position of the SiPM's active area with respect to the center of its ceramic packaging features an important tolerance of $\pm 250 \mu\text{m}$ [55]. It is possible to adjust the SiPM position thanks to the fact that usually the SiPM's pins are not tightly clamped by the PCB pin holes but are somewhat able to move. In order to determine the appropriate alignment of the SiPM, a plexiglass mask with alignment holes indicating the fiber positions and four precision peg holes matching the ones from the fiber endplate and the PCB was used. The alignment holes have a diameter of 1.8 mm, which corresponds approximately to the size of a circle circumscribing the square of the active area ($\sqrt{2} \cdot 1.3 \text{ mm} \approx 1.8 \text{ mm}$). The alignment procedure then is as follows:

1. Place all SiPMs on the PCB (putting all of them at once assures that the surface defined by the SiPMs is approximately planar);
2. Mount the plexiglass mask on top of the SiPMs using the precision pegs and make sure it is flush with the surface of the SiPMs (see Fig. 6.25a));
3. View a single SiPM under a digital microscope and adjust its position such that the alignment hole of the plexiglass encircles the active area as accurately as possible (see Fig. 6.25b));
4. Fix the SiPM with the help of a screw (see also description of the longitudinal alignment below);
5. Repeat steps 3 and 4 until all the SiPMs are aligned;
6. Solder the SiPMs.

A well-aligned SiPM is shown in Fig. 6.25c). A few SiPM could not sufficiently be moved to align them perfectly, as can be seen in Fig. 6.25d).

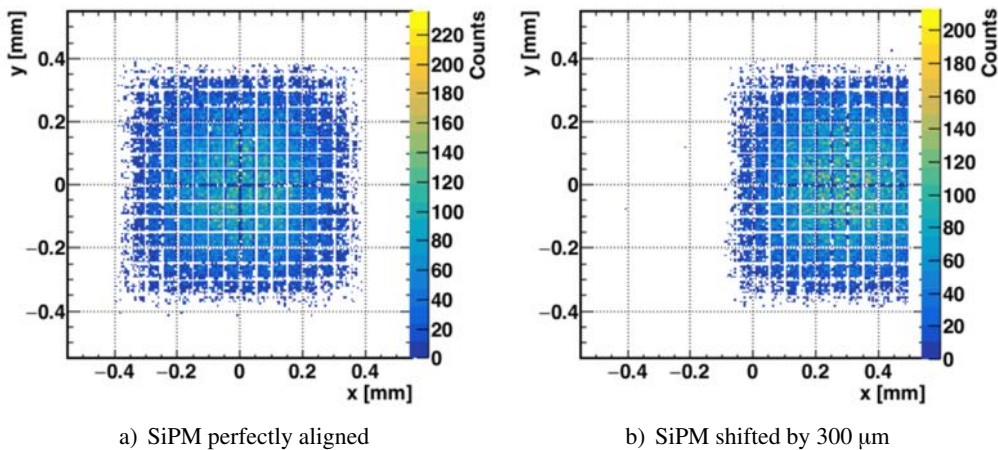


Figure 6.24: Simulated distribution of photons exiting a $250\ \mu\text{m}$ thin squared fiber and impinging on a perfectly aligned and a displaced SiPM of $1 \times 1\ \text{mm}^2$ size, taking into account the effect of the optical grease and the silicone resin window [42].

Alignment in longitudinal direction

As mentioned above, the alignment in the longitudinal direction is roughly guaranteed by placing and fixing all SiPMs with the plexiglass mask prior to the soldering. To ensure that the SiPMs are pressed well against the fiber endplate / frame, every SiPM is neighbored by one or two M2 screws which fix the PCB to the endplate / frame. Any additional misalignments, e.g. due to the SiPM silicone resin window not being flush with the surface of the ceramic packaging, are compensated by the optical grease.

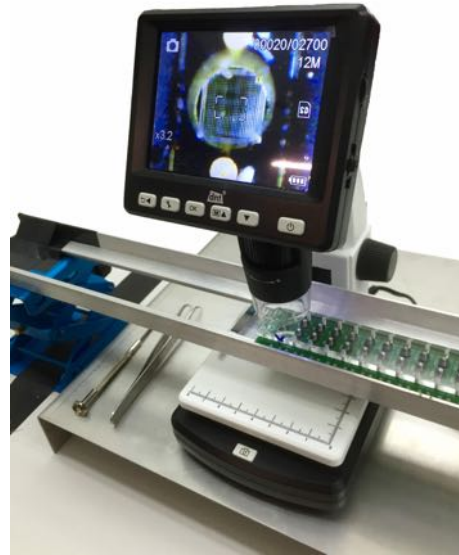
6.4 Front-End Electronics

The preamplifier that was mostly used in the measurements presented here was specifically developed at PSI for the purpose of amplifying SiPMs signals [57]. A picture of the preamplifier and the corresponding electric circuit are shown in Fig. 6.26. It contains two Monolithic Amplifier (MAR)-6 voltage amplifiers and features pole-zero cancellation, which helps to suppress long signal tails, see Fig. 6.27. The preamplifier provides negative signals and a fixed gain of either 20 dB, 30 dB or 40 dB. One disadvantage of the PSI preamplifier is that it is sensitive to magnetic fields due to the inductances and the MAR amplifiers in its circuit. Moreover, the standard preamplifier circuit board occupies a lot of space. In view of the possibility to have an ATAR (see Sect. 4.8.5), a new preamplifier (“Novosibirsk preamplifier”) inspired by the PSI preamplifier and consisting of two stages was developed [58]: a first, compact ($5 \times 6\ \text{mm}^2$) stage to be mounted as close as possible to the SiPMs (e.g. on the US endcap), which is connected to a second amplification board located further away, see Fig. 6.28a). The main motivation of having a first amplification nearby the SiPMs comes from the fact that we want to be able to discriminate the first photoelectron against the noise. The gain of the first and second stage combined

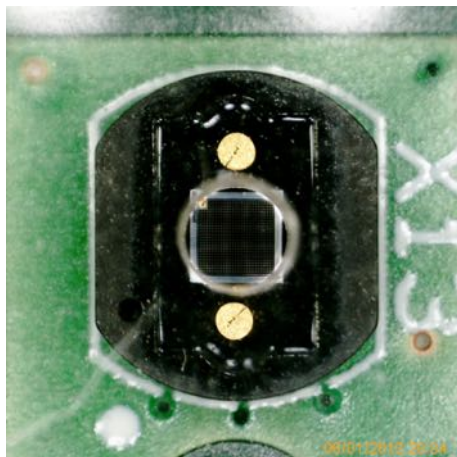
6 R&D of a Scintillating Fiber Detector for Mu3e



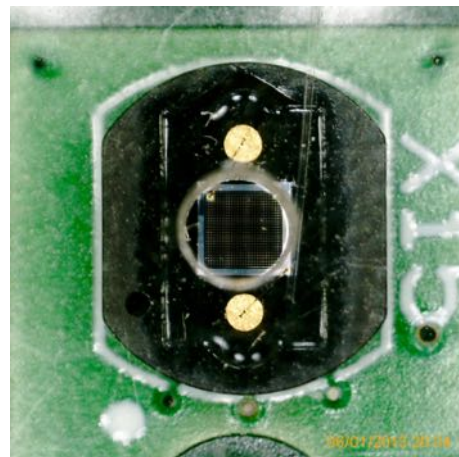
a) PCB with plexiglass alignment mask mounted



b) Digital microscope to align the SiPMs

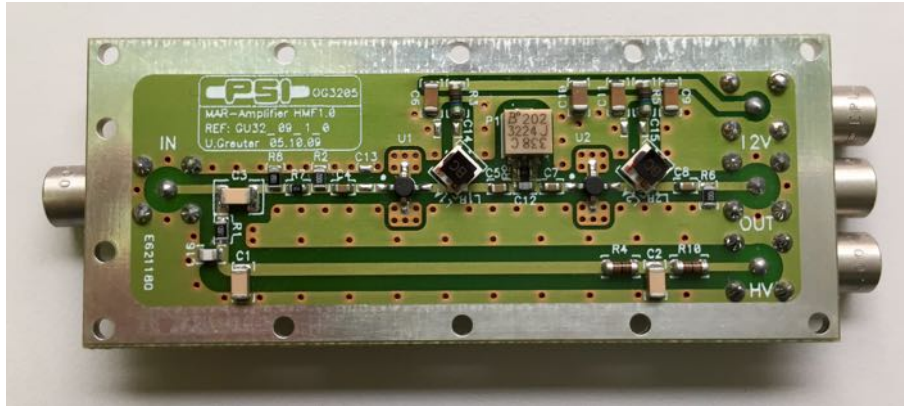


c) SiPM with enough leeway, resulting in a good alignment

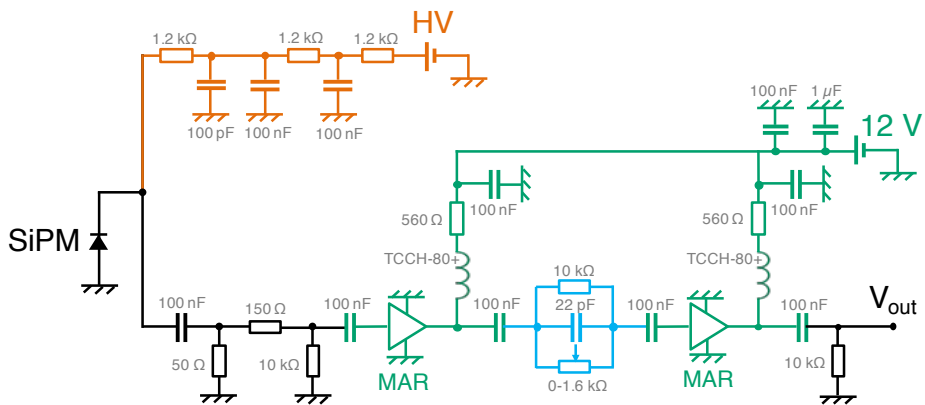


d) SiPM with less leeway, resulting in a poorer alignment

Figure 6.25: Fiber-SiPM-alignment. The top two figures show the tools to align the SiPMs on the PCBs. The bottom two pictures show the comparison between a SiPM which is transversally well-aligned and one which was more difficult to align properly.



a) Picture of the PSI preamplifier



b) Electrical circuit

Figure 6.26: The PSI preamplifier [57], used for most of the measurements presented in this thesis, is shown in a). The preamplifier provides negative signals and a fixed gain of 20 dB, 30 dB or 40 dB. The electrical circuit is given in b). The orange part depicts the high voltage supply, the green part the amplification and the blue part the signal shaping (pole-zero cancellation).

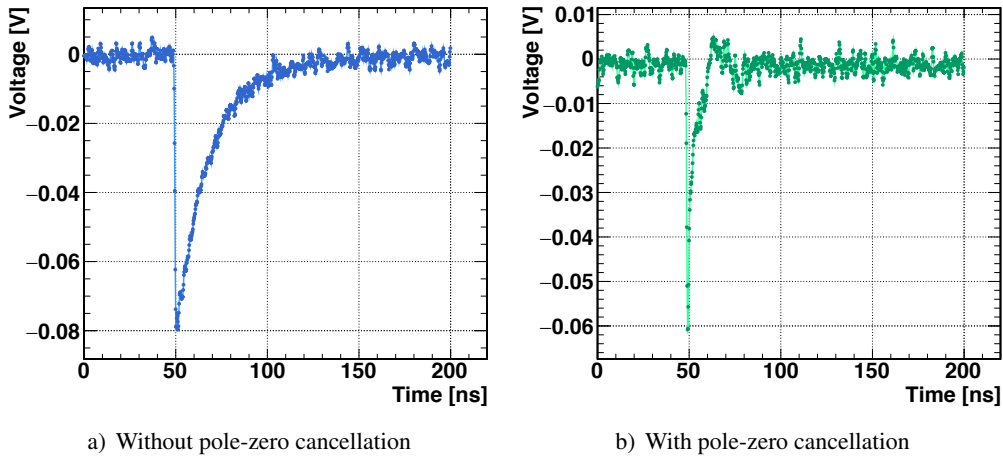


Figure 6.27: Waveforms with and without pole-zero cancellation. The SiPM's pulse duration is reduced from 100 ns to about 20 ns.

corresponds to about 30 dB. The Novosibirsk preamplifier is based on transistors rather than on the MAR amplifiers, making it immune against magnetic field environments. In fact, when operating in the experimental hall, one could clearly observe large gain variations over time for the PSI preamplifiers, whereas the Novosibirsk preamplifiers were much more stable and less noisy, see Fig. 6.28b). In the laboratory however, the two types of preamplifiers behaved equivalently. The amplitude of the first photoelectron for the old and the new SiPM series are shown in Table 6.5.

Table 6.5: Amplitude of the first photoelectron for the old and the new SiPM series when operating them in the standard conditions and connecting them to the preamplifiers described in the text.

Gain	S12825-050C (old)	S13360-1350CS (new)
30 dB	≈ 30 mV	≈ 60 mV
40 dB	≈ 60 mV	≈ 120 mV

6.5 Data Acquisition System

The data acquisition system used in the framework of this R&D was based on the DRS V5 evaluation board [59, 60] shown in Fig. 6.29. The board is equipped with a DRS4 chip described in detail in Sect. 4.6.2, allowing to digitize the channels at a speed between 0.7 GSPS and 5 GSPS with 1024 sampling points. The maximum data acquisition rate is equal to about 600 Hz. It features four analog input channels of 1 V peak-to-peak input range, which are sampled with a depth of 14 bits. The input range can be configured to cover either the range $(-0.5, +0.5)$ V, $(-0.05, +0.95)$ V or $(0, 1)$ V. Typically, a sampling speed of 5 GSPS and a range $(-0.5, +0.5)$ V

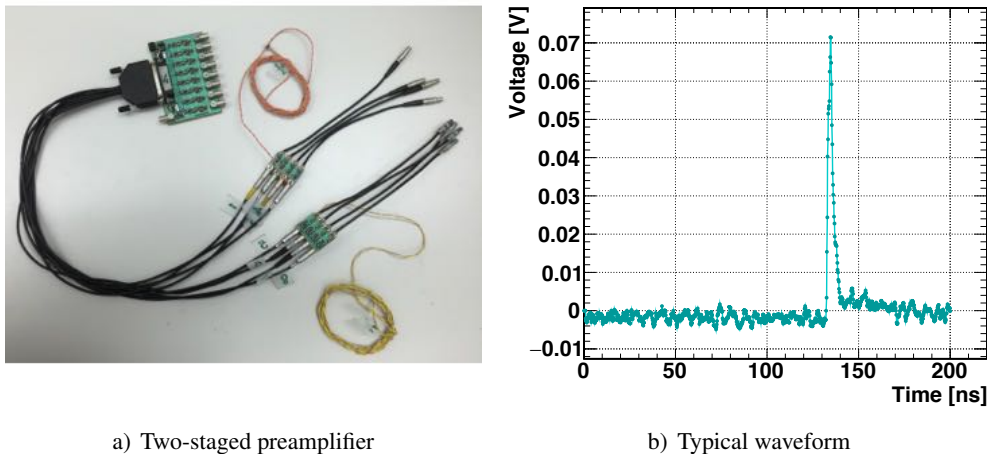
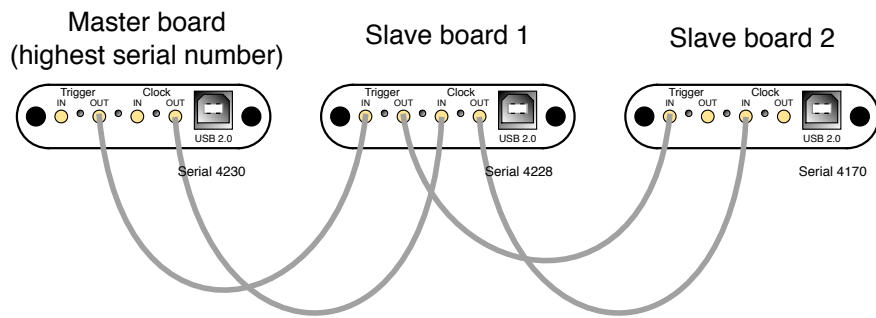


Figure 6.28: Novosibirsk preamplifier [58]. It consists of two stages: A first compact stage (the two small cards in the picture) and a second stage (the big card). It is based on transistors rather than MAR-6 amplifiers, making it immune against magnetic fields (and thus gain variations). The right plot shows a typical waveform of this preamplifier. Compared with the ones displayed in Fig. 6.27, one can also observe a slight improvement in terms of noise.

was used here, since the signals provided by the PSI preamplifier presented in the previous section are negative. Every channel possesses a discriminator with a programmable threshold. These can be used to trigger either on an individual channel or on a simple combination thereof (e.g. on a logical AND of the first, the second and the third channel, or on a logical OR of the first and the second channel etc.). The data is written to disk in the form of raw binary or XML files. The DRS evaluation board allows to board-internally calibrate the DRS4 chip in terms of voltage and timing. After calibrating the voltage, the noise level due to the chip is as low as 0.35 mV (RMS). For the purpose of timing calibration, an internal clock signal is used to determine the effective bin width of every cell, which can differ by up to ± 100 ps from the nominal value of 200 ps when sampling at 5 GSPS. After the execution of the timing calibration procedure, the timing resolution is of few ps (RMS). The DRS evaluation board comes along with a software (“DRS Oscilloscope”) which allows to configure the board, steer the discriminator thresholds, set the trigger logic etc. In addition, the DRS evaluation board features four channels for clock and trigger signals. These allow several boards to be combined in a “daisy chain” mode, such that more than four channels can be digitized. The maximum data acquisition diminishes approximately linearly with the number of evaluation boards. The trigger signal is provided either externally or by the first board (“master”) and propagated to the remaining ones (“slaves”). In the latter case, only the channels on the master board can be used to build the trigger. At a sampling speed of 5 GSPS, the time jitter between channels from different boards is about 400 ps, which is due to the fact that the clock signal propagates through the FPGAs. It can be reduced to about 60 ps by either feeding the clock signal to the designated



a) DRS evaluation board



b) Daisy chain

Figure 6.29: The DRS evaluation board V5 [60] used as DAQ system during the fiber detector R&D. It is based on the DRS4 chip and digitizes four analog input channels. Several evaluation boards can be concatenated into a “daisy chain” to record more than four channels at a price of lower acquisition rate.

channels on the DRS evaluation board, or by attaching a periodic signal (e.g. a sine wave) to one analog input channel on every board and synchronizing them offline.

6.6 Hodoscope Prototypes and Experimental Setup

The following section describes the prototypes used in this thesis, afterwards the detector setup is illustrated in more detail. The last section is dedicated to the description of the waveform analysis.

6.6.1 Prototypes

After gaining experience with several single- and multifiber setups [42], a first telescope prototype referred to as “Prototype Version 4.1” was built, see Fig. 6.30. It consists of seven 250 μm thin squared, multiclad fibers arranged in two layers of three fibers each, plus an extra fiber for

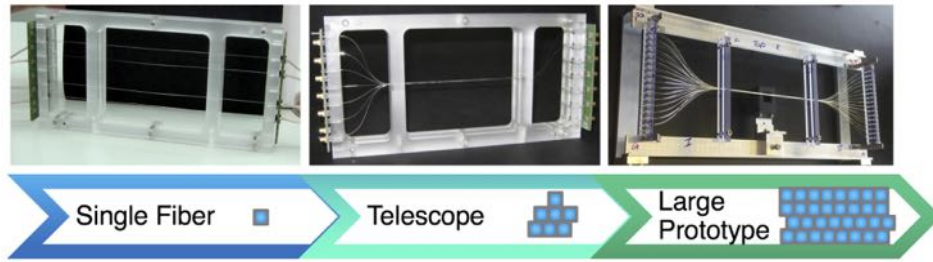


Figure 6.30: Prototype history: The R&D started off with the study of a single fiber, proceeded with the construction of a telescope (“Prototype Version 4.1”) made of seven fibers and culminated in the “Large Prototype” consisting of 32 fibers.

triggering purposes. All fibers are read out individually, adding up to 14 channels. Every fiber is coated with 100 nm of aluminum deposited by physical vapor deposition (see Sect. 6.1.3). Later on, a very similar prototype was constructed in an upscaled version (“Large Prototype”), shown in Fig. 6.31. It features four layers consisting of eight 250 μm fibers each, with a total of 32 fibers. The purpose of the first layer is to act as trigger for the following three layers, which model a part of a Mu3e hodoscope ribbon. Again, every fiber is read out individually, resulting in 64 channels. Every SiPM was aligned with its fiber according to the procedure described in Sect. 6.3.2. The scope of this prototype was to measure what timing resolutions and efficiencies are achievable with one, two and three layers of fibers: the individual fiber readout allows to study in detail the detector behavior, having also the liberty to combine the channels offline so as to mimic a SiPM array readout (see also Sect. 6.8). Once assured that the mechanics allowed a sufficiently good alignment of the fiber with respect to the SiPM, two additional prototypes were built: (1) a beam monitoring tool described in detail in Sect. 7.1 and (2) a prototype comparing different kind of fiber samples, which we have already encountered in Sect. 6.8.

6.6.2 Standard Setup

A typical setup is drawn in Fig. 6.32. The fiber prototype was placed inside a light-tight box. The SiPM board’s outputs were connected via Lemo cables to the preamplifiers located outside the box. The high voltage was fed by an Array 3645A series DC power supply, where usually the SiPMs which were mounted on one PCB board were all biased with the same voltage. The signals provided by the preamplifiers (either 30 or 40 dB, depending on the situation) were sent to the DRS evaluation board inputs. The SiPMs were calibrated one-by-one offline, which was possible thanks to the waveforms being recorded by the DRS. The standard trigger consisted in the coincidence of three channels, namely two SiPMs connected to one particular fiber and an “external trigger”. The external trigger helped to reject dark count events and served as a calorimeter to select MIPs. It was mounted just behind the fibers in line with the beam / collimated source, and was available in two versions:

- A $4 \times 4 \times 18 \text{ mm}^3$ scintillator (BC400) cuboid coupled to a SiPM (Hamamatsu S12572-050C) with an active area of $3 \times 3 \text{ mm}^2$. The SiPM signal was sent to a 20 dB PSI preamplifier.

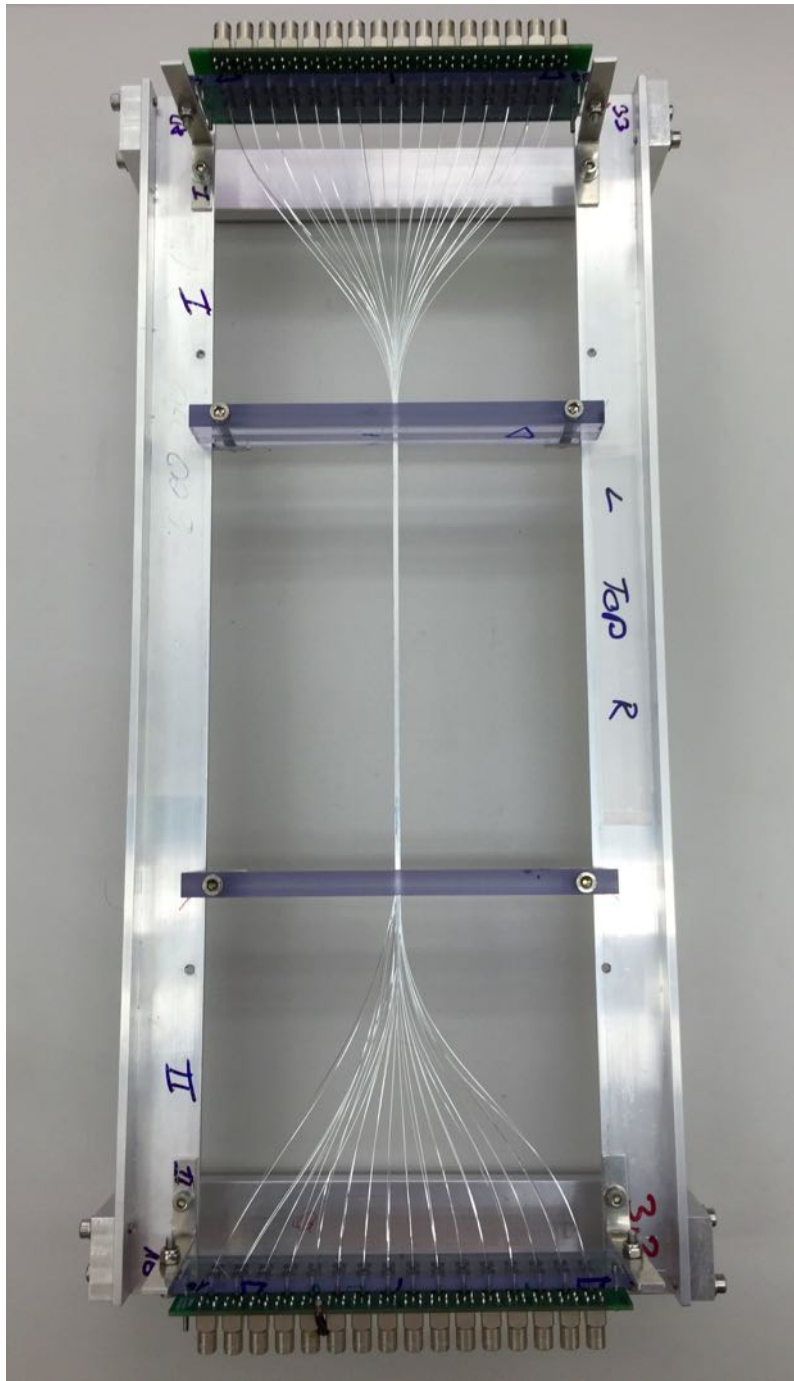


Figure 6.31: The Large Prototype, made of 32 squared, multicladd fibers of 250 μm thickness. Every fiber is coated with 100 nm of aluminum and read out individually by a SiPM on each of its ends.

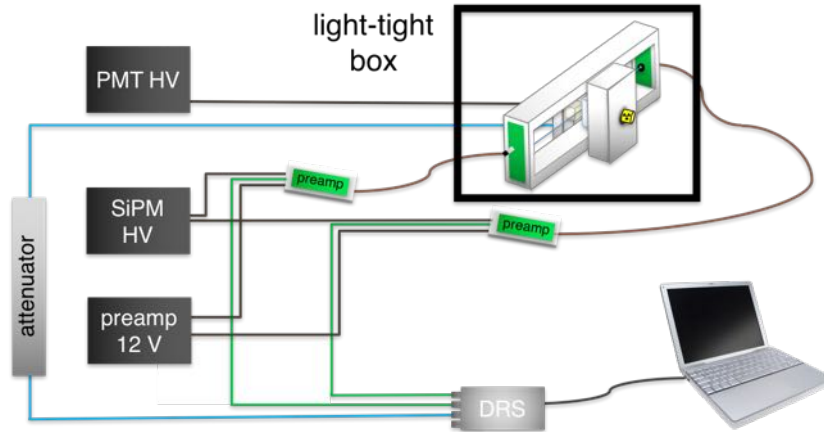


Figure 6.32: Sketch of the laboratory setup.

- A $18 \times 18 \times 23 \text{ mm}^3$ scintillator (BC400) cuboid coupled to a PMT (Hamamatsu R7600U).

Usually, the external trigger's signal required some attenuation to match the voltage input range of the DRS evaluation board.

In the case of tests concerning the timing performance of the detector for which several channels on different daisy-chained DRS evaluation boards were involved, a 25 MHz sine wave provided by a function generator (Stanford Research Systems DS345) was attached to one input of every board in order to reduce the time jitter between the DRS boards (see also Sect. 6.5).

Laboratory Setup

For the laboratory tests, the prototype was placed inside a light-tight, wooden box covered with copper and revetted with black cloth, as shown in Fig. 6.33a). A ^{90}Sr source with an activity of 1.9 MBq was utilized to irradiate the fibers. ^{90}Sr undergoes β -decay with a half-life of 28.5 y to ^{90}Y and the emission of an electron with an endpoint energy of 546 keV. The ^{90}Y β -decays in basically 100% of the cases to ^{90}Zr with a half-life of 64 h while giving off an electron with an endpoint energy of 2.28 MeV. The radioactive source was housed in a plexiglass collimator of 2 cm thickness. The standard collimator had a hole of rectangular cross section with a size of $1 \times 1 \text{ mm}^2$. Other collimators with sizes of $0.25 \times 0.25 \text{ mm}^2$, $0.5 \times 0.5 \text{ mm}^2$ and $0.75 \times 0.75 \text{ mm}^2$ were used, too, on certain occasions. The collimator was fixed to a linear three-axis translation stage (Thorlabs PT3/M) which can travel 25 mm in all three directions with a distance reading unit of $10 \mu\text{m}$. In order to accurately evaluate the performance of the fiber detector, only the MIP (particles with an energy $E > 1.5 \text{ MeV}$) should be considered. For that purpose, the external trigger was mounted in line with the collimated source in order to select the appropriate particles.

Beam Test Setup

Apart of course from the particle source and the light-tight box, the setup for tests in the accelerator beams was identical to the one in the laboratory. The prototype was placed inside a box made

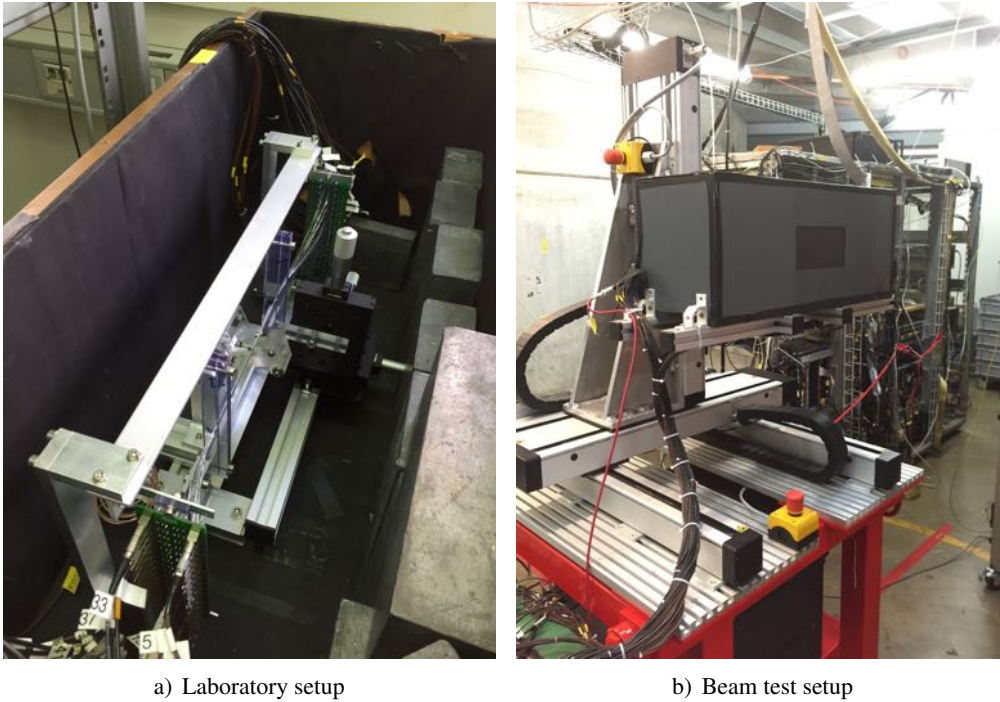


Figure 6.33: Pictures of the standard setup in the laboratory and at the beam line. In the laboratory, the fiber prototype is placed inside a light-tight, copper-covered box. When measuring at a beam line, the prototype is housed in a plastic box with a beam entrance and exit window made of Tedlar[®] foil mounted onto a scanner system.

of PVC (opaque plastic) featuring a beam entrance and an exit window made of a $25.4\ \mu\text{m}$ thin foil of Tedlar[®], which is a light-tight, dark gray polyvinyl fluoride foil. The prototypes were usually mounted onto a scanner system, see also Fig. 6.33b). A dedicated LabView software allowed to move the detector along the x -, y - and z -direction and was able to perform an automated scan of the beam (it is the same system that is used to do the measurements with the pill counter, which is the standard beam monitoring tool at PSI's beam lines, see also Sect. 7.1.1). In order to distinguish the different kinds of particles present in the beam (e.g. positrons, muons, pions) by time-of-flight, the RF sinusoidal signal of the proton cyclotron's accelerating cavities was recorded, too, see Sect. 7.2.2 for an example.

6.6.3 Waveform Analysis

All waveforms were recorded and written to a binary file, which was analyzed by a custom-made, ROOT-based [61] C++ program. In a first step, the program reads the first 1000 events' waveforms and creates a waveform template for every channel. From this template, the integration window to be used for the analysis of all the waveforms is calculated channel by channel: After having determined the position of the signal peak t_p , a Gaussian with a width σ (RMS) is fitted to the rising part of the pulse shape and an exponential decay with a time constant τ to the

falling part of the pulse. The integration window is then given by the interval $[t_p - 6\sigma, t_p + 3\tau]$. In a second step, all the events are analyzed, extracting the corresponding waveforms' charge, time and amplitude. This is done by first computing the pedestal of the waveform under consideration according to the following procedure: calculate the RMS of the first 100 sample points (≈ 20 ns at 5 GSPS) and the second 100 sample points of the waveform around their corresponding means. The mean of the 100 samples with the smaller RMS is defined to be the pedestal of that particular waveform⁸. After having subtracted the pedestal, the charge is computed by integrating the waveform over the time window determined in the first analysis step. The waveform's timing is calculated by applying a constant fraction discrimination, for which the threshold $V_{thr} = c \cdot V_A$ is calculated waveform-specifically as being a certain percentage ("fraction" c , here 20 %) of the signal amplitude V_A .

6.7 Results

The first three sections present the most important studies performed with the Large Prototype, namely the measurement of the light yield, the detection efficiencies and the timing resolutions. The fourth section is dedicated to the temperature dependence of the performances, and the last section discussed the fiber alignment.

6.7.1 Light Yield

In order to assess the amount of light detected by 250 μm thin fiber coupled to SiPMs upon the passage of a (minimum ionizing) particle, the Large Prototype was tested at the πM1 channel at PSI (see Sect. 2.3.2). The beam, which irradiated the fibers perpendicularly with respect to their central axes, was composed of e^+ , μ^+ and π^+ with a momentum of $p = 115$ MeV/c. At this momentum, 90 % of the particles are positrons, the remaining 10 % are approximately evenly split between muons and pions. The total beam rate of 1.75×10^6 particles / s at a proton current of 2.2 mA and the beam size $(\sigma_x, \sigma_y) = (6.6 \text{ mm}, 9.4 \text{ mm})$ was measured with a pill counter, which consisted of a BC400 scintillator cylinder (with a diameter of 2 mm and a length of 2 mm) coupled to a PMT. In order to separate the three kind of particles, the signal of the external trigger (the one with the PMT, see Sect. 6.6.2) and the RF signal from the proton accelerator were digitized, too. For these runs the Novosibirsk preamplifiers were used, because they performed better in the experimental area due to their insensitivity to magnetic fields (see Sect. 6.4) and provided charge spectra with a much clearer separation between the photoelectron peaks. It was verified that the average number of photoelectrons measured with the Novosibirsk preamplifiers and the PSI preamplifiers were equivalent.

The light yield of an individual fiber was evaluated in two different configurations: On the one hand by combining the two SiPMs in a logic AND (both SiPM should detect a signal), on the other hand in a logic OR (at least one of the two SiPMs should detect a signal), both with the threshold set at 0.5 photoelectrons⁹ (0.5 Phe). This offline trigger logic is sketched in Fig. 6.34.

⁸The reason to consider two different regions of the waveforms and its corresponding RMS is to avoid to have accidental signals within the window which is used as a basis to calculate the pedestal.

⁹Hence "detecting a signal" means that the SiPM sees at least one photon.

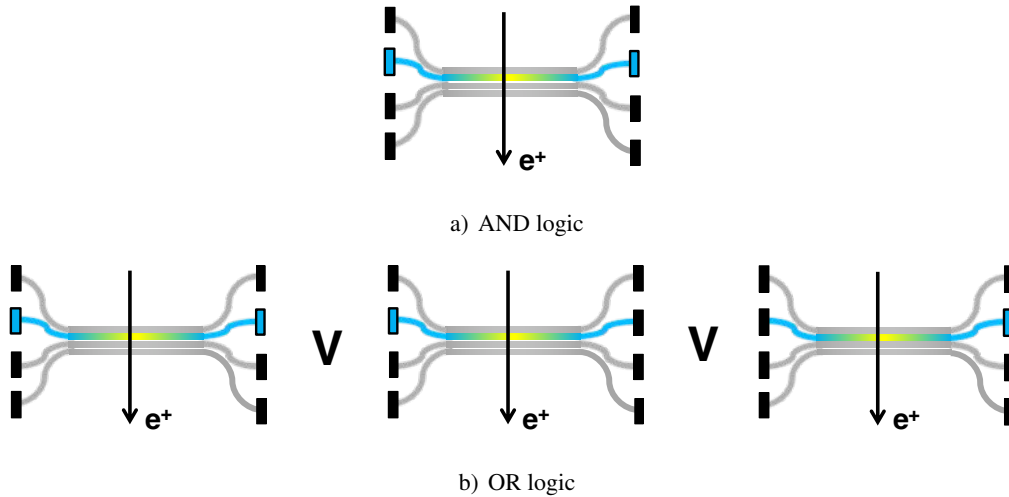


Figure 6.34: Sketch of the two offline trigger configurations. The logic AND requires that both SiPMs attached to the fiber under consideration detect a signal, the OR logic that at least one of the two SiPM detects a signal.

The corresponding coincidence window is determined by the channels' individual waveform integration ranges described in Sect. 6.6.3. A typical charge spectrum of a fiber for the two logic configurations is shown in Fig. 6.35. Through the course of this thesis we will refer to the number of photoelectrons as the mean of such a charge histogram. Perhaps it would be more meaningful to quote the most probable value of those distributions, but it was not possible to come up with a satisfyingly stable fit procedure to determine it.

The detector showed a uniform response in terms of light yield, except for a few outliers, as can be seen from Fig. 6.36. On average, the fibers measured a mean number of photoelectrons of 4.6 (AND logic) and 3.7 (OR logic) when considering the positrons only. Excluding the two outliers, the standard deviation from these two values amounts to 0.25 Phe. The outliers were associated to fibers which were located at the edges of a layer and which were expected to perform a little worse because during the glueing process, a part of their aluminum coating and / or cladding came off. The typical variation observed when considering one particular fiber on a longer timescale or in a different hardware trigger condition was at the level of 0.15 Phe.

Angle Measurements

The effect of having inclined tracks through the fiber detector was studied in the laboratory by irradiating the Large Prototypes with the ^{90}Sr source from different θ - and ϕ -angles, as illustrated in Fig. 6.37. The position of the source collimator was adjusted with the help of a ruler and a simple goniometer. The setup was not always easy to handle due to space constraints, so the values for the angles reported here are not strictly quantitative. A non-zero θ -angle leads to an increased path length inside the individual fibers with the consequence of an increased light yield, which was clearly visible, see Fig. 6.38. At an angle of $\theta \approx 45^\circ$, the average number of photoelectrons increased from 4.8 to 6.2, which is consistent with the expectations. For tracks

6 R&D of a Scintillating Fiber Detector for Mu3e

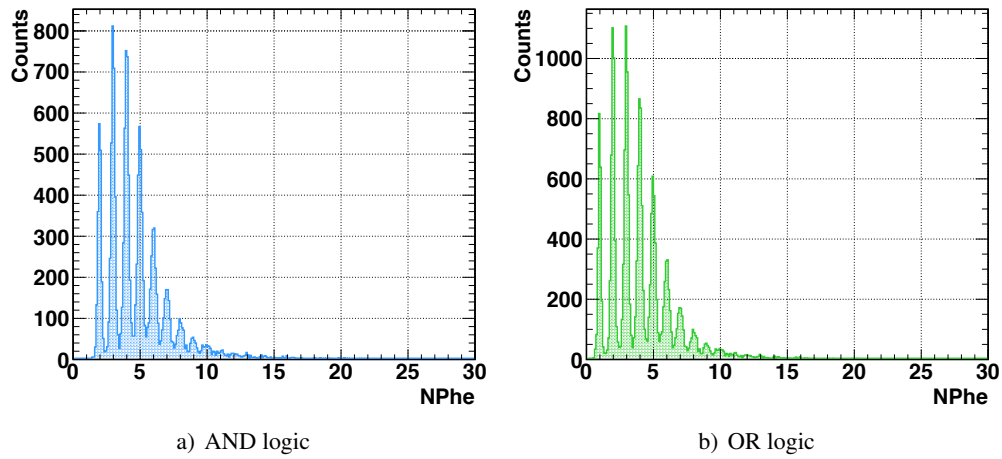


Figure 6.35: Typical charge spectra for the two offline SiPM logic configurations AND and OR with the threshold at 0.5 Phe.

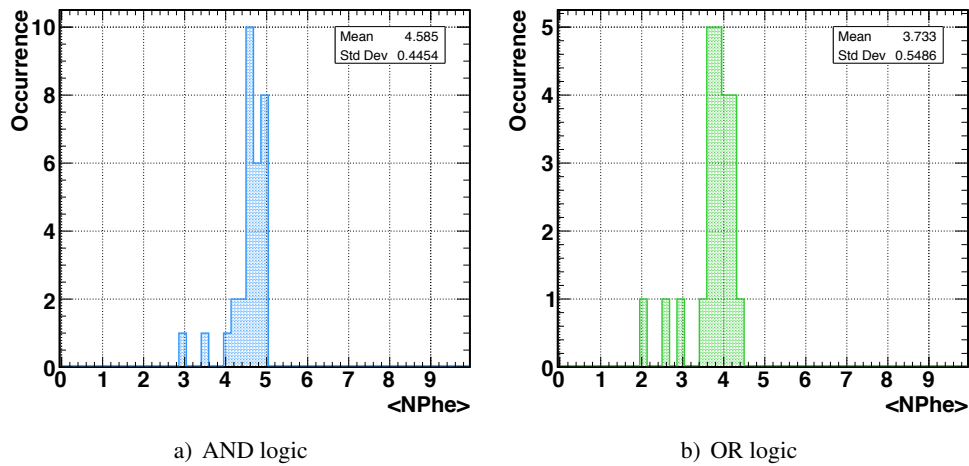


Figure 6.36: Average light yield detected upon the passage of a positron in the two SiPM logic configurations AND and OR at a threshold of 0.5 Phe. These histograms have 31 entries, corresponding to 31 out of the Large Prototype's 32 fibers. The vertical axis shows the number of fibers which measured an average number of photoelectrons $\langle \text{Nphe} \rangle$ on the horizontal axis. On average, the fibers measured a mean number of photoelectrons of 4.6 (AND logic) and 3.7 (OR logic). The corresponding standard deviations without the outliers amount to 0.25 Phe.



a) Rotation of the source around the θ -direction b) Rotation of the source around the ϕ -direction

Figure 6.37: Sketch of the two measurements involving inclined tracks by rotating the source around the θ - and the ϕ -direction.

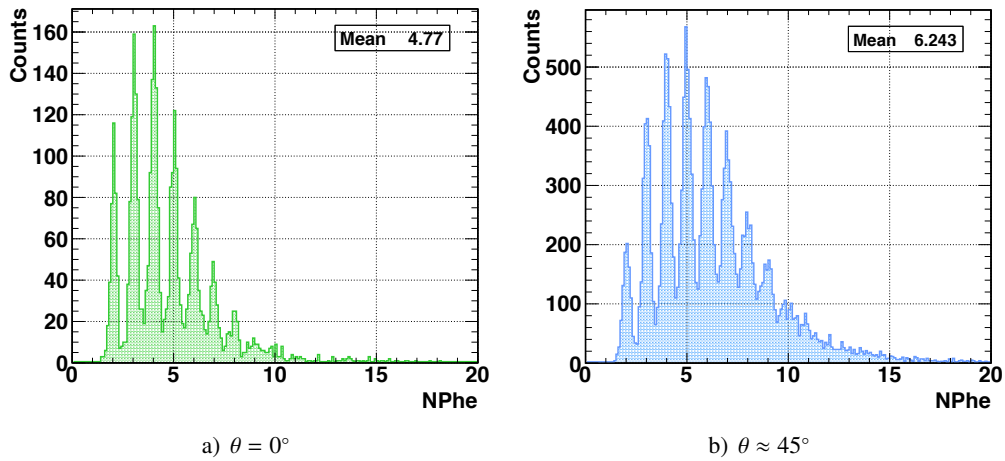


Figure 6.38: The light yield increases significantly for a non-zero θ -angle.

impinging at a non-zero ϕ -angle, no net increase of the light yield is to be expected, since the average path length is about the same as in the case of normal incidence. However, different ϕ -inclinations of course involve different fibers that are hit by the particles. This could also clearly be observed, see Fig. 6.39. Note that for both of these measurements, the trigger had to be put on the fourth instead of the first layer because the particles tended to scatter a lot.

6.7.2 Detection Efficiencies

The detection efficiencies, which are presented in what follows and which are summarized in Table 6.6, were all extracted from the same set of measurements described in Sect. 6.7.1, namely the dataset collected at the π M1 beam line. Only positrons were selected from the beam.

The telescope structure of the Large Prototypes allowed to estimate different kind of efficiencies, which can be categorized into the detection efficiency of the individual fiber and the

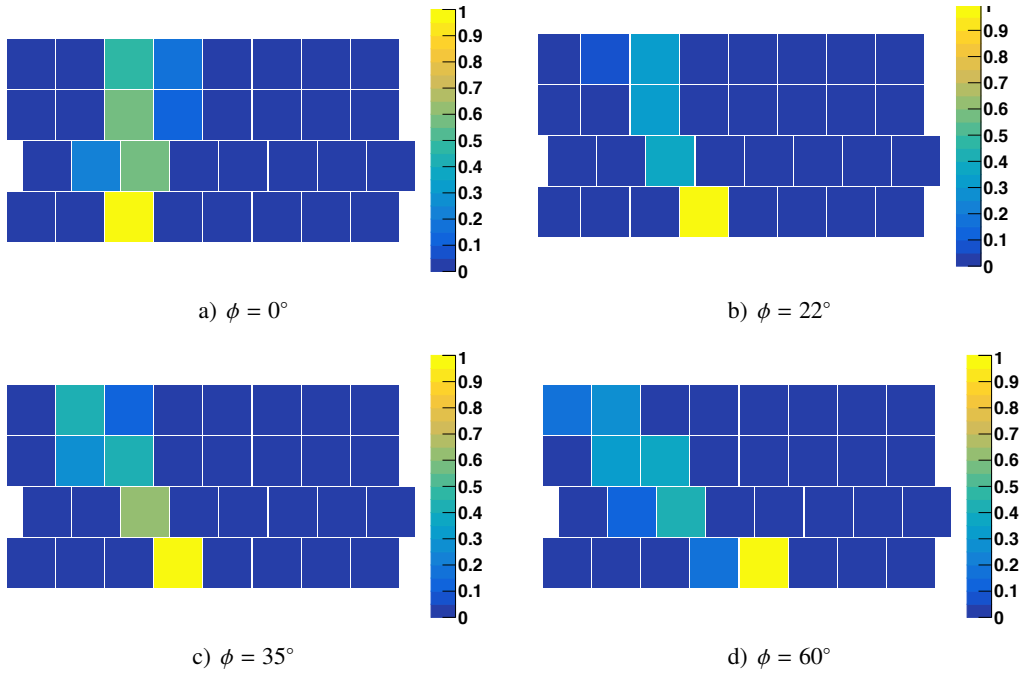


Figure 6.39: Particle tracks observed by the Large Prototype as a function of the inclination angle ϕ . The color scale indicates the number of events involving the corresponding fiber relative to the number of triggered events. The trigger fiber (yellow) lies in the fourth layer.

efficiencies related to multiple fiber layers. In general, the detection efficiency ε is defined as the number of events detected by the fiber(s) of interest divided by the number of triggered events, where the trigger is applied offline. An event is defined to be detected if it satisfies the logic AND (or the logic OR, if stated explicitly) of the SiPMs coupled to the fiber under consideration, where the threshold on the calibrated SiPM charge is set at 0.5 Phe (or 1.5 Phe if indicated). The number of triggered events is determined analogously, i.e. requiring the logic AND of the involved fibers' SiPMs with the threshold set at 0.5 Phe.

Note that in order to obtain an even more reliable measurement of the detection efficiencies (especially concerning the multilayers' ones), the Large Prototype should be combined with e.g. a silicon tracker telescope measuring the trajectory of every particle that passes the fiber array.

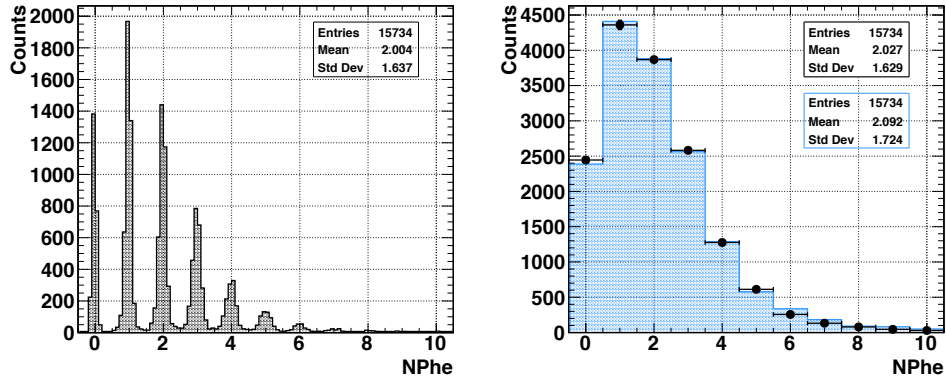
Single Fiber Efficiency

The single fiber efficiency was evaluated by considering several runs with a trigger as shown in Fig. 6.41a). The average MIP detection efficiency was found to be $\varepsilon_{AND}^{single} = 72 \pm 1$ (stat) % for the AND logic and $\varepsilon_{OR}^{single} = 96 \pm 1$ (stat) % for the OR logic, both with a threshold at 0.5 Phe. Measurements with highly ionizing particles such as with surface muons resulted in a detection efficiency which was way higher, namely 97 ± 1 (stat) % (AND logic, 0.5 Phe threshold). The main reason for the MIP detection efficiency not being 100 % lies in working at so low a light level. One can try to do the exercise of taking a measured charge spectrum of a single fiber end attached to a SiPM as shown in Fig. 6.40a) and fit it with a probability distribution given by the convolution of a Landau distribution with a binomial one. The Landau distribution describes the particle's energy deposit and ergo the number of scintillation photons N_{scint} produced, whereas the binomial distribution reflects the probability of detecting N_{Phe} out of N_{scint} photons, given a certain probability p to detect a photon. This probability p is composed of a factor $\approx e^{-L/L_{att,short}}$, due to the fact that the distance L between the location where the scintillation happens and the SiPM corresponds approximately to the short attenuation length component $L_{att,short}$ (see Sect. 6.1.1), and a second factor associated to the PDE of the SiPM (we assume saturation effects to be negligible). As mentioned earlier, it is difficult to find a stable fit procedure to determine the parameters of the Landau and the binomial distribution best describing the data. However, setting by hand the most probable value for the Landau to ≈ 13 photons (consistent with the expected 420 photons multiplied with a 7 % trapping efficiency, resulting in about 15 trapped photons per fiber side) and the probability $p \approx e^{-25 \text{ cm}/20 \text{ cm}} \cdot 40 \% \approx 0.11$, one is able to reproduce the data quite well, as is apparent from Fig. 6.40b). The corresponding probability of not detecting a photon (or more explicitly the weight of the bin with zero photoelectrons) is about 15 %. Consequently, the probability that both SiPMs coupled to a fiber detect at least one photon (AND logic) is $0.85 \times 0.85 \approx 72$ %, and the probability that at least one SiPM is able to detect a signal (OR logic) is $1 - 0.15^2 \approx 98$ %. In that sense, the data is consistent with the expectations.

Multilayer efficiency

The Large Prototype allowed to study also the detection efficiencies of multiple fiber layers. To determine for instance the detection efficiency of two fiber layers, the trigger configuration

6 R&D of a Scintillating Fiber Detector for Mu3e



a) Charge spectrum measured by a SiPM on one fiber end b) Charge spectrum measured by a SiPM on one fiber end (black) with the overlaid probability distribution (blue)

Figure 6.40: The left plot shows a charge spectrum collected by a SiPM on one end of a fiber upon the passage of a MIP. The right plot shows the same charge spectrum with a different binning overlaid with a probability distribution given by the convolution of a Landau distribution (energy deposit and scintillation efficiency) with a binomial one (photon transmission and detection probability). The parameters for the Landau and the binomial distribution which well describe the data are consistent with the expectations.

sketched in Fig. 6.41b) was considered. There, one asks for at least one fiber detecting a signal with the corresponding SiPMs combined in either the AND or OR logic. The average detection efficiency of the double fiber layer amounts to $\varepsilon_{AND}^{double} = 89 \pm 1$ (stat) % for the AND logic and $\varepsilon_{OR}^{double} = 99 \pm 1$ (stat) % for the OR logic, respectively. This is consistent with the expected values of $1 - (1 - 0.72)^2 = 92$ % and $1 - (1 - 0.96)^2 = 100$ %, especially when one keeps in mind that for the trigger configuration shown in Fig. 6.41b), the two layers are staggered with respect to each other, introducing some extra dead material.

The detection efficiency of three fiber layers was evaluated following a similar approach as for the double layer; the trigger configuration is displayed in Fig. 6.41c). The measurements yielded $\varepsilon_{AND}^{triple} = 95 \pm 2$ (stat) % for the AND logic and $\varepsilon_{OR}^{triple} = 98 \pm 1$ (stat) % for the OR logic, respectively. As for the double layer efficiencies, these values are a little lower than the expected $1 - (1 - 0.72)^3 = 98$ % and $1 - (1 - 0.96)^3 = 100$ %. However, these measured values should be understood as lower limits to the detection efficiency since we do not have perfectly under control the particle trajectories, meaning that even though most of the particles should pass through the fiber detector in straight tracks, a few of them might scatter (and can still make it into the external trigger, which is relatively big compared to the fiber dimensions).

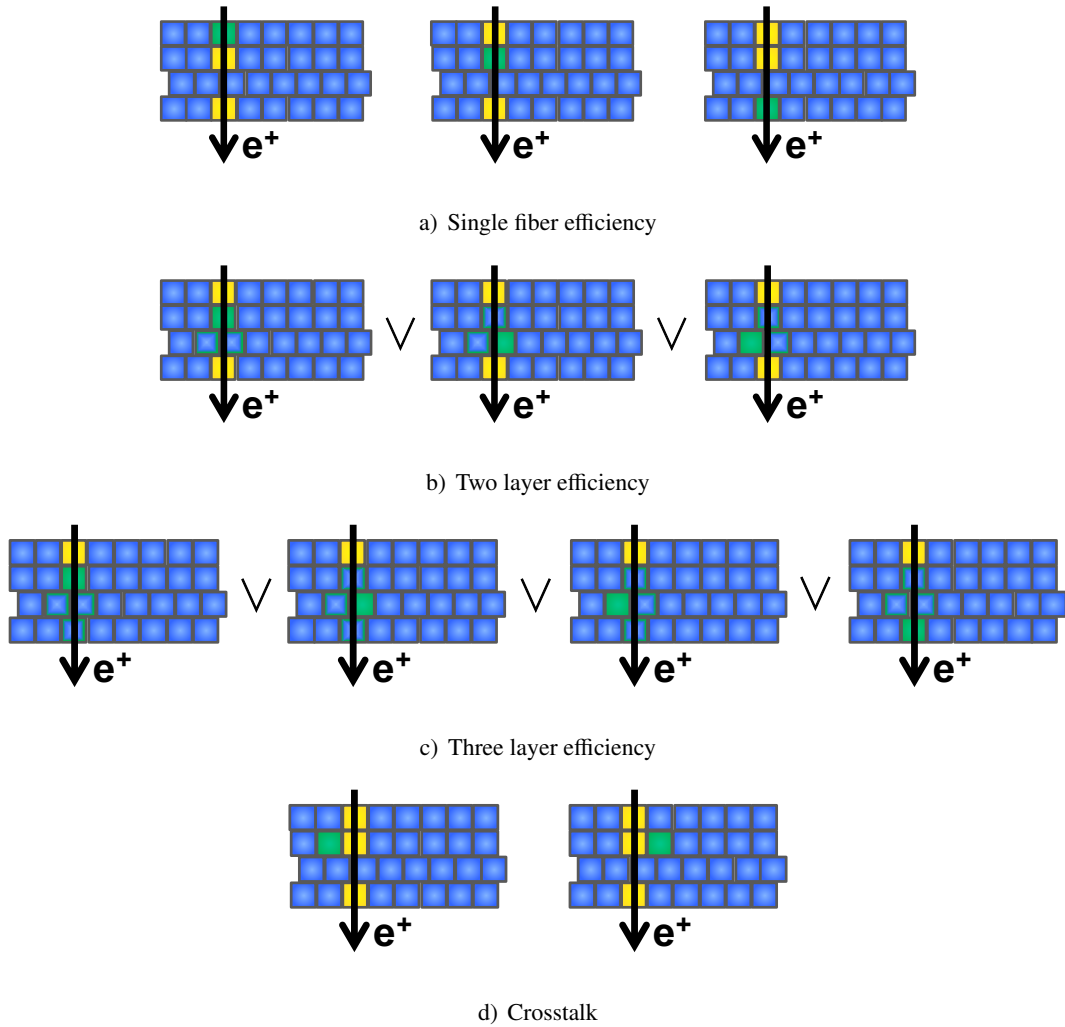


Figure 6.41: Configurations to evaluate the single fiber and multilayer efficiencies as well as the crosstalk. The yellow fibers indicate the ones used as trigger, the green ones the fibers that were under consideration when calculating the single and multilayer fiber efficiency or the crosstalk. The symbol \vee denotes the logic OR.

Table 6.6: MIP detection efficiencies ε_{AND} and ε_{OR} measured by the Large Prototype when triggering at the indicated threshold (0.5 or 1.5 photoelectrons) on the respective SiPMs in the AND and OR logic. The fibers were irradiated perpendicularly to their central axes. The numbers are shown for a single fiber as well as for two and three layers of fibers, where every fiber is read out individually. The errors are statistical.

	Single Layer	Double Layer	Triple Layer
ε_{AND} [%] (0.5 Phe)	72 ± 1	89 ± 1	95 ± 2
ε_{OR} [%] (0.5 Phe)	96 ± 1	99 ± 1	98 ± 1
ε_{AND} [%] (1.5 Phe)	34 ± 1	52 ± 1	67 ± 1
ε_{OR} [%] (1.5 Phe)	79 ± 1	93 ± 1	97 ± 1

Crosstalk

The crosstalk among adjacent fibers was estimated using the trigger configurations shown in Fig. 6.41d). It was found to be less than $< 1\%$ when requiring the logic AND of the two SiPMs and $< 2\%$ when asking for the logic OR, respectively.

6.7.3 Timing Resolution

The timing resolutions described in what follows are summarized in Table 6.7. The single fiber timing resolution was evaluated by considering the distribution

$$T_{single} = \frac{t_1 - t_2}{2}, \quad (6.19)$$

where t_1 and t_2 denote the time extracted from the SiPM's waveform (see Sect. 6.6.3) on the left and the right end of the fiber, respectively. The above defined distribution is described by a double Gaussian, whose corresponding widths (RMS) σ_{core} and σ_{tail} are equivalent to the timing resolution on the mean time $\bar{T} = (t_1 + t_2)/2$. A typical timing distribution measured by a single fiber is shown in Fig. 6.42a). The tails are associated to events in which only few photoelectrons are detected, as can be understood from Fig. 6.42b). Measurements based on the $\pi M1$ dataset described in Sect. 6.7.1 (selecting positrons of 115 MeV/c momentum) yielded a timing resolution of $\sigma_{core} = 682 \pm 7$ (stat) ps and $\sigma_{tail} = 2.23 \pm 0.03$ (stat) ns with a core fraction of $\approx 60\%$ when asking for the logic AND of the two SiPMs (threshold 0.5 Phe), see again Fig. 6.42a). Similar values were measured in the laboratory with the ^{90}Sr source when selecting MIP with the external trigger.

In the case in which a particle traversing the Large Prototype hits more than just one fiber, the mean times of the individual fibers can be combined in order to obtain a more precise timing information, since each fiber acts as an independent detector element. However, the timing resolutions and the core fractions were not observed to improve in the presence of multiple hits, based on the data that were acquired with preamplifiers of 30 dB gain. Intrigued by this unexpected behavior, the timing measurements were repeated in the laboratory with 40 dB PSI preamplifiers, which could not be used during the beam test because they were prone to large

gain variations caused by the environment. For those, an improvement of the timing resolution with an increasing number of involved fibers did indeed manifest. In addition, also the tails were drastically reduced compared to both the Novosibirsk and the PSI preamplifiers with 30 dB gain, as can be seen in Fig. 6.42c). The signal-to-noise ratio (amplitude of the first photoelectron vs. the RMS of the pedestal) was found to be twice as good with the 40 dB PSI preamplifiers compared to the 30 dB PSI preamplifiers. The single fiber timing spectrum measured with the 40 dB preamplifiers is shown again in Fig. 6.43a) in linear scale. The fit of a single Gaussian to the single fiber timing spectrum yielded a timing resolution of $\sigma_{single} = 1.12 \pm 0.01$ (stat) ns (RMS). The combination of the information from two fibers (with the extra index denoting the fiber under consideration)

$$T_{double} = \frac{t_{11} - t_{12}}{4} - \frac{t_{21} - t_{22}}{4}, \quad (6.20)$$

resulted in $\sigma = 820 \pm 3$ (stat) ps, which is consistent with the expectation of $\sigma_{double} = \sigma_{single} / \sqrt{2} = 790$ ps, or if one refers to the single fiber timing distribution's RMS rather than the width of the single Gaussian fit: $\text{RMS}_{double} = \text{RMS}_{single} / \sqrt{2} = 1.16 \text{ ns} / \sqrt{2} = 820$ ps. The corresponding timing distribution is shown in Fig. 6.43b). Similarly, the timing resolution for three fibers, evaluated by computing

$$T_{triple} = \frac{t_{11} - t_{12}}{6} - \frac{t_{21} - t_{22}}{6} - \frac{t_{31} - t_{32}}{6}, \quad (6.21)$$

was found to be $\sigma_{triple} = 673 \pm 4$ (stat) ps, which is also consistent with the expectation of $\sigma_{triple} = \sigma_{single} / \sqrt{3} = 650$ ps or alternatively $\text{RMS}_{triple} = \text{RMS}_{single} / \sqrt{3} = 670$ ps. The corresponding timing distribution is displayed in Fig. 6.43c).

Table 6.7: MIP timing resolutions measured by the Large Prototype when triggering at the indicated threshold (0.5 or 1.5 photoelectrons) on the respective SiPMs in the AND logic and when irradiating the fibers perpendicularly to their central axes. The numbers, which are extracted from single Gaussian fits to the timing spectra, are shown for a single fiber as well as for two and three layers of fibers, where every fiber is read out individually. The errors are statistical.

	Single	Double	Triple
σ_t [ps] (0.5 Phe)	1120 ± 10	820 ± 3	673 ± 4
σ_t [ps] (1.5 Phe)	804 ± 5	608 ± 6	504 ± 6

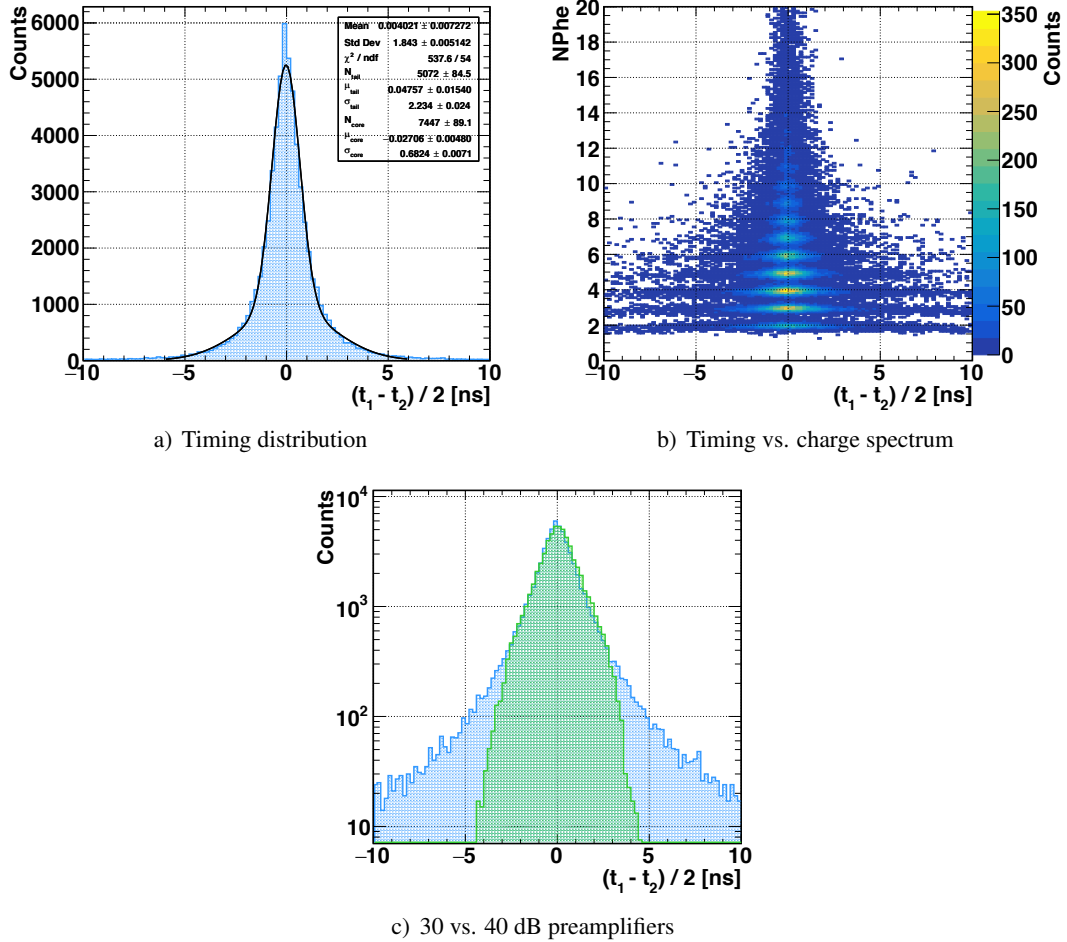


Figure 6.42: The timing distribution shown in a) and fitted with a double Gaussian was measured with a single fiber irradiated by positrons of $p = 115 \text{ MeV}/c$ momentum. The same timing spectrum is shown in b) as a function of the number of photoelectrons. The tails of the timing distribution are associated to events in which only few photons are detected. In c), the timing spectrum measured in the laboratory with 30 dB preamplifiers (blue) is compared with the one measured with 40 dB preamplifiers (green). For the 40 dB preamplifiers, the tails are drastically reduced.

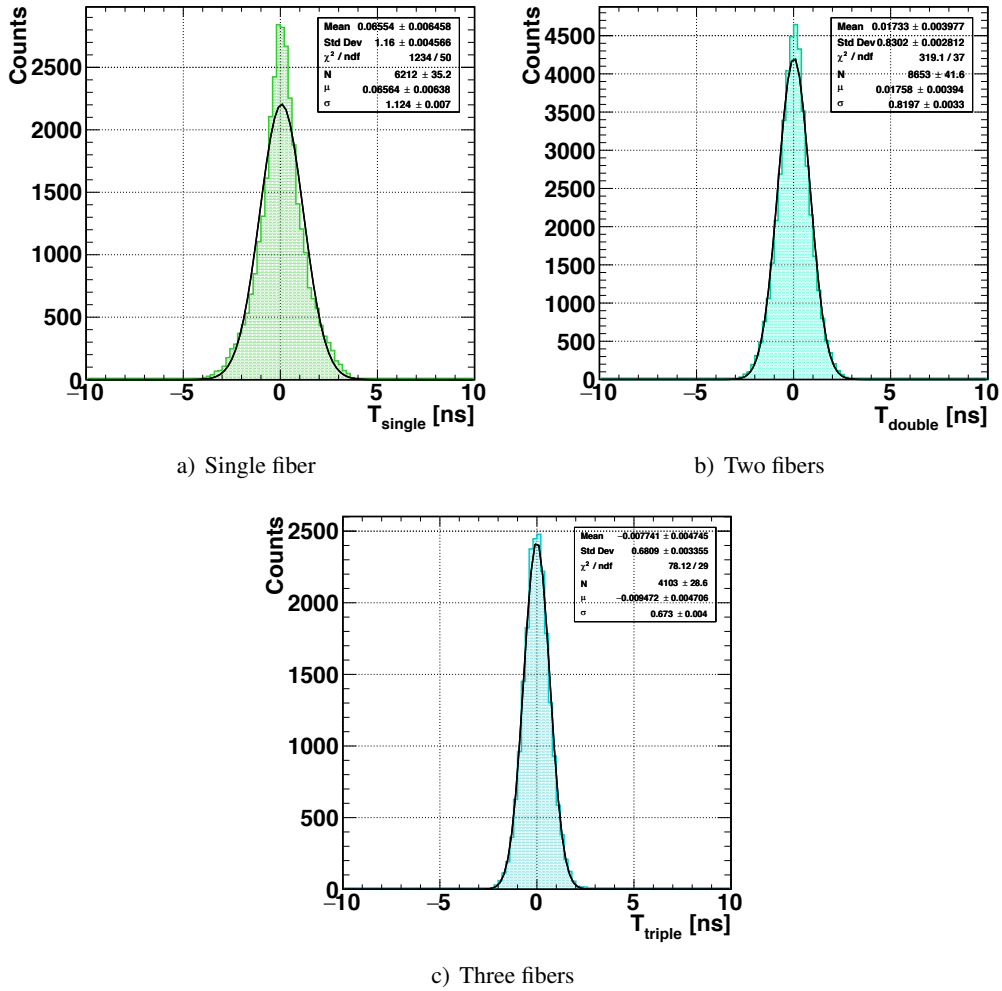


Figure 6.43: Timing distributions measured by a single fiber as well as by combining the information stemming from two and three consecutive fibers. All distributions were fitted with single Gaussians (black lines). These data were taken in the laboratory using PSI preamplifiers with 40 dB (instead of 30 dB) gain.



Figure 6.44: The Prototype V4.1 was placed inside a thermal chamber to study the temperature dependence of the detector response. The temperature was varied between 8 °C and 32 °C.

6.7.4 Temperature Dependence

The temperature dependence of the detector response was studied by considering four channels (i.e. two fibers) of the Prototype V4.1. The fiber setup was placed inside a thermal chamber (Percival I-30NL), see Fig. 6.44. The temperature was set to 8 °C, 16 °C, 24 °C and 32 °C, respectively, with a stability of ± 0.5 °C. In a first step, the SiPMs were studied as a function of temperature and bias voltage. In a second step, the prototype was irradiated with a ^{90}Sr source in the four different temperature conditions while equalizing the gains on a hardware level by extracting the ideal bias voltage working points from the data of the first step. MIPs were selected with the help of the external trigger. As can be seen from Fig. 6.45a), the light yield, after equalizing the SiPM gains, was practically unaltered by the temperature¹⁰. Also the timing did not exhibit any temperature dependence once the gains were equalized: the timing resolution varied by $< 10\%$, see Fig. 6.45b).

6.7.5 Fiber Alignment

The relative alignment of the fibers within the Large Prototype was studied by scanning it with a collimated source. A plexiglass collimator containing the source and featuring a hole with a

¹⁰The careful reader might notice that the mean number of photoelectrons is higher than what was measured with the Large Prototype. This is due to the fact that (1) the fibers were shorter and (2) the SiPMs of the old series featured a higher CTP.

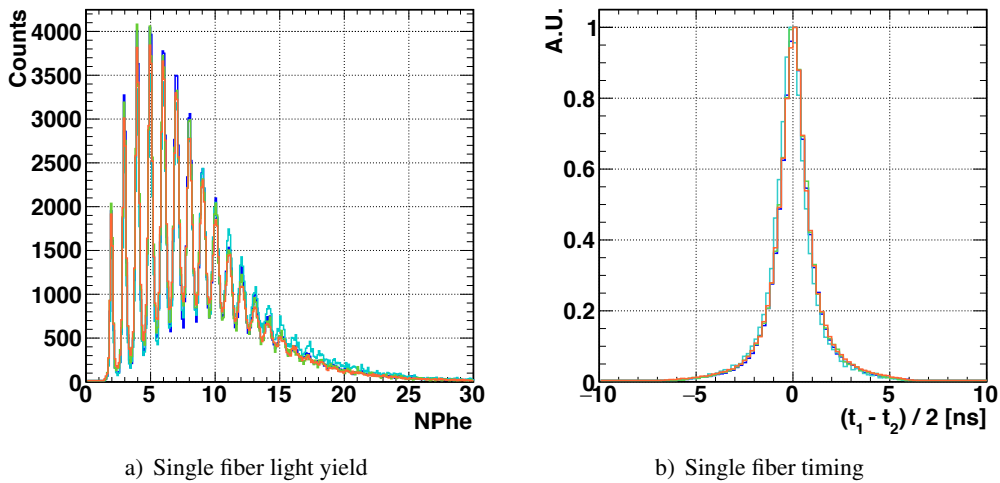


Figure 6.45: Temperature dependence of the light yield (logic AND of the two SiPMs, 0.5 Phe threshold) and the timing of a single fiber for 8 °C (dark blue), 16 °C (light blue), 24 °C (green) and 32 °C (orange) when equalizing the SiPM gains. Once the gains were equalized on a hardware level, the detector’s behavior did not depend on the temperature condition.

cross section of $1 \times 1 \text{ mm}^2$ was moved along the transverse direction y (see also Fig. 6.49 for the definition of the coordinate system), while triggering on the external trigger and measuring simultaneously the hit rate of the individual fibers. The fiber rate was determined by acquiring data with the DRS evaluation board and by counting offline the number of events in which the fiber observed a signal (AND of the two SiPMs, threshold 0.5 Phe), dividing it by the time needed to acquire the data. Note that the fiber rate ($< 20 \text{ Hz}$) as well as the external trigger rate ($< 110 \text{ Hz}$) was far below the DRS evaluation board’s maximal acquisition rate of 600 Hz. The background rate was measured by putting the source into a plexiglass block equivalent to the one of the collimator, but without the hole. The signal-to-noise ratio was found to be ≈ 1000 , so the background was negligibly low. A typical measurement is shown in Fig. 6.46: As the source approaches, the fiber sees more and more of the particle beam exiting the collimator. The curve is well-described by an error function. Assuming that the response of the individual fiber is approximately a unit step function (1 inside the scintillating fiber core, 0 outside the core), the curve’s error function behavior is entirely due to the particle beam’s shape (which therefore is presumably Gaussian). The first, second and fourth layer were all aligned within $20 \text{ }\mu\text{m}$ or better. The third layer is consistently shifted by $\approx 55 \text{ }\mu\text{m}$ towards one direction with respect to the ideal configuration, for which the layer is staggered by exactly half the fiber size compared to the remaining layers. This is coherent with earlier observations concerning the number of tracks passing through either one or the other fiber in the third layer when requiring the passage of a particle through the two outermost layers, compare also for example with Fig. 6.39a). The distance between two neighboring fibers within the same layer was found to be 260 to 270 μm , as expected.

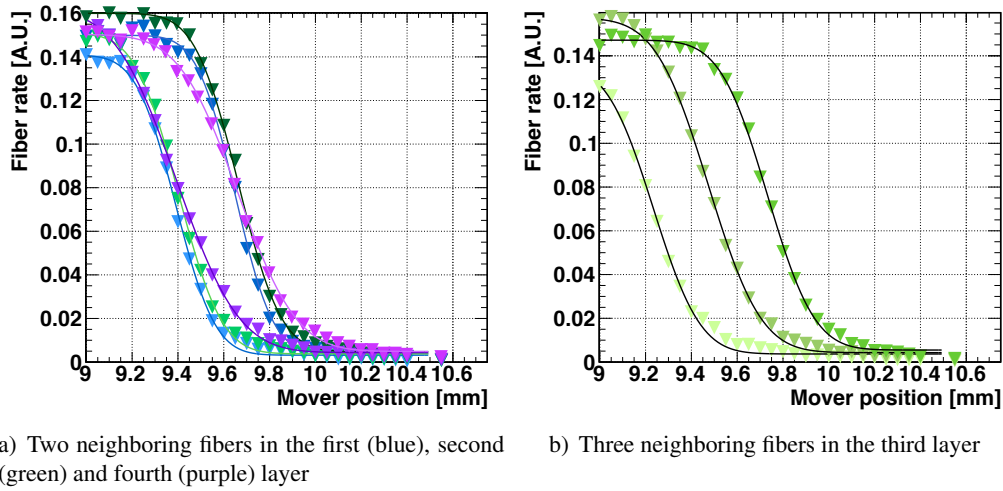


Figure 6.46: Collimator scans to measure the relative alignment of the fibers among a specific layer and among different layers. The horizontal axes of the plots show the collimated source’s position, the vertical axes correspond to the fiber hit rate normalized to the external trigger rate.

6.8 Extrapolation of the Performances to the Final Detector

The baseline design of the Mu3e hodoscope does not foresee an individual fiber readout, but rather a SiPM array, meaning that several fibers are coupled onto a common active area (“channel”) of the SiPM array, see also Sect. 5.3.2. The Large Prototype gave us the possibility to provide a first estimate of the final detector performances by combining the information of several SiPMs, see Fig. 6.47, so as to emulate the situation in which the fibers are coupled to a SiPM array, assuming an “optimal” matching. “Optimal” means that a maximum light collection capability is assured (i.e. having a sufficiently large SiPM active area as well as a good alignment between the fiber and the active area) and that saturation effects are at a negligible level. The results presented in this section are, unless otherwise noted, based again on the positron dataset collected at the π M1 beam line described in Sect. 6.7.1, where the momentum of the particle beam was tuned to $p = 115$ MeV/c.

6.8.1 Light Yield

The charge spectrum, asking for the logic AND and the logic OR of the two “channels” left and right are shown in Fig. 6.48. Each of the two channels contains the information of three consecutive fibers, as displayed in Fig. 6.47. The measurements with the Large Prototype yielded an average number of photoelectrons of $\langle \text{NPhe} \rangle = 10.9 \pm 0.2$ (stat) for the AND logic and $\langle \text{NPhe} \rangle = 10.6 \pm 0.2$ (stat) for the OR logic. In principle, in the experiment the detected light yield should even be a little higher because the tracks will be mostly inclined (see also Sect. 6.7.1) and the fibers will be shorter.

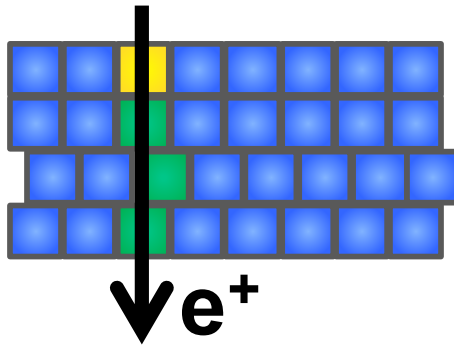


Figure 6.47: Configuration used to emulate the array readout. The yellow fiber indicates the one used as trigger, the waveforms of the SiPMs associated to the green fibers were combined offline (three SiPMs on one end (“left”), three SiPMs on the other end (“right”) of the detector).

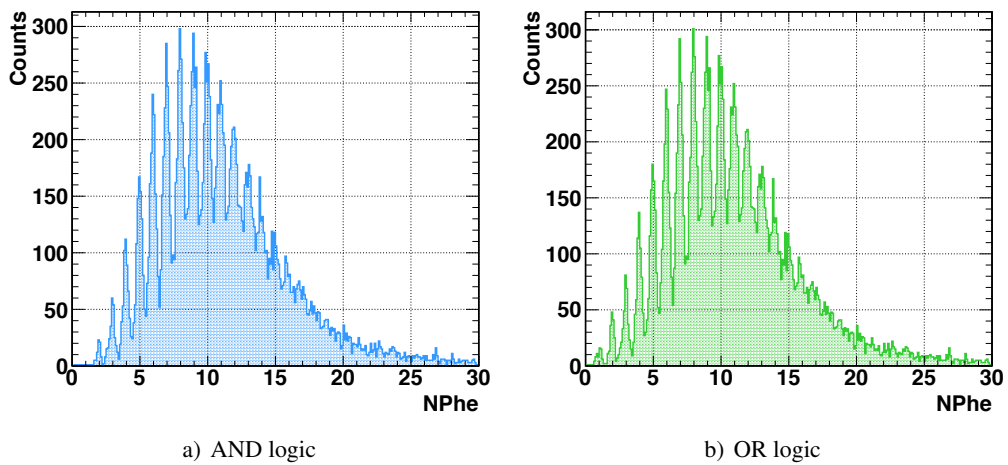


Figure 6.48: Typical offline array charge spectra for the two SiPM logic configurations AND and OR with the threshold set at 0.5 Phe.

6.8.2 Detection Efficiency

The efficiency to detect a MIP requiring the logic AND of the left and the right channel was found to be $\varepsilon_{AND}^{array} = 95.8 \pm 0.2$ (stat) %, and in the case of the logic OR $\varepsilon_{OR}^{array} = 98.3 \pm 0.2$ (stat) % for a threshold of 0.5 Phe. For a threshold of 1.5 Phe, the measurements yielded $\varepsilon_{AND}^{array} = 88.0 \pm 0.3$ (stat) and $\varepsilon_{OR}^{array} = 97.5 \pm 0.2$ (stat) %. The results are summarized in Table 6.8.

Table 6.8: MIP detection efficiencies for the offline SiPM array channel readout combining three consecutive fibers. These efficiencies were measured with the Large Prototype when triggering offline at the indicated threshold (0.5 or 1.5 photoelectrons) on the respective array channels in the AND and OR logic. The fibers were irradiated perpendicularly to their central axes. The errors are statistical.

	Array
$\varepsilon_{AND}^{array}$ [%] (0.5 Phe)	95.8 ± 0.2
ε_{OR}^{array} [%] (0.5 Phe)	98.3 ± 0.2
$\varepsilon_{AND}^{array}$ [%] (1.5 Phe)	88.0 ± 0.3
ε_{OR}^{array} [%] (1.5 Phe)	97.5 ± 0.2

Efficiency vs. Impact Position

Another interesting measurement consists in determining the efficiency of the fiber detector as we move axially along the fiber (x -direction), as shown in Fig. 6.49. The measurement was performed in the laboratory, using a collimated source. The absolute detection efficiency of the Large Prototype is impractical to assess with the ^{90}Sr source because the particles have difficulties in passing the four fiber layers without scattering. So we limited ourselves to the study of the light yield left vs. right, the detection efficiency relative to the central position ($x = 0$) as well as the timing resolution as a function of x (for the timing resolution, see the next section). The threshold on the external trigger was set to a sufficiently high a level so as to select MIPs. The position x was varied in an interval of $[-6 \text{ cm}, +6 \text{ cm}]$ around the approximate center of the fibers, the mechanics of the Large Prototype prevented the study of a wider range. The light yield relative to the central position and the relative fractions measured on the left and the right side of the detector (“array charge”, see Sect. 6.8.1) with respect to the total detected light yield as a function of the impact position x are shown in Fig. 6.50. The absolute light yield did not change significantly; the largest difference between two positions (with the exception of an outlier at 5 cm) amounted to < 10 %. Also the relative fractions of the number of photoelectrons left–right changed only by about 5 % with respect to the central position. The single fiber detection efficiency was evaluated by considering events with a hit in the first, third and fourth layer as trigger, and verifying in how many cases the particles had left a hit in the second layer. The detection efficiency at the most extremal positions (± 6 cm) and the central positions (1 cm, 0 cm, -1 cm) agreed within 6 %. In summary, no drastic changes in the detection efficiency were observed when moving the source along the fiber. This is expected since the fibers are per se quite long (≈ 50 cm) already, and the distance between the source and the fiber end was always

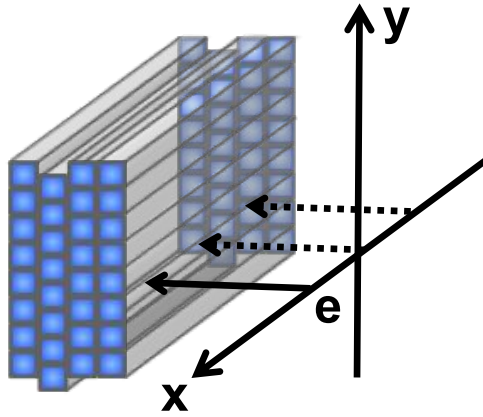
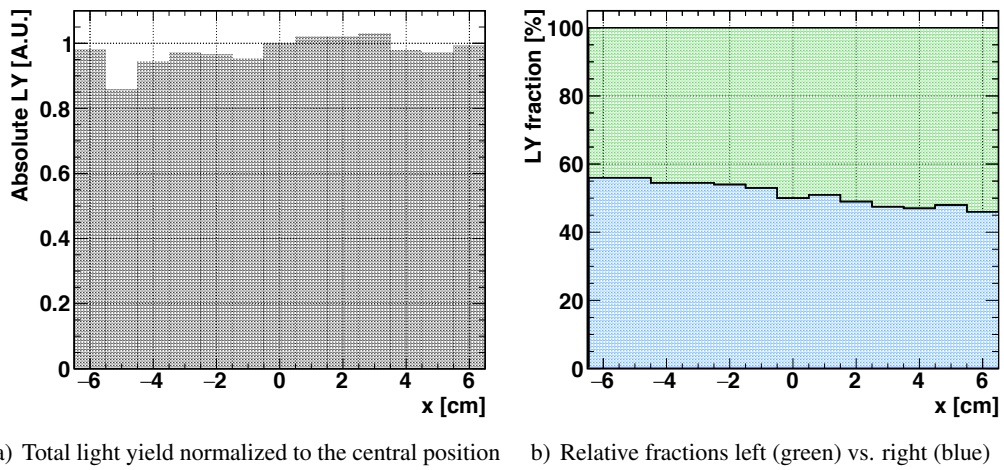


Figure 6.49: Sketch of the scan along the fiber (axial fiber scan).



a) Total light yield normalized to the central position b) Relative fractions left (green) vs. right (blue)

Figure 6.50: Light yield vs. impact position on the fiber.

of the order of the short attenuation length. The distance from the particle's impact position to one of the two fiber ends in the most extremal source positions was about 30 cm. This implies that no big surprises are to be expected in the Mu3e experiment in terms of detection efficiency as a function of the impact position, since the 30 cm correspond to the approximate fiber length foreseen in the baseline design of the Mu3e hodoscope.

6.8.3 Timing Resolution

The timing for the optimized array (see Fig. 6.47) was evaluated by summing offline the waveforms of the concerned SiPMs on the left and the right side of the detector, respectively. The corresponding timing distribution is shown in Fig. 6.51. It is well-described by a double Gaussian resolution with a core width (RMS) $\sigma_{core} = 572 \pm 6$ (stat) ps and a tail width $\sigma_{tail} = 2.36 \pm 0.05$ (stat) ns, where the fraction of the core amounts to $\approx 75\%$. The analogous analysis using a leading edge rather than a constant fraction discrimination yielded $\sigma_{core} = 601 \pm 5$ (stat) ps, $\sigma_{tail} = 2.91 \pm 0.05$ (stat) ns and a core fraction of 76%. Not surprisingly, the two timing methods yield similar values, which is just symptomatic of the fact that very often the signal from which one extracts the time consists of just one photoelectron, because even if more than one photon is detected, they arrive with a certain temporal separation and thus do not produce a waveform with an amplitude equivalent to two or more photoelectrons.

The results obtained with the Large Prototype, which are summarized in Table 6.9, represent an important milestone in the development of the Mu3e fiber hodoscope, because they show that timing resolutions of < 1 ns with a detection efficiency $> 95\%$ are achievable with as little as three layers of 250 μm thin fibers.

Table 6.9: Summary table of the Mu3e fiber detector prototyping described in this chapter. The errors are statistical.

		Single	Double	Triple	Array
σ_t [ps]	(0.5 Phe)	1120 ± 10	820 ± 3	673 ± 4	572 ± 6
σ_t [ps]	(1.5 Phe)	804 ± 5	608 ± 6	504 ± 6	537 ± 5
ϵ_{AND} [%]	(0.5 Phe)	72 ± 1	89 ± 1	95 ± 2	95.8 ± 0.2
ϵ_{AND} [%]	(1.5 Phe)	34 ± 1	52 ± 1	67 ± 1	88.0 ± 0.3

Timing Resolution vs. Impact Position

Next to the light yield and the efficiency, also the timing resolution of the array configuration was studied as a function of the impact position. The largest difference between the array timing resolutions (fitted with a single Gaussian) amounted to 10% within the scanned interval (see Sect. 6.8.2 for details on the scan).

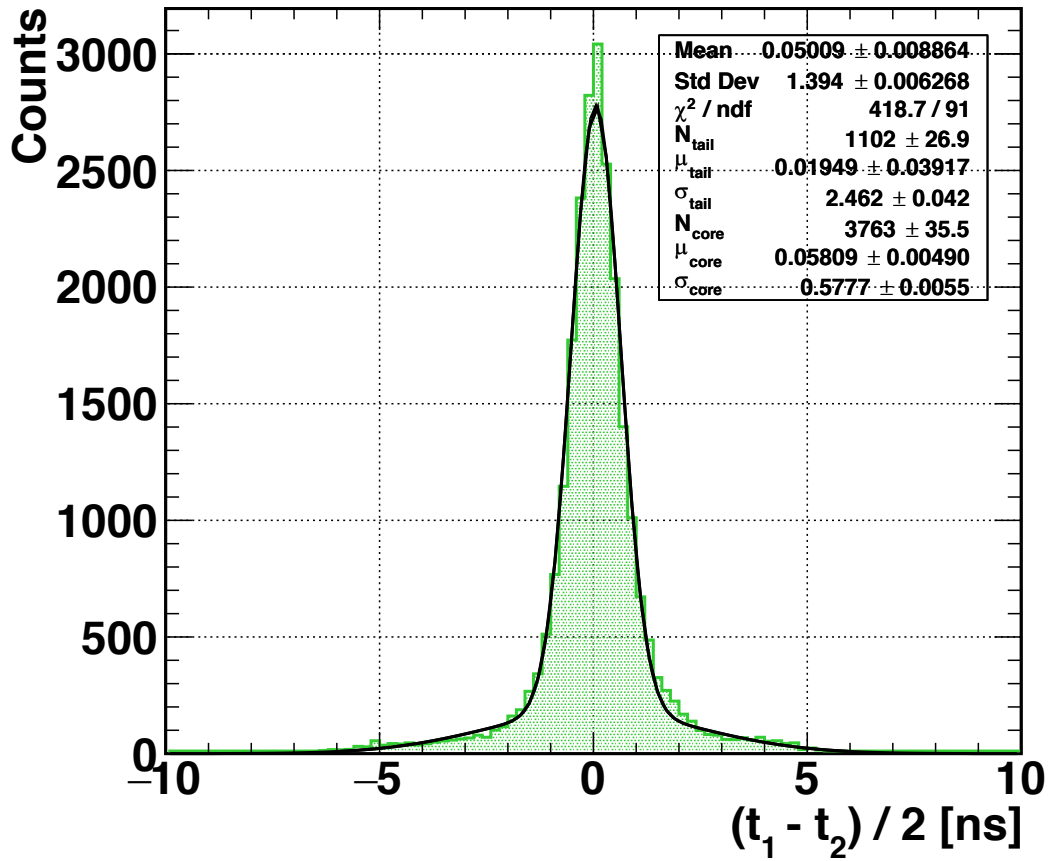
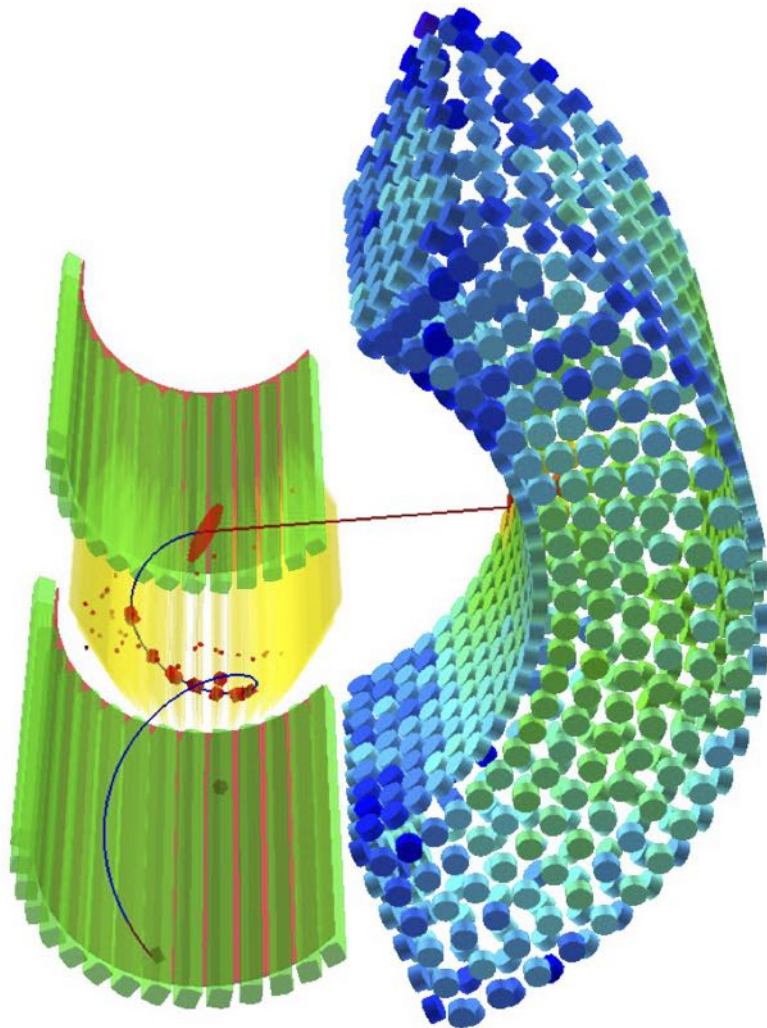


Figure 6.51: Timing distribution for the emulated (“optimized”) array readout, obtained by summing the waveforms of the SiPMs of three consecutive fibers on the left and the right side of the Large Prototype, respectively (see also Fig. 6.47).

Part III

The MEG Experiment

The second part of this thesis is dedicated both to the MEG and the MEG II experiment. It starts off with the description of the results of the R&D activities concerning auxiliary detectors for MEG II based on scintillating fibers, following up the discussion of the previous chapter. Thereafter, the study of a novel calibration method for the MEG / MEG II positron spectrometer based on a Mott scattered positron beam is presented. The last chapter is dedicated to the recently published final result of the MEG experiment.



7 R&D of Auxiliary Detectors Based on Scintillating Fibers

The scintillating fiber technology leaves a lot of freedom in the design of the detector and it provides a magnetic field insensitive, high rate sustaining solution. Apart from that, it opens up the possibility to perform particle identification by charge discrimination or by time-of-flight. Possible implementations of auxiliary detectors based on scintillating fibers have been discussed in Sect. 4.8.5. In the following sections, the R&D for beam monitoring applications and particle identification is presented. Lastly, the issue of radiation hardness is discussed.

7.1 Beam Monitoring

The idea of a beam monitor based on scintillating fibers is to provide a fast, quasi-non-invasive measurement of the beam size and rate, with the possibility to discern positrons from surface muons. Considering a grid composed of 250 μm thin fibers with a pitch of a couple of mm, most of the particles can pass the beam monitor without being disturbed, and the few particles that traverse the fibers do not lose too much energy, such that notably the muon stopping efficiency of the MEG target is minimally compromised.

A first test of a scintillating fiber detector as a tool to measure the beam profile and rate had been performed with the prototype V4.1 presented previously in Sect. 6.6.1. In the later course of the R&D, a dedicated prototype (“beam monitor prototype”) was constructed. The following paragraphs describe the setup and the results obtained with the beam monitor prototype.

7.1.1 Experimental Setup

The beam monitor prototype, displayed in Fig. 7.1, consists of two orthogonal layers with 21 aluminum coated, 250 μm thin squared multiclاد BCF-12 fibers (Saint-Gobain Crystals) each, where the fibers have a length of 20 cm and are spaced by 5 mm within a layer. The two layers are separated by a 2 mm gap and cover a common area of $10 \times 10 \text{ cm}^2$. The upstream layer’s fibers are oriented along the y -axis, such that this layer measures the profile in x . The fibers of the downstream layer are oriented along the x -axis, hence measuring the y -profile. Every fiber is read out on both ends by a SiPM from Hamamatsu (S13360-1350CS), resulting in 84 channels. The design of the endplates and the PCBs carrying the photosensors is completely analogous to and partially recycled from the Large Prototype (see Sect. 6.6.1). The fiber grid is cased in a cylindrical, light tight structure (built to be used in air). Both the US and DS beam window of the cylinder have an aperture of 13 cm and consist of a 25.4 μm thin Tedlar foil (see Sect. 6.6.2), guaranteeing light tightness with little material.

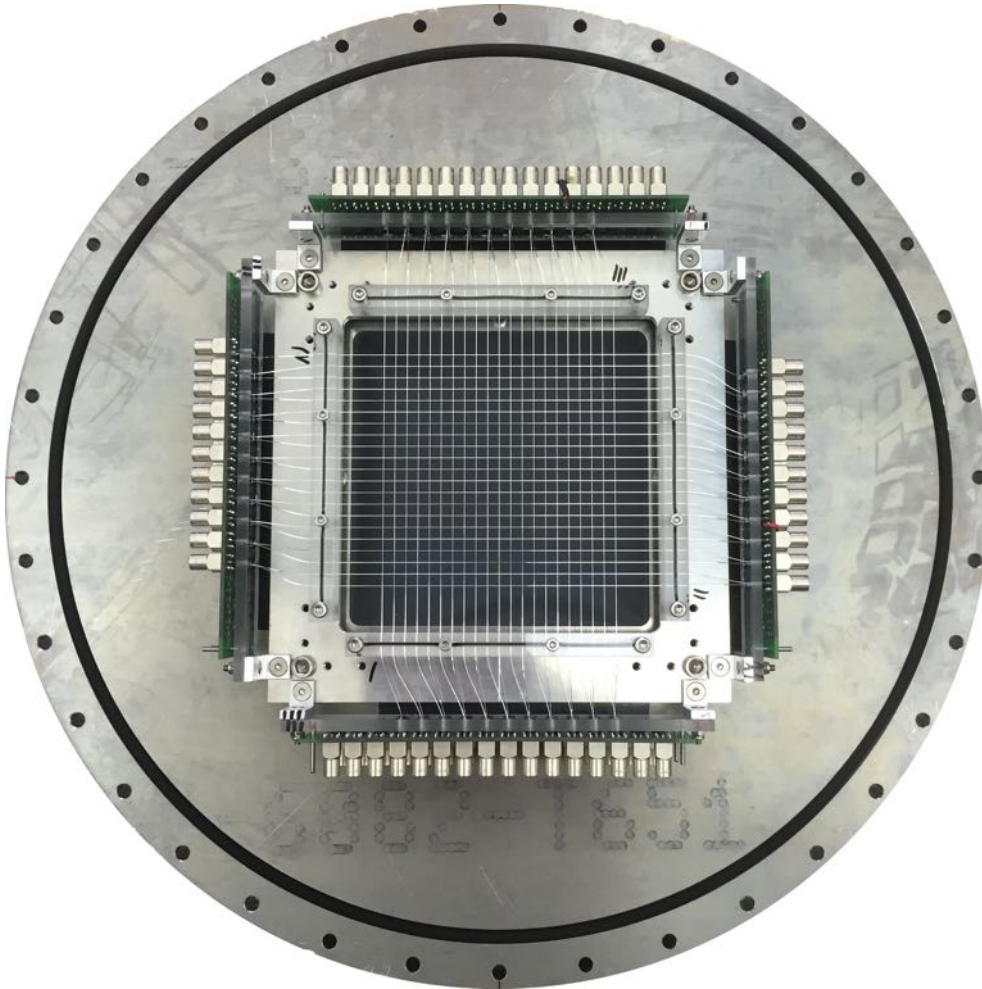


Figure 7.1: Scintillating fiber beam monitor prototype. The beam monitor prototype consists of two orthogonal layers with 21 aluminum coated, 250 μm thin squared multicladd fibers each, where the fibers have a length of 20 cm and are spaced by 5 mm within a layer. Every fiber is read out on both ends by a SiPM, summing up to 84 channels.

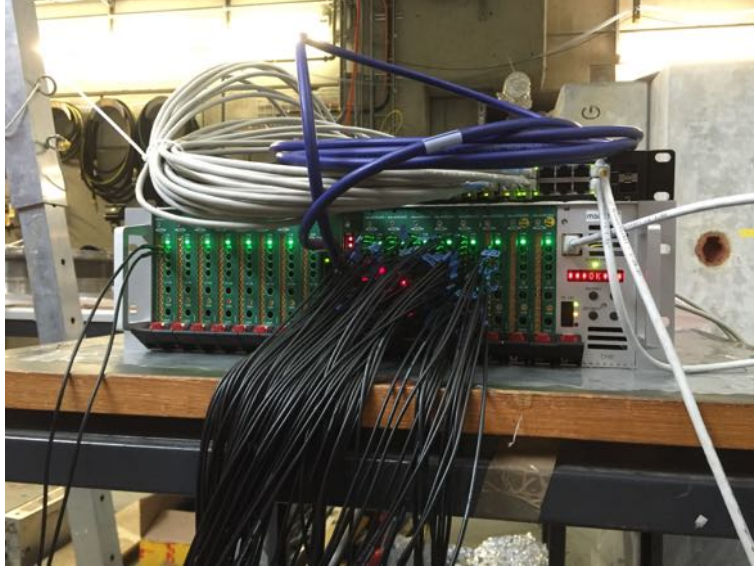


Figure 7.2: Crate with sixteen WaveDREAM boards used for the fiber beam monitor beam tests.

The beam monitor was tested with a prototype version of the final electronics, more specifically with one prototype WaveDREAM crate shown in Fig. 7.2 and the trigger system. The WaveDREAM boards digitize the waveforms based on the DRS4 chip and provide the SiPM bias voltage as well as the signal amplification and shaping, see Sect. 4.8.4. The beam monitor's 84 SiPMs were all directly attached to the WaveDREAM input channels and individually biased with their own operation voltage provided by the data sheet. The gain was set to 40 dB with pole-zero cancellation and with a voltage input range of $(-0.5, +0.5)$ V. The sampling speed was fixed at 2 GSPS. The trigger thresholds were set to a common level for all channels. The trigger system allowed to trigger on the logic OR of the fibers' left-right-coincidences (in other words: trigger on the logic OR of the logic AND of two SiPMs belonging to the same fiber). In addition, every fiber had a corresponding scaler counting the number of times that it triggered.

The beam monitoring system was tested in MEG's experimental area $\pi E5$ (see Sect. 2.3.1 and 4.2), tuning the beam momentum to $p = 28$ MeV/c. The target support was mounted on a tripod and was installed just downstream of the collimator system at a distance of 5 cm from the 190 μm Mylar beam window, see Fig. 7.3. In order to have a reference measurement, PSI's Muon Beam Group operated in parallel a pill counter mounted on a moving stage. The pill consisted of a cylindrical piece of NE102A plastic scintillator of 1 mm radius and 2 mm thickness coupled to a PMT. It was placed at a distance of 6 cm downstream of the fiber detector support. Because the beam was approximately focused at the point where the fiber detector was located, the non-zero beam divergence implicated an enlarged beam size at the position of the pill, such that the comparison in the situations in which both detectors were present was rather qualitative than quantitative. A more quantitative measurement was performed right after the removal of the fiber detector by installing the pill at the spot where the beam monitor stood, adding also a foil of Tedlar as for the fiber beam monitor support's beam window.

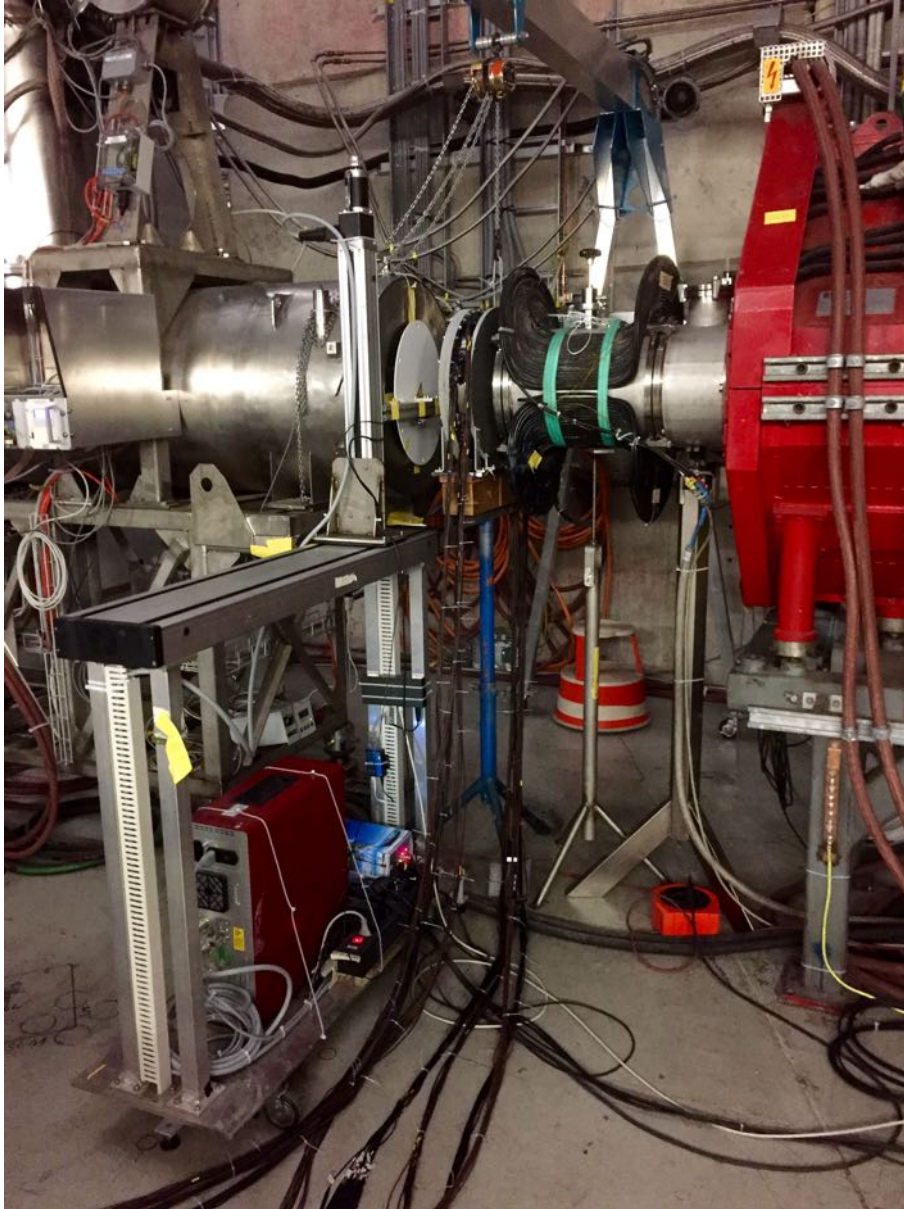


Figure 7.3: Setup of the beam monitor prototype in $\pi E5$. The beam monitor prototype's support was mounted onto a tripod (blue) and placed 5 cm downstream of the collimator system. At a distance of 6 cm from the beam monitor support, a pill counter was installed on a scanning system in order to have a reference measurement. The red magnet on the right is the last magnet of the second quadrupole triplet, the solenoid on the left just downstream of the pill counter is the BTS (see also Sect. 4.2).

7.1.2 Results

The following paragraphs present the results concerning beam profile and rate measurements as well as the measurement of the residual range in Mylar.

Beam Profiles and Rates

An example of a beam profile in x and y in the standard conditions (threshold at 0.5 photoelectrons) is shown in Fig. 7.4a) and 7.4b). The scaler values were read back every ten seconds, such that the beam profile could be monitored in time, see Fig. 7.4c). One can nicely see how the drops in proton beam current shown in Fig. 7.4d) are reflected in the temporal progression of the measured muon beam profile. The rate of the central fibers amounted to 450 kHz when running at $\approx 8 \times 10^7 \mu^+ / \text{s}$ and with the cyclotron providing¹ a proton beam current of 1.7 mA. This is consistent with a rough back-of-the-envelope calculation. The combination of the information from the x - and y -profile into a 3D plot is shown in Fig. 7.5.

The beam profiles are well-described by Gaussians, with the respective sigmas (RMS, “beam size”) being 18.05 ± 0.01 mm in x and 17.78 ± 0.01 mm in y . The measurement performed with the pill at the location where the fiber beam monitor stood gave a $\approx 2\%$ and $\approx 4\%$ smaller beam size for x and y , respectively. The beam rates were extracted separately from the x - and from the y -profile. The grid which was located more US (the one measuring the x -profile) consistently measured a higher rate, where the difference fluctuated in the range between 0.5% and 1.5%. In absolute terms, the first layer of the fiber detector measured a rate of $R_\mu = 1.11 \pm 0.01$ (stat) $\times 10^8 \mu^+ / \text{s}$ when normalizing to a proton current of 2.2 mA. This is very close to the value of $R_\mu = 1.13 \times 10^8 \mu^+ / \text{s}$ at 2.2 mA proton current obtained with the pill counter when performing a simple cross-scan (i.e. scan the beam along the x -axis and along the y -axis). A more accurate, but also more time-consuming raster-scan (scanning a grid with 5 mm step size), yielded $R_\mu = 1.20 \times 10^8 \mu^+ / \text{s}$ at 2.2 mA proton current. In conclusion, it is fair to say that the measurements of the fiber detector and the pill agree well.

As an exercise, the beam was changed by manipulating the beam line magnet currents and the separator settings. Alterations in the current of the second triplet’s last quadrupole for example resulted in a defocused beam, well visible in Fig. 7.6. Shifts in the beam position caused by changes of the separator’s magnetic field were also clearly visible, see Fig. 7.7. All of these changes could be traced in real-time.

Positron beam profiles and rates were measured with the Prototype V4.1 and were found to be consistent with the pill counter measurements after correcting for the MIP detection efficiency.

Range Curve

In addition to the beam profiles, a measurement of the surface muons’ range in Mylar was performed using the central fiber of the beam monitor’s first grid layer. For that purpose, the fiber hit rate was measured as a function of the Mylar thickness added in front of the detector, resulting in a range curve. The range curve is approximately given by a cumulative Gauss distribution, where the width of the corresponding Gaussian reflects the straggling (i.e. statistical fluctuation

¹A problem with the SINQ target prevented the facility to run at 2.2 mA at that time.

7 R&D of Auxiliary Detectors Based on Scintillating Fibers

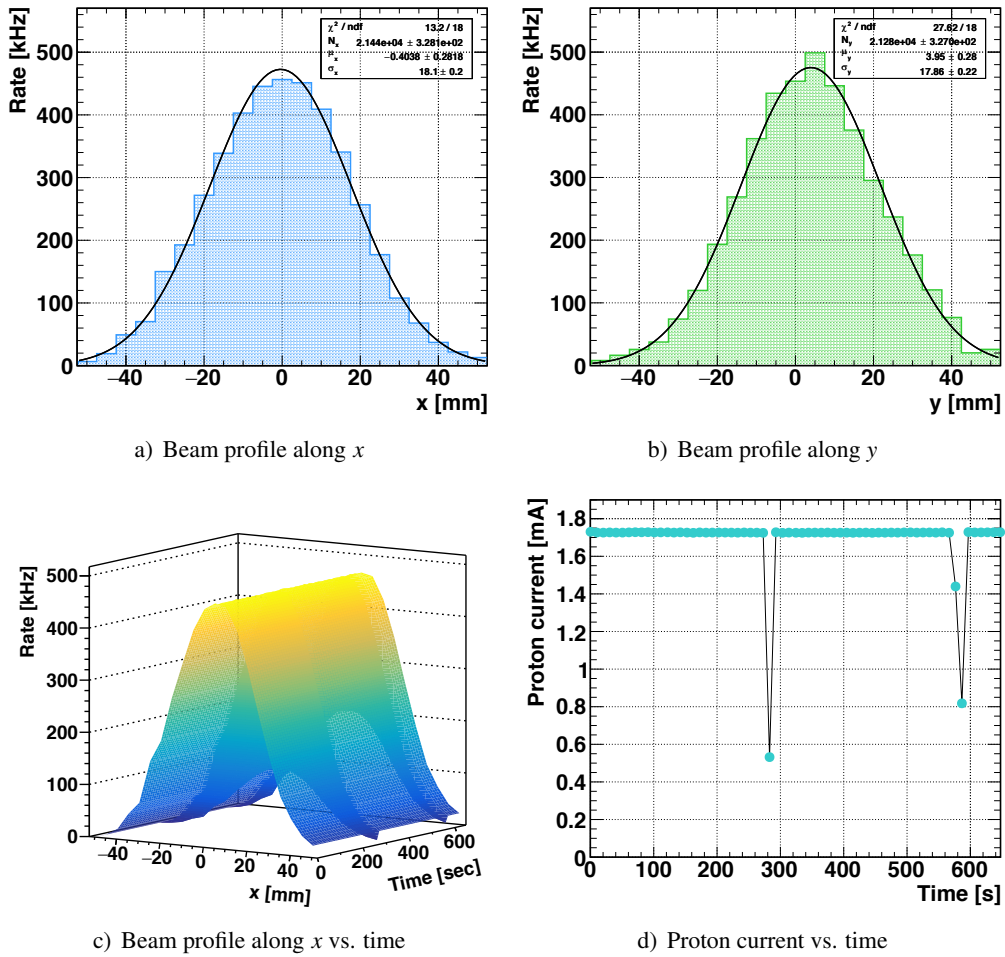


Figure 7.4: Muon beam profiles measured with the beam monitor prototype. The time it takes to get a profile as shown in a) and b) is about ten seconds.

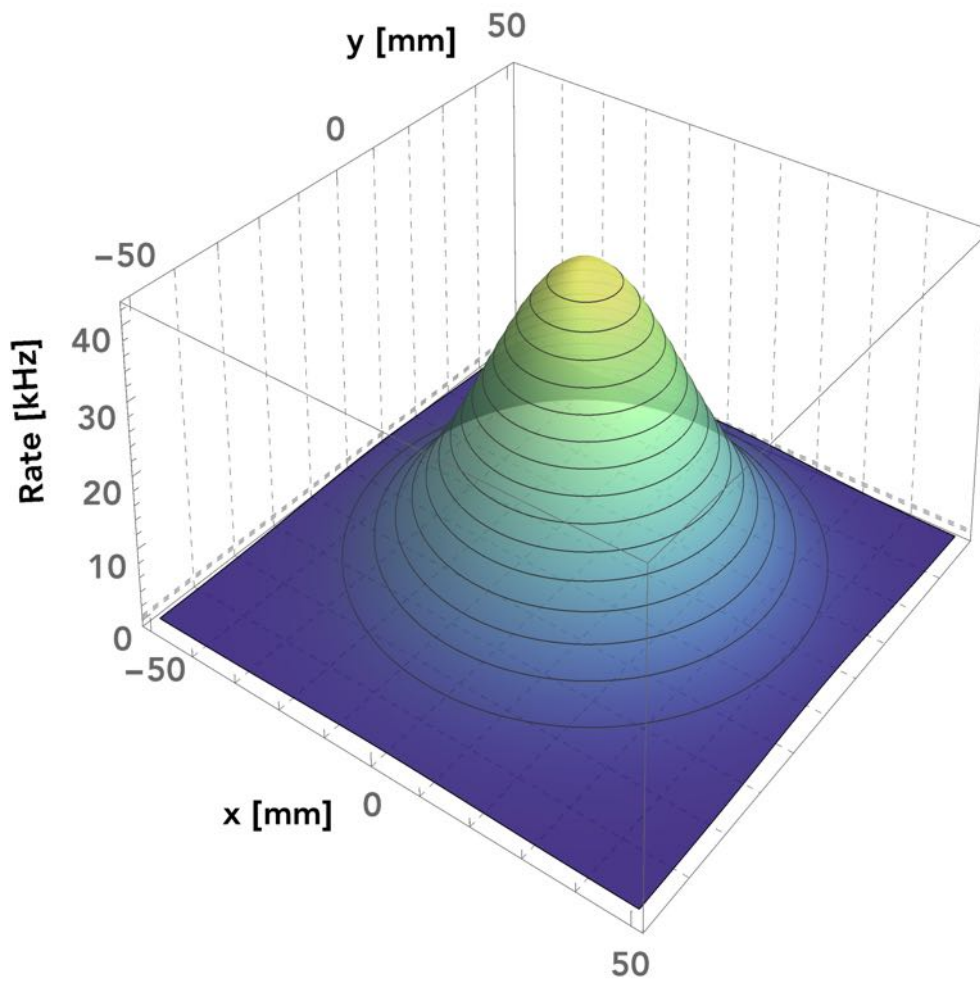


Figure 7.5: 3D muon beam profile obtained by combining the information from the two separate profiles along x and y measured by the scintillating fiber beam monitor prototype.

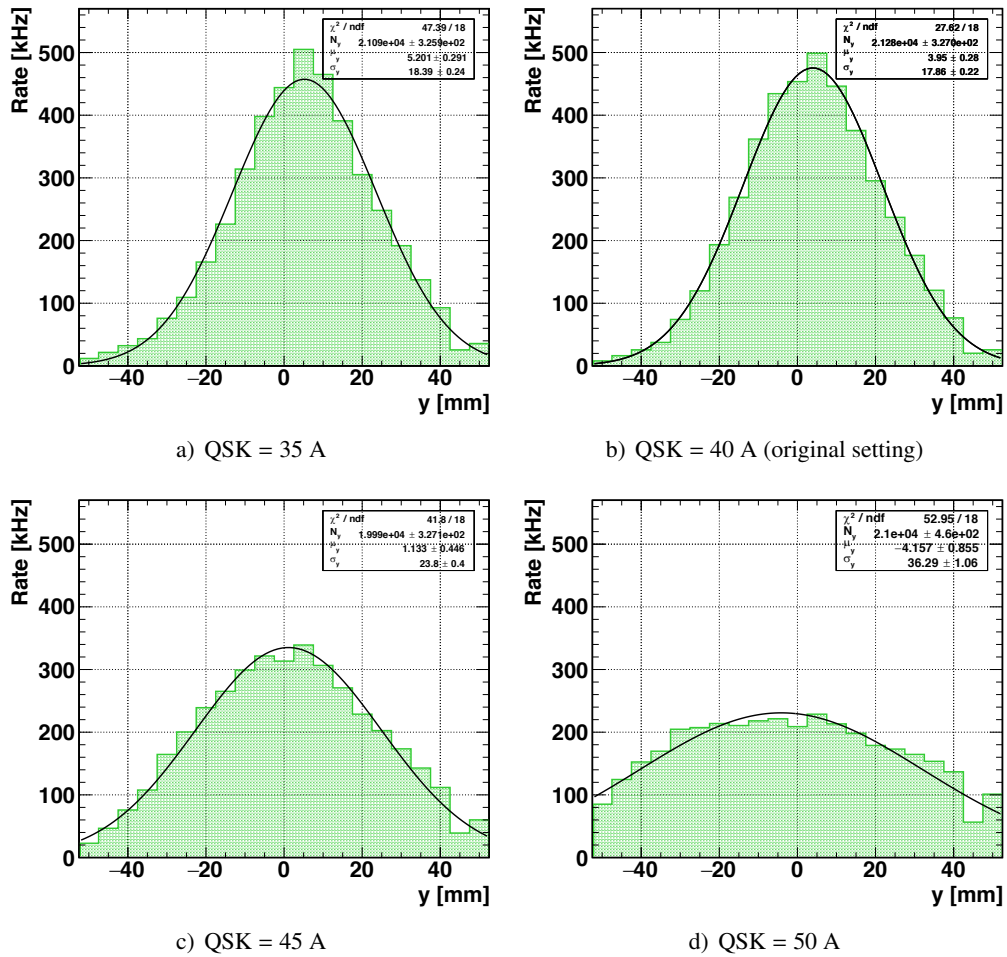


Figure 7.6: Muon beam profiles for different beam focusing as measured by the fiber beam monitor. The focusing was altered by changing the current of the last quadrupole of the second triplet (QSK). The original setting is shown in b).

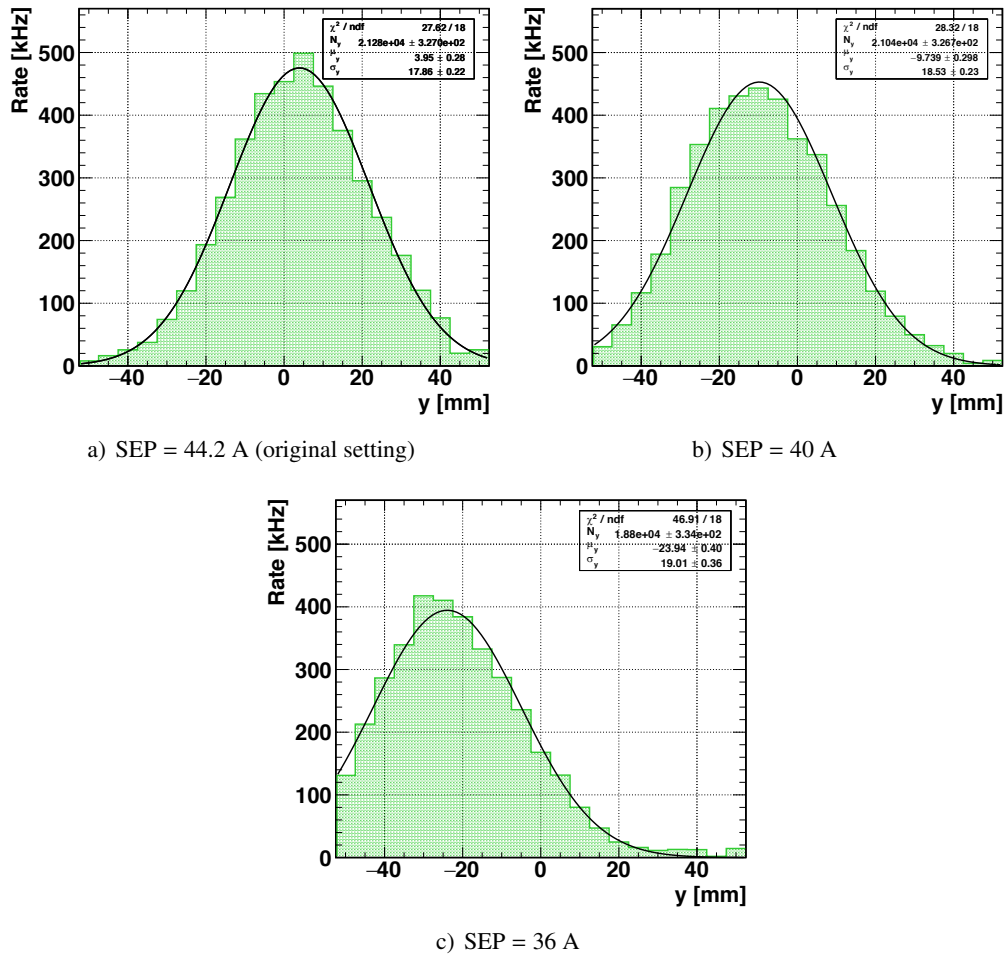


Figure 7.7: Muon beam profiles for different beam positions as measured by the fiber beam monitor. The beam position was changed by varying the separator magnet current (SEP). The original setting is shown in a).

of the energy deposit left by the muons). The material thickness at the inflection point of this curve is referred to as the “mean range”.

The Mylar material consisted in 50 μm thin foils that were added step by step, until the fiber hit rate dropped to basically zero. The measured range curve is shown in Fig. 7.8a) when the SiPM signals were subject to a low threshold (0.5 Phe for both SiPMs). The same measurements for an intermediate (≈ 1 Phe) and a high threshold (≈ 1.3 Phe) are displayed in Fig. 7.8b) and 7.8c). One expects a certain amount of positron contamination, namely when enough material is present such as to stop the muons, which subsequently decay. In fact, for the low threshold, the counting rate does not drop to zero when putting a lot of material thanks to the positron contamination. In contrast, for the high threshold, the fraction of detected positrons is relatively small as can be understood from the range curve at big degrader thicknesses. At a high threshold, a mean residual Mylar range of $r = 534 \pm 7$ (stat) μm was extracted from the fit to the range curve. Accounting for the uncertainty in the Tedlar foil’s density, which may vary from 1.37 to 1.72 g/cm^3 according to the data sheet [62], the mean residual range in Mylar is $r = 534 \pm 7$ (stat) ± 3 (sys) μm . This is consistent with the pill counter measurement, which yielded a residual range of $r_{pill} = 529 \pm 5$ μm in Mylar, where the material configuration was essentially identical to the fiber measurement with the only difference of the pill being covered by an aluminum foil of 20 μm thickness, equivalent to ≈ 30 μm Mylar, instead of having a Tedlar beam window, equivalent to 25 to 31 μm Mylar (depending on the density). In addition, also the beam profile was measured as a function of the degrader thickness, see Fig. 7.9. As expected, one can observe an enlargement of the beam due to the increasing amount of material.

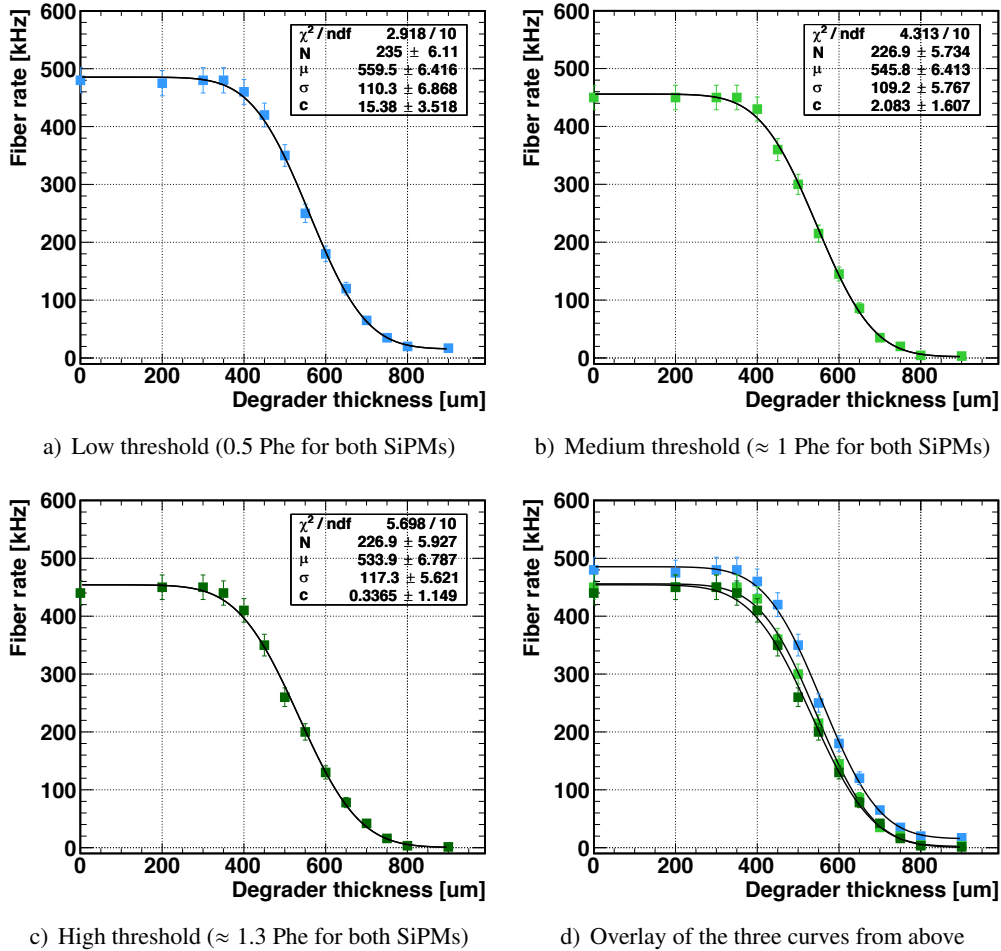


Figure 7.8: Muon range curve in Mylar for a low, a medium and a high threshold, obtained with the central fiber of the beam monitor's first grid layer (logic AND of the two SiPMs). The “pedestal” at low threshold is due to the positron contamination originating in stopped muon decay. The curves are all fitted with a function f (black lines) of the form $f(x) = N \cdot \text{Erfc} \left[(x - \mu) / \sqrt{2}\sigma \right] + c$, with Erfc denoting the complementary error function.

7 R&D of Auxiliary Detectors Based on Scintillating Fibers

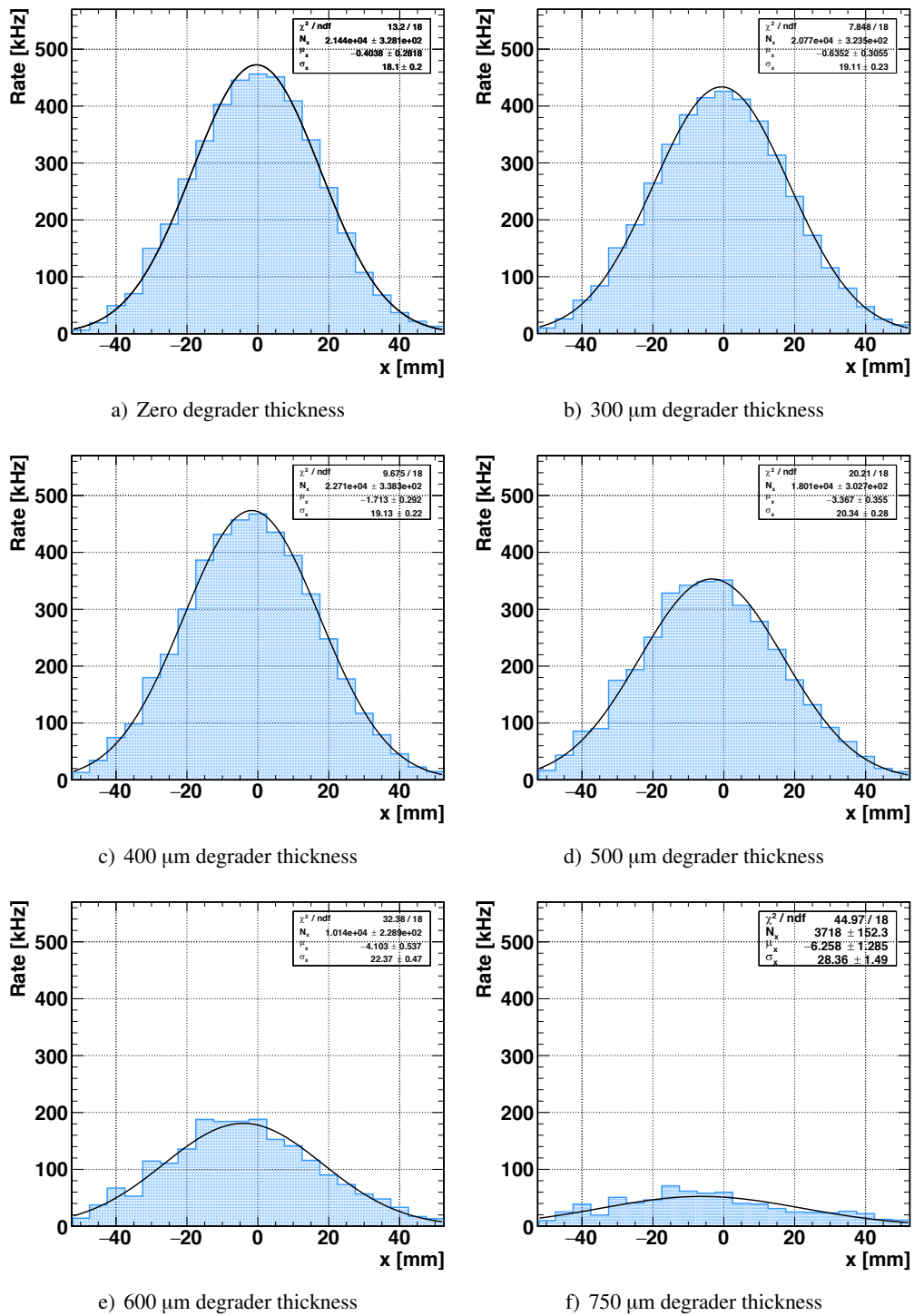


Figure 7.9: Beam profile in x -direction as a function of the Mylar degrader thickness.

7.2 Particle Identification

The discrimination of positrons and surface muons is important for all three kinds of scintillating fiber detectors in MEG II, and is also very useful when thinking about more general applications. The next sections present two approaches to identify the particle types with the help of the fiber beam monitor tool, which are (1) charge discrimination and (2) discrimination by time-of-flight.

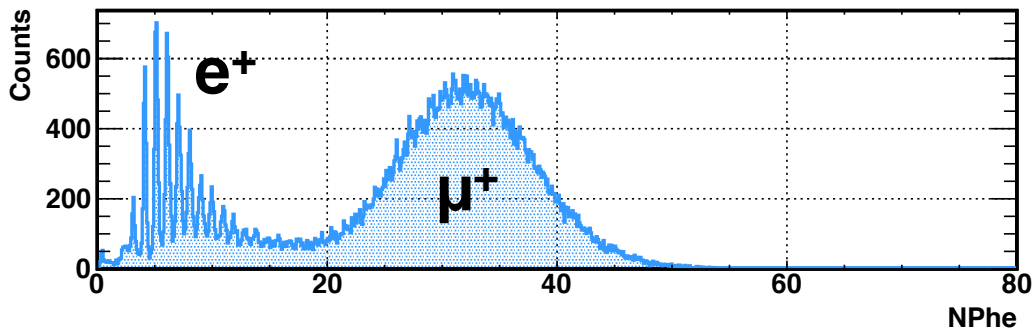
7.2.1 Charge Discrimination

Because MEG / MEG II uses a surface muon beam with a momentum of $p = 28 \text{ MeV}/c$, the muons and positrons differ a lot in terms of stopping power: The positrons are minimum ionizing, whereas the muons are highly ionizing. This translates into a difference in terms of the energy deposited in the fiber and consequently in the amount of light collected, such that the two particles can be discriminated on the basis of their waveforms' charge. Fig. 7.10 gives a feeling about how well highly and minimum ionizing particles can be distinguished with a $250 \mu\text{m}$ thin fiber. This measurement was performed at the πE1 beam line at PSI using a muon and positron beam with $p = 28 \text{ MeV}/c$.

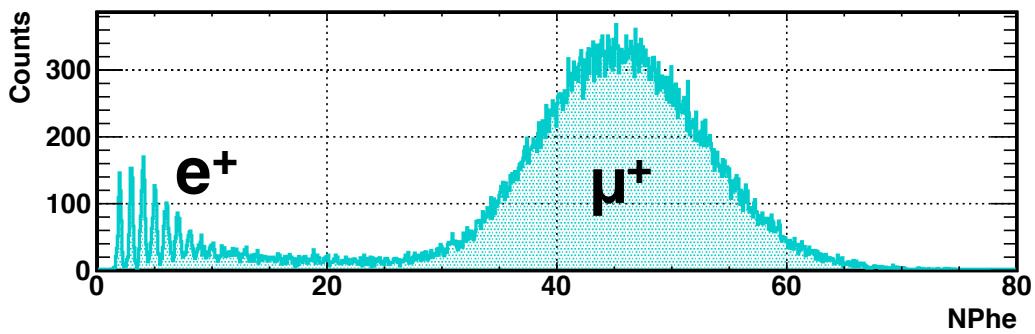
7.2.2 Time-Of-Flight

For higher momenta it is possible to discriminate different particle kinds by a Time-Of-Flight (TOF) measurement relative to the proton cyclotron's RF signal, together with a charge measurement to identify the particle type. An example is shown in Fig. 7.11: These data were taken at the πM1 beam line at PSI (see Sect. 2.3.2). The beam channel accepts positrons, muons and pions, which are all time-correlated with the RF cyclotron signal. Thanks to the fact that they possess equal momenta, but different masses, the time it takes for them to travel from the meson production target to the end of the beam line or the detector is distinct for the three kind of particles e , μ and π . The beam momentum was set to $p = 115 \text{ MeV}/c$, which is one of the tunes at the πM1 beam line for which the different particles are best separated. The three peaks in the TOF spectrum associated to the three particle kinds are well visible (left column of Fig. 7.11). By considering the charge collected by the photosensors as a function of the TOF (right column of Fig. 7.11), one is able to determine which species belongs to which peak in the time spectrum: The positrons are essentially minimum ionizing; the other two kind of particles are near minimum ionization but feature slightly different stopping powers, where specifically the pion is a little more ionizing than the muon due to its larger mass. The above exercise of measuring the TOF and the charge spectrum was performed with the pill counter (see Sect. 6.6.2) as well as with fibers of $500 \mu\text{m}$ and $250 \mu\text{m}$ size (prototype V4.1, see Sect. 6.6.1), as shown again in Fig. 7.11. As expected, for the pill and the $500 \mu\text{m}$ fibers the TOF spectrum is quite sharp and the charge spectrum exhibits appreciable differences for the various particle types. For the $250 \mu\text{m}$ fibers, the TOF is naturally a little worse due to the lesser amount of light (i.e. worse time resolution), but the particles can be well-identified after applying an additional quality cut which affects the absolute detection efficiency for MIPs by maximally 10 %.

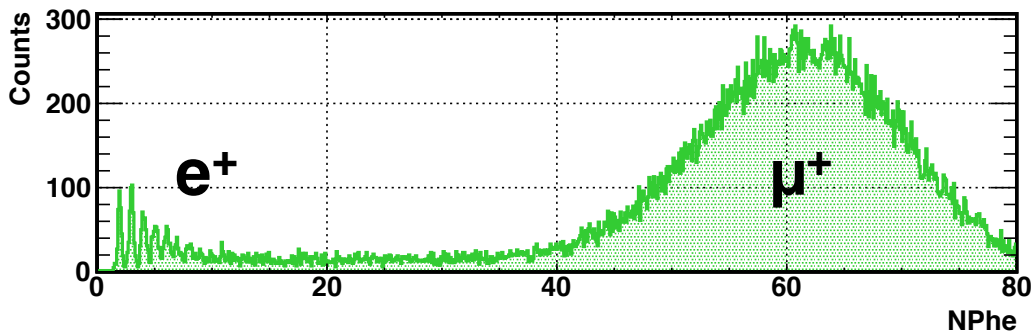
7 R&D of Auxiliary Detectors Based on Scintillating Fibers



a) 75 μm Mylar beam window, 105 mm of air, 25.4 μm Tedlar foil, 120 mm of air, equivalent to $\approx 285 \mu\text{m}$ Mylar in total



b) As above + $\approx 260 \mu\text{m}$ fiber (polystyrene and glue), equivalent to $\approx 485 \mu\text{m}$ Mylar in total



c) As b) + $\approx 260 \mu\text{m}$ fiber (polystyrene and glue), equivalent to $\approx 685 \mu\text{m}$ Mylar in total

Figure 7.10: Particle identification by charge discrimination. The three plots show the light collected by individual fibers located in the first three layers of the Large Prototype, respectively. The captions indicate the amount of material in front of the fiber in the order as a beam particle would have experienced it (so from US towards DS). Note that the first fiber a) was used as trigger, therefore the positron charge spectrum is biased towards higher values (the unbiased spectrum should be similar to the one in b) or c), as these positrons are also MIPs).

7 R&D of Auxiliary Detectors Based on Scintillating Fibers

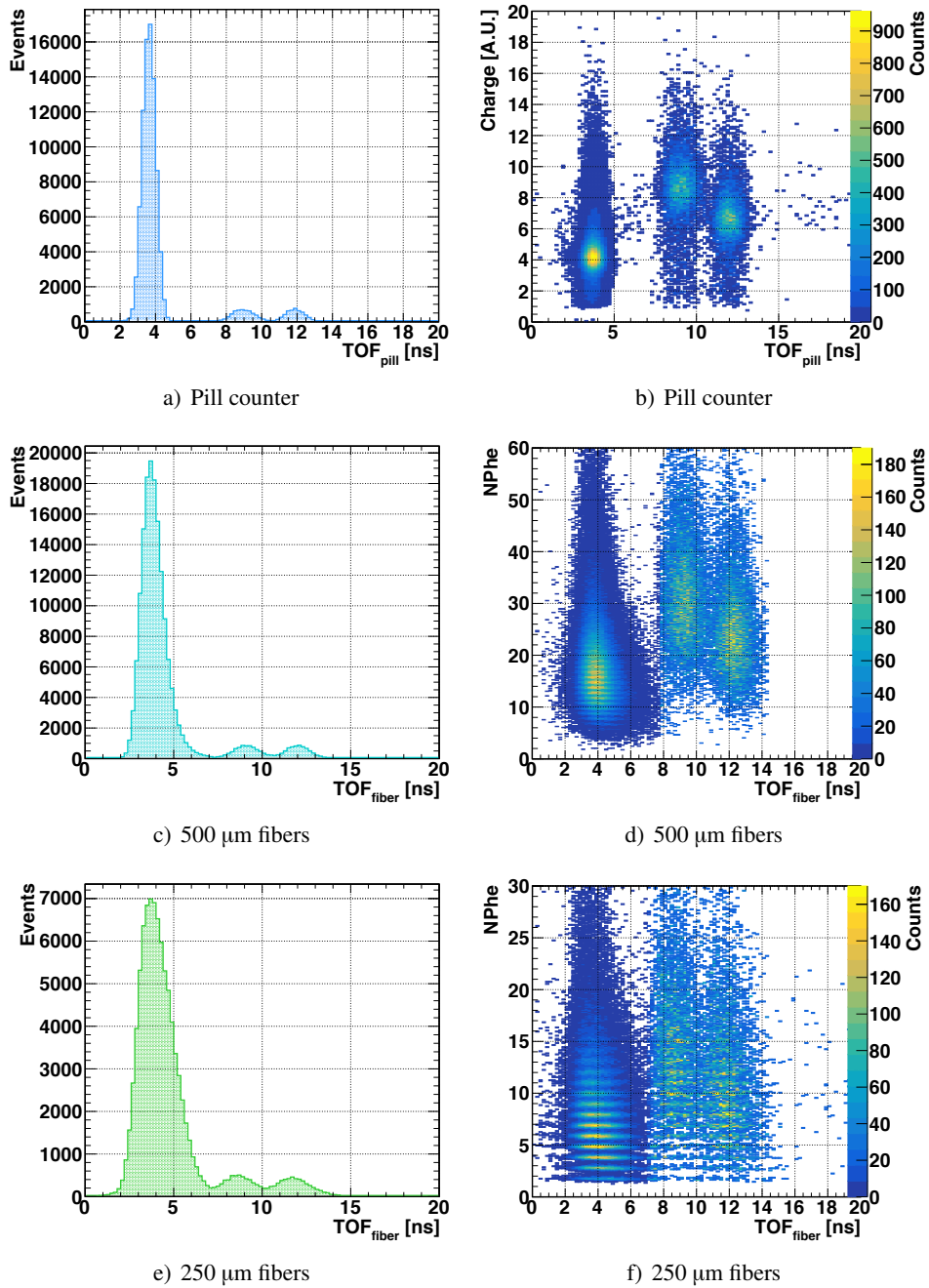


Figure 7.11: Particle identification by Time-Of-Flight (TOF). Left column: TOF spectrum for the pill counter and scintillating fibers of 500 μm and 250 μm thickness. Right column: TOF vs. charge collected by the PMT (pill counter) and the SiPMs (fibers). The three peaks in the TOF spectrum are associated to e^+ , π^+ and μ^+ , reading the spectrum from left to right, based on the information from the plots in the right column. The charge spectra of the muons and pions were scaled by a factor of twenty for visibility.

7.3 Radiation Hardness

Radiation hardness of plastic scintillators is (literally) a hot topic and has been widely reported about in the literature, however, the process of radiation damage as well as annealing seems not to be fully understood yet, as the numbers often disagree. Therefore, it is admittedly difficult to give a prediction for the radiation damage of the fiber detectors in the MEG II experiment, because both the damage and the annealing appear to depend a lot on parameters which are usually not under control in beam test conditions (e.g. atmospheric composition). The only thing that we can do here is to give a rough estimate of the energy dose absorbed by the fibers throughout the experiment. Here we address the beam monitor tool.

Let us assume that during MEG II we will have the “standard” surface muon beam with a momentum of $p = 28 \text{ MeV}/c$ (equivalent to a muon kinetic energy $E_{kin} = 3.65 \text{ MeV}$) and an intensity of $10^8 \mu^+/\text{s}$. Let us further always consider the one, individual fiber of the detector which is maximally exposed (i.e. whose location coincides with the beam’s center). The fiber has a cross section of $A = 250 \times 250 \mu\text{m}^2$ and a density equal to $\rho = 1.06 \text{ g}/\text{cm}^3$. We consider a scenario in which the beam monitor is mounted in a position where the beam is relatively large, as for example in the beam test presented in Sect. 7.1.2, where the beam had a size of $\sigma_{x,y} \approx 18 \text{ mm}$. We saw from those measurements that the typical maximal rate is about 450 kHz at 1.7 mA proton current. Scaling this rate to 2.4 mA proton current and allowing for a generous safety margin, let us assume that the rate on the fiber is about 750 kHz. Muons of $E_{kin} = 3.65 \text{ MeV}$ in polystyrene feature a stopping power of $dE/dx \approx 18.2 \text{ MeV}/\text{cm}$ [63], which means that they lose $E \approx 460 \text{ keV}$ in the fiber. The deposited energy E_{dep} per day is therefore:

$$E_{dep} = 0.46 \text{ MeV} \times 750 \text{ kHz} \times 86,400 \text{ s/d} \quad (7.1)$$

$$= 3.0 \times 10^{16} \text{ eV/d} \quad (7.2)$$

$$\approx 4.8 \text{ mJ/d.} \quad (7.3)$$

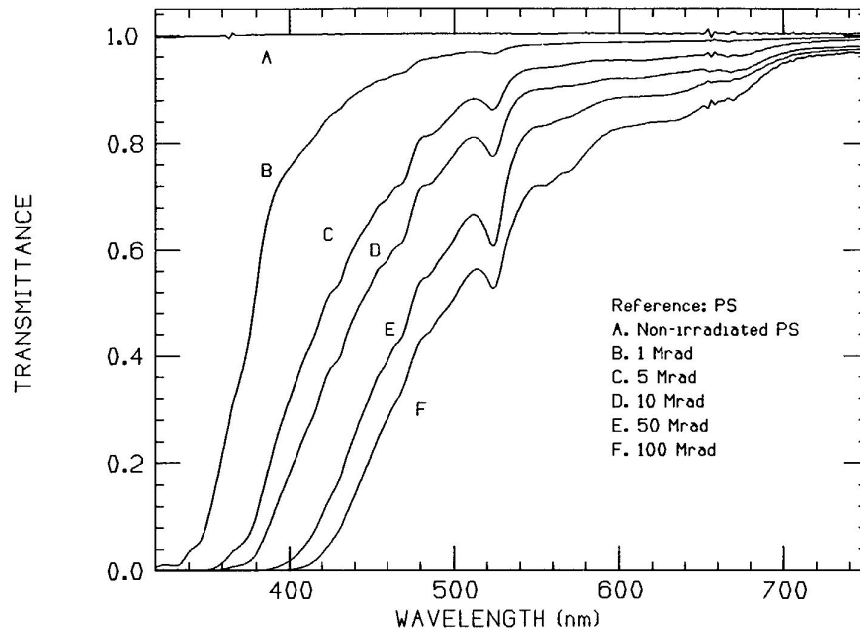
The energy dose absorbed by a material is usually given in units of gray (1 Gy = J/kg = 100 rad). Assuming for the sake of simplicity that the fiber is evenly illuminated within the full-width-half-maximum $2.35 \sigma_x \approx 4.2 \text{ cm}$, the material exposed to the ionizing radiation amounts to $m = 4.2 \text{ cm} \cdot A \cdot \rho \approx 2.8 \text{ mg}$. The absorbed energy dose is thus:

$$D \approx \frac{4.8 \text{ mJ/d}}{2.8 \text{ mg}} = 1.7 \text{ kGy/d,} \quad (7.4)$$

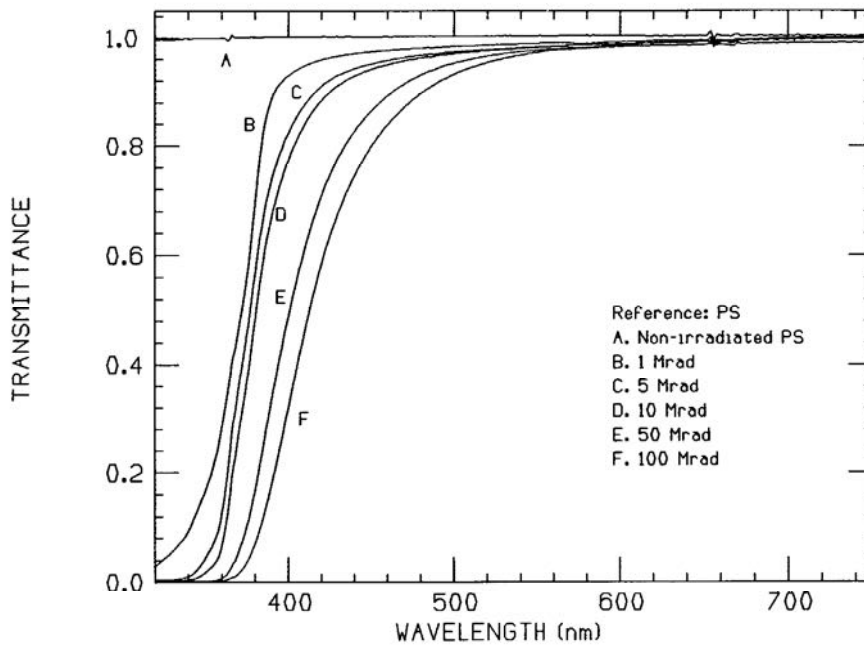
meaning that the detector is subject to a substantial amount of radiation dose. In general, the literature appears to agree on the fact that radiation damage does not necessarily imply the destruction of the fluorescence centers (i.e. a loss in scintillation light yield), but rather the creation of absorption centers which diminish the optical transmission of the light in the plastic scintillator (i.e. reduce the attenuation length). Studies of BCF-12 fibers of 1 mm diameter irradiated by a 100-keV X-ray tube showed that radiation damage depends strongly on the dose rate and the oxygen concentration dissolved within the fiber, where the oxygen appears to anneal the radiation damage (at least partially) [64]. The authors in [65] give an account of the transmission spectrum after irradiating pure polystyrene disks in a nitrogen atmosphere with different doses between and 10 kGy and 1 MGy at a rate of 10 kGy/h. The measured transmission spectra

just after irradiation and after annealing in an oxygen atmosphere are shown in Fig. 7.12a) and 7.12b), respectively. The permanent irradiation damage seems to affect mostly the transmission of the light in the UV / blue region, whereas the annealable damage chiefly derogates the transmission in the green region [64, 65]. Assuming that the scintillating fibers used in this thesis were to behave in a similar way, the permanent radiation damage (i.e. after annealing) is expected to decrease the transmission by $\approx 10\%$ after 30 DAQ days continuously using the beam monitoring tool.

As already mentioned previously, these numbers are just educated guesses; at this stage, no conclusive statement can be made. No deterioration in the amount of detected light was observed during the few days of beam tests performed with the fiber prototypes presented in Sect. 6.6 and Sect. 7.1 (irradiation in air). The radiation hardness needs to be assessed with a dedicated beam test under controlled conditions and is currently being planned. If the radiation damage should be an issue, the beam monitor tool will be implemented in a way that allows to move it into the beam during the beam calibration measurement and out again, therefore reducing the exposure to the radiation.



a) Transmission spectrum just after irradiation



b) Transmission spectrum after annealing in oxygen

Figure 7.12: Transmission spectrum of pure polystyrene disks after irradiation in nitrogen with different doses at a dose rate of 10 kGy /h just after irradiation and after annealing [65].

8 The Mott Scattering Calibration Method

For an experiment which looks for a very rare decay it is essential to understand and control the properties of the detectors, as high resolutions in space, time and energy as well as a good knowledge of the scales are required. For MEG, a large variety of calibration methods have been developed (see Sect. 4.5). In the following we will concentrate on one particular calibration method for the positron spectrometer involving Mott scattered positrons.

8.1 Introduction

The standard calibration methods for the MEG positron spectrometer comprise the optical survey of the DCH system and the target, runs of cosmic ray data and samples of positrons from RMD ($\mu^+ \rightarrow e^+ \nu_e \bar{\nu}_\mu \gamma$) and Michel ($\mu^+ \rightarrow e^+ \nu_e \bar{\nu}_\mu$) decays, which are recorded with a dedicated, prescaled trigger during the MEG physics run. The optical survey forms the basis of the alignment of the target and the DCH modules, which is later refined by software methods. The cosmic ray data are also used to align the DCH system, because they leave straight tracks in the spectrometer. However, if one is interested in the behavior of the positron spectrometer at the $\mu^+ \rightarrow e^+ \gamma$ signal energy, these cosmic ray data cannot be used since the spectrometer is optimized for charged particles with momenta between 40 and 55 MeV/c. Michel positrons provide such tracks, but they feature a continuous energy spectrum with a sharp edge around $E_{\mu}/2 = 52.8$ MeV. In order to study the positron spectrometer at the $\mu^+ \rightarrow e^+ \gamma$ signal energy, a new calibration method based on a Mott scattered positron beam tuned to the central beam momentum of $p \approx 52$ MeV/c was proposed. Apart from providing a new, independent calibration tool for MEG, the Mott scattering method is interesting in view of the upgraded experiment MEG II, because it represents a powerful instrument with which to explore the newly designed, complex spectrometer (see Sect. 4.8.2).

In the framework of this thesis, the Mott scattering calibration was investigated on the basis of beam test data acquired with the MEG spectrometer in order to study the method's potentialities and reveal possible limitations which could be remedied in the upgrade. Even if the beam test was limited to a few days, the Mott data turned out to be very useful for the MEG analysis, thus contributing to the latest limit on the $\mu^+ \rightarrow e^+ \gamma$ branching ratio presented in Chapter. 9.

8.1.1 Mott Scattering Mechanism

Mott scattering describes the relativistic, elastic scattering of spin $\frac{1}{2}$ particles (for instance positrons) from a massive, point-like nucleus with nuclear charge Ze and with zero spin [66, 67]. This is a good approximation for elements that satisfy $\frac{Z}{137} \ll 1$, which clearly is the case here since the MEG target is made of polyethylene and polyester (CH_2). In the laboratory frame, the

scattering cross section is given by [67]

$$\left(\frac{d\sigma}{d\Omega}\right)_{\text{Mott}} = \left(\frac{Ze^2}{2E_0}\right)^2 \frac{\cos^2(\theta/2)}{\sin^4(\theta/2)} \frac{1}{1 + \frac{2E_0}{Mc^2} \sin^2(\theta/2)} \quad (8.1)$$

where E_0 (p_0) denotes the initial energy (momentum) of the incident positron, M is the target nucleus' mass and θ corresponds to the scattering angle. The Mott scattering cross section features a strong dependence on the polar angle θ , with the particles scattering preferably in the forward direction, as can be understood from Fig. 8.1. The outgoing momentum p of the positron is

$$p = \frac{p_0}{1 + \frac{p_0}{M}(1 - \cos\theta)}, \quad (8.2)$$

so typically, the 52 MeV/c momentum is modified by up to ≈ 400 keV / c when scattering off carbon at angles within the MEG acceptance, off hydrogen up to ≈ 4 MeV/c. It is important to notice that the scattering cross section is proportional to Z^2 , such that positrons will scatter mainly off the carbon nuclei. With the approximation $E_0 \approx p_0$ we can simplify Eq. (8.1) to

$$\left(\frac{d\sigma}{d\Omega}\right)_{\text{Mott}} = \left(\frac{Ze^2}{p_0}\right)^2 \frac{(1 + \cos\theta)}{(1 - \cos\theta)^2} \frac{p}{p_0}. \quad (8.3)$$

Accounting for a finite nuclear size, the Mott scattering cross section reads

$$\frac{d\sigma}{d\Omega} = \left(\frac{d\sigma}{d\Omega}\right)_{\text{Mott}} |F(Q)|^2 \quad (8.4)$$

where $F(Q)$ corresponds to the nuclear form factor and Q stands for the transferred momentum. The momentum transfer squared, the scattering angle and the in- and outgoing positron momenta are related by

$$Q^2 = 4pp_0 \sin^2(\theta/2). \quad (8.5)$$

A rough, but still sufficiently precise approximation of the form factor is [66]

$$F(Q) \approx 1 - \frac{Q^2 \langle R^2 \rangle}{6} + \dots \quad (8.6)$$

with $\sqrt{\langle R^2 \rangle}$ equal to the RMS nuclear radius. The above relationship for the form factor is valid in the regime where QR is small. The term QR is essentially a measure for how deeply the electron penetrates the nucleus, or in other words to what extent it perceives the nuclear structure. For values of QR close to zero, the nucleus appears essentially point-like ($F(Q) \approx 1$), for large QR , the scattering is sensitive to the actual nuclear charge distribution. In the case of 52 MeV/c positrons scattering off a ^{12}C carbon nucleus, whose radius was measured to be $R = 2.464 \pm 0.012$ fm [68], QR is ≈ 1 within the MEG angular acceptance. An even better approximation of the form factor for carbon is given by [66]

$$F(Q) = 3 \frac{\sin(QR_u) - QR_u \cos(QR_u)}{(QR_u)^3}, \quad (8.7)$$

where the carbon nucleus is assumed to be a uniformly charged sphere with radius R_u . The RMS radius R and R_u are related by

$$R_u = \sqrt{\frac{5}{3}} R, \quad (8.8)$$

resulting in $R_u = 3.12$ fm. The plot in Fig. 8.1 shows the scattered positrons' angular distribution simulated on the basis of Eq. (8.4), where the form factor was computed by Eq. (8.7).

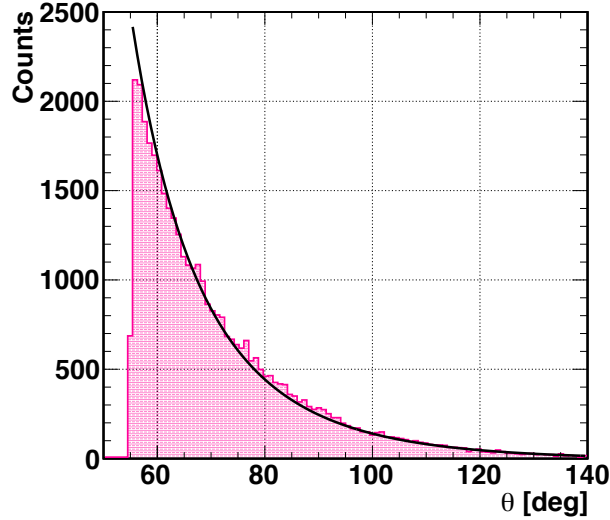


Figure 8.1: Angular distribution for positrons Mott scattering off the MEG target within the MEG acceptance limits (pink hatched histogram). This distribution was simulated on the basis of Eq. (8.4), which is shown as a black curve.

Radiative corrections to Eq. (8.4) were shown to affect the overall, absolute value of the cross section by about 10% [69]. The corrections vary by $\approx 1\%$ across the angular acceptance of the MEG spectrometer, such that the angular distribution is essentially unaffected. Notably, this implies that any deviation from the expected angular distribution is caused by inhomogeneities in the MEG apparatus' tracking and / or trigger efficiency. Note that in principle, a non-zero beam polarization transverse to the scattering plane causes an azimuthal asymmetry in the differential scattering cross section (exploited in the so-called Mott polarimetry) due to electron spin-orbit interactions [70]. However, the positron beam used here is expected to be unpolarized and the asymmetry is anyhow weak for scattering from low Z materials and particles with $\beta \approx 1$. In addition to that, the scattering of positrons (rather than electrons) is known to be less sensitive to the asymmetry [71].

8.1.2 Realization

The setup for the Mott scattering calibration is virtually the same as for the physics run with the natural exception of the beam tune settings. The desired beam positrons are promptly produced in the meson production target by $\pi^0 \rightarrow \gamma\gamma$ plus the subsequent pair production, thus they are

strongly time-correlated with the 50 MHz cyclotron signal. In addition to the beam positrons, the beam contains also contaminations in the form of pions π^+ , positrons which stem from the Michel decay of the cloud muons surrounding the meson production target (see Sect. 2.1) and positrons from muons decaying along the beam line. To distinguish the background from the desired positrons one exploits the fact that the different kind of particles have distinct Time-Of-Flights (TOFs) from the meson production target to the detectors, measured relative to the RF signal. An example of such a TOF spectrum is shown in Fig. 8.2. The sharp peak for instance is caused by the beam positrons, whereas the small peak on the left is associated to the pions. The broad peak on the right is consistent with the cloud muon decay positrons. The flat background is caused by the positrons from Michel decays along the beam line, since for those the time-correlation with the RF signal is completely lost. From the measurements presented in Sect. 8.3, the momentum byte $\Delta p/p$ of the beam was estimated to be ≈ 500 keV in 2012 and ≈ 350 keV in 2013. Currently, no direct measurement of the energy spread is implemented in the experimental setup.

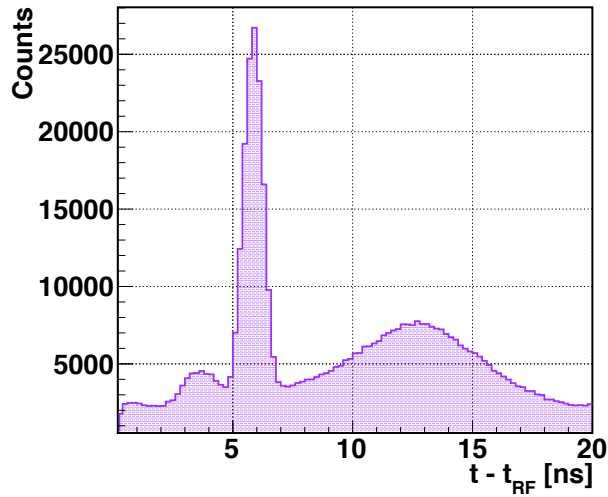


Figure 8.2: Relative time between the RF signal and the Mott scattered particle's time measured by the spectrometer. The sharp peak is associated to the desired positrons, the other two peaks are presumably due to pions (left) and cloud muons (right). The flat background is caused by positrons originating in Michel decays.

The Mott runs were collected utilizing the same trigger as the one used for Michel events, requiring a drift chamber track with at least five consecutive DCH hits and a timing counter hit. The beam intensity was sufficiently high as to saturate the MEG DAQ. During the Mott run in 2012, about 1350 runs of 2000 events each were collected in five days, in 2013 about 630 runs were acquired in 2.5 days. The data were analyzed by the standard MEG reconstruction algorithms and were selected by applying the standard cuts on the quality of the reconstructed tracks. An additional cut on the TOF spectrum shown in Fig. 8.2 was included in order to reject the beam-correlated background.

8.2 Distribution of Mott Scattering Vertices on the Target

An example of a distribution of Mott scattering vertices on the target obtained by extrapolating the reconstructed tracks back to the target plane is given in Fig. 8.3. The screws which hold the target foil in its frame feature a higher material density and a larger thickness than the rest of the target, thus a larger number of particles scatter in these domains. The holes punched into the target foil appear as dips. From these plots it became obvious that the beam was not well-centered on the target and that it featured a somewhat strange halo, especially in 2012. For the future MEG II setup, the beam as well as its impact position will be better understood and fine-tuned using the proposed beam monitor tool(s) (see Sect. 4.8.5 and Chapter 7). A centered beam would boost the potentialities of the Mott calibration method even further.

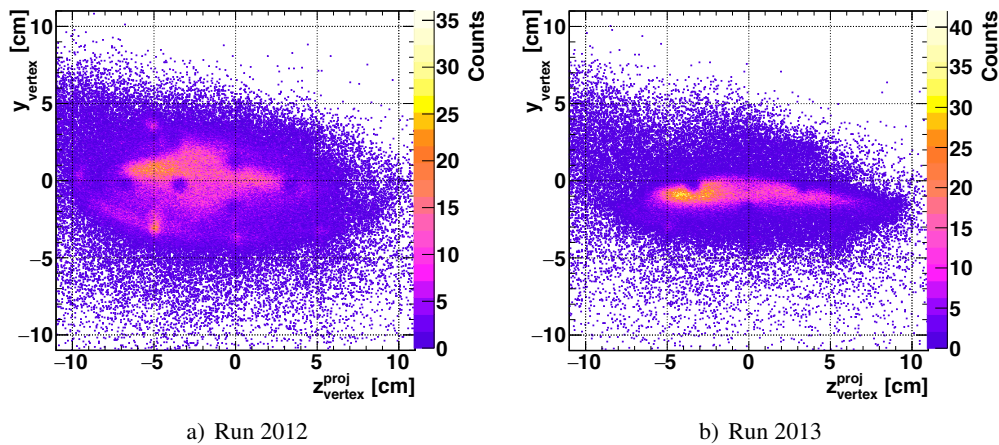


Figure 8.3: Distribution of reconstructed Mott scattering vertices for the 2012 and 2013 run projected onto the MEG target. The screws of the target frame and the holes in the target are clearly visible. The beam was shifted towards positive x (i.e. mainly hitting the part of the target located US).

8.3 Mott Monochromatic Energy Line

Since the positrons lose only little momentum through the scattering process (< 500 keV when scattering off carbon), one expects an approximately monochromatic line in the momentum spectrum of the scattered particles. An example is shown in Fig. 8.4a). Effects which broaden the line are on the one hand the ionization and radiation losses inside the target, together with the outgoing momentum's dependence on the scattering angle, on the other hand the non-zero momentum byte of the beam. The first class of effects is intrinsic to the Mott scattering method, whereas the momentum byte is primarily determined by the opening of the momentum selection slits, which in both runs was adjusted to the minimum possible setting. For the 2012 run, the intrinsic contribution was estimated from Monte Carlo simulations to be ≈ 350 keV and the beam momentum byte ≈ 500 keV. The momentum byte could additionally be decreased by

≈ 150 keV in 2013 by reducing the opening of the intensity slits, as can be seen from Fig. 8.4b). Albeit the beam energy spread being too large as to extract immediately the energy resolution intrinsic to the spectrometer (≈ 300 keV), methods exist to extract it by using double turn tracks, as we will see in Sect. 8.5.

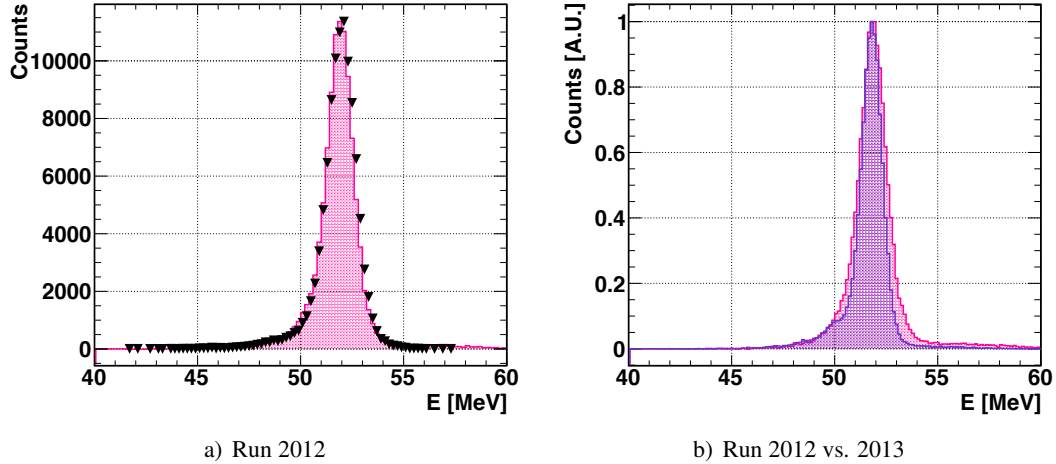


Figure 8.4: Mott monochromatic energy spectrum (“line”). The first plot shows data from 2012 (hatched magenta histogram) together with the Monte Carlo simulation (black triangles). The right plot shows the energy spectrum 2012 (magenta histogram) vs. the energy spectrum in 2013 (purple histogram).

8.4 Theta Angular Distribution

An example of a measured distribution of the polar angle θ is shown in Fig. 8.5. The small dip in the detection efficiency at $\theta \approx 90^\circ$ is due to the tracking algorithm being slightly less efficient for those tracks with small longitudinal momentum. The other minor irregularities come from the fact that the acceptance in θ is a function of the scattering vertex’ z -coordinate, as can be understood by the geometrical considerations shown in Fig. 8.6. Together with a beam spot which is not perfectly centered but shifted a little upstream, the resulting θ -distribution is slightly modified.

8.5 Spectrometer Resolutions from Double Turn Tracks

This section explains how to extract the positron spectrometer resolutions from double turn tracks. First, the method will be explained, then the outcome of this analysis applied to Mott positron data will be presented and compared with results obtained from Michel positron data.

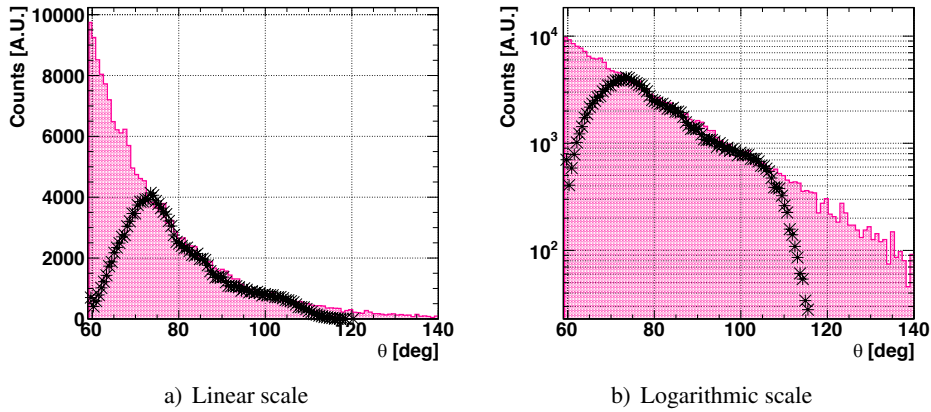


Figure 8.5: Measured (black stars) and theoretically expected (pink hatched histogram) angular distribution of the Mott scattered positrons in linear and logarithmic scale.

8.5.1 Methodology

As we have seen previously, the Mott positron beam exhibits a non-zero momentum byte, for which no direct and independent measurement is available. In particular, it means that the spectrometer’s momentum resolution cannot be extracted from the Mott energy line width since the contribution from the momentum spread is unknown. However, there is a possibility how to circumvent this problem. The trick is to use so-called “double turn tracks”, i.e. tracks which cross the DCH system twice. A typical double turn track is shown in Fig. 8.7a). In order to determine the spectrometer’s resolutions, every turn is treated and reconstructed as an independent track. Each turn is then propagated towards the target plane, where the observables of interest ζ are compared by computing $\Delta\zeta = \zeta_{\text{turn } 1} - \zeta_{\text{turn } 2}$. The procedure described above is shown schematically in Fig. 8.7b). Applying this algorithm to all available double turn tracks results in a double Gaussian distribution for every observable ζ , which are: the momentum p , the polar and azimuthal angles θ and ϕ and the vertex coordinates (x, y) on the target. The spectrometer’s performance is quantitatively assessed by considering the standard deviations (RMS) as well as the core fraction of these distributions¹. The very same method is applied to Michel positron data. In both cases, a positron with an energy $E > 50$ MeV is required. Moreover, the positron track is asked to fulfill minimal quality requests and it should possess at least seven hits for each turn. The Mott positrons are additionally required to stay within the beam positron window in the TOF spectrum shown in Fig. 8.2. Note that in principle the extracted double turn resolutions should be corrected on the basis of Monte Carlo simulations, because the double turn track sample is biased [1]. However, these corrections were omitted here, and we limit ourselves to the comparison between the resolutions obtained with Mott and Michel positron data.

¹The positron resolutions that are used in the actual MEG analysis are evaluated event by event by multiplying the track fitting error matrix with a pull distribution which is computed for each year separately from a double turn track sample of Michel positrons.

8 The Mott Scattering Calibration Method

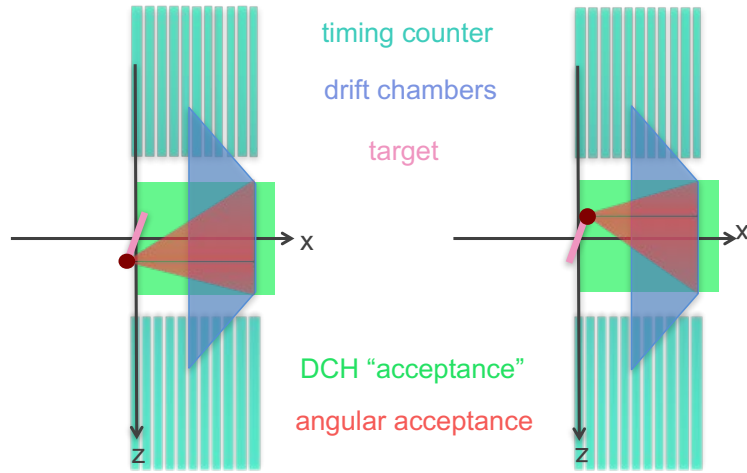


Figure 8.6: The acceptance in the polar angle θ depends on the scattering vertex' z -coordinate (red dot) on the target. Particles scattering from the US (DS) region of the target are accepted with comparatively small (large) θ -angles.

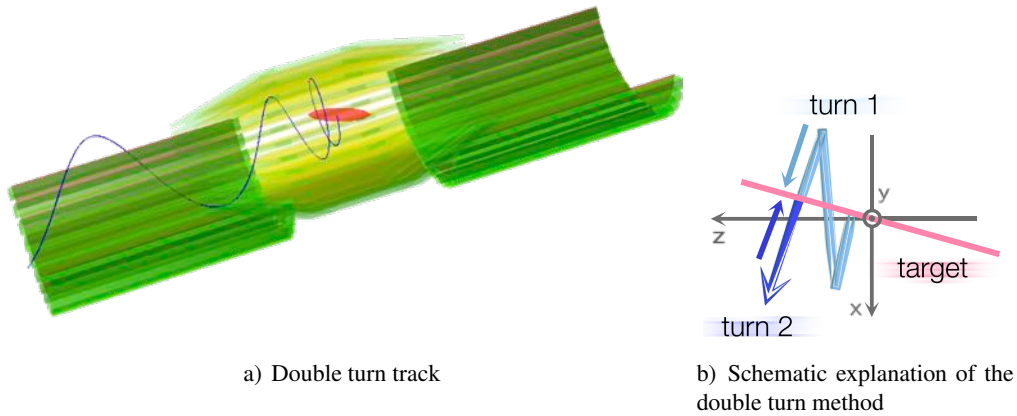


Figure 8.7: Illustration of the double turn method. The left plot shows a measured, reconstructed double turn track (blue) together with the MEG target (red), the DCH modules (yellow) and the TC bars (green). The right plot depicts the procedure to extract the spectrometer resolutions from double turn tracks.

8.5.2 Results

An example of the double Gaussian distributions, which reflect the spectrometer's resolutions on the observables of interest, are shown in Fig. 8.8. They were obtained from a sample of Mott positron double turn tracks recorded throughout the beam test in 2012. Table 8.1 summarizes the double turn resolutions obtained with the Mott data from 2012 and 2013 as well as the ones evaluated from two Michel positron samples acquired temporally close to the respective Mott runs. Surprisingly enough, the double turn resolutions on the positron variables measured in

Table 8.1: Comparison of the double turn resolutions (Gaussian standard deviation of the core σ^{core} , tail σ^{tail} and core fraction f) on the five positron observables momentum (p), polar angle (θ), azimuthal angle (ϕ) and the vertex coordinates (x, y) obtained from Mott and Michel positron data. The yellow color indicates values of the resolutions and core fractions obtained from the Mott data which agree with what the Michel positron data yielded within the given statistical errors. Correspondingly, the green color indicates Mott data values which are better compared to the one's from Michel data.

	Mott 2012	Mott 2013	Michel 2012	Michel 2013
σ_p^{core} [keV / c]	288 ± 5	241 ± 6	300 ± 8	290 ± 10
σ_p^{tail} [MeV/c]	0.94 ± 0.05	0.74 ± 0.04	1.04 ± 0.4	1.10 ± 0.04
f_p	0.91 ± 0.01	0.87 ± 0.02	0.79 ± 0.02	0.83 ± 0.01
σ_ϕ^{core} [mrad]	11.0 ± 0.3	10.4 ± 0.3	12.3 ± 0.5	13.3 ± 0.4
σ_ϕ^{tail} [mrad]	32 ± 2	32 ± 2	38 ± 2	42 ± 2
f_ϕ	0.82 ± 0.01	0.83 ± 0.02	0.78 ± 0.02	0.83 ± 0.02
σ_θ^{core} [mrad]	9.2 ± 0.3	8.9 ± 0.4	9.2 ± 0.6	9.7 ± 0.5
σ_θ^{tail} [mrad]	21 ± 1	21 ± 2	20 ± 1	20 ± 1
f_θ	0.83 ± 0.03	0.85 ± 0.04	0.70 ± 0.06	0.76 ± 0.06
σ_y^{core} [mm]	1.72 ± 0.03	1.56 ± 0.04	1.91 ± 0.06	1.86 ± 0.06
σ_y^{tail} [mm]	5.7 ± 0.2	5.4 ± 0.3	6.6 ± 0.2	6.6 ± 0.3
f_y	0.86 ± 0.01	0.86 ± 0.01	0.78 ± 0.02	0.80 ± 0.02
σ_z^{core} [mm]	2.36 ± 0.09	2.33 ± 0.09	2.53 ± 0.18	2.64 ± 0.16
σ_z^{tail} [mm]	5.8 ± 0.3	5.7 ± 0.3	6.2 ± 0.3	6.4 ± 0.4
f_z	0.77 ± 0.03	0.79 ± 0.4	0.65 ± 0.06	0.71 ± 0.05

the Mott data were found to be better than what was measured in the Michel data: in the 2012 dataset, the Mott and Michel double turn resolutions showed differences of up to 10%. In the 2013 data sample, the discrepancy was even more apparent, ranging from 10 to 20%. Several possible causes were investigated. It is worthy to mention that the resolutions measured in the Mott positron data were consistently better both US and DS². The only striking difference found was the average number of hits N used to reconstruct a track: For example in 2013, the Michel positrons featured about $\langle N_{Michel}^{2013} \rangle \approx 22$ hits on average per double turn track. Instead, the Mott positron data exhibited $\langle N_{Mott}^{2013} \rangle \approx 26$ hits per double turn track, as can be seen in Fig. 8.9a). Also the number of hits for each turn separately was larger in the Mott data, see Fig. 8.9b) and 8.9c).

Generally, one expects that an increased number of hits N leads to a better track estimate and consequently to superior positron variable resolutions. This is in fact observed in the data: An example is shown in Fig. 8.9d), which represents the momentum resolution extracted from

²One would expect a difference between the *overall* Mott and Michel positron resolutions because the Mott positrons scatter predominantly DS, whereas the Michel positrons go off mainly US, thus encountering more material on average. The separate resolutions US and DS though are expected to be similar.

8 *The Mott Scattering Calibration Method*

Michel positron double turn tracks as a function of N . The more hits are used in the track reconstruction, the better the resolution gets. The difference in the number of hits used in the reconstruction may be puzzling at first sight, because in principle the detector should not care about whether a positron came from a Michel decay or from Mott scattering. The reason lies in the detector conditions: In the Michel (i.e. also the physics) runs, the environment is much busier, the trigger rate for instance is 10^4 times higher for the Michel runs compared to the Mott runs. It could be imaginable that from time to time, in the presence of a lot of signals, the reconstruction algorithm gets confused when it comes to assign hits to the tracks, such that on average the number of hits used in the reconstruction of a track decreases. In fact, this trend was also observed in the simulation when studying different pile-up situations, see Fig. 8.10. The larger the amount of pile-up is, the smaller is the average number of hits used in the reconstruction of a track.

In conclusion, it is important to note that the actual double turn resolutions (or more precisely the pull distributions) used to construct the probability density functions of the MEG analysis (see Sect. 9.3) need to be measured in the Michel data, because they provide them in the same conditions as when physics runs are taken. This point is also important to keep in mind when studying the resolutions of the future MEG II drift chamber system.

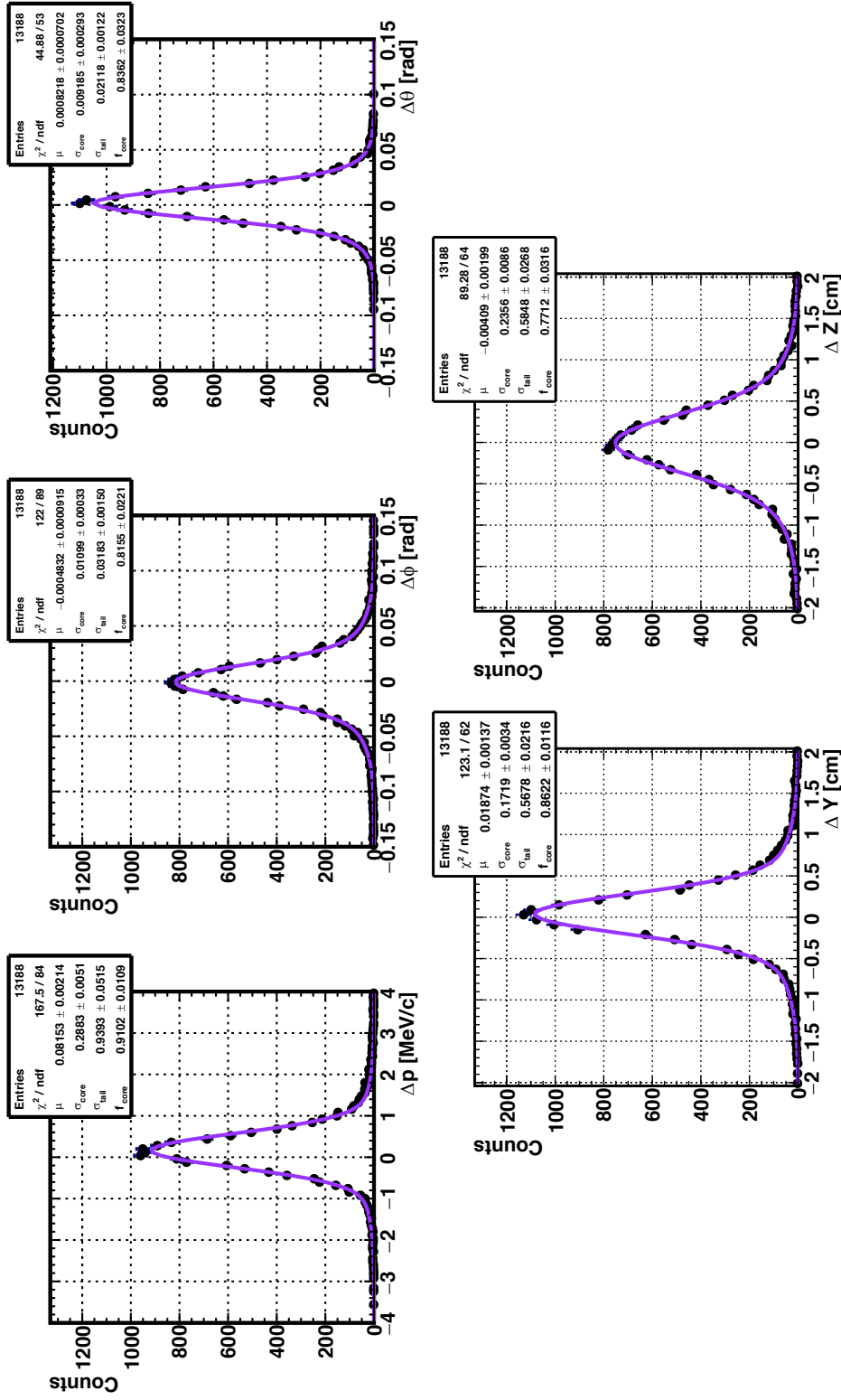


Figure 8.8: Double turn resolutions on the five positron observables momentum (p), polar angle (θ), azimuthal angle (ϕ) and the vertex coordinates (x, y) measured with Mott positrons (dataset 2012). The solid lines correspond to double Gaussian fits.

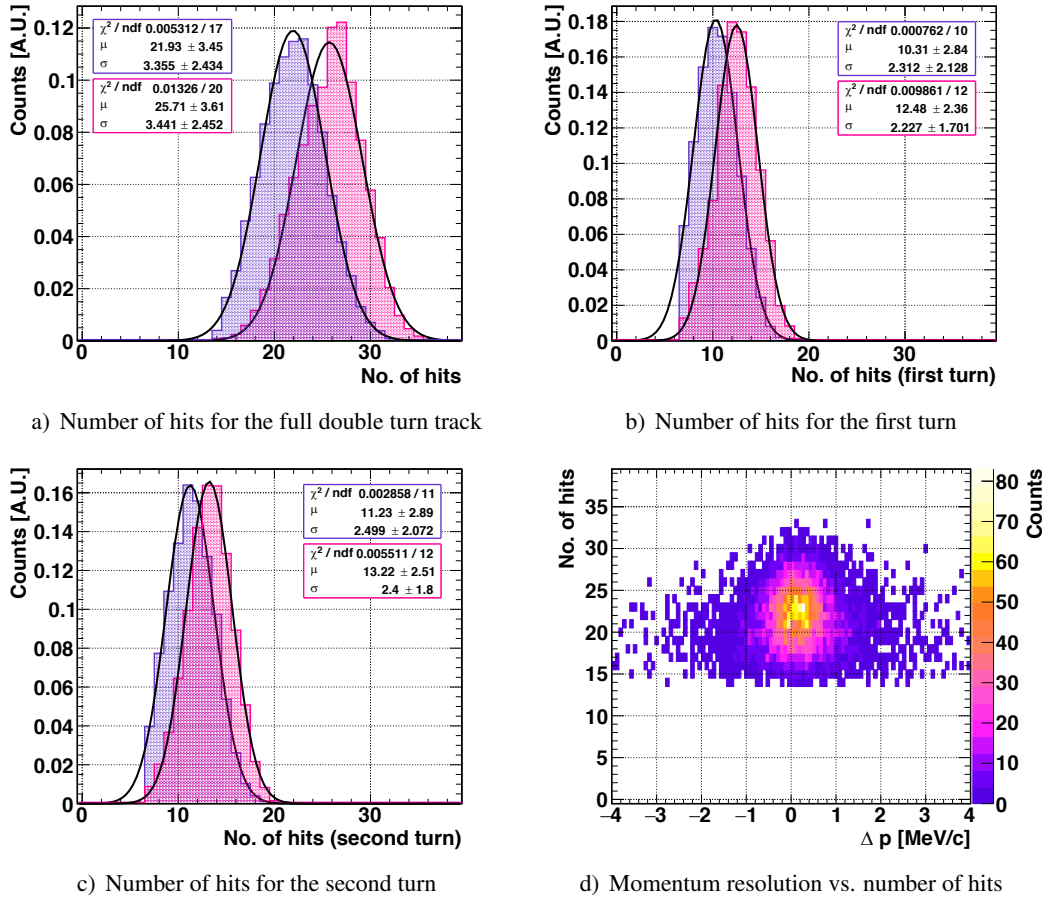


Figure 8.9: Number of hits used in the reconstruction of double turn tracks for Mott scattered positrons (magenta) and Michel positrons (purple) for the full track and the first and second turn separately. The last plot shows the momentum resolution Δp measured with Michel positron double turn tracks as a function of the number of hits used in the reconstruction.

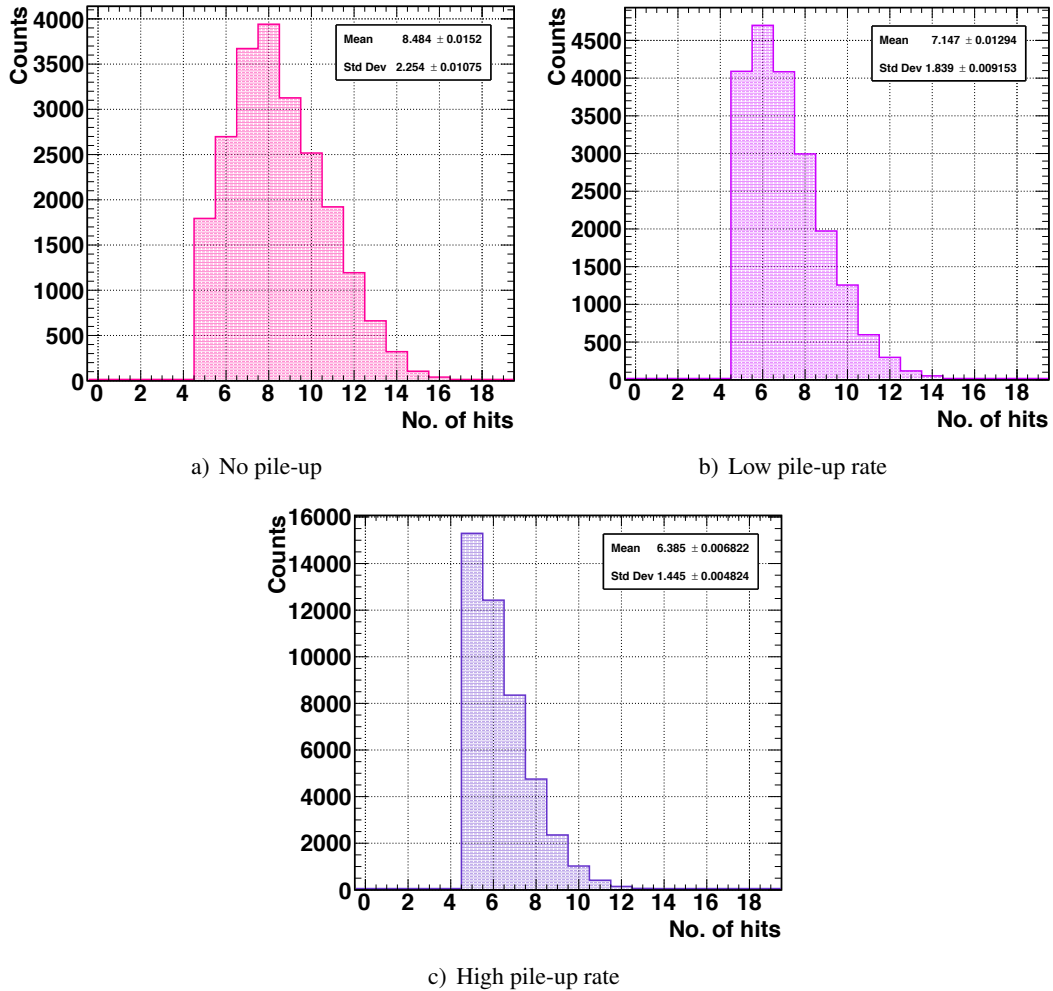


Figure 8.10: Monte Carlo simulation of the number of hits used in the reconstruction of tracks for different pile-up conditions. The number of hits shown in these plots should not be taken explicitly, but should only be interpreted in relative terms for the sake of comparison, because the tracks considered here were mostly single turn tracks and the sample does not describe the exact experimental situation of the real data taking.

8.6 Drift Chamber Alignment

In order for the positron tracks to be properly reconstructed, it is necessary to know precisely every DCH module's position and orientation with respect to each other and relative to the COBRA magnetic field. In MEG, three different types of alignment methods were available:

1. A theodolite and a laser tracker based alignment of the installed DCH modules, which were precisely surveyed in the laboratory prior to the installation and whose frames were equipped with reference markers. The resolution of this method was estimated to be about 0.2 mm in each coordinate [1].
2. An alignment based on cosmic ray runs acquired with the COBRA magnetic field switched off. The DCH modules were aligned by considering the reconstructed tracks and minimizing the corresponding residuals with respect to the expected straight tracks by applying the Millipede algorithm [72]. Thereby, each module was assumed to be a rigid body possessing three translational and three rotational degrees of freedom, where each coordinate was determined with an accuracy of 150 μm .
3. An alignment based on Michel positron tracks, to which an iterative algorithm was applied that minimized the residuals between the reconstructed tracks and the actual drift chamber hits. This method is explained in more detail in Sect. 8.6.2.

The first section presents a method to compare the different alignments based on the Mott scattering data, the second section describes the application of the third technique listed above to the Mott data.

8.6.1 Checks of the Drift Chamber Alignment

The Mott data turned out to be a very useful control sample to check and compare the different DCH module alignments obtained by the means described above. Under the assumption that the detector exhibits a uniform response with respect to ϕ , the position of the Mott monochromatic line's peak \hat{p} should be independent of ϕ . This behavior is indeed observed in the Monte Carlo simulation, see Fig. 8.11a). There, the DCH modules were assumed to be located at their nominal position. As soon as the DCH modules are badly aligned, this curve features a strong ϕ -bias.

For the 2012 data, the three different kinds of alignments performed similarly, as can be seen in Fig. 8.11b), and the small ϕ -bias, even if not zero, was under control and taken into account in the MEG analysis. For the 2013 run however, a problem with the survey arose. The issue became strikingly apparent by looking at the Mott data, displayed in Fig. 8.11c), for which the ϕ - \hat{p} curve was obviously distorted. Consequently, also the Mott monochromatic line was broader and biased, as shown in Fig. 8.11d). This behavior could be reproduced by the Monte Carlo simulation, which assumed the drift chambers to be misaligned by an amount equal to the difference between the drift chamber positions given by the survey 2013 and the survey 2012, see again Fig. 8.11c). The culprit was a mistake in the survey measurements of the six DCH modules which had been newly built for the 2013 run. After resolving the problem, the alignment was alright, as one can realize from Fig. 8.11c) and 8.11d).

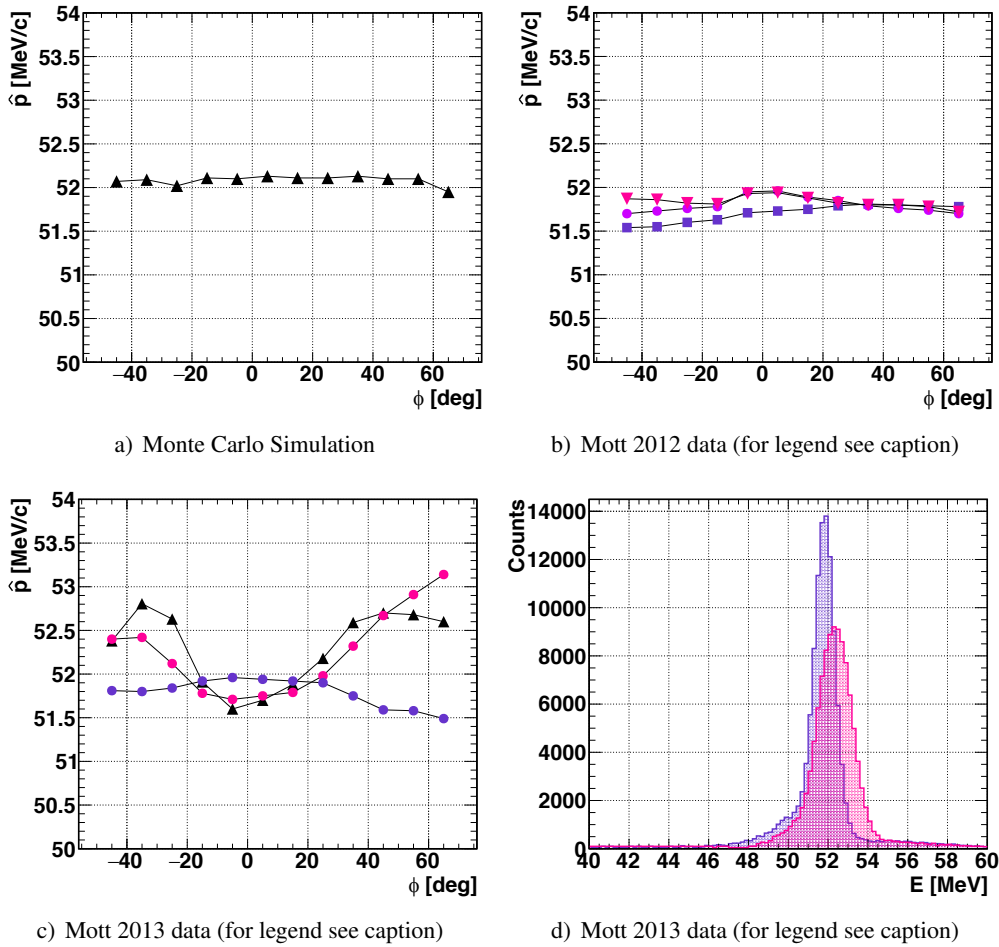


Figure 8.11: The first three plots show the Mott monochromatic line's peak position \hat{p} as a function of ϕ . The error bars are not visible, since the determination of the Mott monochromatic peak's position is quite precise. For perfectly aligned DCH modules, this curves should be flat, as can also be seen also from the Monte Carlo simulation a). In b), the following alignment methods are compared for the Mott 2012 data: Optical survey (dots), cosmic ray based alignment (squares), Michel positron based alignment (triangles). The curves are all very similar and essentially flat, indicating a satisfactory alignment. The last two plots show the 2013 data processed with the input of the survey alignment before (magenta) and after (purple) discovering the mistake in the survey measurement. For the wrong alignment the curve is clearly distorted, as displayed in c). This is also reproduced by the Monte Carlo simulation (black triangles). Accordingly, the positron energy spectrum is broadened and biased, as shown in d).

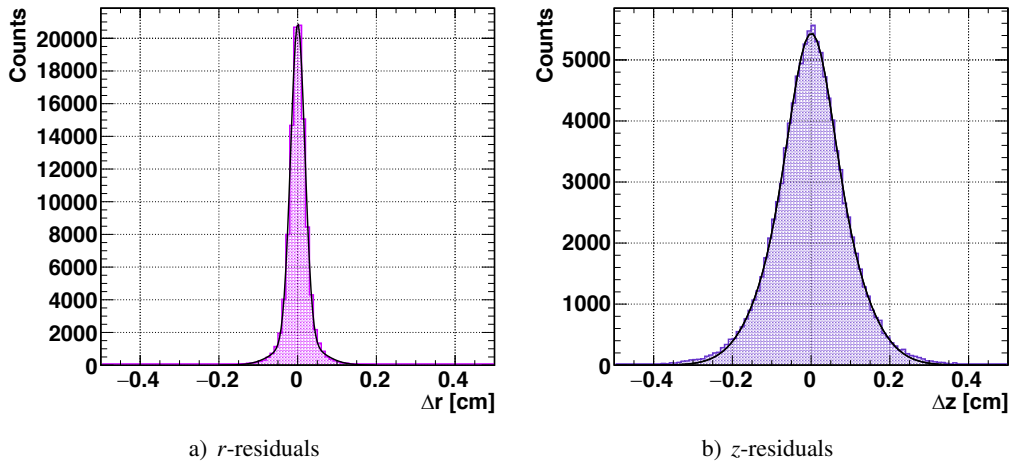


Figure 8.12: Example of a drift chamber’s distributions of the residuals in r and z between the reconstructed tracks and the DCH hits. It is worthy to note that from these distributions one can see that, as expected, the determination of the z -coordinate is less precise than the one of the r -coordinate (see also Sect. 4.3.2).

8.6.2 Performing the Drift Chamber Alignment with Mott Data

One of the three alignment procedures presented at the beginning of this section is based on an iterative algorithm which was applied to Michel positron data. Here, its application to Mott positron data is described. The algorithm is explained in what follows. The DCH modules were considered to be rigid objects with just two degrees of freedom, namely the radial position r and the longitudinal position z . Additionally, one assumed an initial position of the DCH modules (in general given by the optical survey). Then, the following steps were undertaken:

1. Process a set of raw data with the current alignment.
2. For every DCH module histogram the residuals in r and z between the reconstructed tracks and the actual DCH hits, resulting in double Gaussian distributions. Extract from a fit to these histograms the average residual in r and z . An example for the two distributions is displayed in Fig. 8.12.
3. For every DCH module subtract from its fitted average residual obtained in the previous step the average residual over *all* chambers, such that the mean of these modified residuals in both r and z over all chambers is equal to zero by construction. This makes sure that the alignment is to a certain extent tied to the alignment assumed at the very beginning.
4. Correct the position of the individual DCH modules by the amount obtained in the previous step and hand over the new positions to the data base.

This procedure was repeated until the residuals converged to $\lesssim 50 \mu\text{m}$. The alignment method was tested with Mott positron data from 2013, using the optical survey as a starting point. It

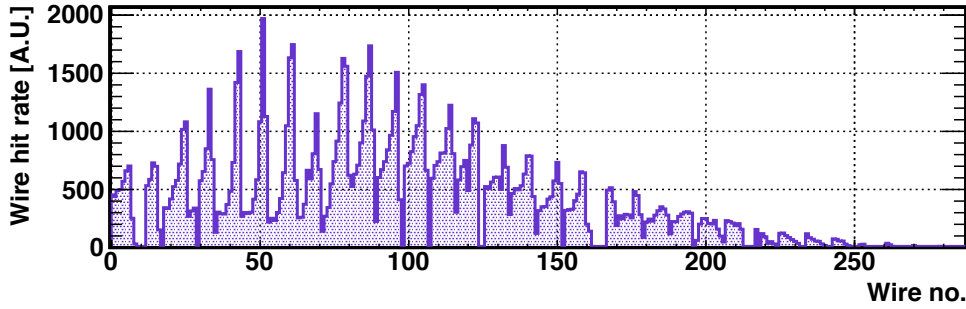


Figure 8.13: Wire hit map for the Mott 2013 data. The last few chambers are less densely populated due to trigger bias effects.

took four iterations for the residuals to fulfill the aforementioned condition. The amount of data, equivalent to 2.3 DAQ days, was sufficient, though it would have been advantageous to have additional data in order to increase the statistics in the last few DCH modules, as one can realize from Fig. 8.13. These last chambers were less populated because the trigger asks for five consecutive DCH hits, while the positrons move in the negative ϕ -direction with the consequence that at large, positive ϕ -angles, additional tracks which would normally lie outside the MEG signal acceptance (since the corresponding gamma does not match the calorimeter) pass the selection. The last two chambers were aligned on the basis of about 500 and 200 events, respectively, whereas the chambers with the highest statistics were aligned with $\mathcal{O}(100,000)$ tracks. The outcome of the alignment based on Mott data is shown and compared with the Michel positron data alignment in Fig. 8.14 by studying the Mott data itself. The behavior of the \hat{p} - ϕ curve (see Sect. 8.6.1) is very similar for both methods, with the consequence that also the Mott positron energy spectrum is practically identical. The number of reconstructed events was just slightly larger for the data processed with the Michel alignment, and also the peak position and the width were only marginally different, as shown in Table 8.2. In summary, the alignment with the Mott data worked fine and confirmed the results obtained by the application of the alignment procedure to Michel positron data.

Table 8.2: Comparison of the Mott monochromatic energy spectrum's parameters (number of events, peak position \hat{p} and the line's core Gaussian width σ_{core}) for data reprocessed based on the alignment obtained with Mott vs. Michel data (2013 dataset).

Parameter	Michel Alignment	Mott Alignment	Difference (Mott – Michel)
No. of events	80,339	79,059	-1.6 %
\hat{p} [MeV/c]	51.793 ± 0.003	51.762 ± 0.003	-31 keV/c
σ_{core} [keV/c]	491 ± 2	507 ± 3	+16 keV/c

8 The Mott Scattering Calibration Method

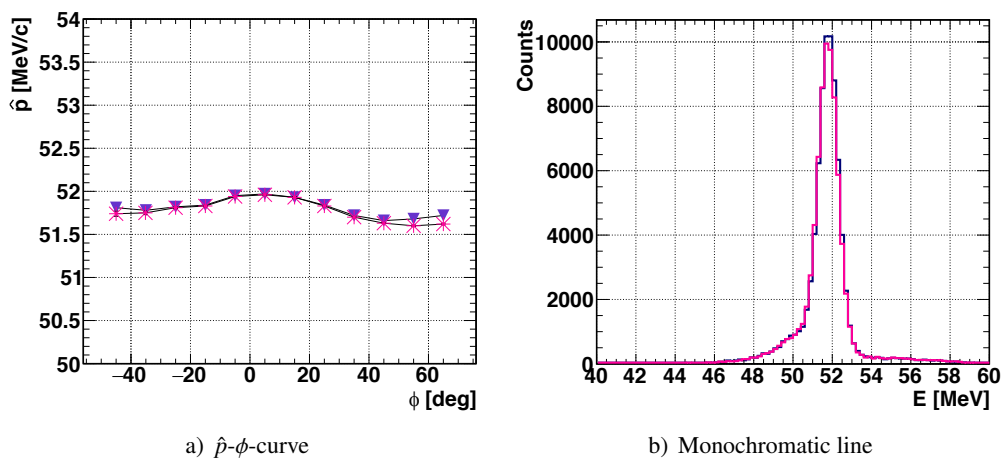


Figure 8.14: Results of the DCH alignment based on the Mott 2013 data (pink stars) vs. the Michel 2013 data (purple triangles), studied by looking at the Mott data itself. Both the \hat{p} - ϕ -curve and the Mott monochromatic energy spectrum are very similar.

9 The Final MEG Result

Based on the data accumulated in the years 2009 to 2013, the MEG experiment did not find any $\mu^+ \rightarrow e^+\gamma$ signal excess compared to the expected background and established the world's most stringent upper limit on the branching ratio of the $\mu^+ \rightarrow e^+\gamma$ decay [1],

$$\mathcal{B}(\mu^+ \rightarrow e^+\gamma) < 4.2 \times 10^{-13} \quad (90\% \text{ confidence level}). \quad (9.1)$$

This is a 30 times stronger bound than the one provided by the predecessor experiment MEGA [37].

The $\mu^+ \rightarrow e^+\gamma$ signature that MEG sought consisted in a muon decaying at rest into a $e^+\gamma$ -pair emitted time-coincidentally ($t_{e\gamma} = 0$), monochromatically ($E_\gamma = E_{e^+} = E_\mu/2$) and in a back-to-back configuration ($\Theta_{e\gamma} = 0$ or equivalently $\theta_{e\gamma} = 0$, $\phi_{e\gamma} = 0$). The average signal resolutions and detection efficiencies are reported in Table 4.1. Generally speaking, when one looks for a rare decay, one proceeds in two steps: First, one estimates the number of rare decay signal events N_{sig} (or an upper limit thereof) observed in the experiment. Second, one converts this number into a branching ratio by estimating the total number of muon decays k observed throughout the experiment's lifetime. The MEG collaboration performed a blind maximum likelihood analysis to estimate the number of signal events. The normalization factor k was determined based on two statistically independent samples. The confidence interval was calculated following the frequentist Feldman-Cousins approach. The next sections explain the procedure to extract the above result, the full analysis in all its details can be found in [1, 73].

9.1 Dataset and Blinding Procedure

The data used for the final MEG result were collected from 2009 to 2013, with regular proton accelerator shutdown periods of four to five months in between. The accumulated number of muons stopped on target is shown in Fig. 9.1. The first half of the dataset, namely data from the years 2009 to 2011, had already been published in the past and yielded a limit $\mathcal{B}(\mu^+ \rightarrow e^+\gamma) < 5.3 \times 10^{-13}$ at 90% confidence level. For the analysis of the full dataset, these older data were reblied and reprocessed, since in the meantime the reconstruction algorithms were updated.

In a first step, the data were preselected requiring at least one positron track candidate together with a loose cut on the relative timing between the LXe and the TC such as to reduce the data size. Whenever these data were reprocessed, and whenever an event fell into the blinding box defined by the window $48 \text{ MeV} < E_\gamma < 58 \text{ MeV}$ and $|t_{e\gamma}| < 1 \text{ ns}$, the event was written to a file inaccessible to the collaboration, in order to avoid the experimenters to be biased. The data which lay outside the blinding box ("sidebands") were used to check the data quality, optimize the algorithms, and estimate the backgrounds. Once the analysis algorithms and the calibrations were finalized, the blinding box was opened and the events therein analyzed. To estimate the number of signal events, the following subset ("analysis window") of the blinding box was used:

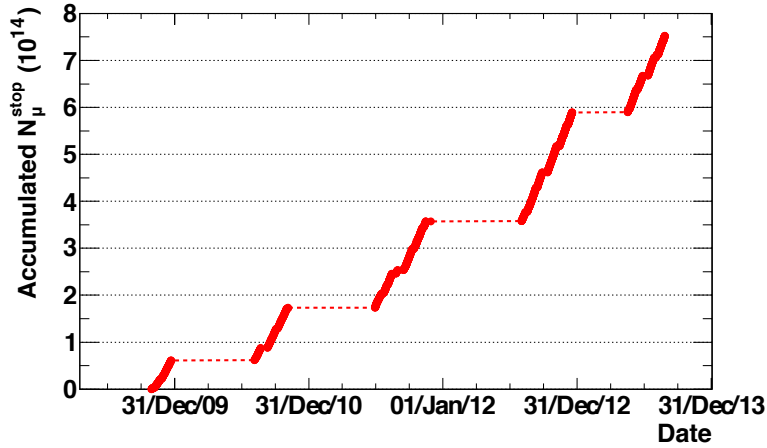


Figure 9.1: Accumulated number of muons stopped on target as a function of time. The dashed horizontal lines correspond to the proton accelerator shutdown periods.

- $48 < E_{\gamma} < 58$ MeV;
- $50 < E_e < 56$ MeV;
- $|t_{e\gamma}| < 0.7$ ns;
- $|\theta_{e\gamma}| < 50$ mrad;
- $|\phi_{e\gamma}| < 75$ mrad.

This window, with a size equivalent to five to twenty times the experimental resolutions, was sufficiently large to avoid the loss of good events and at the same time it was sufficiently small to keep the number of events to be fitted at an acceptable level. The $\phi_{e\gamma}$ -window was chosen a little wider because of the problems related to the target (see Sect. 9.9). The projection of the analysis window and the sidebands onto the $t_{e\gamma}$ - E_{γ} -plane is shown in Fig. 9.2. The timing sidebands contain mainly accidental background, the RMDs instead are located in the energy sideband in the region of zero relative timing.

9.2 Background Studies

As described in Sect. 1.4.1, the two sources of background to the $\mu^+ \rightarrow e^+\gamma$ decay search with MEG consisted in either RMDs $\mu^+ \rightarrow e^+\nu_e\bar{\nu}_{\mu}\gamma$ in which neutrinos carry away little energy, or in the accidental overlap of a positron from Michel decay $\mu^+ \rightarrow e^+\nu_e\bar{\nu}_{\mu}$ and a gamma originating in either AIF or RMD. The accidental and the RMD background were thoroughly studied based on the sideband data before opening the blinding box.

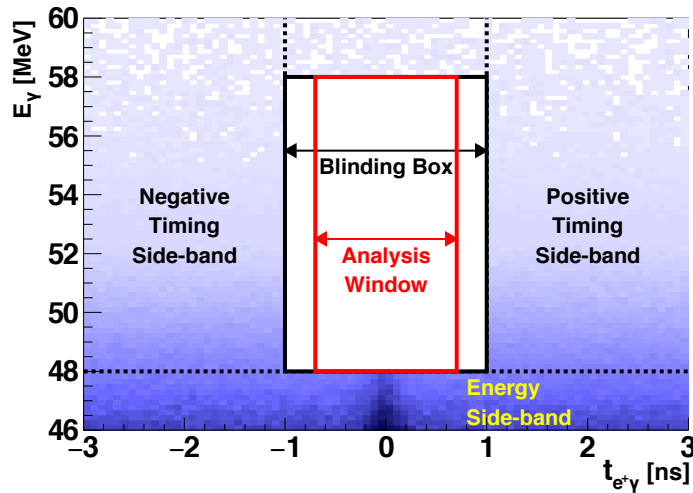


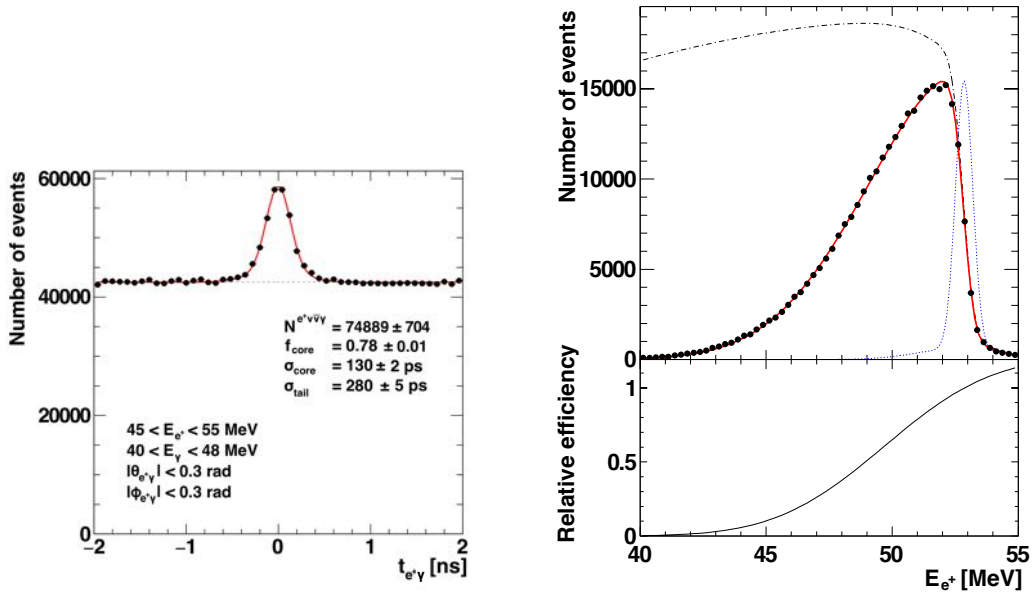
Figure 9.2: Blinding box and analysis window in the $t_{e\gamma}$ - E_γ -plane together with the timing and energy sidebands.

9.2.1 Radiative Muon Decay

The RMD data was studied in the energy sideband defined by $43 < E_\gamma < 48$ MeV, $48 < E_{e^+} < 53$ MeV, $|\phi_{e\gamma}| < 300$ mrad and $|\theta_{e\gamma}| < 300$ mrad. The distribution of the relative timing in this energy sideband (which contains both RMD and accidentals) is depicted in Fig. 9.3a). The rates and the differential distributions of the number of RMD events were found to be in good agreement with the leading order SM calculations. A detailed study of the RMD in the MEG experiment can be found in [74]. As an example, Fig. 9.4 shows the projected distributions as a function of the positron and gamma energy. The number of RMD events in the sidebands was extrapolated to the analysis window, where this estimate was used as a statistical constraint in the maximum likelihood analysis explained in the next section. The effective RMD branching ratio in the analysis window is highly suppressed, as can be understood from Fig. 9.5a).

9.2.2 Accidentals

The accidental background was studied in the timing sidebands. It was the dominant contribution to the MEG experiment, being ten to twenty times larger than the background caused by RMDs, see Fig. 9.5b). The energy spectrum of the accidental positrons, which stem essentially all from Michel decays, was extracted with high precision from data and is shown in Fig. 9.3b) together with the theoretically expected Michel spectrum. The theoretical spectrum is strongly distorted by the spectrometer's design, and the non-zero momentum resolution leads to a softening of the Michel decay's sharp kinematical edge. The photons instead may come from RMD or from AIF, where the positron annihilates with an electron in the material somewhere along its track and where the most energetic gamma reaches the LXe calorimeter. From simulations, the integrated photon yield is approximately equally shared between RMD photons and AIF photons for $E_\gamma \gtrsim 48$ MeV. For higher energies, AIF becomes dominant, while at the same time the



a) Relative positron-gamma timing distribution

b) Michel positron energy spectrum (top) and relative positron detection efficiency as a function of energy (bottom)

Figure 9.3: Relative positron-gamma timing and Michel positron energy spectrum measured in the sideband data (black dots). The flat part in a) is due to the accidental background, the peak is caused by RMD events. In b), the theoretical Michel positron energy spectrum (black dotted-dashed line), double Gaussian resolution function (blue dotted line) and the relative positron detection efficiency are shown, too.

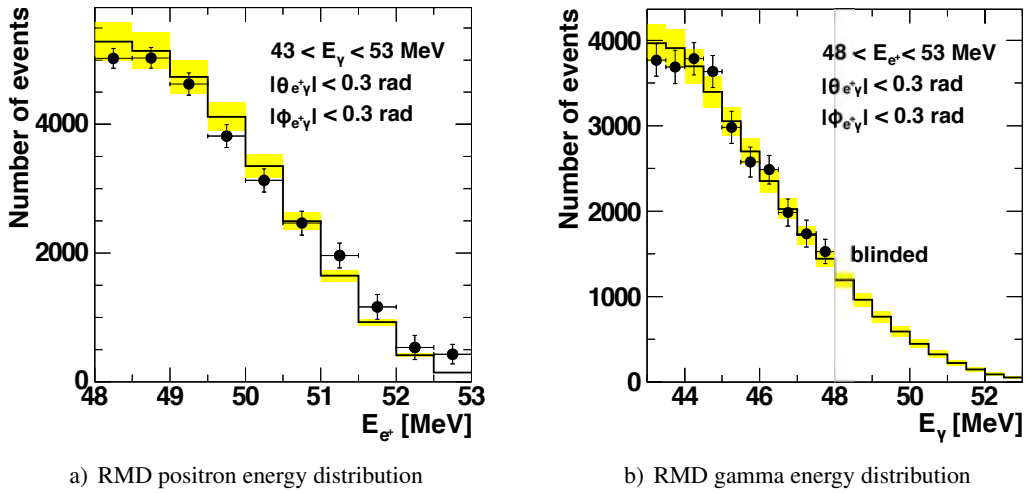


Figure 9.4: Differential distributions of RMD events measured in the energy sidebands (black dots with error bars). The black histogram, with the uncertainties shown as yellow bands, indicates the SM expectation folded with the detector response.

photon spectrum rapidly decreases. Other contributions such as pile-up photons or cosmic ray photons account for at most 6 % of the background and are rejected by dedicated algorithms and by topological cuts, respectively. The energy spectrum of the accidental photons, after applying the above algorithms and cuts, was directly measured in the sideband data.

9.3 Estimation of the Number of Signal Events

The number of signal events was estimated following the approach of maximum likelihood. For that purpose, one constructs the likelihood function \mathcal{L} , which is defined as

$$\mathcal{L}(\text{data} | \theta) = \prod_{i=1}^N p(\mathbf{x}_i | \theta), \quad (9.2)$$

with the Probability Density Functions (PDFs) $p(\mathbf{x}_i | \theta)$ and where the index i runs over the number of events N in the data. Each of these PDFs $p(\mathbf{x}_i | \theta)$ describes the probability to find the set of observables \mathbf{x}_i associated to the event i , given a set of parameters θ (e.g. the number of signal events) of the statistical model. In order to determine the best estimator $\hat{\theta}$ for the parameter set θ , \mathcal{L} is maximized with respect to θ , given the data. In the specific case of the MEG experiment, one used the extended likelihood, which takes into account the fact that the number of observed events in the analysis window is not known a priori and needs to be estimated itself (Poisson statistics):

$$\mathcal{L}(\text{data} | \theta) = \frac{N^{N_{\text{obs}}} e^{-N}}{N_{\text{obs}}!} \prod_{i=1}^{N_{\text{obs}}} p(\mathbf{x}_i | \theta). \quad (9.3)$$

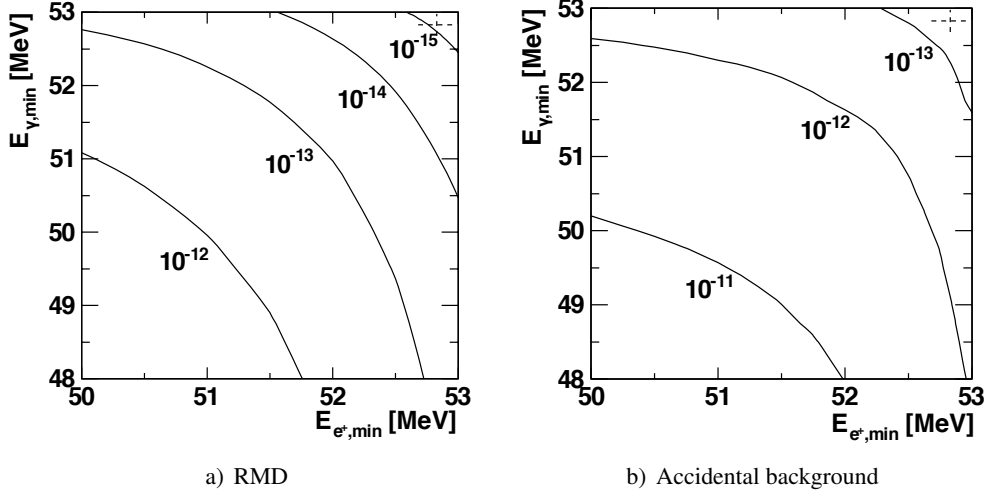


Figure 9.5: Effective branching ratios of the backgrounds in the MEG analysis window. The accidental background is about ten to twenty times higher than the background due to RMD.

For MEG, the parameter set encompasses the number of signal events N_{sig} , the number of RMD events N_{RMD} and the number of accidental background events N_{acc} , which are related by $N = N_{sig} + N_{RMD} + N_{acc}$. In addition, a parameter $\mathbf{t} = (z_0, k_t)$ associated to the position and the deformation of the target (see Sect. 9.9) was introduced. Actually, the only parameter of interest is N_{sig} . The remaining ones are so-called nuisance parameters, which means that later on, when calculating the confidence intervals, they are “integrated out” (“profiling”, see further below). These nuisance parameters are constrained by measurements in the sideband or by calibrations. The PDF $p(\mathbf{x}_i | \theta)$ is given by the weighted sum of the individual PDFs $S(\mathbf{x}_i, \mathbf{t})$, $R(\mathbf{x}_i)$ and $A(\mathbf{x}_i)$ for the signal, RMD and accidental background, respectively:

$$p(\mathbf{x}_i | \theta) = \frac{N_{sig}}{N} \cdot S(\mathbf{x}_i, \mathbf{t}) + \frac{N_{RMD}}{N} \cdot R(\mathbf{x}_i) + \frac{N_{acc}}{N} \cdot A(\mathbf{x}_i). \quad (9.4)$$

The set of observables $\mathbf{x}_i = \{E_\gamma, E_e, t_{e\gamma}, \phi_{e\gamma}, \theta_{e\gamma}\}$ comprises the gamma and the positron energy, the relative timing $t_{e\gamma}$ and the relative polar and azimuthal angles $\phi_{e\gamma}$, $\theta_{e\gamma}$ (the latter two are treated separately because the experimental resolutions are different). Putting everything together, the likelihood function used for the MEG analysis is:

$$\mathcal{L}(N_{sig}, N_{RMD}, N_{acc}, \mathbf{t}) = \frac{e^{-N}}{N_{obs}!} \times C(N_{RMD}, N_{acc}, \mathbf{t}) \times \prod_{i=1}^{N_{obs}} (N_{sig} \cdot S(\mathbf{x}_i, \mathbf{t}) + N_{RMD} \cdot R(\mathbf{x}_i) + N_{acc} \cdot A(\mathbf{x}_i)), \quad (9.5)$$

where the term C denotes the constraints on the nuisance parameters. For N_{RMD} and N_{acc} , the constraints consisted of Gaussians whose means and widths were given by the corresponding

values and errors estimated from the sidebands.

The PDFs $S(\mathbf{x}_i, \mathbf{t})$, $R(\mathbf{x}_i)$ and $A(\mathbf{x}_i)$ were all constructed on an event-by-event basis in order to take into account the dependence of the experimental resolutions from the detector conditions and the location where the muon decayed or where the particles were tracked. Also correlations among the observables (such as e.g. the correlation between the photon angle and the positron position error at the target) were considered event by event. The three PDFs were constructed in the following way:

- The signal PDF $S(\mathbf{x}_i, \mathbf{t})$, remembering that for the $\mu^+ \rightarrow e^+ \gamma$ decay the relative timing, the relative angle and the energies of the positron and gamma are fixed, is simply given by the product of the detector response functions for each of the five observables. The detector response of the LXe calorimeter in terms of energy was measured by the CEX calibration (see Sect. 4.5.2). The PDF for the relative timing $t_{e\gamma}$ was determined by considering RMDs in the energy sideband. The resolutions on the observable q entering the positron PDF were computed by multiplying the tracking variable's fitting error σ'_q with the corresponding pull parameter s_q which was extracted from double turn tracks (see Sect. 8.5.1). The pull parameters were identical for all events of a given DAQ period. In order to take into account a potential reconstruction bias due to the target displacement and deformation, the center of the $\phi_{e\gamma}$ PDF was shifted by a geometrically computed amount which was parametrized by \mathbf{t} (see Sect. 9.9).
- The PDF $R(\mathbf{x}_i)$ of the RMD is a convolution of the theoretically expected RMD kinematic distributions with the detector response functions described above.
- The PDF $A(\mathbf{x}_i)$ for the accidental background was constructed by considering the data in the timing sidebands, with the exception of $t_{e\gamma}$ whose distribution was assumed to be flat (verifying that it is truly flat in the sidebands).

Note that the PDFs for the accidental and RMD background are not functions of \mathbf{t} , since the effect of the target alignment and deformation for these two was measured in the respective sidebands. Once all PDFs and the nuisance parameter constraints were established, the number of signal events was estimated by maximizing the likelihood in Eq. (9.5) with respect to the parameters N_{sig} , N_{RMD} , N_{acc} and \mathbf{t} .

9.4 Toy Monte Carlo Simulations

The construction of the confidence interval and the assessment of the experiment's sensitivity described in the next few sections required to run some toy Monte Carlo simulations. These are not full simulations including all the single details of the experimental apparatus, the simulation of waveforms etc., but are rather based solely on the PDFs. Running many toys enables us to make some statistical statement about the experiment's outcome, on the one hand providing a confidence interval to the number of signals measured in the experiment, on the other hand calculating the sensitivity of the experiment. To study the statistical behavior of the experiment, the PDFs are sufficient since they already incorporate all our knowledge about the detectors. Every single toy Monte Carlo simulation ("pseudo-experiment") corresponds to one possible outcome

of the experiment, assuming a certain $\mu^+ \rightarrow e^+\gamma$ signal strength with the number of signal events being Poisson distributed. Systematic uncertainties are included by letting the relevant parameters vary randomly from toy to toy (but keeping them fixed for a particular toy). The following systematic uncertainties were taken into account: The uncertainty on the normalization factor k , the target alignment parameters (position and shape), the alignment of the LXe detector with the positron spectrometer, the E_γ scale, the E_e bias, the center of the $t_{e\gamma}$ PDF, the shapes of the signal and background PDFs and the correlation between errors of the positron observables. The target parameters were “profiled” (see below), the remaining ones were randomly varied within their uncertainties.

9.5 Construction of the Confidence Interval

Once the number of signal events has been estimated, the next step consists in providing a confidence interval, i.e. an upper and possibly a lower limit to the number of signal events yielded by the measurement or by the toy Monte Carlo simulation. The MEG collaboration adopted a frequentist perspective by constructing the confidence interval following the Feldman-Cousins unified approach [75] using the profile likelihood ratio ordering [76], explained in more detail below. In the frequentist interpretation, the confidence interval refers to the region which contains the true value N_{sig}^{true} with a probability specified to a certain level. For that purpose, one considers a statistical test of a hypothesis that assumes a particular number of signal events N_{sig} . By scanning the (physically sensible) values of N_{sig} , one tries to find the number of signal events N_{sig}^{UL} for which the corresponding hypothesis would be rejected at the specified confidence level (which in the case of MEG is 90 %), given the best estimate \hat{N}_{sig}^{data} from the data. The value N_{sig}^{UL} constitutes the upper limit at the specified Confidence Level (C.L.).

The test statistics is constructed from the profile likelihood ratio $\lambda = \lambda(N_{sig})$, defined as

$$\lambda(N_{sig}) = \begin{cases} \frac{\mathcal{L}(N_{sig}, \hat{\theta}(N_{sig}))}{\mathcal{L}(\hat{N}_{sig}, \hat{\theta})} & \text{if } \hat{N}_{sig} \geq 0 \\ \frac{\mathcal{L}(N_{sig}, \hat{\theta}(N_{sig}))}{\mathcal{L}(0, \hat{\theta})} & \text{if } \hat{N}_{sig} < 0 \end{cases} \quad (9.6)$$

where $\hat{\theta}$ and \hat{N}_{sig} denote the respective best estimates obtained by the maximum likelihood analysis when all the parameters N_{sig} , N_{RMD} , N_{acc} and \mathbf{t} can float freely, whereas $\hat{\theta}(N_{sig})$ indicates the corresponding best estimates when the number of signal events N_{sig} is fixed. Using this approach, the nuisance parameters are “profiled away”. The test statistics is given by

$$q(N_{sig}) = -2 \ln(\lambda(N_{sig})), \quad (9.7)$$

i.e. whenever the N_{sig} that we put subject to this test agrees well with the best estimate \hat{N}_{sig} , q is close to zero, whereas q tends to be large for N_{sig} which are incompatible with \hat{N}_{sig} . To compute the confidence interval for the estimated number of signal events in the data, one runs a lot of toy Monte Carlo simulations assuming a specific signal strength N_{sig} . For each of these toys, first, the best estimate \hat{N}_{sig} and the corresponding q -value is determined. In a second step, one calculates the q -value $q_{data}(N_{sig})$ of the data. This procedure is repeated for several

9 The Final MEG Result

values of N_{sig} . The confidence interval is given by the one¹, particular value N_{sig}^{UL} for which the corresponding q -value of the data is

$$q_{data}(N_{sig}^{UL}) < q_{toy}(N_{sig}^{UL}) \quad (9.8)$$

in 90 % (or the specified confidence level) of all the toy Monte Carlo simulations which assumed the signal strength N_{sig}^{UL} .

9.6 Evaluation of the Sensitivity

The sensitivity of MEG to the $\mu^+ \rightarrow e^+ \gamma$ decay was evaluated using toy Monte Carlo simulations which assume the background-only hypothesis, i.e. $N_{sig} = 0$, while on the one hand letting the number of accidental and RMD events, N_{acc} and N_{RMD} , fluctuate according to the Poisson statistics around the values estimated from the sideband studies, and on the other hand including the systematic uncertainties mentioned previously. For each of these pseudo-experiments, the 90 % C.L. upper limit on the branching ratio was calculated. The median of the so-obtained upper limits distribution is defined as the experiment's sensitivity. In order to study the contributions of the individual systematics, the sensitivity was calculated by including all systematics except the one under consideration.

9.7 Normalization

In order to convert the number of estimated signal events N_{sig} into a (limit on the) branching ratio \mathcal{B} , one needs to know how many muon decays k (“normalization factor”) were recorded during the physics run. Then, the branching ratio is given by

$$\mathcal{B}(\mu^+ \rightarrow e^+ \gamma) = \frac{\Gamma(\mu^+ \rightarrow e^+ \gamma)}{\Gamma_{total}} = \frac{N_{sig}}{k}, \quad (9.9)$$

where the Γ 's are the respective decay rates. The number of stopped muons N_μ and k are related by

$$k = N_\mu \times \langle A \times \varepsilon \rangle_{e\gamma}, \quad (9.10)$$

where A and ε denote the acceptance and efficiency of the MEG experiment. One often quotes the “single event sensitivity” defined by k^{-1} and which corresponds to the rare decay's branching ratio for which the experiment would be able to observe one event. The normalization factor was evaluated from two independent data samples: On the one hand from a sample of Michel decays, on the other from a sample of RMDs. The Michel decays were acquired with a dedicated, pre-scaled trigger which was enabled during the physics run. The RMDs sample consisted in the energy sideband data collected with the MEG signal trigger. Both samples are independent of the instantaneous beam rate because they were collected in parallel with the physics data. The

¹In the case of a one-sided limit, else the confidence interval is given by two values.

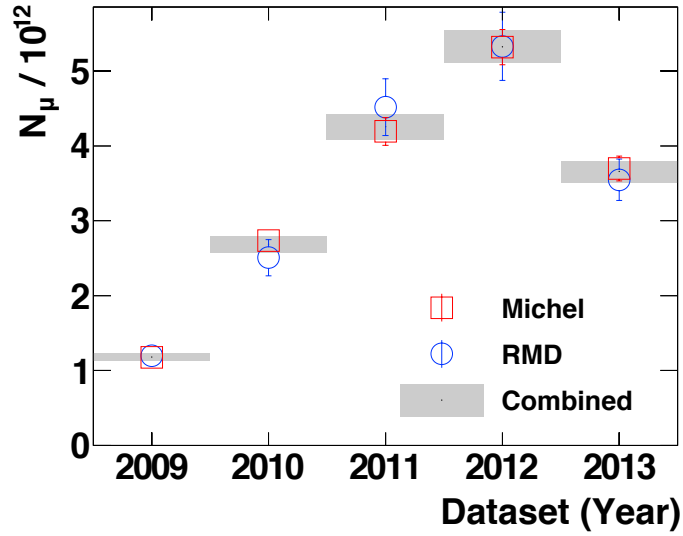


Figure 9.6: Normalization factor k for every year's dataset. The normalization factors were obtained from two independent samples (one consisting of Michel decays, one of RMDs) and combined by weighted averaging.

normalization factor is given by the number N_{Michel} , N_{RMD} of counted Michel decays and RMDs corrected for the corresponding branching fractions, acceptances and efficiencies,

$$k_{Michel, RMD} = \frac{N_{Michel, RMD}}{\mathcal{B}_{Michel, RMD}} \times \frac{\langle A \times \varepsilon \rangle_{e\gamma}}{\langle A \times \varepsilon \rangle_{Michel, RMD}}. \quad (9.11)$$

The two independent normalization factors agreed well and were combined by weighted averaging, yielding the normalization factor for the full dataset of $k = (1.71 \pm 0.06) \times 10^{13}$ muons (7.5×10^{14} muons stopped on target) or equivalently the single event sensitivity of $k^{-1} = (5.8 \pm 0.2) \times 10^{-14}$. The normalization factors for the different years' datasets are shown in Fig. 9.6.

9.8 Improvements in the Analysis

With respect to MEG's previous publication [77], two major improvements in the analysis were introduced: first, a new algorithm to recover tracks with a missing first turn, and second an algorithm to improve the AIF background rejection.

9.8.1 Missing First Turn Algorithm

Usually, the helicoidal positron tracks cross the DCH system more than once: On average they make 1.5 turns before hitting the TC. The tracking algorithm reconstructs each turn individually and in a second step tries to merge the turns into one trajectory, but occasionally it fails in doing so. Consequently, when the tracking algorithm misses the first turn, the decay vertex and ergo

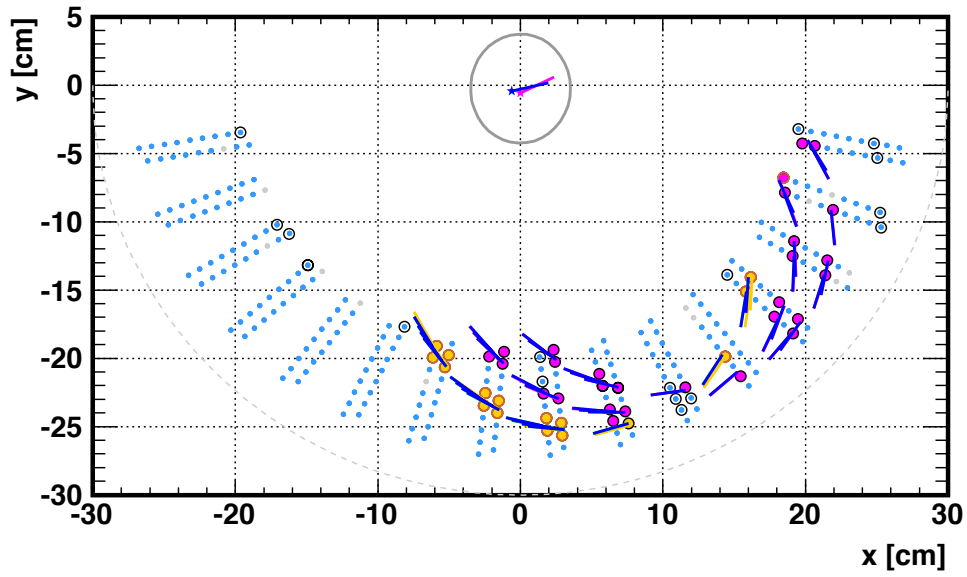
also the timing as well as the positron angles are wrongly reconstructed. In order to mitigate this effect, an additional algorithm was introduced to identify tracks with a missing first turn and refit them. An example of a recovered track is shown in Fig. 9.7. The overall positron track reconstruction efficiency could, as evaluated from Michel decay data, be increased by $\approx 4\%$ around the $\mu^+ \rightarrow e^+\gamma$ signal energy.

9.8.2 Annihilation-in-Flight Analysis

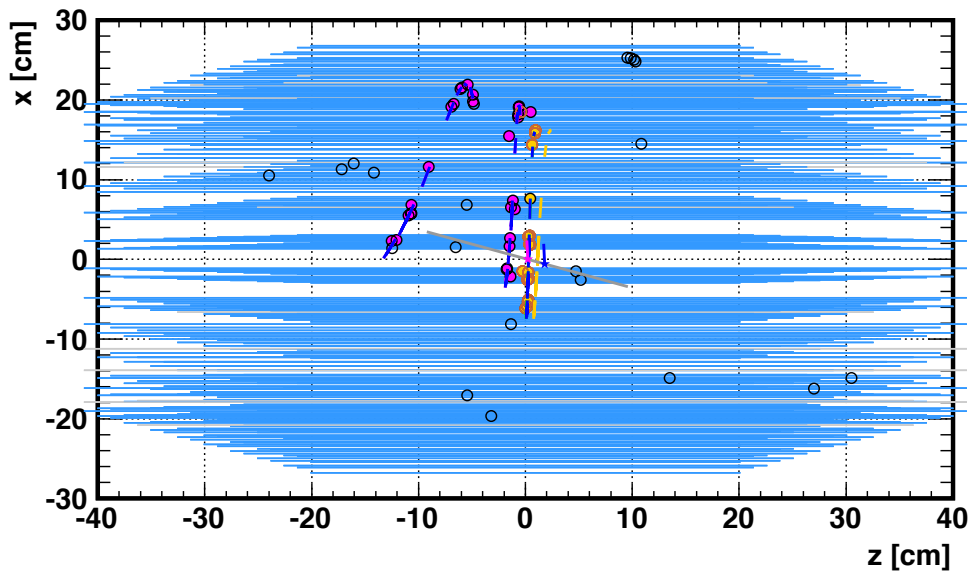
In order to increase the capability to reject background photons entering the calorimeter and stemming from AIF, which is the major photon background source in the energy region around the $\mu^+ \rightarrow e^+\gamma$ signal, an additional algorithm was applied to the data. This algorithm looks for DCH hits correlated with a gamma in the LXe that pertain to positrons which annihilate at some point in the DCH system. An example of a reconstructed AIF event is shown in Fig. 9.8. For every potential $e_{AIF}^+\gamma$ -pair (“candidate”), the relative timing and angular differences are computed, and, if there is more than one candidate in an event, ranked accordingly. Events with an AIF candidate featuring a relative angle close to zero were cut away. The fraction of additionally rejected AIF background amounted to $\approx 2\%$, with an additional inefficiency of $\approx 1\%$ on the detection of the $\mu^+ \rightarrow e^+\gamma$ signal.

9.9 Target Deformation Issue

In order to accurately reconstruct the muon decay vertex and the positron emission angles, it is essential to know the exact position of the target with respect to the DCH system, since the vertex is not directly measured, but is determined by propagating the reconstructed track back to the target. The alignment parameter with the largest impact on the vertex determination is the one along the axis perpendicular to the target plane. The target position was measured by surveying the cross marks on the target (see Sect. 4.2) with a theodolite. It became clear from these cross mark measurements that the target developed an increasing aplanarity with time, which was presumably caused by radiation damage and / or the dry helium atmosphere that the target was exposed to. The suspicion of dealing with a non-planar target was confirmed by a high-precision 3D laser scanner measurement performed at the end of 2013, shown in Fig. 9.9a). To do justice to the situation, the target was assumed to have a paraboloidal shape rather than being a simple plane. This is a fair approximation, since most of the vertices were concentrated at the center of the target, see Fig. 9.9b). For every year, the paraboloid’s extremum and the paraboloid curvatures were fitted to the cross mark measurements. An example of such a paraboloid fit is displayed in Fig. 9.9c) for the year 2013. The fitted values were cross-checked by examining the position of the target holes extracted from the reconstructed vertex distribution, in which the holes appear as dips. A dependence of the hole positions as a function of ϕ_e for example would suggest a systematic shift perpendicular to the target plane. From these considerations, the systematic uncertainty on the paraboloid’s fitted extremum was estimated as $\sigma_{z_0}^{sys} \approx 0.3$ mm for 2009 to 2012 and $\sigma_{z_0}^{sys} \approx 0.5$ mm for 2013, where z_0 denotes the paraboloid extremum’s z -coordinate in the target’s local coordinate system and which was included as a nuisance parameter. To take into account the non-paraboloidal deformations, a 2D-map of the difference

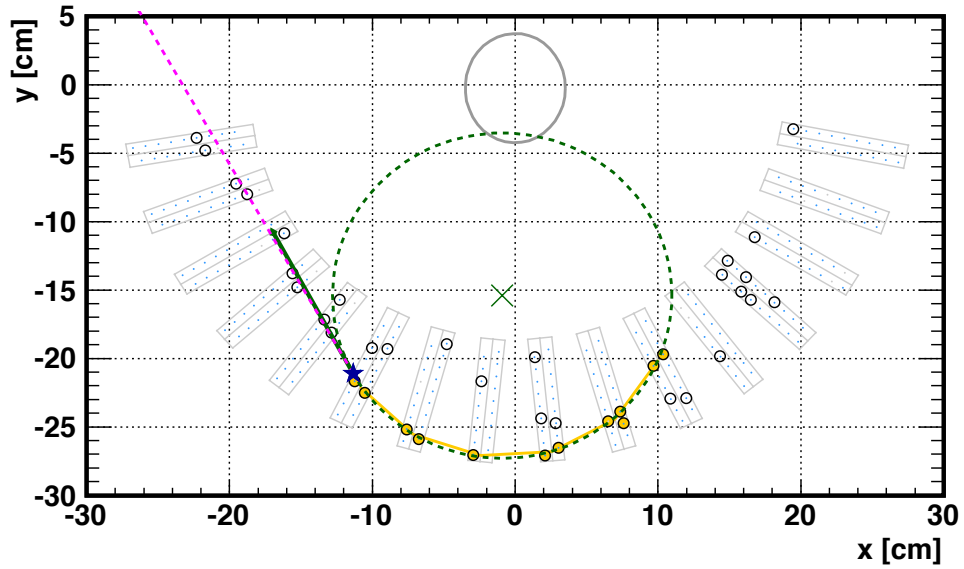


a) Transverse view

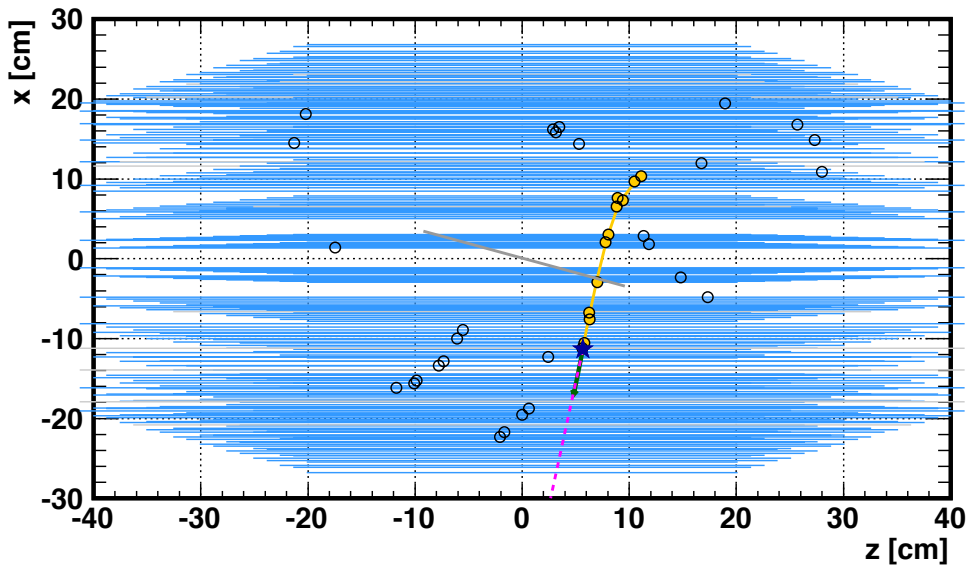


b) Longitudinal view

Figure 9.7: An example of a multitrack with a recovered first turn: The magenta points / star show the track / vertex reconstructed by the standard tracking algorithm. The yellow points / blue star show the track / vertex recovered by the missing first turn algorithm. The respective positron momentum vectors are also shown.

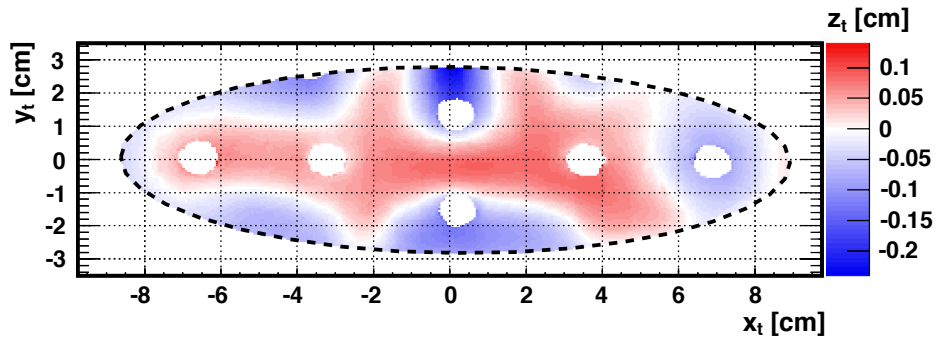


a) Transverse view

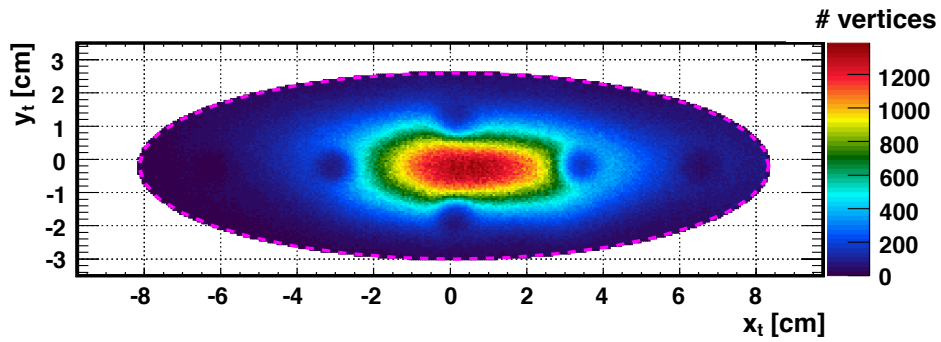


b) Longitudinal view

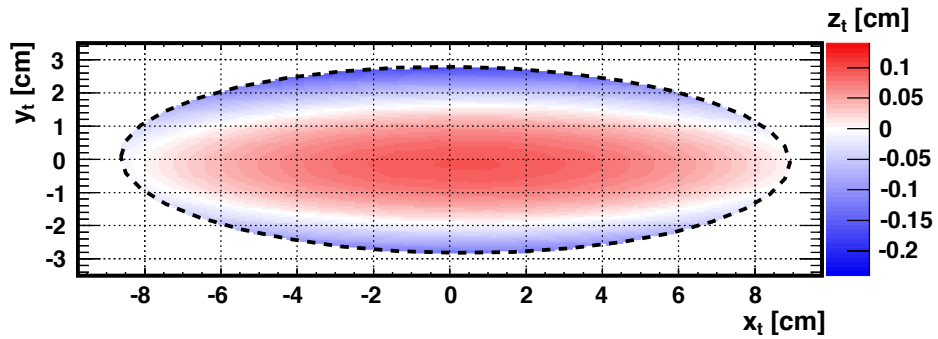
Figure 9.8: An example of a reconstructed AIF positron: The yellow points indicate the hits that the positron left in the DCH system before annihilating, the reconstructed vertex where the positron annihilated is shown as a blue star, the AIF direction is shown as a green arrow, and the magenta dashed line connects the AIF vertex with the photon interaction vertex in the LXe calorimeter.



a) Laser scan



b) Distribution of reconstructed vertices



c) Paraboloid fit

Figure 9.9: The muon stopping target exhibited an obvious aplanarity, as can be seen from a), which shows the 3D laser scan measurement performed at the end of 2013. The reconstructed decay vertex distribution on target is shown in b). The paraboloidal approximation to the deformed target is displayed in c). The paraboloidal fit and the laser scan agree well at the center of the target, where most of the muon decay vertices are located.

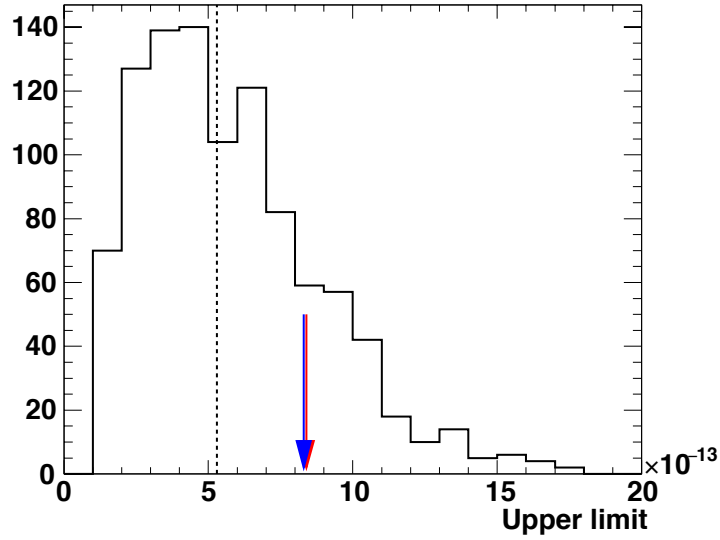


Figure 9.10: Distribution of the 90 % C.L. upper limits obtained from toy Monte Carlo simulations assuming the null-signal hypothesis. The MEG experiment’s sensitivity (dotted line) to the $\mu^+ \rightarrow e^+\gamma$ decay is given by the median upper limit of this distribution, and is equal to 5.3×10^{-13} . The red and blue arrows indicate the two upper limits determined from the left / right timing sideband as a consistency check of the analysis (see also Sect. 9.11).

between the paraboloidal fit and the laser scan was built, and the map was scaled by a year-dependent factor k_t entering the analysis as a nuisance parameter, too. The nuisance parameter constraints for z_0 were given by Gaussians with widths equivalent to the year-dependent systematic uncertainties, the constraints for the non-paraboloidal target deformation’s scaling factor k_t consisted in uniform distributions in year-dependent intervals.

9.10 Results

The full MEG dataset’s sensitivity is 5.3×10^{-13} , equivalent to the median of the upper limit distribution shown in Fig. 9.10 obtained from toy Monte Carlo simulations assuming the null-signal hypothesis. The uncertainty on the target alignment was found to be the major systematic uncertainty, degrading the sensitivity by 13 % on average; all the other uncertainties contributed $< 1\%$. In the analysis box, $N_{obs} = 8344$ events were found, without any significant correlated excess. The event distributions are displayed in Fig. 9.11. The corresponding best fit values were found to be $(\hat{N}_{sig}, \hat{N}_{RMD}, \hat{N}_{acc}) = (-3.8 \pm 3.6, 625 \pm 28, 7739 \pm 38)$, consistent with the null-signal hypothesis. Converting the fitted value for N_{sig} into a branching ratio yielded the best fit branching ratio of $(-2.2 \pm 2.1) \times 10^{-13}$. The negative log-likelihood ratio $-2 \ln(\lambda(N_{sig}))$ (see also Eq. (9.5) and (9.6)) as a function of the branching ratio is shown in Fig. 9.12. The

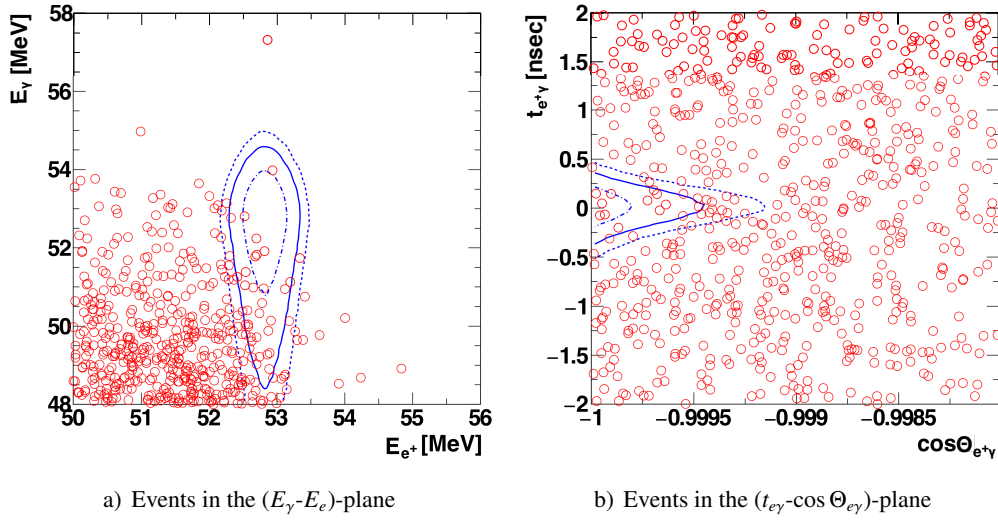


Figure 9.11: Event distributions in the analysis window projected onto the $(E_\gamma - E_e)$ - and $(t_{e\gamma} - \cos \Theta_{e\gamma})$ -plane together with the averaged 1σ , 1.64σ and 2σ signal PDF contours (blue curves). In the analysis box, $N_{obs} = 8344$ events were found. No significant correlated excess was observed.

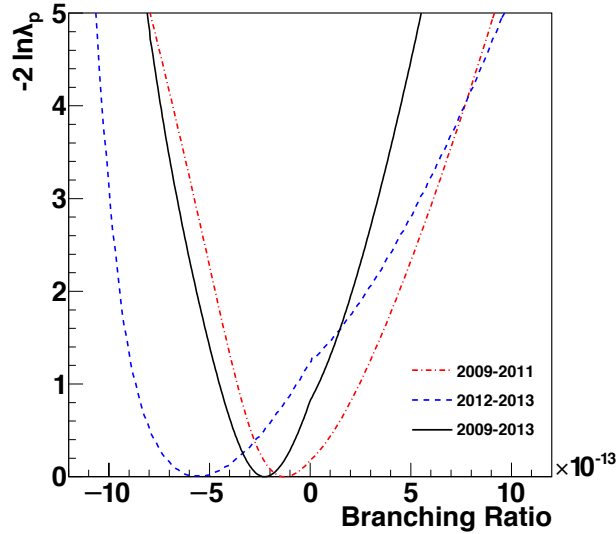


Figure 9.12: Negative log-likelihood ratio $-2 \ln(\lambda(N_{sig}))$ as a function of the branching ratio for the different data subsets. The best fitted branching ratios are given by the zero-crossings of these curves. The kink in the curves transiting from negative to positive values of the branching ratio is caused by the profiling of the target deformation parameter.

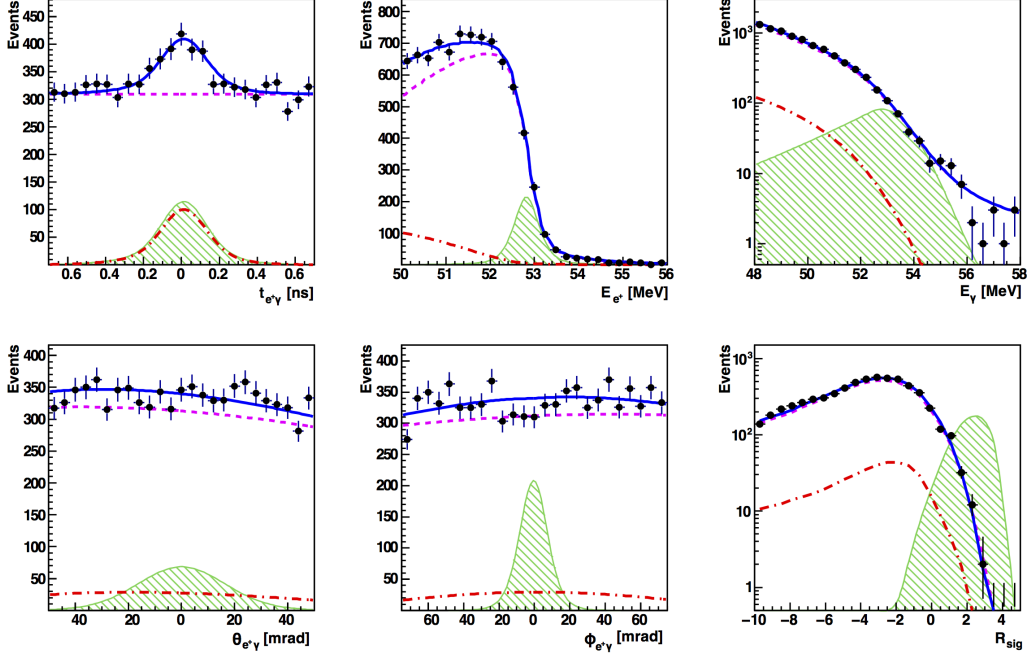


Figure 9.13: Projections of the best fitted likelihood function (blue line) to the five observables $t_{e\gamma}$, E_e , E_γ , $\theta_{e\gamma}$ and $\phi_{e\gamma}$ and the relative signal likelihood R_{sig} (defined in the text) together with the MEG data (black dots). The red dotted-dashed line indicates the fitted contribution of RMD background, the magenta dashed line represents the accidental background contribution, and the green histogram correspond to the $\mu^+ \rightarrow e^+\gamma$ signal PDF with a strength equivalent to 100 times the upper limit obtained from the MEG dataset.

kink in the curve transiting from negative to positive values of the branching ratio is caused by the profiling of the target parameter and is especially apparent for the 2012 to 2013 dataset, for which the target deformation had a non-negligible effect. The projections of the best-fitted functions on top of the data for each of the five observables is displayed in Fig. 9.13, showing a good agreement. The last plot Fig. 9.13f) shows the relative signal likelihood R_{sig} distribution, where

$$R_{sig} = \log_{10} \left(\frac{S(\mathbf{x}_i)}{f_R R(\mathbf{x}_i) + f_A A(\mathbf{x}_i)} \right), \quad (9.12)$$

with $f_R = 0.07$ and $f_A = 0.93$ denoting the expected fractions of RMD and accidental background events estimated from the sidebands.

The upper limit on the $\mu^+ \rightarrow e^+\gamma$ decay at 90 % C.L. was found to be $\mathcal{B}(\mu^+ \rightarrow e^+\gamma) < 4.2 \times 10^{-13}$. The systematic uncertainty due to the target alignment issue contributed 5 % to the upper limit, whereas all the other systematics made up $< 1\%$. The best fit branching ratios, the upper limits and the sensitivities for different subsets of the 2009 to 2013 dataset are listed in Table 9.1. The sensitivity of the MEG experiment reached by the end of the data taking in 2013 could not be further increased by collecting more statistics, since the background became too important.

In fact, the upgraded experiment MEG II is expected to feature experimental resolutions which are improved by a factor two, increasing the capability to reject the background and allowing to run at a higher muon beam rate (see Sect. 1.4.1 and 4.8).

Table 9.1: Best fitted branching ratios \mathcal{B}_{fit} , 90 % C.L. upper limits \mathcal{B}_{90} and sensitivities S_{90} for different subsets of the 2009 to 2013 dataset.

Dataset	2009 – 2011	2012 – 2013	2009 – 2013
$\mathcal{B}_{fit} \times 10^{-13}$	-1.3	-5.5	-2.2
$\mathcal{B}_{90} \times 10^{-13}$	6.1	7.9	4.2
$S_{90} \times 10^{-13}$	8.0	8.2	5.3

9.11 Additional Checks

The MEG result was cross-checked by performing an analysis using the relative stereo angle $\Theta_{e\gamma}$ and which was based on constant rather than event-by-event PDFs. The respective upper limit of $\mathcal{B}(\mu^+ \rightarrow e^+\gamma) < 4.3 \times 10^{-13}$ at 90 % C.L. was found to be in good agreement with the standard analysis. Running a dedicated set of toy Monte Carlo simulations showed a clear correlation between the upper limits of the two analyses, where the event-by-event PDF analysis featured a 20 % better sensitivity on average, as can be seen from Fig. 9.14. In addition, the analysis was repeated without setting any constraints on the nuisance parameters N_{RMD} and N_{acc} , and again the result was well-compatible with what was obtained by the default analysis. Moreover, the analysis was performed also in two fictitious analysis windows (more specifically in the timing sidebands centered at $t_{e\gamma} \pm 2$ ns) with a size equal to the standard MEG analysis window. The corresponding upper limits obtained were 8.4×10^{-13} and 8.3×10^{-13} , thus in good agreement with the expected sensitivity, see also Fig. 9.10. An additional check consisted in the comparison of the previously published result [77] of the 2009 to 2011 dataset,

$$\mathcal{B}(\mu^+ \rightarrow e^+\gamma) < 5.7 \times 10^{-13} \quad (90\% \text{ confidence level}). \quad (9.13)$$

with the present analysis. Since the analysis was revised, small changes were expected. The sensitivity turned out to be slightly worse and the upper limit a bit less stringent than the former result due to the more conservative systematic uncertainty attributed to the target alignment.

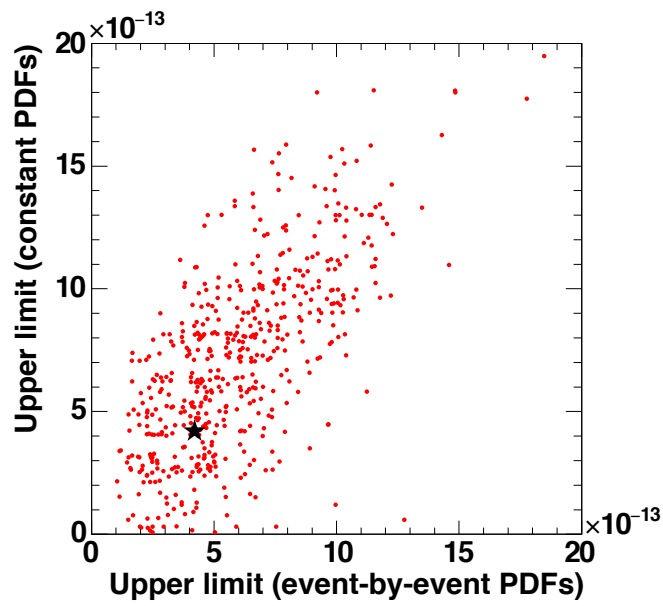


Figure 9.14: Upper limits at 90 % C.L. obtained from toy Monte Carlo simulations (assuming the null-signal hypothesis) with event-by-event PDFs and constant PDFs. The results of the two analyses are clearly correlated. The analysis based on event-by-event PDFs exhibits a $\approx 20\%$ better sensitivity than the one with the constant PDFs. The upper limit extracted from the data is shown as a black star.

Part IV

Synopsis

10 Summary Mu3e

The results obtained within the framework of this thesis show that the challenging demands posed by the future Mu3e experiment of having a scintillating fiber detector with a timing resolution below one nanosecond and a high detection efficiency for minimum ionizing particles with as little as three layers of 250 μm thin squared multicladd scintillating fibers read out by SiPMs can in principle be met. These studies investigated in depth and in a quantitative manner all the ingredients which enter the detector performances, from the point where the scintillation light is produced up to the photosensor that detects it. The most important results are summarized in Table 10.1.

Table 10.1: Timing resolutions σ_t together with the detection efficiencies ε_{AND} when triggering at the indicated threshold (0.5 or 1.5 Phe) on both sides of the fiber / detector (AND logic) and when irradiating the fibers perpendicularly to their central axes. The numbers are shown for a single fiber as well as for two and three layers of fibers, where every fiber is read out individually. In these cases, σ_t (RMS) was extracted from single Gaussian fits to the timing spectra. Additionally, the timing resolutions for the array configuration, where the information from three fibers in consecutive layers is combined offline and which comes closest to the proposed SiPM array readout, are presented. In these cases, σ_t represents the double Gaussian's core widths (RMS), where the core fraction is typically 75 %. The errors are statistical.

		Single	Double	Triple	Array
σ_t [ps]	(0.5 Phe)	1120 ± 10	820 ± 3	673 ± 4	572 ± 6
σ_t [ps]	(1.5 Phe)	804 ± 5	608 ± 6	504 ± 6	537 ± 5
ε_{AND} [%]	(0.5 Phe)	72 ± 1	89 ± 1	95 ± 2	95.8 ± 0.2
ε_{AND} [%]	(1.5 Phe)	34 ± 1	52 ± 1	67 ± 1	88.0 ± 0.3

From these numbers one can expect the requested timing resolutions and efficiencies to be achievable with the given baseline design if one is able to trigger at a threshold of 0.5 photoelectrons. Increasing the threshold to 1.5 photoelectrons would reduce the SiPM readout rate and improve the timing resolution at the cost of a detection efficiency drop.

The R&D concerning the understanding of the physics of the scintillating fibers can be considered to be concluded. The next steps in the development towards the construction of the full Mu3e fiber hodoscope are:

- Study of a fiber ribbon with the proposed SiPM array (Hamamatsu S10943) and MuTRiG readout electronics;

10 Summary Mu3e

- Study of the effects of the SiPM radiation damage (radiation damages of the scintillating fibers should not be an issue for Mu3e);
- Finalization of the mechanics, cooling and integration into the Mu3e experiment.

11 Summary MEG

The MEG experiment did not find any $\mu^+ \rightarrow e^+\gamma$ signal and set a new upper limit on its branching ratio,

$$\mathcal{B}(\mu^+ \rightarrow e^+\gamma) < 4.2 \times 10^{-13} \quad (90\% \text{ confidence level}),$$

based on the dataset collected in the years 2009 to 2013. This is a 30 times stronger bound with respect to the previous limit provided by MEGA [37] and represents an important guard rail for new physics models. A novel, powerful method to calibrate the positron spectrometer and making use of a Mott scattered positron beam, providing monochromatic tracks with energies close to the $\mu^+ \rightarrow e^+\gamma$ signal positron, was presented in this thesis. This calibration method was primarily conceived in view of the newly designed spectrometer of MEG II, which will feature a highly increased complexity with respect to the MEG experimental apparatus. The new calibration method was investigated on the basis of beam test data acquired with the MEG spectrometer. Even if this beam test was limited to a few days, the richness and quality of the data allowed to give also important inputs to the final MEG analysis. It was proven that the Mott calibration data indeed provide an extremely useful tool to study the spectrometer performance by considering the Mott positron energy spectrum as well as double turn tracks. Moreover, it was shown that the Mott calibration data can be used for drift chamber alignment purposes, where on the one hand they offer the possibility to perform a straightforward check of the alignment, and where on the other hand the alignment itself can be carried out on the basis of these calibration data.

In addition, a new auxiliary detector for MEG II in the form of a beam monitor system based on scintillating fibers read out by SiPMs was proposed. This beam monitor, consisting of a grid of 250 μm thin fibers with a pitch of a couple of mm, provides a quasi-non-invasive, fast and online measurement of the beam profiles and rates. It was proven by measurements at the MEG beam line that the beam profiles and rates provided by the scintillating fiber detector agree within better than 10 % with the standard beam monitor tools. In addition, it was shown that the scintillating fiber detector is capable of distinguishing different kinds of particle through charge discrimination or by time-of-flight measurements relative to the cyclotron's RF signal. The fiber beam monitor tool is strongly supported by the MEG collaboration. The radiation hardness of the detector still needs to be assessed in more detail, a dedicated beam test is currently being planned. If the radiation damage should be an issue, the fiber beam monitor will be implemented in a way that allows to move it into the beam during the beam calibration measurement and to retract it again afterwards, thus minimizing the exposure to the radiation.

Backmatter

Bibliography

- [1] A.M. Baldini et al. Search for the lepton flavour violating decay $\mu^+ \rightarrow e^+\gamma$ with the full dataset of the MEG experiment. *Eur. Phys. J. C*, 76(8):434, 2016. doi:10.1140/epjc/s10052-016-4271-x.
- [2] A.M. Baldini et al. MEG upgrade proposal, 2013. arXiv:1301.7225.
- [3] A. Blondel et al. Research proposal for an experiment to search for the decay $\mu \rightarrow eee$, 2013. arXiv:1301.6113.
- [4] U. Bellgardt et al. Search for the Decay $\mu^+ \rightarrow e^+e^+e^-$. *Nucl. Phys. B*, 299:1, 1988. doi:10.1016/0550-3213(88)90462-2.
- [5] Paul Scherrer Institute Database.
- [6] G.W. Bennett et al. Final report of the E821 muon anomalous magnetic moment measurement at BNL. *Phys. Rev. D*, 73(7):072003, 2006. doi:10.1103/PhysRevD.73.072003.
- [7] R. Pohl et al. The size of the proton. *Nature*, 466(7303):213, 2010. doi:10.1038/nature09250.
- [8] R. Pohl et al. Laser spectroscopy of muonic deuterium. *Science*, 353(6300):669, 2016. doi:10.1126/science.aaf2468.
- [9] W.J. Marciano and A.I. Sanda. Exotic Decays of the Muon and Heavy Leptons in Gauge Theories. *Phys. Lett.*, B67:303, 1977. doi:10.1016/0370-2693(77)90377-X.
- [10] T. Kajita. Nobel Lecture: Discovery of atmospheric neutrino oscillations. *Rev. Mod. Phys.*, 88:030501, 2016. doi:10.1103/RevModPhys.88.030501.
- [11] A.B. McDonald. Nobel Lecture: The Sudbury Neutrino Observatory: Observation of flavor change for solar neutrinos. *Rev. Mod. Phys.*, 88:030502, 2016. doi:10.1103/RevModPhys.88.030502.
- [12] G.M. Pruna and A. Signer. The $\mu^+ \rightarrow e^+\gamma$ decay in a systematic effective field theory approach with dimension 6 operators. *Journal of High Energy Physics*, 2014(10):14, 2014. doi:10.1007/JHEP10(2014)014.
- [13] G.M. Pruna and A. Signer. Lepton-flavour violating decays in theories with dimension 6 operators. *EPJ Web Conf.*, 118:01031, 2016. doi:10.1051/epjconf/201611801031.
- [14] A. Crivellin et al. Complementarity in lepton-flavour violating muon decay experiments. 2016. arXiv:1611.03409.

Bibliography

- [15] W. Bertl et al. Search for the decay $\mu^+ \rightarrow e^+e^+e^-$. *Nuclear Physics B*, 260(1):1, 1985. doi:10.1016/0550-3213(85)90308-6.
- [16] L. Bartoszek et al. Mu2e Technical Design Report. 2014. arXiv:1501.05241.
- [17] N. Hiroaki. DeeMe experiment – An experimental search for a mu-e conversion reaction at J-PARC MLF. *Nucl. Phys. B - Proc. Suppl.*, 248:52, 2014. doi:10.1016/j.nuclphysbps.2014.02.010.
- [18] R. Abramishvili et al. COMET Phase-I Technical Design Report, 2016. URL: http://comet.kek.jp/Documents_files/PAC-TDR-2016/COMET-TDR-2016_v2.pdf.
- [19] W. Bertl et al. A search for $\mu \rightarrow e$ conversion in muonic gold. *Eur. Phys. J. C*, 47(2):337, Aug 2006. doi:10.1140/epjc/s2006-02582-x.
- [20] G.M. Pruna et al. Fully differential NLO predictions for the rare muon decay. 2016. arXiv:1611.03617.
- [21] M. Fael and C. Greub. Next-to-leading order prediction for the decay $\mu \rightarrow e(e^+e^-)\nu\bar{\nu}$. 2016. arXiv:1611.03726.
- [22] R.M. Djilkibaev and R.V. Konoplich. Rare muon decay $\mu^+ \rightarrow e^+e^-e^+\nu_e\bar{\nu}_\mu$. *Phys. Rev. D*, 79:073004, 2009. doi:10.1103/PhysRevD.79.073004.
- [23] K. Nagamine. *Introductory Muon Science*. Cambridge University Press, 2003. doi:10.1017/CB09780511470776.
- [24] F. Berg et al. Target Studies for Surface Muon Production. *Phys. Rev. Accel. Beams*, 19(2):024701, 2016. doi:10.1103/PhysRevAccelBeams.19.024701.
- [25] P.-R. Kettle. HiMB: Towards a new high intensity muon beam. 2015. Future Muon Sources Workshop, University of Huddersfield. URL: <https://indico.cern.ch/event/356972/>.
- [26] V. Tishchenko et al. Detailed report of the MuLan measurement of the positive muon lifetime and determination of the Fermi constant. *Phys. Rev. D*, 87:052003, 2013. doi:10.1103/PhysRevD.87.052003.
- [27] J. Adam et al. The MEG detector for $\mu^+ \rightarrow e^+\gamma$ decay search. *Eur. Phys. J. C*, 73:2365, 2013. doi:10.1140/epjc/s10052-013-2365-2.
- [28] PiM1 beam line. URL: http://aea.web.psi.ch/beam2lines/beam_pim1.html [cited 2016-11-22].
- [29] R. Gilman et al. Technical Design Report for the Paul Scherrer Institute Experiment R-12-01.1: Studying the Proton “Radius” Puzzle with μp Elastic Scattering, 2016. URL: http://www.physics.rutgers.edu/~rgilman/elasticmup/muse_tdr_new.pdf.
- [30] PiE1 beam line. URL: <https://www.psi.ch/smus/pie1> [cited 2016-11-22].

Bibliography

- [31] H. Augustin et al. Technical Design Report: The Phase I Mu3e Experiment. 2017. In preparation.
- [32] I. Perić. A novel monolithic pixelated particle detector implemented in high-voltage CMOS technology. *Nucl. Instr. and Meth. in Phys. Res. A*, 582(3):876, 2007. doi:10.1016/j.nima.2007.07.115.
- [33] N. Berger et al. A tracker for the Mu3e experiment based on high-voltage monolithic active pixel sensors. *Nucl. Instr. and Meth. in Phys. Res. A*, 732:61, 2013. doi:10.1016/j.nima.2013.05.035.
- [34] H. Augustin et al. MuPix7 - A fast monolithic HV-CMOS pixel chip for Mu3e. *J. of Instr.*, 11(11):C11029, 2016. doi:10.1088/1748-0221/11/11/C11029.
- [35] H. Chen et al. MuTRiG: a mixed signal Silicon Photomultiplier readout ASIC with high timing resolution and gigabit data link. *J. of Instr.*, 12(01):C01043, 2017. doi:10.1088/1748-0221/12/01/C01043.
- [36] MIDAS. URL: <http://midas.psi.ch>.
- [37] M.L. Brooks et al. New limit for the lepton-family-number nonconserving decay $\mu^+ \rightarrow e^+\gamma$. *Phys. Rev. Lett.*, 83(8):1521, Aug 1999. doi:10.1103/PhysRevLett.83.1521.
- [38] A.M. Baldini et al. Muon polarization in the MEG experiment: predictions and measurements. *Eur. Phys. J. C*, 76(4):223, 2016. doi:10.1140/epjc/s10052-016-4047-3.
- [39] M. Cascella et al. Cluster Counting/Timing Techniques for Drift Chambers. *Nucl. Phys. B - Proc. Suppl.*, 248-250:127, 2014. doi:10.1016/j.nuclphysbps.2014.02.025.
- [40] Z. Hodge. PhD thesis, ETH Zurich and PSI Villigen, 2017. In preparation.
- [41] F. Berg. PhD thesis, ETH Zurich and PSI Villigen, 2017. In preparation.
- [42] E. Ripiccini. *An active target for the MEG experiment*. PhD thesis, Sapienza, Università di Roma, 2015.
- [43] J.B. Birks. *The Theory and Practice of Scintillation Counting*. Pergamon Press Oxford, 1964. URL: <http://www.sciencedirect.com/science/book/9780080104720>.
- [44] H. Kolanoski and N. Wermes. *Teilchendetektoren, Grundlagen und Anwendungen*. Springer-Verlag Berlin Heidelberg, 2016. doi:10.1007/978-3-662-45350-6.
- [45] Scintillating Optical Fibers Product Brochure. URL: <http://www.crystals.saint-gobain.com/sites/imdf.crystals.com/files/documents/fiber-brochure.pdf> [cited 2016-12-08].
- [46] W.B. Allan. *Fibre Optics, Theory and Practice*. Plenum Press London New York, 1973. doi:10.1007/978-1-4684-2040-1.

Bibliography

- [47] F. Barchetti. PSI Villigen, Switzerland.
- [48] Dr. M. Hildebrandt. PSI Villigen, Switzerland. Private communication.
- [49] BC-600 Optical Cement Data Sheet. URL: http://www.crystals.saint-gobain.com/sites/imdf.crystals.com/files/documents/sgc-bc600-data-sheet_69724.pdf [cited 2016-12-06].
- [50] M. Horisberger. PSI Laboratory for Scientific Developments and Novel Materials, Villigen, Switzerland. URL: <https://www.psi.ch/ldm-no-computing/sputtering-lab>.
- [51] T. Schneider. CERN Thin Film Lab Geneva, Switzerland. URL: <https://ep-dep-dt.web.cern.ch/thin-film-glass-service>.
- [52] S. Piatek. Physics and operation of the MPPC silicon photomultiplier, 2014. URL: http://www.hamamatsu.com/jp/en/community/optical_sensors/articles/physics_and_operation_of_mppc/index.html [cited 2016-12-08].
- [53] S. Piatek. Measuring the electrical and optical properties of the MPPC silicon photomultiplier, 2014. URL: http://www.hamamatsu.com/jp/en/community/optical_sensors/articles/measuring_characteristics_of_mppc/index.html [cited 2016-12-08].
- [54] Y. Munwes et al. Single photon time resolution with silicon photomultipliers using the STiC readout chip. *IEEE Nuclear Science Symposium and Medical Imaging Conference*, 2015. doi:10.1109/NSSMIC.2015.7581738.
- [55] Hamamatsu MPPC13360CS Data Sheet. URL: http://www.hamamatsu.com/resources/pdf/ssd/s13360_series_kapd1052e.pdf [cited 2016-12-06].
- [56] Hamamatsu MPPC12825-050C Data Sheet.
- [57] A. Stoykov, R. Scheuermann, and K. Sedlak. A time resolution study with a plastic scintillator read out by a Geiger-mode Avalanche Photodiode. *Nucl. Instr. and Meth. in Phys. Res. A*, 695:202, 2012. doi:10.1016/j.nima.2011.11.011.
- [58] Dr. Y. Yudin. Budker Institute of Nuclear Physics and Novosibirsk State University, Novosibirsk, Russia.
- [59] S. Ritt et al. Application of the DRS chip for fast waveform digitizing. *Nucl. Instrum. and Meth. A*, 623(1):486, 2010. doi:10.1016/j.nima.2010.03.045.
- [60] DRS4 Evaluation Board V5 Manual. URL: https://www.psi.ch/drs/DocumentationEN/manual_rev51.pdf.
- [61] ROOT. URL: <http://root.cern.ch>.

Bibliography

- [62] DuPont Tedlar Polyvinyl Fluoride (PVF) Films Datasheet, 2014. URL: http://www.dupont.com/content/dam/dupont/products-and-services/membranes-and-films/pvf-films/documents/DEC_Tedlar_GeneralProperties.pdf [cited 2016-12-08].
- [63] NIST PSTAR Stopping-Power and Range Tables for Protons. URL: <http://physics.nist.gov/PhysRefData/Star/Text/PSTAR.html>.
- [64] W. Busjan et al. Shortlived absorption centers in plastic scintillators and their influence on the fluorescence light yield. *Nucl. Instr. and Meth. in Phys. Res. B*, 152(1):89, 1999. doi:10.1016/S0168-583X(98)00974-4.
- [65] A.D. Bross and A. Pla-Dalmau. Radiation induced hidden absorption effects in polystyrene based plastic scintillator. *ACS Symp. Ser.*, 475:578, 1991. doi:10.1021/bk-1991-0475.ch037.
- [66] R. Hofstadter. Electron Scattering and Nuclear Structure. *Rev. Mod. Phys.*, 28:214, 1956. doi:10.1103/RevModPhys.28.214.
- [67] R. Hofstadter. Nuclear and Nucleon Scattering of High-Energy Electrons. *Ann. Rev. of Nucl. Sci.*, 7(1):231, 1957. doi:10.1146/annurev.ns.07.120157.001311.
- [68] W. Reuter et al. Nuclear charge distribution and rms radius of ^{12}C from absolute elastic electron scattering measurements. *Phys. Rev. C*, 26:806, 1982. doi:10.1103/PhysRevC.26.806.
- [69] C. Bemporad et al. Radiative and other Corrections to Coherent Mott Scattering on Light Nuclei. MEG Technical Note TN087, 2013. Unpublished.
- [70] N. Sherman. Coulomb Scattering of Relativistic Electrons by Point Nuclei. *Phys. Rev.*, 103:1601, 1956. doi:10.1103/PhysRev.103.1601.
- [71] R. Idoeta and F. Legarda. Calculation of electron polarization in the elastic electron and positron scattering by point nuclei. *Nucl. Instr. and Meth. in Phys. Res. B*, 88(3):203, 1994. doi:10.1016/0168-583X(94)95312-0.
- [72] V. Blobel. Software alignment for tracking detectors. *Nucl. Instr. and Meth. in Phys. Res. A*, 566:5, 2006. doi:10.1016/j.nima.2006.05.157.
- [73] D. Kaneko. *The final result of $\mu^+ \rightarrow e^+\gamma$ search with the MEG experiment*. PhD thesis, The University of Tokyo, 2016. URL: https://meg.web.psi.ch/docs/theses/kaneko_phd_final.pdf.
- [74] A.M. Baldini et al. Measurement of the radiative decay of polarized muons in the MEG experiment. *Eur. Phys. J. C*, 76:108, 2016. doi:10.1140/epjc/s10052-016-3947-6.
- [75] G.J. Feldman and R.D. Cousins. Unified approach to the classical statistical analysis of small signals. *Phys. Rev. D*, 57(7):3873, 1998. doi:10.1103/PhysRevD.57.3873.

Bibliography

- [76] K.A. Olive et al. Review of particle physics. *Chin. Phys. C*, 38:090001, 2014. doi: 10.1088/1674-1137/38/9/090001.
- [77] J. Adam et al. New constraint on the existence of the $\mu^+ \rightarrow e^+\gamma$ decay. *Phys. Rev. Lett.*, 110:201801, 2013. doi:10.1103/PhysRevLett.110.201801.

Acronyms

ADC	Analog-to-Digital Converter
AIF	Annihilation-In-Flight
APD	Avalanche Photodiode
ASIC	Application Specific Integrated Circuit
ATAR	Active Target
BGO	Bismuth Germanium Oxide (Bismuth Germanate) $\text{Bi}_4\text{Ge}_3\text{O}_{12}$
BNL	Brookhaven National Laboratory
BSM	Beyond the Standard Model
BTS	Beam Transport Solenoid
CAD	Computer Aided Design
CCD	Charge-Coupled Device
CERN	Conseil Européen pour la Recherche Nucléaire
CEX	Charge Exchange
C.L.	Confidence Level
cLFV	charged Lepton Flavor Violation
CMBL	Compact Muon Beam Line
COBRA	Constant Bending Radius
CTP	Crosstalk Probability
CW	Cockcroft-Walton
DAQ	Data Acquisition
DC	Direct Current
DCB	Data Concentrator Board
DCH	Drift Chamber
DRS	Domino Ring Sampler
DS	Downstream
ECR	Electron Cyclotron Resonance
FPGA	Field Programmable Gate Array
G-APD	Geiger Avalanche Photodiode
GEANT	Geometry And Tracking
GPU	Graphics Processing Unit
GSPS	Giga Samples Per Second
HIP	High Intensity Proton Accelerator
HV-MAPS	High Voltage Monolithic Active Pixel Sensor
IC	Internal Conversion
LED	Light Emitting Diode
LVDS	Low Voltage Differential Signaling
LXe	Liquid Xenon

Acronyms

LYSO	Lutetium Yttrium Oxyorthosilicate
MAR	Monolithic Amplifier
MIDAS	Maximally Integrated Data Acquisition System
MIP	Minimum Ionizing Particle
MPPC	Multi Pixel Photon Counter
MuLan	Muon Lifetime Analysis
MuPix	Mu3e Pixel Sensor
MUSE	Muon Scattering Experiment
μSR	Muon Spin Resonance
MuTRiG	Muon Timing Resolver Gigabit-link
PCB	Printed Circuit Board
PDE	Photon Detection Efficiency
PDF	Probability Density Function
PET	Positron Emission Tomography
PLL	Phase-Locked Loop
PMMA	Polymethylmethacrylate C ₅ H ₈ O ₂
PMNS	Pontecorvo-Maki-Nakagawa-Sakata
PMT	Photomultiplier tube
PSI	Paul Scherrer Institute
PVD	Physical Vapor Deposition
RDC	Radiative Decay Counter
RF	Radio Frequency
RGE	Renormalization Group Equation
RMD	Radiative Muon Decay
RMS	Root Mean Square
SCA	Switched Capacitor Array
SES	Single Event Sensitivity
SiPM	Silicon Photomultiplier
SINQ	Swiss Spallation Neutron Source
SM	Standard Model
SPTR	Single Photon Timing Resolution
STiC	SiPM Timing Chip
TC	Timing Counter
TCB	Trigger Concentrator Board
TOF	Time-Of-Flight
US	Upstream
VME	Versa Module Eurocard
VUV	Vacuum Ultra Violet
WaveDREAM	Waveform DRS4 based Readout Module